

DEVELOPMENT AND CHARACTERIZATION OF HIGH POWER DENSITY
CATHODE MATERIALS FOR LITHIUM-ION BATTERIES

A THESIS SUBMITTED TO
THE GRADUATE SCHOOL OF NATURAL AND APPLIED SCIENCES
OF
MIDDLE EAST TECHNICAL UNIVERSITY

BY

ŞAFAK DOĞU

IN PARTIAL FULFILLMENT OF THE REQUIREMENTS
FOR
THE DEGREE OF DOCTOR OF PHILOSOPHY
IN
MICRO AND NANOTECHNOLOGY

MAY 2015

Approval of the Thesis:

**DEVELOPMENT AND CHARACTERIZATION OF HIGH POWER
DENSITY CATHODE MATERIALS FOR LITHIUM-ION BATTERIES**

Submitted by **ŞAFAK DOĞU** in partial fulfillment of the requirements for the degree of **Doctor of Philosophy in Micro and Nanotechnology Department, Middle East Technical University** by,

Prof. Dr. Gülbin Dural Ünver
Dean, Graduate School of **Natural and Applied Sciences** _____

Prof. Dr. Tayfun Akın
Head of Department, **Micro and Nanotechnology** _____

Prof. Dr. Mehmet Kadri Aydınol
Supervisor, **Metallurgical and Materials Engineering Dept., METU** _____

Prof. Dr. Zafer Evis
Co-Supervisor, **Engineering Sciences Dept., METU** _____

Examining Committee Members:

Prof. Dr. Tayfur Öztürk
Metallurgical and Materials Engineering Dept., METU _____

Prof. Dr. Mehmet Kadri Aydınol
Metallurgical and Materials Engineering Dept., METU _____

Assoc. Prof. Dr. Y. Eren Kalay
Metallurgical and Materials Engineering Dept., METU _____

Assoc. Prof. Dr. H. Emrah Ünalın
Metallurgical and Materials Engineering Dept., METU _____

Assoc. Prof. Dr. Z. Göknur Cambaz Büke
Material Science and Nanotechnology Engineering Dept., TOBB-ETU _____

Date: .../.../.....

I hereby declare that all information in this document has been obtained and presented in accordance with academic rules and ethical conduct. I also declare that, as required by these rules and conduct, I have fully cited and referenced all material and results that are not original to this work.

Name, Surname: ŞAFAK DOĞU

Signature:

ABSTRACT

DEVELOPMENT AND CHARACTERIZATION OF HIGH POWER DENSITY CATHODE MATERIALS FOR LITHIUM-ION BATTERIES

Doğu, Şafak

Ph.D., Department of Micro and Nanotechnology

Supervisor : Prof. Dr. Mehmet Kadri Aydınol

Co-supervisor: Prof. Dr. Zafer Evis

May 2015, 175 pages

In this thesis, facile and cost efficient aqua based synthesis method is developed to synthesize power dense and fast rechargeable LiFePO_4 cathode materials. In order to obtain nano sized crystal morphology, nucleation controlled techniques were studied on precursor synthesis. These techniques are freeze (cryogenic) drying with co-precipitation and ultrasound assisted sub-sequential precipitation with vacuum drying at low temperatures (<350 K).

In co-precipitation with freeze drying synthesis, star-like platelet LiFePO_4 was synthesized while ultrasound assisted sub-sequential precipitation synthesis yielded 2D polycrystalline nano-plate structures around 100 nm thickness which has high tap density. The morphology of particles was diverted by manipulation of nucleation and crystallization processes and then preserved with carbon encapsulation strategy before LiFePO_4 formation through calcination. The highest discharge capacity is found as 140.3 mAhg^{-1} at 0.1C cycling rate for LiFePO_4/C synthesized by ultrasound assisted sub-sequential precipitation and carbonized via CVD.

The highest and durable electrochemical performance was achieved with sucrose encapsulated LiFePO_4/C where the thinnest plate-like LiFePO_4 (40 – 100 nm) was synthesized via ultrasonicated formation of vivianite precursors. The rechargeable

capacities are found as 125.1 and 89.2 mAhg⁻¹ at slow (0.1C) and fast (1C) discharge rates, respectively. Regarding to these slow and fast rated discharge capacities, higher capacity retentions (82 – 90%) were observed as 103.8 and 81 mAhg⁻¹ coulombic capacities even after less than 1 hour fast charging. Through this synthesis technique, especially in fast charging, it is able to achieve more discharge capacity than other high temperature hydro/solvothermal synthesis.

Keywords: Ultrasound, reactive crystallization, sub-sequential precipitation, co-precipitation, freeze drying.

ÖZ

LİTYUM İYON BATARYALAR İÇİN YÜKSEK GÜÇ YOĞUNLUKLU KATOT MALZEMESİ GELİŞTİRİLMESİ VE KARAKTERİZASYONU

Doğu, Şafak

Doktora, Mikro ve Nanoteknoloji Bölümü

Danışman : Prof. Dr. Mehmet Kadri Aydınol

Eş danışman : Prof. Dr. Zafer Evis

Mayıs 2015, 175 sayfa

Bu tezde, yüksek güç yoğunluklu ve hızlı şarj edilebilen LiFePO₄ katot malzemelerinin sentezlenmesi amacıyla kolay ve düşük maliyetli su bazlı sentez yöntemi geliştirilmiştir. Nano boyutlu kristal morfolojinin elde edilmesi için çekirdeklenme kontrollü öncül sentez teknikleri üzerine çalışılmıştır. Bu teknikler dondurucu (kriyojenik) kurutma ile takip edilen eş-çöktürme ve düşük sıcaklıklarda (350K) yapılan vakum kurutma kullanılan ultrasonik ardışık çöktürme yöntemleridir.

Dondurarak kurutma uygulanan eş-çöktürme yönteminde yıldız şekilli levha morfolojisinde LiFePO₄ üretilirken, ultrasonik ardışık çöktürme yöntemiyle 100 nm kalınlığında, yüksek sıkıştırma yoğunluğuna sahip iki boyutlu, çok kristalli nano tabakalı yapılar elde edilmiştir. Parçacık morfolojisi çekirdeklenme ve kristalizasyon prosesleri yönlendirilerek çeşitlendirilmiş ve ardından kalsine edilerek yapılan LiFePO₄ oluşumundan önce karbonla sarma stratejisi ile korunmuştur. En yüksek deşarj kapasitesi, 0,1C çevrim hızında CVD yöntemiyle karbon kaplanan ultrasonic ardışık çöktürmeyle sentezlenmiş LiFePO₄/C malzemesinde 140,3 mAhg⁻¹ olarak elde edilmiştir.

En yüksek ve dayanıklı elektrokimyasal performans, ultrasonlanmış viviyanit öncül bileşiklerinin oluşumu ile gerçekleştirilen ultrasonik ardışık çöktürme yöntemi kullanılarak üretilen en ince tabakalı LiFePO₄ (40 – 100nm) sukrozla sarmalanmış halinden elde edilmiştir. Tekrar şarj edilebilir yük kapasiteleri sırasıyla 0,1C ve 1C deşarj akımlarında 125,1 ve 89,2 mAhg⁻¹olarak bulunmuştur. Bu yavaş ve hızlı şarj kapasitelerine göre, bir saatten az sürede gerçekleştirilen hızlı şarj (1C) işleminden sonra dahi, sırasıyla, 0,1 ve 1C deşarj akımlarında; 103,8 ve 81 mAh g⁻¹kulombik kapasite veren yüksek kapasite tutma oranları (82 – 90%) gözlenmiştir. Bu sentez yöntemiyle, özellikle 1C hızlı şarj akımında, yüksek sıcaklıklı hidro/solvotermal sentez yöntemlerine kıyasla daha yüksek deşarj kapasitelerine ulaşmak mümkündür.

Anahtar Sözcükler: Ultrason, reaktif kristalizasyon, ardışık çöktürme, eş-çöktürme, dondurarak kurutma.

DEDICATION

*My light, and my pot,
My dream, and my hope,
My fellow! Feed my soul;
My secret fire! Kindle my core.*

To my lovely wife...

ACKNOWLEDGMENTS

I would like to express my sincere gratitude to my supervisor, Prof. Dr. Mehmet Kadri Aydınol, for all of his endless support and valuable comments. Sharing his knowledge and scientific guidance helped this thesis to become real. It has been a unique and inspiring experience.

I am also glad to share our group laboratories with my helpful lab-mates Berke Pişkin, Orkun Mugan, Esin Camcı, and Burcu Kayıplar, Burçin Kaygusuz. I also appreciate the support and self-denying efforts from Barış Alkan and Hazar Şeren as my voluntary lab-mates, namely, I've had the pleasure and opportunity to work with.

My honest regards go to Dr. Eren Kalay for his enlightening suggestions, provisions and care throughout my research. Without the scientific talks that I had with him, it would not be possible to find answers for challenges. His patience and endless support apart from the research inspired me for future. I also would like to thank to his group members, Mustafacan Kutsal, and Mertcan Başkan, for helping me many times in kind. And I would like to specially thank to Serkan Yılmaz for his great effort in TEM sessions during my studies in electron microscopy facilities.

Furthermore, many thanks go to Dr. Göknur Cambaz Büke and my co-advisor Dr. Zafer Evis for their advices and guidance in writing this dissertation.

I wish to extent my thanks Dr. Raşit Turan and his group members Olgu Demircioğlu, Mehmet Karaman, Serim Kayacan İlday, for their inevitable helps, friendship, and scientific discussions.

I would like to acknowledge Department of Metallurgical and Material Engineering at METU for providing access to their facilities. I also want to thank to Ministry of Science, Industry and Technology (SANTEZ project no. 00714.STZ.2010-2) for financial support during my research studies. I wish to thank my former manager Dr. Hulki Büyükkalender, for providing his valuable time and keen interest in every stage of my career. His scientific approaches and mentoring kept my enthusiasm up.

I owe a deep appreciation to my family, Kamuran & Aytufan Dođu, and Mustafa & Fatma Kçükayan for their unconditional love, endless emotional support and encouragement during my life to kindle my passion for science.

I am most grateful to my wife Gke Kçükayan Dođu for her never-ending love and encouragement to restore my self-confidence in every harsh moment in this journey. Her belief in me always inspired me throughout my career. Her consistent support and motivation have meant everything to me. I could not imagine to complete this dissertation without her supports.

TABLE OF CONTENTS

1. Future of energy demand and storage technology	1
1.1 Fundamentals of electrochemical storage and batteries	2
1.2 Thesis objectives	3
1.2.1 Originality of the study.....	5
2. Background and literature.....	7
2.1 Rechargeable lithium ion batteries	7
2.1.1 Kinetics of intercalation compounds.....	8
2.2 Cathode materials for lithium-ion batteries	10
2.3 Structure and properties of LiFePO_4	12
2.3.1 Lithium diffusion mechanism in LiFePO_4 crystals and nano structured materials.....	14
2.3.2 Electrical and ionic conductivity in LFP	15
2.4 Recent developments in cathode materials for lithium-ion batteries	16
2.5 Synthesis of LiFePO_4	17
2.5.1 Co-precipitation	17
2.5.2 Freeze drying	18
2.5.3 Sub-sequential precipitation	20
2.5.4 Ultrasonic wave treatment and sonocrystallization.....	21
2.5.5 Other synthesis methods for LiFePO_4 cathode material.....	25
3. Methodology	27
3.1 Raw materials.....	28

3.2	Precursor synthesis for LiFePO ₄ formation	29
3.2.1	Co-precipitation	31
3.2.2	Sub-sequential precipitation	34
3.3	Preparing LiFePO ₄ /C cathode powders by calcination and carbonization ..	39
3.3.1	Calcination as a solid state transformation to LiFePO ₄ /C nano-composite	39
3.3.2	Carbon coating and encapsulation strategies	40
3.4	Material characterization.....	42
3.4.1	Scanning Electron Microscopy and Energy Dispersive X-Ray analysis.	42
3.4.2	Transmission Electron Microscopy and Selected Area Electron Diffraction analysis	42
3.4.3	X-Ray diffraction analysis	43
3.4.4	Raman spectroscopy	43
3.4.5	Particle size measurement	43
3.4.6	Differential scanning calorimetry	44
3.4.7	Electrode and cell making procedures	44
3.4.8	Galvanostatic measurements and electrochemical impedance spectroscopy	44
4.	Results and Discussions	46
4.1	Co-precipitation	46
4.1.1	Effect of iron sources and pH on precipitation products	46
4.1.2	Effect of pH and carbon existence on phase morphology and crystallinity	48

4.2	Freeze drying with co-precipitation	51
4.2.1	Temperature (cryogenic) and pH controlled nucleation in co-precipitation with freeze drying	52
4.2.2	Effect of cation concentration	58
4.2.3	Effect of pH and reactant stoichiometry.....	60
4.2.4	Optimization of calcination temperature on LiFePO ₄ powder synthesis.	63
4.2.5	Effect of carbonization on LiFePO ₄ /C nano composite formation	66
4.2.6	Electrochemical performance of nano structured LiFePO ₄ /C materials synthesized with freeze drying.....	76
4.3	Ultrasound assisted sub-sequential precipitation	81
4.3.1	Ultrasound assisted vivianite nano-plate precursor synthesis.....	83
4.3.2	Ultrasound assisted AFP nano-plates synthesis	120
4.3.3	Optimization of encapsulation strategy and carbon coating during calcination	126
4.3.4	Localized orientation distribution in the nano plate LiFePO ₄ structure... ..	138
4.4	Electrochemical performance of nano structured LiFePO ₄ /C cathode materials	144
5.	Conclusion and future remarks	155
6.	References.....	160

LIST OF TABLES

Table 1. The precursor types used for the experiments	29
Table 2. Freeze Drying Parameters.....	33
Table 3. Galvanostatic cell test parameters with currents and respective rates	45
Table 4. (020) peak intensity ratio over other planes.	71
Table 5. Raman D/G band area ratio of cathode material as synthesized and coated with different carbonaceous agents and methods	76
Table 6. Elemental analysis results based on EDX for each crystals as referred in Figure 80.	119
Table 7. D/G band area ratio of cathodes coated with different methods.....	133

LIST OF FIGURES

Figure 1. Ragone diagram. ¹	2
Figure 2. Power and energy capacity of today's technology. ²	3
Figure 3. Intercalation and conversion reactions in electrochemical energy storage. ⁸	9
Figure 4. Schematic illustration of lithium – ion battery reaction mechanisms. ⁹	10
Figure 5. Three main types of host structure of different cathode materials. ¹⁸ ...	11
Figure 6. Expanded view of the framework built on FeO ₆ octahedral and PO ₄ tetrahedral, with Li ions in red ²¹	13
Figure 7. Illustration of undesired site occupancy in 1D crystal structure of LFP ²²	14
Figure 8. Unblocked volume change with respect to the particle size according to change in defect concentration. ²²	15
Figure 9. Conduction mechanism in cathode materials. ²⁴	15
Figure 10. Co-precipitation procedure explained.....	18
Figure 11. TEM images of the sample (a) LiFePO ₄ nanoparticles surrounded by a carbon web; (b) aggregated LiFePO ₄ particles and amorphous carbon; (c) bigger LiFePO ₄ grains covered in carbon ⁴⁴	19
Figure 12. Illustration of sub-sequential precipitation procedure and reaction mechanism. ⁵¹	21
Figure 13. Energy and pressure scale in time domain with respect to some generation phenomena. ⁵²	22
Figure 14. Ultrasonic wave irradiated cavitation behavior in liquid media. ⁵⁹	23
Figure 15. Flowchart showing the steps followed within this thesis.....	28

Figure 16. Schematic illustration of experimental routes used to synthesize nano-structured LFP cathode materials.	30
Figure 17. Schematic of the co-precipitation procedure manipulated with freeze drying.	32
Figure 18. A schematic illustration showing general experimental procedure in co-precipitation method with DSC and XRD analysis.	34
Figure 19. Schematic representation of sub-sequential precipitation procedure and mechanism.	35
Figure 20. Schematic representation of sequential precipitation controlled by surface dissolution.	36
Figure 21. Experimental setup and instruments as US rod immersion (left) and US flow cell (right) for ultrasonic wave assisted precipitation and crystallization.	37
Figure 22. Schematic representation for US assisted sub-sequential synthesis of LiFePO ₄ /C nano-composite cathode.	38
Figure 23. Schematic of equivalent circuit for EIS of cell test.	45
Figure 24. XRD analysis of precipitated products prepared with iron gluconate (a), iron sulfate (b) and iron nitrate (c) after co-precipitation and drying under room condition.	47
Figure 25. SEM image of co-precipitated structures at pH (a, c) 4.0 and (b, d) 6.0 by using iron sulfate (a, b) and iron gluconate (c, d)	49
Figure 26. XRD patterns of co-precipitated samples by using different iron (II) precursors as iron sulfate (a, b) and iron gluconate (c, d) at pH 4.0 (b, d) and 6.0 (a, c)	50
Figure 27. Heat flux profiles (exo-up) in DSC analysis (40 K min ⁻¹) of temperature and pH driven precipitated samples with Fe:Li mole ratio of (a) 1:3 and (b) 1:1.2.	54

Figure 28. XRD patterns of temperature driven precipitates in heat treatment as increasing temperature from 0 to 175 °C, and calcined at 700 °C.	55
Figure 29. XRD patterns of pH driven precipitates after heat treatment.	56
Figure 30. Proposed phase transformation mechanisms during heat treatment following (a) pH driven, and (b) temperature driven precipitation.	57
Figure 31. SEM images of synthesized LiFePO ₄ via freeze drying of temperature (a, c) and pH driven (b, d) precipitated samples at pH values of 2.0 (a), 3.5 (c), 4.5 (b), and 6.0 (d).	57
Figure 32. SEM images of the samples after calcination, which are precipitated by using iron (II) gluconate at various concentrations of 0.1M (a, c) and 0.05M (b, d) within pH 4.0 (a, b) and 6.0 (c, d) in suspension	59
Figure 33 SEM images of the freeze dried samples before calcination which are precipitated by using iron sulfate at concentrations of (a, b) 0.1M and (c, d) 0.05M within pH 4.0 (a, c) and 6.0 (b, d) in suspension	60
Figure 34. XRD pattern phase analysis of synthesized cathodes within different pH values of (a) 3.0, (b) 4.5, (c) 6.0, (d) 9.0 in co-precipitation media by using iron gluconate.	62
Figure 35. XRD pattern phase analysis of synthesized cathodes within different pH values (a) 3.0, (b) 4.5, (c) 6.0, and (d) 9.0 in co-precipitation media using iron sulfate.	63
Figure 36. XRD patterns of the cathode material calcined at 600 °C and 700 °C in second annealing step, with iron sulfate source and ex-situ carbonization.	65
Figure 37. EDX mapping analysis of freeze dried cathode material obtained through temperature driven precipitation using iron sulfate source and ex-situ carbonization.	65
Figure 38. SEM images of as synthesized cathode materials via in-situ (before drying) carbonization of ascorbic acid (0.01M) (a, d); citric acid (0.01M) (b, e),	

CTAB (0.01M) (f); and ex-situ carbonization (after drying) with sucrose (5wt.%) saturation (c) prepared by pH driven (a, b) and temperature driven (c, d, e, f) nucleation methods.	68
Figure 39. XRD patterns for samples prepared by Temperature driven (spray freezing) freeze drying method through (a) no addition, (b) CTAB, (c) Citric acid, (d) Ascorbic acid addition.	70
Figure 40. SEM images of synthesized samples by freeze drying with iron sulfate precursor and ascorbic acid addition (a) before and (b) after the calcination.	72
Figure 41. XRD patterns of LiFePO ₄ /C cathode materials synthesized via temperature (I) and pH (II) driven freeze drying method in-situ carbon addition with iron gluconate (a) ascorbic acid (c) and ex-situ carbon addition on pristine (b) and ascorbic acid added (d) samples.	73
Figure 42. XRD pattern and qualitative analysis of cathode prepared with iron sulfate precursor and ascorbic acid.	75
Figure 43. Raman spectrum of cathode materials synthesized by freeze drying with respect to carbon coating methods (during precipitation: ppt, external saturation: sat) and substances (ascorbic acid: AA, sugar: S) respectively.	75
Figure 44. Discharge capacity results on cathode materials as synthesized via freeze drying method as pristine without solution addition and external sugar carbonization (a), with only iron gluconate source (b), with ascorbic acid addition and external sugar carbonization (c), with only ascorbic acid addition in solution (d). pH and temperature driven nucleation represented as ■ and ●, respectively.	78
Figure 45. EIS measurements after galvanic cycling done on button cells with cathode materials synthesized in temperature (I) and pH driven processes (II) followed by in-situ carbonization with iron gluconate (a, d), ascorbic acid (b, e), and ex-situ carbonization with sugar saturation (f) and both in-situ ascorbic acid + ex-situ sugar saturation (c, g).	79

Figure 46. Schematic illustration of AFP crystal formation by sub-sequential precipitation	82
Figure 47. Schematic illustration of VVT crystal formation by sub-sequential precipitation	82
Figure 48 SEM images of AFP (a, c) and VVT (b, d) precursor particles with (a, b) and without (c, d) US treatment.	83
Figure 49. Particle size distribution analysis with LD measurement of Li_3PO_4 seed materials as synthesized with US L equipment or without US irradiation.	84
Figure 50. Ultrasonic wave irradiated precipitates of micro spherical seed lithium phosphate crystals achieved by ultrasonic rod immersion (a, b, c), and flow cell reactor (d, e, f).....	85
Figure 51. SEM images (a) of lithium phosphate precipitates produced without ultrasonic irradiation; SEM and TEM images (b, c) of ultrasonic wave irradiated precipitates of micro spherical seeds of lithium phosphate crystals.	86
Figure 52. Further agglomeration on the LP micro seeds material upon further ultrasonic treatment after 75 min US irradiation.....	86
Figure 53. SEM images of micron sized vivianite crystals synthesized (a) non-treated VVT from bulky Li_3PO_4 and (b) US treated VVT from micro spherical Li_3PO_4 seeds	88
Figure 54. XRD patterns of sequentially precipitated precursor materials synthesized in acidic (pH: 4.5 – 5.0) suspension with (US) or without (None) ultrasonic irradiation during first-and second precipitation step (1 st – 2 nd), (a) US – US, (b) None – US, (c) US – None, (d) None – None.	89
Figure 55. Vivianite crystal structure, viewed along a (a), b (b), and c (c) crystallographic axes and plate orientation (d) (JCPDS # 83-2453 with Diamond 3.2)	90

Figure 56. SEM micrograph of well distributed nano sized plate of iron (II) phosphate precursors synthesized by US wave assisted sub-sequential precipitation...	91
Figure 57. SEM micrographs of precipitated (before calcination) samples synthesized with (a) or without (b) US wave irradiation with bulk LP and with (c) or without (d) US wave irradiation with US treated LP micro seeds.	92
Figure 58. XRD pattern of sequentially precipitated (without calcination) precursor materials synthesized in basic (pH > 6.0) suspension with (US) or without (None) ultrasonic irradiation at each step (1 st – 2 nd); (a) US – US, (b) None – US, (c) US – None, (d) None – None	93
Figure 59. SEM images of US treated (b) or not treated (a) Li ₃ PO ₄ and vivianite precursors synthesized with (US) or without (None) ultra-sonication during first-and second precipitation (pH ~ 6.0) step (1 st – 2 nd); US – US(d), None – US (c), US – None (f), None – None (e).	95
Figure 60. Nucleation and growth process in crystallization depending on time and monomer concentration, Lamer diagram (a), and Formation rate of nucleation and growth (b). ¹¹⁵	96
Figure 61. Solubility (a) and molar ratio of species in metastable Li-Fe(II)-P-H ₂ O system with Li ⁺ excess. ⁹³	98
Figure 62. XRD patterns of materials as precipitated (before calcination) by US wave assisted sub-sequential precipitation with different pH at (a) 4.5, (b) 5.0, (c) 5.5, (d) 6.0.	100
Figure 63. Calculated average thickness of plate like vivianite particles from SEM images	100
Figure 64. SEM images of all US assisted synthesized particles within given pH (a) 4.5, (b) 5.0, (c) 5.5, (d) 6.0 before calcination.	101

Figure 65. XRD pattern of calcined samples synthesized with (US) or without (None) ultrasonic wave irradiation at each precipitation step (1 st – 2 nd); US – US (a), None – US (b), US – None(c), None – None (d) (pH ~ 6.0).	103
Figure 66. SEM images from (a) Li ₃ PO ₄ and (b, c) vivianite to (d) LFP structure produced via sub-sequential precipitation without US wave irradiation (arrows are indicating on going procedure).	104
Figure 67. XRD patterns with SEM images of cathode materials calcined with (a) and without (b) carbonization of precursors which synthesized via sub-sequential precipitation without US treatment.	104
Figure 68. Schematic representation of US assisted dissolution-reaction (1), nucleation-crystallization (2) and consumption-growth step (3) mechanisms on solubility curve with metastable zone width reduction effect of ultrasound. ¹¹⁹	107
Figure 69. Schematic representation of proposed mechanism of ultrasound assisted sub-sequential precipitation synthesis of LiFePO ₄	108
Figure 70. LFP and Li ₃ PO ₄ crystal morphologies detected by Fe and P rich region, respectively, from EDX mapping analysis after calcination step	110
Figure 71. SEM images of synthesized powders after calcination of US assisted precursors with 0.005 M (a), 0.025 M (b), 0.1 M (c, d, e, f) CA addition at pH 3.0 (d), 4.0 (e), 5.0 (f), 6.0 (a, b, c).	111
Figure 72. XRD patterns of precipitated (without calcination) samples synthesized via US assisted sub-sequential precipitation with citric acid addition	111
Figure 73. XRD patterns of calcined samples synthesized via US assisted sub-sequential precipitation with citric acid addition	112
Figure 74. XRD patterns of precipitated (without calcination) samples synthesized via US assisted sub-sequential precipitation at various pH values with 0.1M citric acid	112

Figure 75. XRD patterns of calcined samples synthesized via US assisted sub-sequential precipitation at various pH values with 0.1M citric acid.....	113
Figure 76. XRD patterns of synthesized LFP with 0.25M citric acid addition via US assisted sub-sequential precipitation within given reaction times.	114
Figure 77. XRD patterns of cathode materials (a, b) as synthesized from precursors (c, d) with addition of EG to LP suspension (a, c) or FeSO ₄ solution (b, d)	117
Figure 78. SEM images of US wave assisted precipitated vivianite nano-plates (a, c) and LFP cathode nano-plate (b, d) materials synthesized with addition of ethylene glycol into LP suspension (a, b) and FS solution (c, d).	118
Figure 79. XRD patterns of calcined materials after sub-sequential precipitation with non-US synthesis with 20 wt.% (a), 40 wt.% (c) EG addition on FS and 20 wt.% (b) EG addition on LP sources	118
Figure 80. EDX point analysis related with the crystal morphology into the respective SEM images of cathode material with EG addition on LP suspension (LP and LFP crystals indicated with red and blue circles respectively)	119
Figure 81. TEM images of polycrystalline LFP nano platelet as synthesized via US assisted sub-sequential precipitation with EG addition on LP suspension	120
Figure 82. Crystal structure of AFP and LFP as given transformation on crystallographic axes. ¹²⁴	121
Figure 83. SEM images of NH ₄ FePO ₄ ·H ₂ O nano-plate structures synthesized with (a) and without (b) US wave irradiation	122
Figure 84. SEM images of LFP nano-plate structures synthesized with various lithiation compound as lithium acetate (a) and lithium hydroxide (b) via US assisted sub-sequential AFP route.	122
Figure 85. In-situ XRD patterns from samples calcined at various temperatures using different lithiation sources via US treatment of NH ₄ FePO ₄ ·H ₂ O	124

Figure 86. SEM images of AFP (a) and LFP (b, c, d) nano plates synthesized with calcination at 700°C after lithium nitrate (b), lithium hydroxide (c) and lithium acetate (d) solution impregnation.	125
Figure 87. XRD patterns of nano-plate LFP cathodes calcined at different temperatures with sucrose carbonization.	127
Figure 88. SEM images of synthesized LFP materials at 500 °C (a, b) and 700 °C (c, d) with (a, c) and without (b, d) sucrose carbonization	128
Figure 89. XRD patterns of samples calcined at 500 °C (a, b) and 700 °C (c, d); with (b, d) and without (a, c) sucrose (S) saturation	129
Figure 90. Electrochemical charge/discharge curves of 12 wt.% (a), 5 wt.% (b), 2 wt.%, and 0 wt.% carbon coated LiFePO ₄ cathodes at 0.1C rate	130
Figure 91. TEM images of encapsulated LiFePO ₄ cathode particles with grain structures (a) and a cross section view from thinnest edge (b) encapsulated with sucrose saturated carbon coating (b, c) after calcination process	131
Figure 92. Raman spectrum from multiple cathode materials non-coated and coated by using CVD, sucrose saturation and EG solution method.....	132
Figure 93. EIS analysis of cathodes synthesized with US assisted VVT route as coated fine and coarse particles with CVD and sucrose saturation (suc. sat.) methods.	133
Figure 94. Electrochemical performance test of carbon coated cathode materials via CVD or sucrose saturation (Suc) method	134
Figure 95. SEM images of carbon coated fine (a, b) and coarse (c, d) LFP cathode particles by CVD	135
Figure 96. EDX mapping analysis of nano plate structure synthesized by US-US sub sequential precipitation.....	137
Figure 97. TEM image of nano-plate LFP cathode materials with electron diffraction analysis on selected sub-grains (1, 2, 3) represented with circular SAED	

aperture (yellow) and calculated zone axis directions in [uvw] form which makes different angles as 35°, 44°, 90° with [010] direction, respectively.....	139
Figure 98. TEM image of US assisted synthesized LiFePO ₄ /C cathode particles with (c) and without (a, b) ethylene glycol addition represented with SAED (yellow) and orientation analysis results (simulated with Carine 3.1)	140
Figure 99. Dark (down) and bright field (up) TEM images of nano-plate structures as synthesized with US irradiation in both sub-sequential precipitation from vivianite metastable structure	141
Figure 100. Comparison of parallel beam (PB) and standard beam (StdB) XRD analysis for localized orientation distribution around (020) plane in LFP (a) 80 – 100 nm, (b) 120 – 150 nm, (c) 220 – 250 nm thick nano-plates as synthesized via US assisted sub-sequential precursor precipitation without addition.	142
Figure 101. Standard (a) and parallel (b) beam XRD patterns of cathode materials synthesized via US assisted sub-sequential precipitation with AFP route.....	143
Figure 102. Capacity test results of carbon coated cathode materials as synthesized with (US) and without (None) US assistance for related precipitation sequences (1 st – 2 nd) with (EG) or without ethylene glycol addition.....	145
Figure 103. EIS analysis results of cathodes materials as synthesized with (US) and without (None) US assistance for related precipitation sequences (1 st – 2 nd) and with (EG) or without ethylene glycol addition.	146
Figure 104. Galvanic discharge capacities at high (1C) and low (0.1C) charging rates for 2D LFP nano-plate cathode materials synthesized via US assisted sub-sequential precipitation with respect to their thickness	148
Figure 105. EIS analysis of nano plate cathode materials synthesized by precursor routes; Fe ₃ (PO ₄) ₂ ·8H ₂ O (VVT) having different thicknesses and NH ₄ FePO ₄ ·H ₂ O (AFP) calcined with different lithiation compounds (LH, LAc) as all synthesized via US assisted sub-sequential precipitation	149

Figure 106. EIS analysis of cathodes as synthesized via US assisted sub-sequential precipitation methods 152

Figure 107. SEM images of carbon coated nano-plate LFP cathode materials as synthesized by US assisted sub-sequential precipitation having different average thickness as 60nm (a, b), 140nm (c, d), and 250nm (e, f). 154

LIST OF ABBREVIATIONS

AA: Ascorbic acid

AFP: Ammonium iron phosphate mono hydrate

CA: Citric acid

C_{\max}^{nu} : Maximum nucleation concentration

C_{\min}^{nu} : Minimum nucleation concentration

C_S : Saturation concentration

CTAB: Cetyl trimethyl ammonium bromide

CVD: Chemical vapor deposition

D band mode: Disorder mode

DEC: Diethylene carbonate

LD: Laser diffraction

DSC: Differential scanning calorimetry

EC: Ethylene carbonate

EDX: Energy dispersive X-ray spectroscopy

EG: Ethylene glycol

EIS: Electrochemical impedance spectroscopy

FN: Iron nitrate

FS: Iron sulfate

FG: Iron gluconate

G band mode: Tangential (graphitic) mode

JCPDS: Joint committee on powder diffraction standards

TEM: Transmission electron microscopy

LAc: Lithium acetate
LFP: Lithium iron phosphate
LFP/C: Lithium iron phosphate and carbon nano composite
LH: Lithium hydroxide
LN: Lithium nitrate
LP: Lithium phosphate
MSZW: Meta stable zone width
NMP: N-methyl pyrrolidione
PVDF: Poly vinylidene di floride
ppt: Precipitated
Q: Capacitance
RAMAN: Raman spectroscopy
R_E: Electrolyte resistance
R_{CT}: Charge transfer resistance
R_{SF}: Surface film resistance
sat: Saturated
S: Sucrose
SEM: Scanning electron microscopy
SAED: Selected area electron diffraction
TEM: Transmission electron microscopy
US: Ultrasound
VVT: Vivianite
W: Warburg resistance
XRD: X-ray diffraction
 Θ : Diffraction angle in degree

1ST CHAPTER

1. Future of energy demand and storage technology

Nowadays the demand for electrical power has increased much more than ever has been before. Also it is needed in right place and right time just before to be used. Energy consumption strategy needs more localized and mobile solutions. Moreover, power has to be delivered more efficiently than already does. With this point of view, electrochemical storage technology seems to be the most efficient way to convert the energy between electrical and chemical forms.

Electrical energy storage can be done by capacitors and batteries. While the capacitors are rapid, batteries are slow because of their low molecular mobility during chemical reactions. In Figure 1, a relation between specific power and specific energy is explained for energy source devices. Fuel cells can provide high energy with low power while super capacitors have more power with less energy. In high battery systems, the aim is to achieve the highest power capacity especially for electrical drive systems in automotive technology.

In the recent decades, a tremendous interest has been placed to develop better electrochemical energy storage systems and batteries. There are several driving factors for this attraction. One is about the environmental pollution caused by internal combustion engines. It is well known that the combustion of fossil fuels causes the emission of pollutant materials. Pollutants accumulate in nature as greenhouse gases resulting in global warming and poisonous atmospheric gases threatening the public health.

Pollution density is not same in everywhere. It is high in cities with high population and industrial areas. Regulations have been used to limit the emission related to automotive industry. These regulations forced the automotive industry to find more efficient and ecological solutions. Alternative fuels and energy storage media should be developed for vehicle propulsion systems. Electrified vehicles can be a solution in which power is supplied by battery. Afterwards, hydrogen fuel cell can be next.

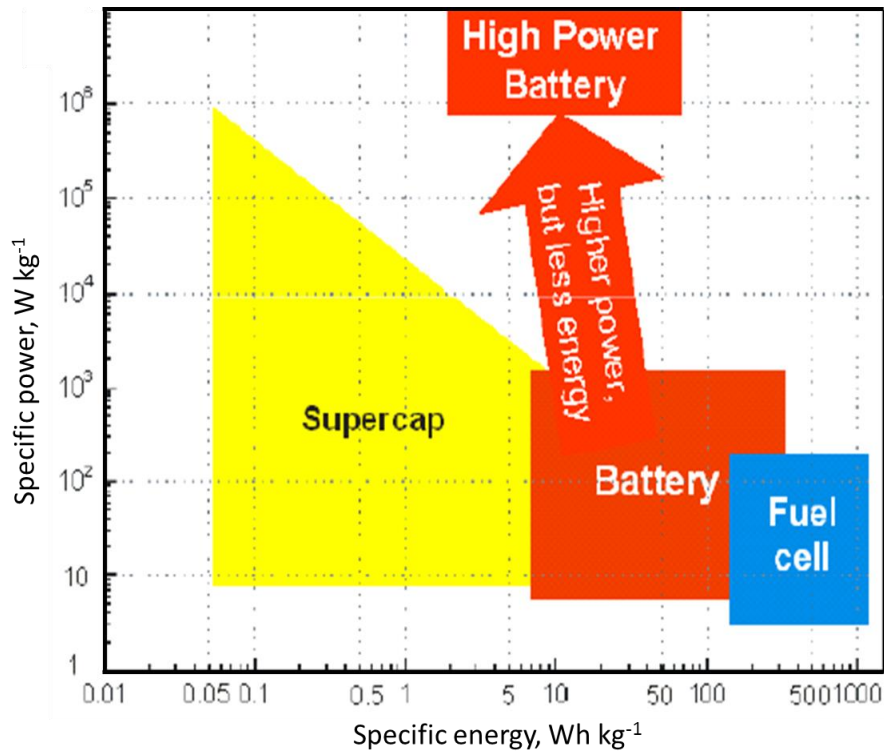


Figure 1. Ragone diagram.¹

In order to provide sufficient range during urban routes, and adequate acceleration, relatively large amounts of power and energy must be suited in the vehicle. Thus, power amount must be supplied from a battery solution. Moreover, weight reduction is also an important parameter in automotive applications.

1.1 Fundamentals of electrochemical storage and batteries

Rechargeable battery is a device which reversibly stores energy for future delivery by an electrochemical reaction. Energy density of the battery is important in portable and mobile applications, like cellphones, portable computers and video cameras. However, conventional batteries have a limiting parameter on battery life, rate capability, and capacity as seen in specific power and energy graphics provided in Figure 2. Among them, the most beneficial target would be the fast charge acceptance to reach the goal of being an alternative power source for electric vehicles.

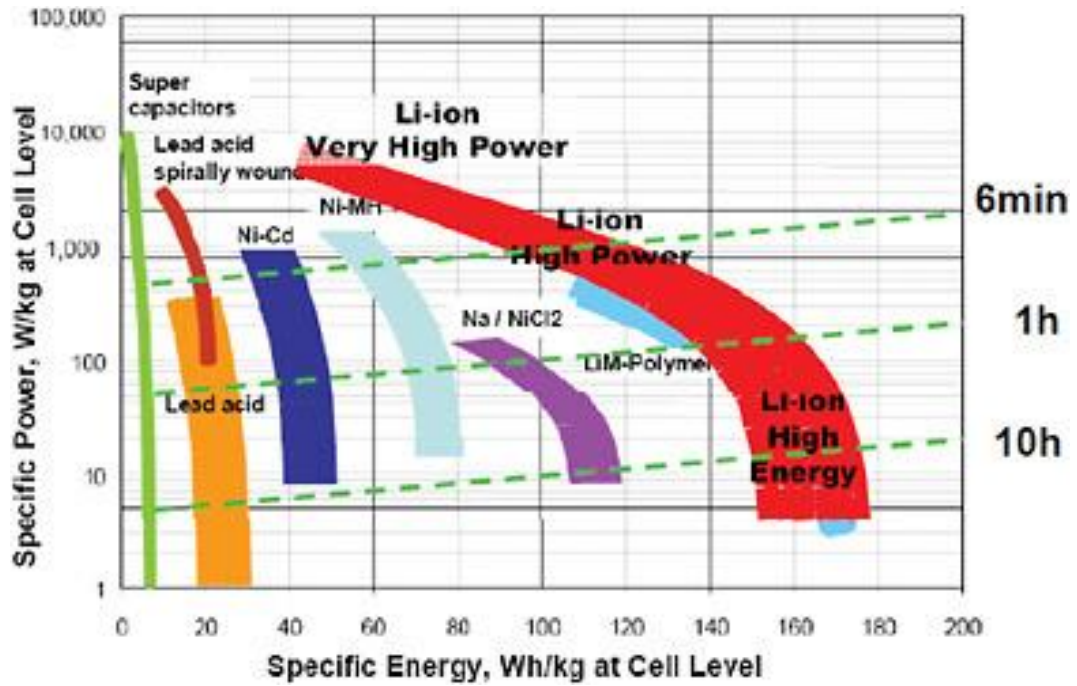


Figure 2. Power and energy capacity of today's technology.²

1.2 Thesis objectives

As an iron based cathode material, LiFePO_4 has been studied because of its abundance, safety and reliability for high power application in electric vehicle energy storage systems. The most important development is the power acceptance improvement of LiFePO_4 cathode material. Fast rechargeability is the key obstacle for commercialization. Although, fast charging target within 5 minutes with pumping of a fuel tank may be an achievable limit with novel nanostructured materials and designs. At the same time, developing a sufficient synthesis with reasonable cost is much more important than getting the top notch results on a lab bench.

Size reduction of crystalline LiFePO_4 material has unexpected effects on capacity and rate capability of cathode at nanoscale because of its lithium diffusion anisotropy. This is explained by refining Li^+ ion diffusion length and reducing defect concentration in lattice. Nano crystalline materials look promising if large scale and affordable production capacities can be achieved.

LiFePO_4 (LFP) based electrode kinetic is controlled by poor electronic conductivity and the low lithium ion diffusion in the structure. After reviewing production methods for fast kinetic mechanism by enhancing poor ionic and electronic conductivity with

fast electrochemical kinetic supporting high power application was focused in this thesis.

In last decade, the general research motivations focused on to synthesize a cathode material having superior parameters as listed in below;

- I. Performance parameters
 - i. Energy density
 - ii. Power density (Rate capability)
 - iii. Fast rechargeability
 - iv. Cycleability
 - v. Durability (Self discharge)
- II. Safety parameters
 - i. Flame retardancy
 - ii. Self-shutting down to avoid explosion
 - iii. Temperature limitations
 - iv. Toxicity
- III. Cost efficiency

Fast rechargeability is a key role that leads the traction battery application in automotive industry. High rate capability during charging is required for easy and quick regeneration of the energy from the high current and power feedback system. Improving the power capability and fast rechargeability of the cathode materials is the purpose for synthesis of nanostructures via low cost and facile methods.

The long and stable cycle life is essential for the easy management during all service life time of the battery. To collect all generated current in a fast way and to enhance the utilization of active mass, cathode material must be electronically conductive.

Rate limiting step for lithium ion diffusion through the inner part of cathode material is important for 1D structures like olivines. So reducing this pathway may have tremendous effect on electrochemical reaction kinetic. To achieve a high rate charge-discharge capability of LiFePO_4 electrodes, the particle size refining should be focused. Recently, organic (carbon) phase or other electronic conductive agents having only surface contacts for each cathode particle provided that the electron-conducting phase also percolates the whole electrode material.

To achieve a relatively high power, enough conductivity is required to act as a conductive additive. It may also be possible to form nano powders as well as nano rods or flakes. It is believed that the nano structures enhance the Li diffusivity and significantly reduce the defect concentration by limiting the size of crystallites. LiFePO₄ crystal structure, having anisotropic diffusivity of Li⁺ ions, the reduction on the length of transportation route into the structure should increase the fast rechargeability by localization of crystallographic directions along with preferred orientations. This yields an improvement in intra- and inter-conductivity of the particles.

Reducing the intrinsic resistance of the cathode material by controlling the size and crystal structure with the help of external manipulating effects on aqua based precipitation synthesis is the motivation of this thesis. For manipulating the final structures towards nanoscale, first issue was to gain control on nucleation and growth mechanism by controlling the nucleation temperature and adding surface active organic compounds.

Alternatively, modulate the final LFP/C structure, heterogeneous nucleation and slow dissolution kinetic of sub-sequential precipitation was used as a metamorphological synthesis of 2D LiFePO₄ cathode material by transformation of 2D intermittent precursors. Additional manipulating effect of ultrasound irradiation on precipitation and recrystallization reactions was studied in an aqueous environment.

1.2.1 Originality of the study

In the thesis, fast rechargeability and power capability of LFP is tried to be enhanced by nanotechnology processing techniques. To overcome drawbacks of olivine type of LiFePO₄ which are lack of electrical and ionic conductivity, it is proposed to synthesize cathode material in nano-sized particles. Throughout the thesis, mainly two techniques are used which are freeze drying co-precipitation and ultrasonic wave assisted sub sequential precipitation to obtain nano crystalline and preferentially oriented nano plate structures of LiFePO₄ materials. In order to develop a facile and cost effective implementation, it is also aimed to design a synthesis processes that is compatible with aqua based environment and solution chemistry.

Although there are some studies reported using freeze drying method for synthesis of LiFePO_4 ,^{2,3} there is still a need to improve electronic conductivity in order to achieve high efficiency and low resistance during charge/discharge at high rates. In the thesis, temperature and pH controlled co-precipitation methods are studied within freeze drying procedure in order to obtain refined crystallite size for enhanced electrochemical performance. Effects of temperature and pH, separately as a driving force of co-precipitation process, are investigated with the help of cryogenic drying condition against oxidation. Rapid freezing was implemented on both pH driven and temperature driven nucleated precursors. Reaction mechanisms were proposed by differential scanning calorimetry and x-ray diffraction analysis.

During synthesis, agglomeration is important during production phase and thus this effect should be eliminated by minimizing the surface energy. In order to reduce surface energy during crystallization, different encapsulating agents such as CTAB (Cetyl trimethyl ammonium bromide), ascorbic acid, and citric acid are used. These encapsulation agents can transform into a conducting layer during the calcination step by keeping the particle away from further agglomeration along the whole synthesis process. Furthermore, this helps to slow down and control the nucleation and growth mechanism of precipitated products by limiting the diffusion in the solution phase. The effect of these compounds is investigated on morphology of active material and their effect on nucleation, growth and agglomeration mechanisms.

The sub-sequential precipitation method is also studied with sono-crystallization. The promising effect of ultrasonic wave assisted crystallization process is to produce nano-plate LFP refined especially in one dimension. Preservation of these individually well distributed and crystallized nano-sheet materials is achieved by transformation of vivianite crystals into LFP. During this transformation, in-situ carbonization of surface active carbonaceous materials is performed during calcination where conductivity of resulted material increases.

To high energy and power density, homogeneous and thin carbon layers has to be maintained while keeping the particle size refined after synthesis of LFP/C particles. In this research, in-situ carbon coating and encapsulating strategies are combined to reach an optimum crystallite size and shape regarding the crystallographic orientation.

2ND CHAPTER

2. Background and literature

Achieving high performance capacity and regenerability while reducing the weight of energy storage system is the purpose. Due to the recent technological developments especially in mobile devices such as laptops, phones and cars, weight of storage system matters as well as its performance. Since the discovery of lithium ion batteries by Whittingham,⁴ the most convenient solution to mobile applications is lithium ion batteries in the field of electronic devices. Almost all laptops, multimedia devices and medical devices use lithium-ion batteries. Lithium ion battery performance should be studied. Nowadays, more research studies focus on battery kinetics and nano technology point of view since the lighter and faster energy storage and conversion solutions are desired in both automotive and portable device industry.

2.1 Rechargeable lithium ion batteries

Lithium has become a good candidate for anodic compound batteries due to its high energy density like a host material for Li⁺ ions during intercalation. However, early models of this type of lithium ion batteries had many problems about safety. During test phase, short circuit explosion experience because of the dendritic formation of lithium between recharging cycles raised the public concerns up. Finally Besenhard and Fritz⁵ has introduced graphite as another intercalating compound for lithium. Graphite layers helped to solve the dendritic growth problem by layered structure of graphite and waiving of capacity. After the discovery of LiC₆ intercalation in graphite material as an anodic compound by Yazami and Tazian,⁶ use of lithium ion batteries has dramatically increased in commercial applications.

Lithium rechargeable batteries offer high power, light weight, and advanced electrochemical performance. With those prominent characteristics, lithium ion batteries dominates the market for portable rechargeable power tools such as personal electronic and communication devices and medical devices. Batteries with high energy density, efficient cyclability and durable chemistry are the purpose. This feature is coming from its endurable nature in charge - discharge cycles by having no memory

effect which provides more flexible usage for multiple applications.

Lithium ion batteries seem to be likely the best alternative energy storage device for the next generation transportation industry. Despite its reliable capacity and long service life, main drawback is its limited rate capability during both charging and discharging processes. Especially, enhanced power density would be an important driving force for electric vehicle technology.

2.1.1 Kinetics of intercalation compounds

Lithium ion rechargeable battery electrodes are based on intercalation compounds of lithium, which reversibly accommodate lithium ions into their crystal framework. In contrary to conversion electrode reactions, intercalation compounds are able to conserve their crystal structure during charge and discharge reactions. This mechanism allows high power and cycle ability because of stable structure during charge and discharge reactions. However, intercalation compounds have limited capacity around 250 mAhg^{-1} which is equal to one electron redox potential.⁷ On the other side, conversion reaction compounds can reach higher energy storage capacity than intercalation mechanism. Schematic illustration for these mechanisms is shown in Figure 3. The cathode and anode in conventional lithium ion batteries typically have either a layer or a tunnel structure.

Figure 4 illustrates a typical lithium cell design. During discharge, lithium is oxidized at the negative electrode and released into the ionic conductive electrolyte. Then lithium ions travel through the electrolyte towards the positive electrode, where the lithium ions are reduced in case of entering to the host framework of the positive active material. In order for this process to occur, electrons must also move from the negative electrode to the positive. The electrolyte is not electronically conductive, so the electric current must pass through an external circuit, producing electrical work. During charge, these processes are reversed, requiring an electrical charge input. Amount of power extracted from the discharge process is proportional to the current, or reaction rate. Cell potential is related to the difference between the anodic and cathodic chemical potential of lithium in these two host compounds. The open circuit or theoretical standard potential of the lithium ion cell is described as changing chemical

potential of Li ions (*Equation-1*) at each state in between anodes and cathodes as a rocking chair movement.

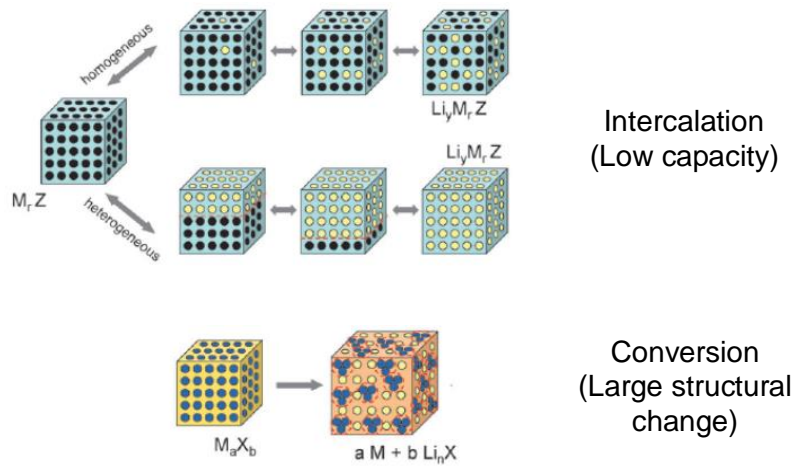


Figure 3. Intercalation and conversion reactions in electrochemical energy storage.⁸

$$E_0 = -(\mu_{Li/+} - \mu_{Li/-})/nF \quad (1)$$

Here, E_0 is the equilibrium cell potential, $\mu_{Li/+}$ and $\mu_{Li/-}$ are the chemical potentials of lithium in positive and negative electrodes, respectively; n is the number of electrons involved in the reaction, and F is Faraday's constant.

In high power cell, electrolyte should sustain a high current on formed species during each cycle without suffering from irreversible processes, and side products such as solid electrolyte interface (SEI). Otherwise, galvanic cell potential decreases further from open circuit voltage which decreases the battery power and cycle time. There are certain kinetic requirements of an electrode materials for high power cell as below:

- High lithium intercalation capacity
- Large gap of electrochemical potential between positive and negative electrodes vs. the Li/Li^+ couple
- Facile lithium intercalation kinetics
- High diffusivity of lithium in the solid
- Electronically conductive (or compatible with conductive additives)

- Stable to electrochemical cycling

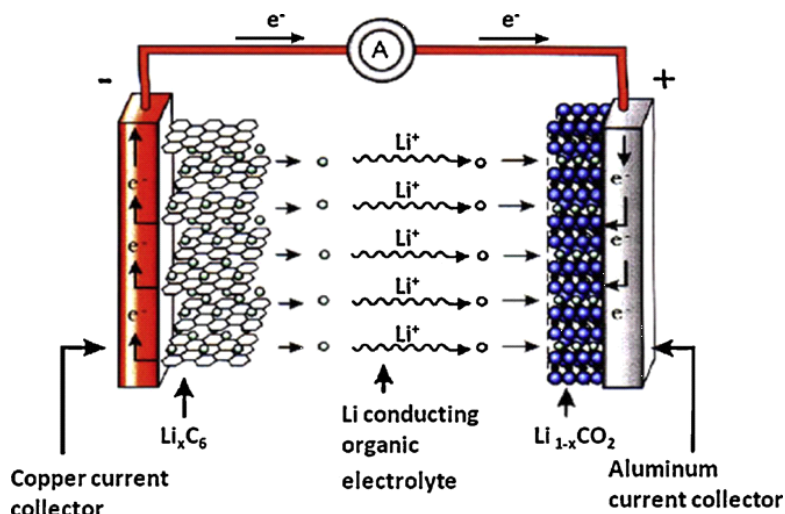


Figure 4. Schematic illustration of lithium – ion battery reaction mechanisms.⁹

These requirements are fulfilled for the negative electrode by many materials, including graphite, certain metal alloys, some transition-metal oxides,¹⁰ and lithium metal.¹¹ Lithium metal is not used commercially due to safety concerns, but it is widely subjected to research projects, particularly when characterizing positive electrode materials because it displays a constant electrochemical potential during charge and discharge.

A wide variety of cell chemistry fulfill the electrochemical requirements for positive electrodes. For example; LiCoO_2 has found extensive commercial application due to its high energy density and long-term stability in repeated electrochemical cycling.

High power requirements would be achieved by modulating structural properties of electrode materials.¹² Recent studies show that particle size refinement on electrode materials results in better electrochemical properties.^{13,14} Furthermore, increase in porosity of active mass helps in fast ionic and electronic conduction in electrode.¹⁵

2.2 Cathode materials for lithium-ion batteries

There are three main host structures for cathode materials which are spinel, layered and olivine structure (Figure 5). The spinel structure has 3D openings through the inner galleries. In this type of structure, ions are free to move in all axis and Li ions can diffuse through each surfaces. $\text{Li}_2\text{Mn}_2\text{O}_4$ is a well-known type of structure.¹⁶ It has less

toxicity, more abundant from natural resources and intercalation/extraction ratio changes between $0 < x < 2$.

Main drawback of spinel structured cathode materials is caused by phase transition between charged and discharged states. Transition between cubic and distorted tetragonal structures causes large volume change which leads to a limited capacity with $120 - 125 \text{ mAhg}^{-1}$. Capacity degradation due to phase transition occurs at moderate temperatures ($50\text{-}70^\circ\text{C}$) that can easily be reached early in most applications.

The layered cathode materials have 2D structure where diffusion occurs along a specific direction of the crystal structure (Figure 5). LiCoO_2 is a common cathode material used for most of the industry scale productions. LiCoO_2 cathode can be easily synthesized using both solid-state and chemical approaches. It has excellent cycle ability at room temperature especially when Li_xCoO_2 having stoichiometric ratio at the range of $0.5 < x < 1.0$. Out of this stoichiometric range the crystal structure tends to collapse and are destroyed permanently. Specific capacity and theoretical capacity of LiCoO_2 are 140 mAhg^{-1} , and 273 mAhg^{-1} , respectively.¹⁷

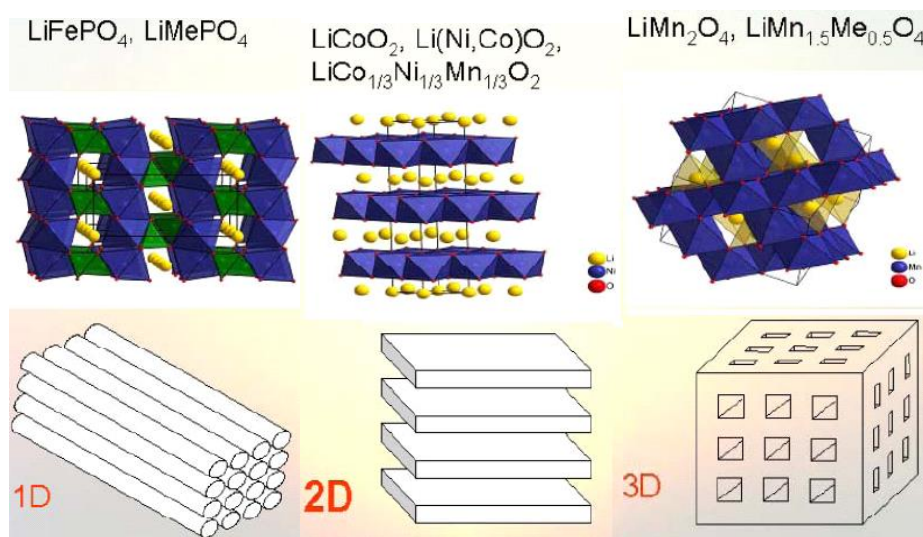


Figure 5. Three main types of host structure of different cathode materials.¹⁸

LiCoO_2 is widely used as cathode material for portable devices. In large scale battery packs, especially for electric vehicle application, operation fluctuation brings the difference in cell structure that cannot be easily managed during dynamic charge and

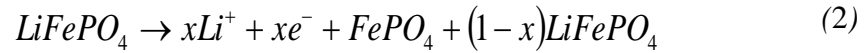
discharge sequences. Therefore, this causes disintegration on cathode materials especially during high ampere discharge. Excessive amount of heat can be released and localized in the battery which can yield safety concerns in automotive industry. In addition to these concerns, cobalt ingredient makes LiCoO_2 cell very expensive. Moreover, mass production of this Co included cathode material for transportation brings serious questions on collection and recycling of the large amount of used batteries. For high Co content, LiCoO_2 is highly toxic and must be recyclable. Furthermore, recyclability of LiCoO_2 has not been properly solved yet.

The third cathode material structure is olivine type which has Li diffusion channel in one direction (Figure 5). Generally, this type of host structures is phosphate containing cathodes which may easily be interrupted by disordered structure or non-released atoms. Similar lattice parameters between charged and discharged states of phospho-olivines cause small amount of volume changes during cycling. Olivine type cathode materials also provide good thermal stability and excellent cycling performance.¹⁹ Raw materials for synthesis of these type of materials are well abundant in nature and therefore inexpensive. Olivine type cathode has relatively a large theoretical capacity²⁰ of 170 mAhg^{-1} . It shows good stability at relatively high temperature and safe even in abusive uses. The olivine structures give more stable open circuit voltage of 3.45V and flat curve during discharge; however, it is hardly diagnosed and managed in package configuration. Moreover, excellent cycle ability can be observed during service life. No complete transformation is allowed in cathode material because of the structural collapse.

2.3 Structure and properties of LiFePO_4

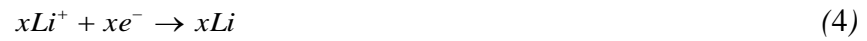
Fully discharged, lithium inserted, LiFePO_4 cathode material forms from tetrahedral and octahedral sandwich layers. During charge and discharge reactions, Fe atom at the center of octahedron is oxidized and reduced, respectively while Li^+ ions are extracted and inserted with reduction and oxidation in the same order (*equations (2)-(5)*). LiO_6 octahedral share edges and Li ions may diffuse along [010] and [001] directions.

Cathode reactions: Charging



Anode reactions:

Charging



Unit cell volume²¹ of FePO₄ is 272.4 Å³ while that of LiFePO₄ is 291.4 Å³. After the extraction of Li⁺ ions the lattice volume is reduced. This volume change being very strict gives high stability and mechanical cohesion during cycles between two phases. Figure 6 represents the structure with Li atoms which easily hop to the sites in the green octahedrons through diffusion path lying on the way of *b* axis.

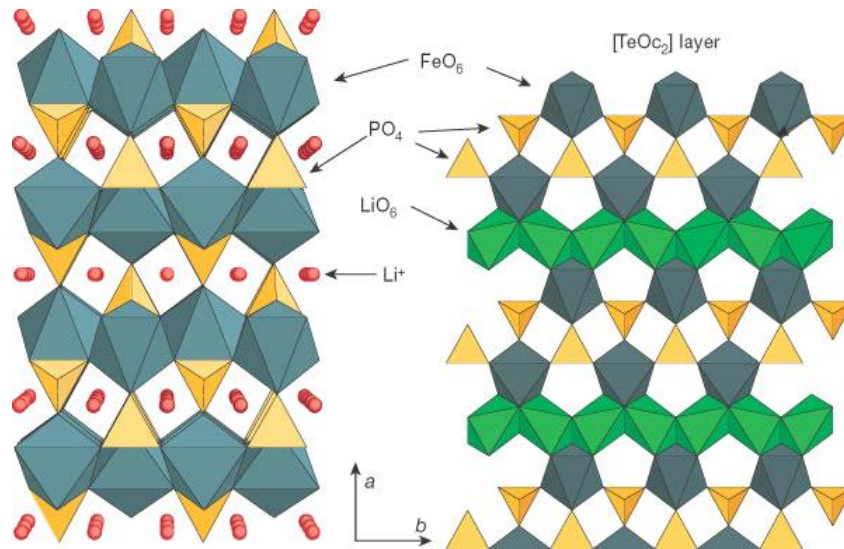


Figure 6. Expanded view of the framework built on FeO₆ octahedral and PO₄ tetrahedral, with Li ions in red²¹.

On the other hand, Li[M]PO₄ (M: Fe, Co, Ni, Mn) structure shows poor electronic conductivity because of the oxygen atoms suited in PO₄³⁻ tetrahedral. This interrupts the electron paths for conduction and makes the electrical conductivity of active

material is very poor. Due to the nearly close packed hexagonal oxygen atom array provides a relatively small free volume for lithium ions having small migration speeds at ambient temperature.

2.3.1 Lithium diffusion mechanism in LiFePO_4 crystals and nano structured materials

Lithium diffusion is the main step responsible step of kinetics limiting charge and discharge in the crystal structure and thus, lithium ion diffusion is very dependent on crystal orientation of cathode material. LFP is a good candidate in term of structural properties since it has channel like structure that makes it easy for lithium ion diffusion path in the crystal.

A number of computational research studies has shown that the lithium diffusion could be much faster and have less potential barrier through $[010]$ direction then other crystal directions.²² By reducing the length in this diffusion path, which is normal of (020) plane, Li^+ ions can move freely along b axis of lattice. Also against the chance of defects concentration or undesired site occupancy which has blocked the channels as unusable volume can be reduced dramatically. According to a study by Ceder et al.²³, Li ions with nanometer long channels can diffuse more easily facing on few obstacles than micron size particles have (Figure 7 and 8). Calculations of surface redox potentials can provide insight into the possible Li insertion / extraction mechanisms, particularly for materials with small particle size, where surface effects on the lithiation thermodynamics are expected to be significant.

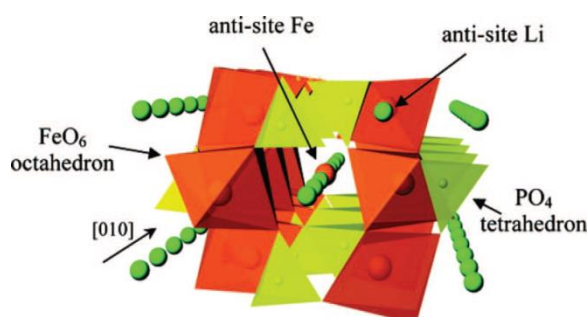


Figure 7. Illustration of undesired site occupancy in 1D crystal structure of LFP²².

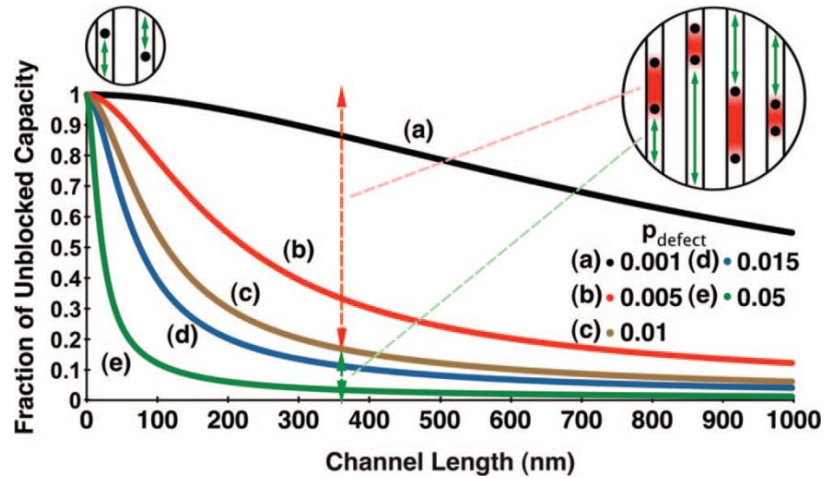


Figure 8. Unblocked volume change with respect to the particle size according to change in defect concentration.²²

2.3.2 Electrical and ionic conductivity in LFP

There are three main mechanisms occur in a cell during charge / discharge process where lithium ions move from cathode to anode through the electrolyte or vice versa (Figure 9). These mechanisms are as below;

- Lithium ion diffusion within solid state electrode materials (rate determining)
- Charge transfer reaction at the interface between the electrode and electrolyte
- Lithium ion movement in the electrolyte.

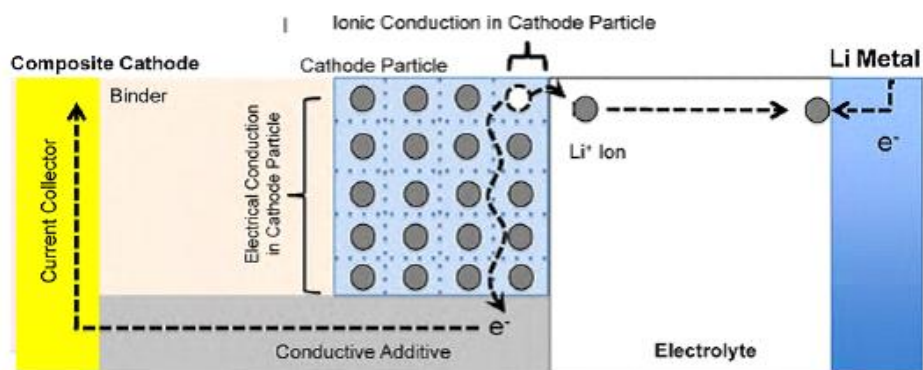


Figure 9. Conduction mechanism in cathode materials.²⁴

Slow rate is determining step in lithium diffusion of solid state at macro scale.²⁴ Therefore, nano-structured cathode materials may enhance the reaction kinetic by decreasing the diffusion length dramatically.²⁵ Therefore, it is shown that morphology

and size of LFP cathode materials play crucial role in improving fast cycling. High power cathode materials for lithium ion batteries should have small particles, fast ionic and electronic conduction, and thin electrode component.

There are two main problems related to olivine structure. First is poor electronic conduction and second is limited diffusion due to the 1D (one dimensional) structure. Nano painting with carbon sources can be a part of solution but nanometer scale results in more conductivity as compared to bulk phase.

Nano-structured materials have been extensively explored to enhance kinetic properties by decreasing the diffusion length to nanometer scale. In bulk compounds, achieving the stability at intermediate lithium concentrations by increasing the temperature is not a practical or safe solution for a battery electrode. Another approach is to use nanotechnology. It is expected that lithium diffusion length is greatly reduced in nano fibrils, which can allow fast kinetics and good utilization rates.²⁶ On the other hand, diffusion mechanism of lithium ions should be improved during electro-insertion and extraction. Therefore, diffusion length in the structure must be refined.

2.4 Recent developments in cathode materials for lithium-ion batteries

Lithium rechargeable batteries are recently dominating the market for portable power devices used in laptops, cell phones and medical implants, etc. due to their high power, light weight, and advanced electrochemical performance. The key point of the spreading feature is coming from its enduring nature in charge / discharge cycles caused by having no memory effect. Oxide materials such as LiCoO_2 and LiMn_2O_4 are widely used as cathode materials for lithium ion batteries. However, a drawback on safety cautions comes forward due to their high reactive nature. Alternative to these oxide materials, Padhi et al.²⁷ has introduced olivine type LiFePO_4 as a promising candidate having more stable oxygen atoms shared by octahedral- PO_6 and tetrahedral- FeO_4 . Although LiFePO_4 displays outstanding properties in terms of better cycling stability and safety issues, two major disadvantages are; low electronic conductivity ($\sim 10^{-9} \text{ Scm}^{-1}$) and slow lithium ion diffusion coefficient with poor rate capability ($\sim 1.8 \times 10^{-14} \text{ cm}^2 \text{ s}^{-1}$).²⁸ Nano painting with carbon sources can be a part of solution

but size reduction to nanometer scale results in also extra conductivity as compared to bulk phase.²⁵

Electronic conductivity of LiFePO₄ cathode materials could be improved by carbon coating.²⁹ However, these reports, Gaberscek et al.²⁵ claimed that optimization of the particle size carries more importance than the presence of carbon coating for the enhancement of electrode performance. As particle size decreases, the rate capability of cathode material increases which resulted in high power density. Similarly, carbon free nanoscale LiFePO₄ particles were directly conducted with satisfactory electrochemical properties.³⁰ Hydrothermal method resulted in micron sized particles rather than nano sized structures. In order to gain control on size distribution and provide better homogeneity, co-precipitation method is a most promising technique for the mass production of LiFePO₄ owing to its low cost and facile route.^{28,31–33}

Several solvothermal methods were used to get plate like LFP crystal formation reducing size in [010] direction to achieve better rate capability. However, moderate temperature (180-200 °C) synthesis followed by high temperature (600-800 °C) calcination step was used in solvothermal method.^{34–37} In these methods, organic solvents are widely used to modify the morphological structure.

2.5 Synthesis of LiFePO₄

2.5.1 Co-precipitation

In Co-precipitation method, impurities are transferred to a precipitate concurrently with the deposition of some primary substances from a solution, melt, or vapor containing several substances. Solution should be super saturated with the substance forming the precipitate or when a melt is super cooled. Co-precipitation, the solubility of an ion is lower in mixed ionic solution than in pure ionic solutions. A co-precipitation procedure is seen in Figure 10. Co-precipitation method consists of two steps which are nucleation and precipitation under normal conditions (standard pressure and temperature) subsequently followed by crystallization through thermal treatment³¹. It is also an important method to extract trace amount of impurities which

are generally undesired. However, in some case it would be an efficient way to add dopant materials in to target substance.³⁸

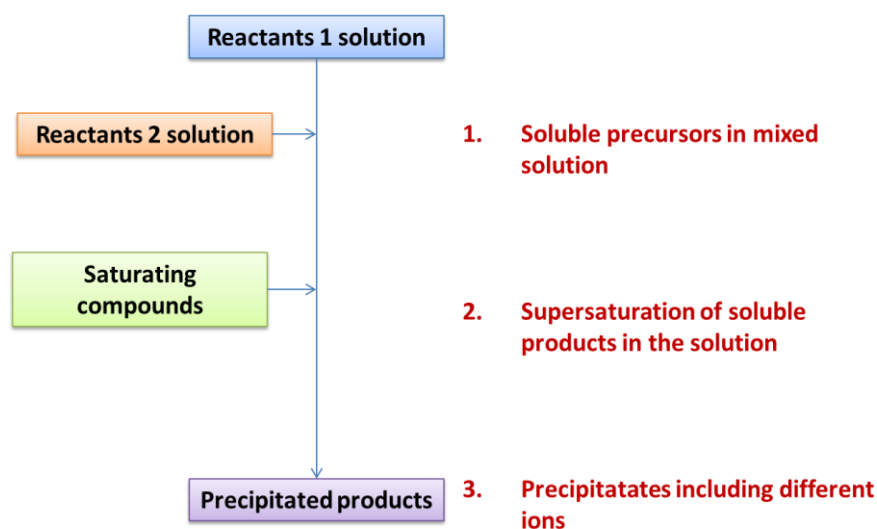


Figure 10. Co-precipitation procedure explained.

2.5.2 Freeze drying

Agglomeration is a challenging problem in order to have small sized cathode materials with high electrochemical properties. Current synthesis techniques mostly include heat treatment processes at early steps of production to get rid of the solvent content. However, this results in bigger and agglomerated LiFePO_4 particles as shown in Figure 11 by Palomares et al.³⁹ Hence, a new cryogenic technique is being introduced to dry precipitated precursors without heat treatment by minimizing the agglomeration for the synthesis of cathode materials.⁴⁰

Freeze drying is a chemical synthesis method under cryogenic conditions. The first step is the preparation of precursor solution in desired stoichiometric ratios. Generally, the aqua based solutions are preferred because of easy vaporization.⁴¹⁻⁴³ However, other solvent materials such as alcohols, ethers, and benzenes can be also chosen for low temperature synthesis. The liquid dispersion is pulverized into liquid nitrogen and suddenly frozen. Particles dehumidified in a freeze dryer have to be calcined in an inert atmosphere with two steps after drying in a cryogenic atmosphere. Then, frozen solid phase is evaporated by releasing nitrogen and solvent under vacuum at low temperatures (cryogenic). Generally, drying is implemented in a freeze dryer at -40 to 0 °C under low pressure (10 – 100 mbar). Drying speed strongly depends on

temperature and pressure profiles. However, the process parameters should be chosen carefully to avoid from melting and degradation of glassy phase. Further thermal investigation was conducted to specify the exact starting point for melting and glassy transition.³⁹

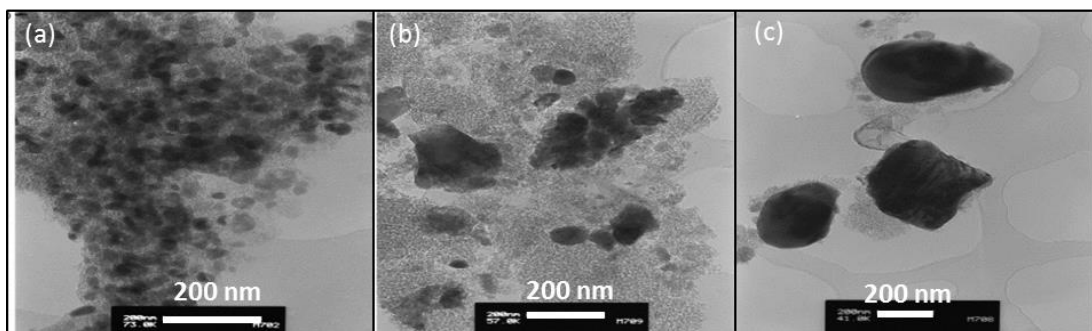


Figure 11. TEM images of the sample (a) LiFePO₄ nanoparticles surrounded by a carbon web; (b) aggregated LiFePO₄ particles and amorphous carbon; (c) bigger LiFePO₄ grains covered in carbon⁴⁴.

After cryogenic drying, solid material is calcined in an inert atmosphere. It is important to eliminate oxidation of iron to a high oxidation state. Thus, inter-metallic compounds can be formed and then lithium insertion occurs at high temperatures (>500 °C).

Even though freeze drying is allowed to produce other common materials such as spinels, it is rarely investigated for olivine type of cathode materials.⁴⁵ This method was applied on LiFePO₄ cathode materials for the first time by Panero et al.⁴⁶ Then Palomares et al. improved the method to achieve higher efficiency.³⁹ Koleva et al.⁴⁷ proposed new formate precursor method in order to get in situ coating with carbon. Both LiFePO₄ and LiMnPO₄ cathode materials were synthesized.⁴⁸ Kang et al. investigated the effect of carbonaceous matrix on the cathode particles.⁴⁹

Freeze-drying method was also used to synthesize in another solvent dispersion in aqua solution as emulsion.^{39,50} However, different organic aqua soluble additives affect different process parameters such as nucleation, growth, crystallization and coating. Moreover, there are lack of knowledge on their effect on precipitation, phase distribution and evaluation.

2.5.3 Sub-sequential precipitation

In recent years, different synthesis methods have been used to synthesize nano materials because of limitations of hydrothermal process. The key strategy should be slowing down the crystallization reactions which can be easily accelerated at high temperatures within liquid suspension. Reactive crystallization rate can be suppressing by especially reducing reactant concentration. This reducing abundance of monomers within close region to newly formed nuclei may be supplied by controlled synthesis of reactant or encapsulated surface by additives.

The sub-sequential precipitation is related to form secondary structures by driving the effect of solubility difference between these compounds. In literature, there are some studies investigating the synthesis of LiFePO_4 using sub-sequential precipitation method. In LiFePO_4 synthesis, Li_3PO_4 (LP) was used as a seed material.

Based on solubility difference, two or more compounds are precipitated within following sequence and separate reaction conditions. The more soluble product is precipitated at first then it is followed by another precipitation reactions to form less soluble compound by adding another reactant or changing the conditions as pH, temperature etc. Second precipitation is controlled by limited mass transportation depends on dissolution of early precipitated compound.

Solubility coefficients of Li_3PO_4 and $\text{Fe}_3(\text{PO}_4)_2$ are different (*Equations (6), (7)*) and reactions continue with respect to this differences. Because of high solubility of LP, reactions slightly go on to right side to form lithium and phosphate ions. Phosphate ions are consumed for crystallization reaction which forms iron (II) phosphate intermittent compound as precursor. The basic illustration of reaction mechanism are represented in Figure 12. Then this is followed by LFP formation by lithium intercalation during calcination.

In meta-morphological synthesis method, the sub-sequential precipitation is used to manipulate and determine the size and shape of final LiFePO_4 crystals by controlling the size and shape of primarily formed precursor particles to achieve nano scale. Therefore, this is only possible because of controlled nucleation and growth reactions of precipitated precursor crystals.

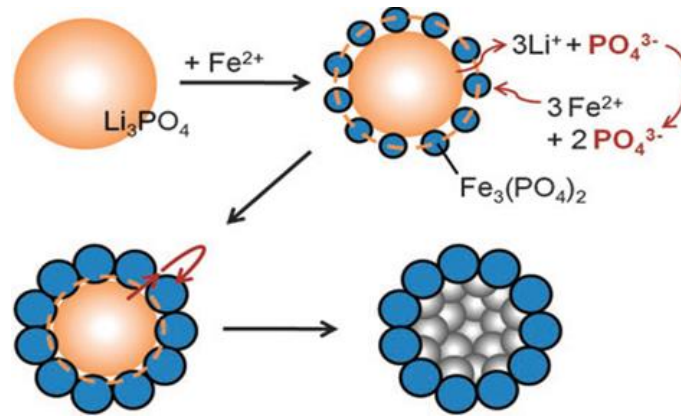


Figure 12. Illustration of sub-sequential precipitation procedure and reaction mechanism.⁵¹



2.5.4 Ultrasonic wave treatment and sonocrystallization

In literature, it is well proven that ultrasound method has a high efficiency to minimize particle size.⁵² This powerful technique has wide applications in industry especially for the production of medicines and dyes where solid materials are dispersed into liquid media homogeneously through Ultrasound (US) waves. Furthermore, US technique is also used for grinding processes of hard materials such as metal oxides or ceramic into very small sizes.^{53–56}

Common synthesis techniques, to refine particle size, using disk mills, high shear mixers and homogenizers would not provide sufficient energy to keep materials in range of nano meters. US can increase the reactivity of metal powders by more than 100,000 times (Figure 13) in a short time. US can drive metal particles together at high speeds. They melt at collision point, and ultrasound can generate microscopic flames in cold liquids.

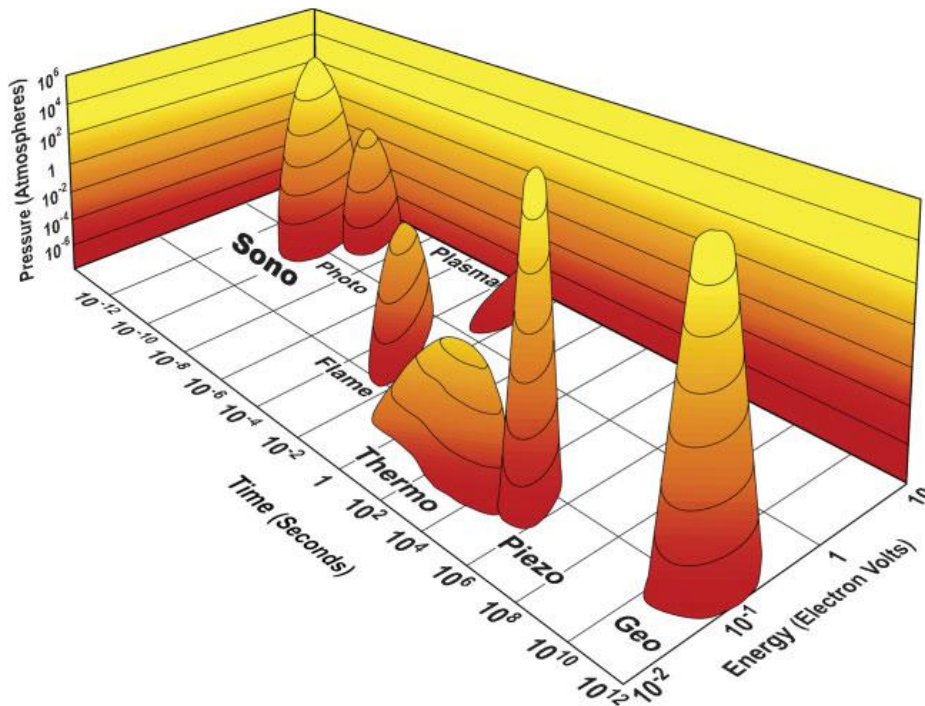


Figure 13. Energy and pressure scale in time domain with respect to some generation phenomena.⁵²

In the process of ultrasonic irradiation, bubbles created by US waves grow, absorb energy and then collapse into a high pressure phase. Figure 14 illustrates how bubbles and waves are formed in a very tiny space and time period. During such an implosion, very high temperatures (5000 K) and very high pressures (approx. 1000 bar) are created locally.⁵⁷ Moreover, high speed liquid jets are formed when these bubbles collapse generating strong shock waves. Reaction processes in ultrasonic emission range, which is called as sonochemistry, can be divided into homogeneous and heterogeneous processes. Homogeneous process proceeds at the hot spot produced by the bubble collapse in the liquid, and the heterogeneous process proceeds at the liquid–solid interface.⁵⁸

During the agitation via ultrasonic method, liquid jets induce particles collide with each other at a high speed which is called “interparticle collision”. Due to the interparticle collision, agglomerates holding together by Van der Waals forces are broken down. This technique is applicable in nanomaterials processing where high shear forces of ultrasound have an advantage of preventing agglomeration.

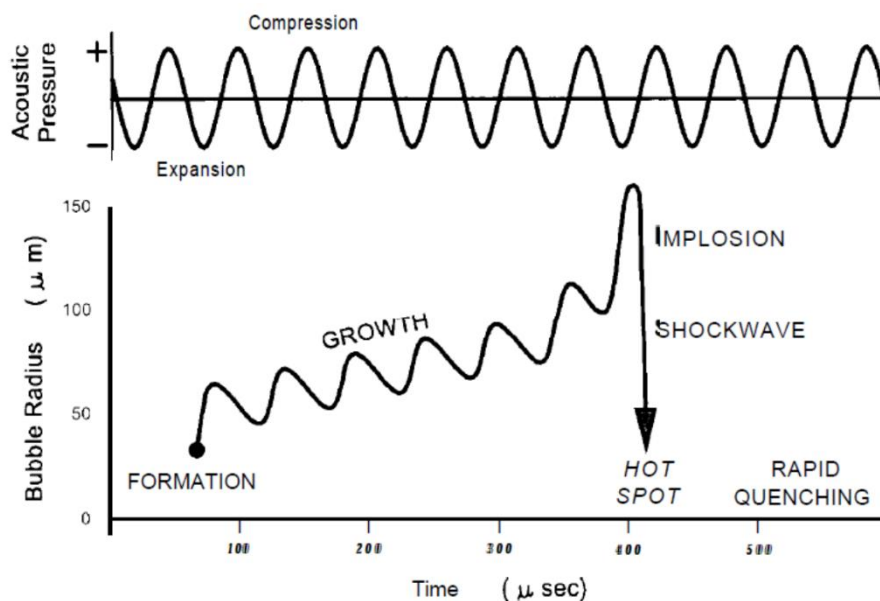


Figure 14. Ultrasonic wave irradiated cavitation behavior in liquid media.⁵⁹

Ultrasound chemical effects arise from the physical processes that create, enlarge and implode gaseous and vaporous cavities in the liquid. Ultrasound waves consist of compression and expansion cycles. Compression cycle exerts a positive pressure on the liquid, keeping the molecules together; expansion cycle exerts a negative pressure, pushing the molecules away from one another. During the expansion cycle, intensity with a sound wave can generate cavities. A liquid is held together by attractive forces, which determines the tensile strength of a liquid. In order to form a cavity, a large negative pressure associated with the expansion cycle of the sound wave is needed to overcome the liquid's tensile strength.

The implosion of cavities establishes an unusual environment for chemical reactions. Gases and vapours inside the cavity are compressed, generating intense heat raising liquid temperature immediately surrounding the cavity and creates a local hot spot. Although temperature of this region is extremely high, region is very small for heat to dissipate quickly. This environment can give unique opportunity to initiate hardly occurred reactions that terminates at an instant.

After increasing the activation of reactions, disintegration or dissolutions within a very short time, the relaxation period comes with a rapid quenching and implosion period (see Figure 14). These sudden and tremendous elevating temperature and pressure within a tiny spot can be restricting action on reaction kinetics. Controlled stimulation

and restriction on desired reactions controlling the other undesired side effects such as further growth, agglomeration, oxidation or solubility and diffusion after very distinctive time periods.

There are generally three types of experimental setup for insonation. Ultrasonic bath, direct immersion of ultrasonic horn, and the ultrasonic flow cell reactor are used in the experiments. The immersion horn and the flow cell reactor were used for sonocrystallization of first and second precipitation reactions. Sonocrystallization is a crystallization process that can be controlled by application of ultrasound energy into crystal growth and nucleation mechanisms. High powered ultrasound can assist the crystallization process in several ways, as initiating the nucleation, controlling the rate of crystal growth, particle size minimization, and surface renewal.⁶⁰

In the industrial crystallization processes, there are several examples about the use of ultrasound assisted crystallization such as zeolite production, food preservation and wine making by its rapid and homogeneous nucleation effect.^{61,62} Furthermore, heterogeneous crystallization is also associated with pressure release from the implosion of bubbles. Their shock waves induce spontaneous formation of new crystals by braking of large crystals to give large number of nuclei for further crystallization. Small and even size crystals appear to be related to increasing rate of nucleation which can be promoted by enhanced power at reduced frequency.⁶³

In literature,^{64,65} ultrasonic irradiation was used for cathode and anode material synthesis in the lithium-ion battery applications. Shen et al.⁶⁶ reported $\text{LiCr}_x\text{Mn}_{2-x}\text{O}_4$ spinel with a uniform particle size distribution which can be obtained by ultrasonic irradiation. Furthermore, Yi et al.⁶⁷ showed that $\text{LiAl}_{0.05}\text{Mn}_{1.95}\text{O}_4$ powder with uniform, nearly cubic structure and octahedral morphology with narrow size distribution has been synthesized via the ultrasonic-assisted sol-gel method. In another study⁶⁸, ultrasonic assisted co-precipitation synthesis was studied by obtaining discharge capacity of 96 mAh g^{-1} (120 mAh g^{-1}) at C/3 (C/10) rate with only size refinement in anisotropic LiFePO_4 particles.

Another effect that needs to be coincide is the anti-site disordering between iron and lithium which could block the [010] channels restricting lithium intercalation. Thus the synthesis of nano-sized LiFePO_4/C material having shorter channel dimension

seems to be an effective route for improved high rate performance. Accordingly, improved specific capacity (increasing from around 80 to 130 mAh g⁻¹) with a up to 60% higher performance was obtained with defect-free material at slow rate (C/20).⁶⁹

2.5.5 Other synthesis methods for LiFePO₄ cathode material

In *solid state reaction method*, precursors for Li, iron and phosphate sources are mixed in solid state. Grinding could be performed at elevated temperature in order to allow degasification. Then second grinding phase is performed with an addition of carbonaceous species to coat on particle's surface. Slightly reductive atmosphere has to be supplied to avoid oxidation.^{70,71}

In *mechanochemical activation*, high energy ball milling is used to achieve small grain sized product. The idea is to keep continuous renewal of contact surfaces to overcome poor reaction rate. This high energetic collisions enhance the diffusion of one component through the product layer.^{72,73}

In *carbothermal synthesis*, precursor mixing and carbonization processes⁷⁴ take place at the same time at a high temperature under hydrogen atmosphere. The key parameter in this technique is the carbon ratio in the reactor causing further reduction in the formation of compounds such as Fe₂P.⁷⁵

By *microwave processing*^{76,77} cathode material is synthesized under atmospheric conditions by rapid oxidation of carbon. In this method, a mixture of solid state precursors (Li₂CO₃, ammonium phosphate) are prepared and then iron source compound is added as a microwave susceptible to absorb microwaves for desired temperature. Reductive atmosphere requirement is supported by an activated carbon which can also absorb microwave. Due to reductive atmosphere, CO₂ is rapidly produced which preserves iron in Fe (II) oxidation state formed as a result of synthesis in air.⁷⁸

Hydrothermal process^{79,80} is a solution based method where pH, concentration and stoichiometric ratios of precursor solutions are important. The uniform distribution of particles in product can be achieved by this method. This is a promising method for doping applications for cathode materials.^{81,82}

Solvothermal process involves thermal treatment at moderate temperatures in a non-aqueous media where precipitation and crystallization reactions occur in organic media.^{83,84} Reactions occur at an elevated temperature and pressure in a specialized autoclave reactor condition.^{51,85} Then further extraction and separation steps are needed to obtain individual LFP crystallites. In this method, the media plays an important role to restrict and direct the crystal growth.⁸⁶ Next step of calcination is needed to increase crystallinity and eliminate the undesired occupancy especially between Fe and Li atoms. Moreover, carbon coating step is crucial and critical step which should have just enough thickness without further resistance for Li ions while increasing the electronic conductivity of the material.

Sol-gel process allows using long or short chain organic compounds as gelation compounds such as polyethylene glycol (PEG). The reactant salts are dissolved in organic solvents generally mediated with alcohol or water/alcohol mixture.⁸⁷ Then this final mixture is stirred slowly and heated slightly up without boiling until the gel is formed. Gel precursor is dried at elevated temperature between 50 and 90°C in an ambient or inert atmosphere. Calcination step is pursued separately by allowing possible intermittent grinding process between low and high temperature steps in inert atmosphere. Calcination and sintering steps, are performed at 300 – 400°C and 600 – 800°C, respectively.^{88,89} Up to 400°C, the decomposition of precursors takes place.

3RD CHAPTER

3. Methodology

Based on the knowledge on lithium ion diffusion in LiFePO₄ crystals²⁴, particle size refinement has a dramatic effect on the rate capability of this material. The immiscible two phase transformation between LiFePO₄ and FePO₄ has been explained with nucleation and phase boundary diffusion in the previous chapter. During lithium transportation, which is parallel to *b* axis, this anisotropic rate of interface movement depends on particle size, shape and crystal orientation. In order to achieve particle size refinement and different morphologies, precursor structures are modulated to gain control on final structure of LFP/C cathode materials in this thesis.

Nucleation mechanisms can be limited to achieve nano-crystalline materials. For this purpose, two different approaches are used to refine the structures' dimensions. In the first approach, which can be referred as bottom-up approach, the desired nanocrystals are allowed to nucleate in a limited condition, which is controlled against further agglomeration and growth. Some sort of surface active organic materials are commonly used as an agglomeration inhibitors. In the second approach, which is called top-down approach, dissolution effect on seed or precursor materials is used with the help of ultrasound. Then crystallization procedure is implemented under control of sound waves.

In the thesis, the aqueous precipitation methods are investigated because they are facile, controllable and economic. Water soluble raw materials are chosen to obtain different precursor structures. The production procedure followed in this thesis consists of multiple steps such as precipitation of precursors, preparation of LFP powders with carbon coating and fabrication of electrodes for testing as shown in the flow chart provided in Figure 15. For the precursor preparation step, two different techniques are chosen; co-precipitation and sub-sequential precipitation. In the thesis, the co-precipitation method is modulated with freeze drying synthesis which allows the control of the particle size and nucleation steps with solution pH.

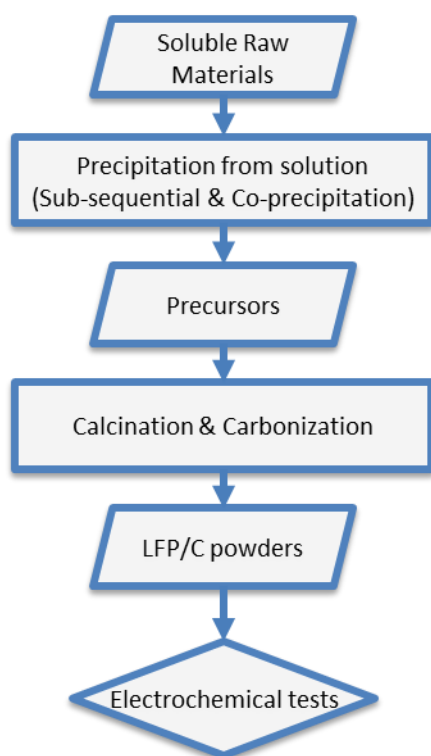


Figure 15. Flowchart showing the steps followed within this thesis.

Sub-sequential precipitation is used to restrict the precursor formation in suspension. The ultrasound effect on precipitation sequence and precipitated structure is also investigated. As seen in this study, the US waves can control the precursor structure and products by manipulating the solubility and rate of the reactions. Two different precursor synthesis methods are implemented based on reaction sequence of sub-sequential precipitation.

3.1 Raw materials

Different types of reactant grade raw materials are used in the synthesis of LiFePO_4 compound. The raw material types are chosen between different salts of Li^+ , Fe^{2+} and PO_4^{3-} ionic species with regard to their high water solubility (Table 1). It is well known for chemical reactions that raw materials have an effect on products as well as the mixing sequences and solution pH values. Hence, in this study, the solution pH changes in regard to mixing sequences and reactant acidity. These changes are examined to investigate the solution pH and reactions resulted in which precipitated products are suitable for the synthesis of lithium iron phosphate in following steps.

Moreover, precipitated powders are recovered from the solution as precursor and analysed by XRD for better understanding about phase structures.

Table 1. The precursor types used for the experiments

Iron sources	Phosphate sources	Lithium sources
FeSO ₄	H ₃ PO ₄	LiOH
C ₁₂ H ₂₂ FeO	(NH ₄)H ₂ PO ₄	LiNO ₃
Fe ₃ (NO ₃) ₃	LiH ₂ PO ₄	LiCH ₃ COO
		LiH ₂ PO ₄

3.2 Precursor synthesis for LiFePO₄ formation

There are two main synthesis methods for precursor preparation as seen in Figure 16. In the first method, co-precipitation, freeze drying is used to manipulate nucleation and growth reactions. In the second method, sub-sequential precipitation is modulated with the help of US waves to synthesize size refined 2D precursors.

In the co-precipitation method, freeze drying procedure is used to slow down the nucleation and growth kinetics, and to prevent further oxidation of the precipitates. In order to make the cryogenic sublimation of water content in freeze dryer, solution or suspension – according to pH – is sprayed into liquid nitrogen for sudden freezing. Two different sequence to start precipitation, are conducted at cryogenic and room temperature conditions. The co-precipitation products are observed at these two different freezing conditions by adjusting the pH to either acidic or neutral region. Cryogenic or temperature driven precipitation term was used for sudden freezing of *solution* by stabilizing the anionic and cationic reactants as completely dissolved in aqueous media within acidic pH. On the other hand, for pH driven precipitation in neutral pH is performed to maintain precipitation at room temperature before sudden freezing of this suspension. The only difference between two routes is the neutral or acidic pH adjustment, to start the nucleation or not, during mixing condition. Then the frozen mix is freeze dried. Thus, the dehumidified powders are prepared to keep the nucleated particles away from further crystal growth and oxidation reactions with water and ambient air.

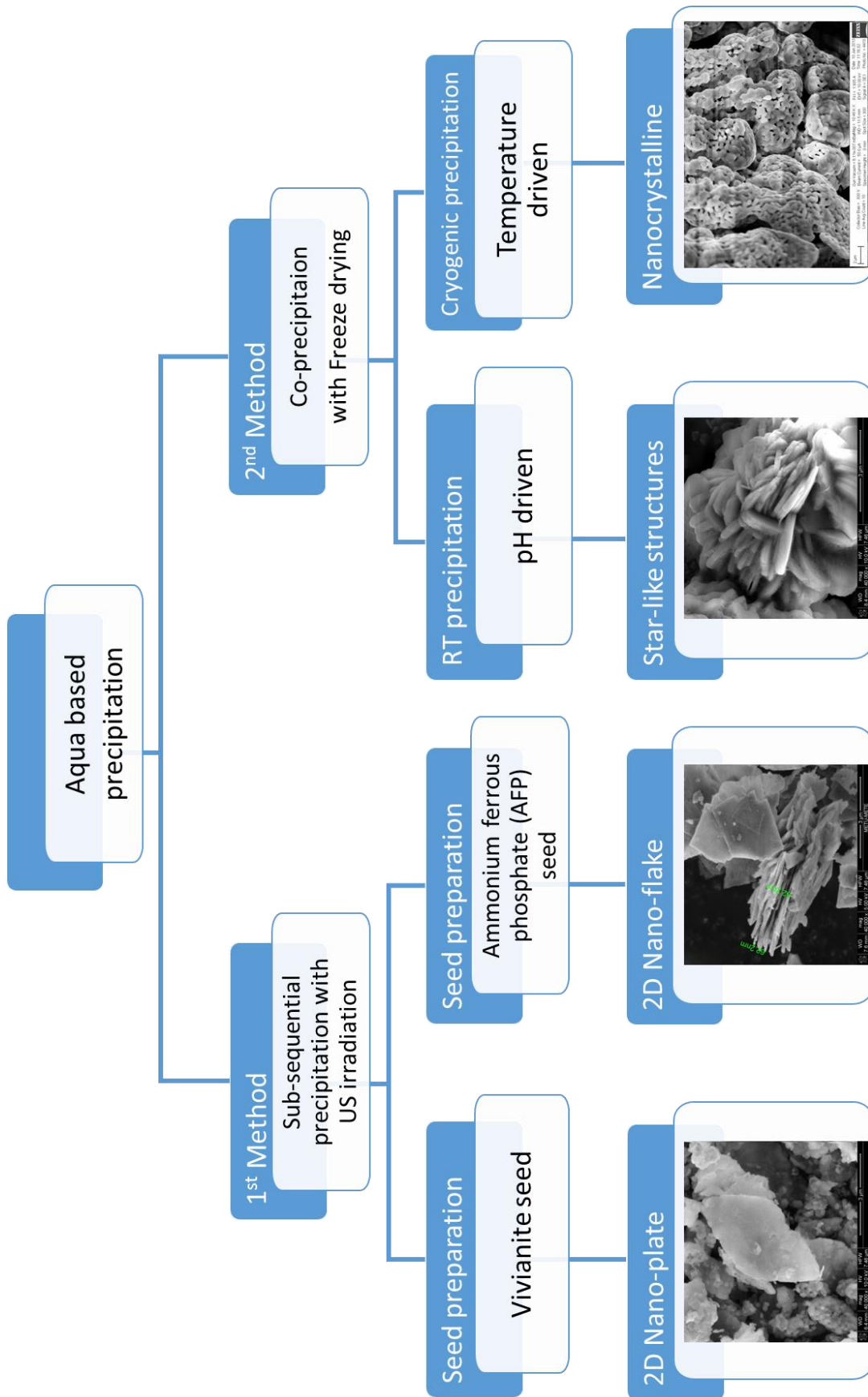


Figure 16. Schematic illustration of experimental routes used to synthesize nano-structured LFP cathode materials.

In the second method, two main sub-sequential precipitation routes are used in conjunction with the US wave irradiation to manipulate the structure of the precipitates. Two types of precursor seeds are prepared, namely vivianite (VVT) and ammonium ferrous phosphate (AFP). The morphology of these crystal precursor seeds have been modified with the help of reducing, stimulating, and reorganizing effect of the US waves on 2D nano structures. The resulting LiFePO_4/C nano-structures and the approaches have been illustrated in Figure 16 after calcination.

The calcination process is used to reach the final nano-structured LFP cathode materials through solid state transformation in slightly reductive atmosphere in furnace. Also, carbon coating is studied by using in-situ and ex-situ carbonization of carbonaceous materials in calcination step.

3.2.1 Co-precipitation

For preliminary understanding of solution based chemical reactions and precipitation products, room temperature co-precipitation synthesis has been investigated with changing pH and reaction precursors. Co-precipitation procedure is summarized in Figure 10 in previous chapter. Co-precipitation method includes further precipitation after the co-existence of all cationic and anionic species in a solution before precipitation.

3.2.1.1 Temperature (cryogenic) or pH controlled co-precipitation in freeze drying synthesis

For the manipulation of nucleation conditions to gain control on size and morphology, freeze drying method is chosen to produce LiFePO_4 using different types of salts. Especially, the salts as raw material should have high solubility for wet chemical reactions. In this method, precursors are mixed then the precipitation occurs as a result of reactions. Final mixture is suddenly frozen by spraying it into liquid nitrogen. The freeze drying step is done under vacuum to dehumidify the precipitate. After this step, samples are calcined through two steps.

In this cryogenic drying method, it is aimed to obtain precipitated materials from iron, phosphate and lithium precursors in an aqueous media by rapid nucleation in a very small scale. At the same time, to recover the intermediate precursor precipitates from the solution, mixture is dried at cryogenic temperatures under vacuum.

During the experiments, solutions are prepared using two different cation (Fe^{2+}) concentrations; that are 0.05M and 0.1M. These two different concentrations are applied for all precursor solutions. The amount of lithium ion concentration is chosen by calculating the stoichiometric ratio of lithium and iron. During the mixing process, pH change and precipitation points are observed and regarding to those, pH adjustment is performed with pH stabilizers.

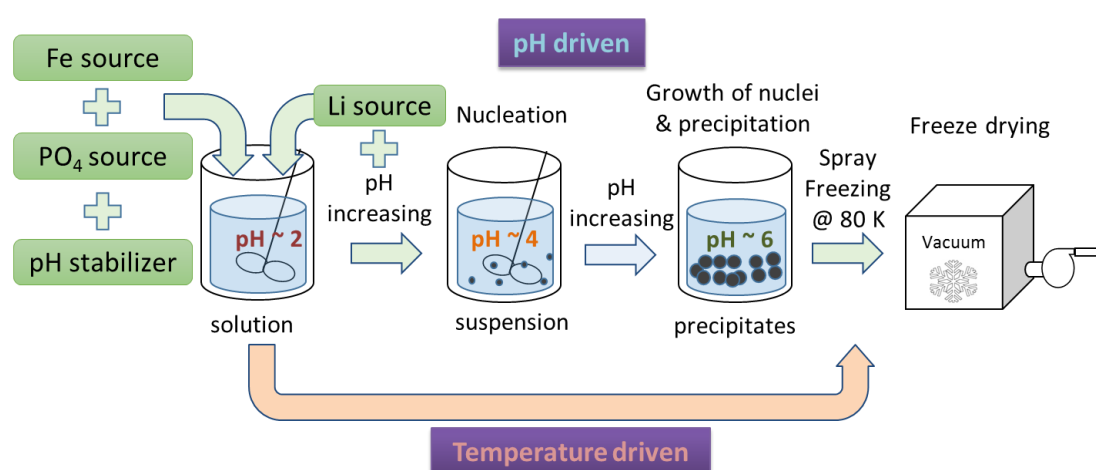


Figure 17. Schematic of the co-precipitation procedure manipulated with freeze drying.

For Fe source, two types of compounds with +2 valance electrons are used such as iron gluconate and iron sulphate. As phosphate source, ammonium di hydrogen phosphate or phosphoric acid; as lithium source, lithium hydroxide or and lithium nitrate are used according to higher and lower pH adjustments, respectively.

Throughout the preliminary experimental study, all mixing reactions are performed under standard ambient condition and precipitates were investigated. All precipitation pH points are recorded according to solution stability. The solution is prepared by adding iron, phosphate, and lithium source as being 0.1M concentration in final mix. In the case of pH driven co-precipitation solution, pH has to be tuned as moving from low pH to higher pH, which reduces the solubility for all solute components. So all

reactants are added in the following order of iron, phosphate, and lithium sources.

For co-precipitation reactions, Fe^{2+} , PO_4^{3-} , and Li^+ sources are prepared in aqua solutions with 1:1:1.2 mole ratio. First, Fe^{2+} and PO_4^{3-} sources are mixed in 80 mL solution. Then, 20 mL concentrated Li source solution is added drop wise into this solution. For the pH driven precipitation, pH is increased to 5.0 and above. Final suspension is frozen by spraying into liquid nitrogen. For the temperature driven precipitation, pH is arranged to be around 2.0 by adding concentrated sulphuric acid as pH stabilizer. Once a clear solution is achieved, it is sprayed and rapidly frozen in the liquid nitrogen in order to obtain precipitated materials from iron, phosphate and lithium precursors in an aqueous media by rapid nucleation in a very small scale. The freeze drying procedure is performed as the same with the rest of the pH driven procedure.

After freezing of mixtures, they are placed into the freeze dryer to evaporate the moisture content to avoid high temperature treatment during drying. Frozen precipitates are dried under vacuum at low temperature freeze drying conditions (–40 to 25 °C). The method is illustrated in Figure 17.

Table 2. Freeze Drying Parameters

Freeze Dryer Program				
Step	Temperature (°C)	Time (min)	Phase	Vacuum, (mmHg)
1	-40	10	Hold	40
2	-30	20	Ramp	40
3	-30	150	Hold	40
4	-25	10	Ramp	40
5	-25	890	Hold	40
6	-20	10	Ramp	40
7	-20	710	Hold	40
8	-10	20	Ramp	50
9	-10	480	Hold	50
10	-5	15	Ramp	30
11	-5	240	Hold	30
12	0	15	Ramp	30
13	0	120	Hold	30
14	20	240	Ramp	30

Then calcination treatment was followed immediately after drying. Further thermal investigation is conducted with the help of DSC and XRD analysis to specify the exact starting point for melting and glassy transition point. Analysis were focused on precipitation condition effect on phase composition change after drying and during calcination reactions. Two different routes, pH and temperature driven precipitation, have been analyzed on the intermittent samples. The schematic illustrations of experimental procedure is shown in Figure 18. For thermal investigation, heat treatment was carried out under slightly reductive atmosphere for 45 and 90 minutes (Ar + H₂ wt.5%) at 80, 130 and 175 °C where after each thermal transition peak point in DSC profile. This thermal treatment has performed with only iron sulfate raw material.

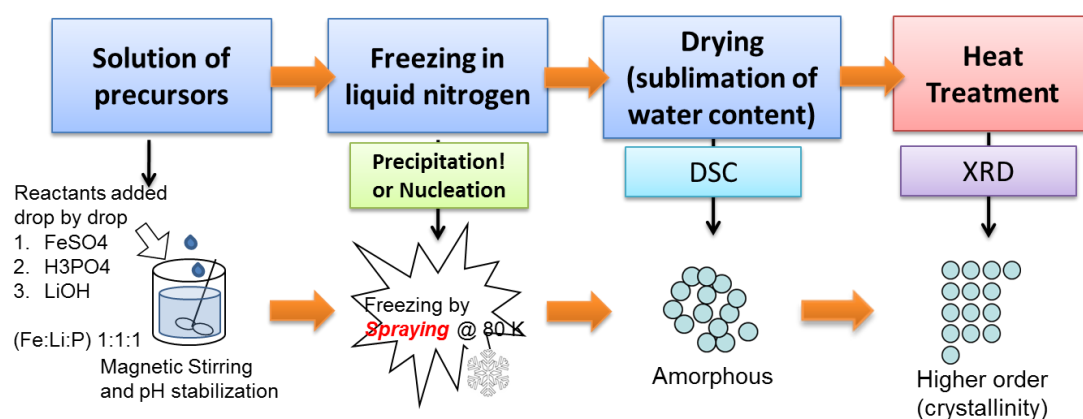


Figure 18. A schematic illustration showing general experimental procedure in co-precipitation method with DSC and XRD analysis.

In order to minimize the increase of thickness and control the shape of the crystallites, the encapsulation of precipitates is done with the surface active additives. As solution based additive, ascorbic acid (AA), citric acid (CA), sucrose (S), and cetyl tri-methyl ammonium bromide (CTAB) compounds has been examined with respect to their existence in low (<2.0) and neutral (>5.0) pH for both temperature and pH driven precipitation routes, respectively. The details are given in section 3.3.2.

3.2.2 Sub-sequential precipitation

Sub-sequential precipitation method consist of two types of precursor materials. They are named as precipitated *precursors* before calcination steps for transformation to LiFePO₄.

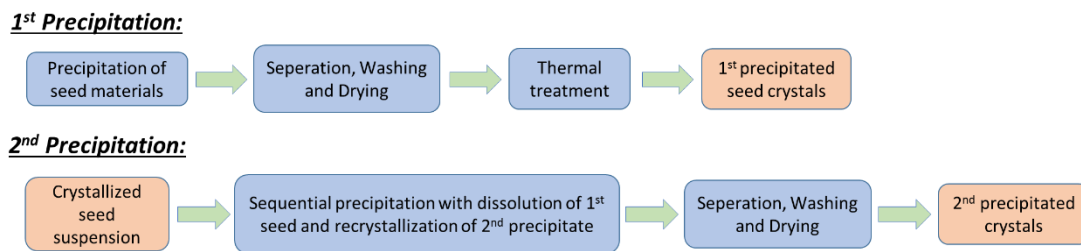


Figure 19. Schematic representation of sub-sequential precipitation procedure and mechanism.

Crystallization of second precipitate are suited on to the surface of first precipitated seeds. Crystal growth process is initiated with dissolution of ionic compounds from first solid precipitate and the concentration is accumulated on the surface region. Thus, second precipitation depends on the rate of dissolution of first phase. So crystal growth mechanism obeys the heterogeneous nucleation approximation on a surface of the seed materials. There are four kinetic steps identified in crystal growth for sequential precipitation.

1. Bulk transport of species through solution
2. Adsorption or attachment to the surface
3. Movement and reaction of ionic species on the surface
4. Attachment of newly formed compound to edges and kinks

The first process is the so-called transport process, whereas items 2 – 4 are indicated as surface processes. Since these different steps normally occur in series, the slowest process will control the overall crystal growth. But for the sequential (secondary) precipitation there are highly accumulated region of newly dissolved ionic species very close to the surface region of first precipitates. Therefore, growth is controlled by the release of phosphate ions from the surface of firstly precipitated particles (Li_3PO_4) (see Figure 20).

In the first route, $\text{Fe}_3(\text{PO}_4)\cdot 8\text{H}_2\text{O}$ (vivianite or VVT) precursor crystals are precipitated after Li_3PO_4 (LP) solid seed particles dissolve. This material is used to combine with iron precursor subsequently. All chemical reactions are slightly evolved with respect to solubility tendency of species. Solubility coefficients, which is the key driving force, are different and so the reactions continue due to this difference. In this study, the effect of LP seed micro structure on precipitation mechanism of precursors is also investigated.

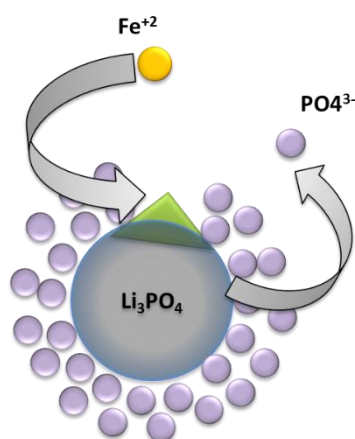


Figure 20. Schematic representation of sequential precipitation controlled by surface dissolution.

3.2.2.1 Ultrasonic wave assisted sub-sequential precipitation synthesis

This section summarizes the method used to achieve well distributed, 2D nano structured precursors and LiFePO_4/C nano composite. By following carbon coating and calcination process, metamorphological transformation leads to the preserved morphology and size. In this method, the sonochemical effect of ultrasound on crystallization process of precipitates is investigated.

Vivianite is well known natural mineral that can be widely found in nature. For sub-sequential precipitation of VVT precursor, lithium phosphate crystals are precipitated because of slightly higher solubility coefficient than ferrous phosphate and its hydrated species. By preparation of lithium phosphate precursors, the ultrasonic irradiation is applied through two different methods which are described as flow cell reactor and rod immersion by powerful US irradiation at 20 kHz. (Figure 21). Precursor nano plate material in 2D was prepared using a powerful US irradiation assisting dissolution, precipitation and following recrystallization reactions in each precipitation step.

This procedure not only involves in first precipitation which yields Li_3PO_4 seed preparation and second precipitation with addition of iron precursor subsequently. All chemical reactions are slowly occurred with respect to solubility tendency of species and so that morphology mediated production could be possible. This procedure has been improved to control the spherical morphology of seeds and the nanostructured precursors by US irradiation during sub-sequential precipitation.



Figure 21. Experimental setup and instruments as US rod immersion (left) and US flow cell (right) for ultrasonic wave assisted precipitation and crystallization.

LiOH and $(\text{NH}_4)\text{H}_2\text{PO}_4$ mixed in a solution to form Li_3PO_4 seed materials through US assisted precipitation. These spherically crystallized seeds are centrifuged and dried in a vacuum environment at $60\text{ }^\circ\text{C}$ followed by a sintering step at $300\text{ }^\circ\text{C}$ in an atmospheric oven.

Sub-sequential precipitation procedure includes two consecutive precipitation steps, which are preparation of Li_3PO_4 (LP) as a seed material and then precipitation of vivianite. As firstly precipitated material, Li_3PO_4 micro-sphere structures are not only used as a seed to supply phosphate ions during second precipitation but also serve as a lithium source during calcination as well.

The key strategy that defines crystal growth limitations and driving the reaction is the solubility difference between Li_3PO_4 ($K_{\text{sp}} = 3.2 \times 10^{-9}$) and less soluble species. LP material is used to combine with iron ions to form $\text{Fe}_3(\text{PO}_4)_2 \cdot 8\text{H}_2\text{O}$ ($K_{\text{sp}} = 1 \times 10^{-36}$) subsequently. All chemical reactions are slightly evolved with respect to solubility tendency of species. As a key source to drive the reaction, solubility coefficients are different and the reactions pursue with respect to this continuous difference. Because of higher solubility of LP, reactions slightly go towards to form iron phosphate intermittent species until LP is consumed.

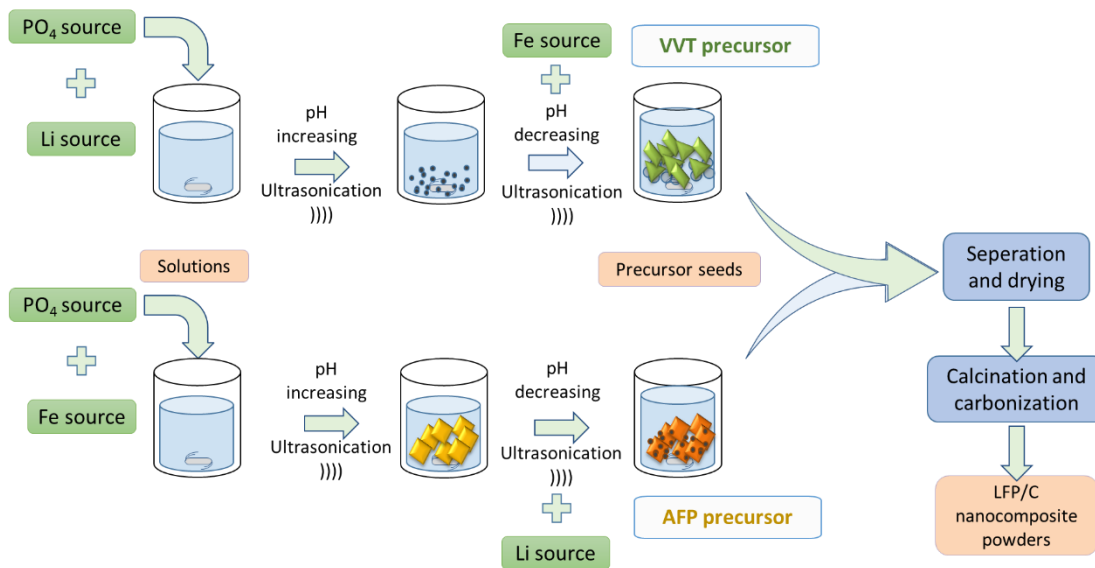


Figure 22. Schematic representation for US assisted sub-sequential synthesis of LiFePO_4/C nano-composite cathode.

The sequential precipitation is accomplished by adding $0.1\text{M FeSO}_4 \cdot 7\text{H}_2\text{O}$ solution to Li_3PO_4 in a 1:1 molar ratio while applying simultaneous US wave irradiation. US wave is used to initiate the fractural dispersion and accelerate the dissolution and recrystallization processes leading to formation of vivianite nano-sheet crystals. Then it is intended to form LFP nano-structures keeping metastable morphology.

Due to the addition of iron source, pH changes are observed. Fe precursor should be added slowly because of the slow dissolution rate of Li_3PO_4 followed by $\text{Fe}_3(\text{PO}_4)_2 \cdot 8\text{H}_2\text{O}$ precipitation. $\text{Fe}_3(\text{PO}_4)_2 \cdot 8\text{H}_2\text{O}$ particles are gradually formed on the Li_3PO_4 seeds until the dissolution of Li^+ and $(\text{PO}_4)^{3-}$ ions are absorbed by the secondary precipitation layer on seed crystals. After the nucleation and formation of vivianite ($\text{Fe}_3(\text{PO}_4)_2 \cdot 8\text{H}_2\text{O}$) micro crystals, phase transformation is occurred by lithium delivery to produce the LiFePO_4 phase as long as solid-state reaction continues.

The same sub-sequential precipitation procedure is implemented with different mixing sequence of 0.1M phosphate and iron source sources at first precipitation which yields $(\text{NH}_4)\text{FePO}_4 \cdot \text{H}_2\text{O}$ precursor. The AFP nano plates are obtained at first precipitation step with and without US by pH adjustment in basic solution. Then lithium sources are used to precipitate with co-existence with AFP nano plates for sequential precipitation. Three different lithium salts were used that are lithium acetate, lithium nitrate and lithium hydroxide for second precipitation, to investigate the effect on morphology and crystal structure of LiFePO_4 cathode powder. Solution of lithiation compounds are

prepared and added on pH adjusted AFP suspension with respect to 1:1 molar ratio of Li:Fe. Sequential precipitation is accommodated by saturation of lithium salts' solution by adsorption and ion exchange reaction between Li^+ and NH_4^+ , which continues through the whole transformation in high temperature calcination towards the LiFePO_4 formation.

3.3 Preparing LiFePO_4/C cathode powders by calcination and carbonization

The same calcination procedure is used for both co-precipitation and sub-sequential precipitation methods. Calcination procedure that has to be applied to gain better crystallinity and ordering has a destructive effect upon morphology by accelerating growth and agglomeration. So the optimized conditions and carbonization methods are investigated for further improvement on the crystallinity besides morphology preservation, size reduction and coating thickness on cathode surface.

3.3.1 Calcination as a solid state transformation to LiFePO_4/C nano-composite

Following the drying process, in order to maintain annealing and final transformation of LFP crystallites, samples were thermally treated under reductive ($\text{Ar} + \text{H}_2$ 5% wt.) atmosphere at 300 and 700 °C for 4 and 6 h, respectively. Regarding to XRD analysis, more than 90% of the product was composed of LiFePO_4 . The rest of the product include other phosphate phases. As a result, LiFePO_4/C (LFP > 95%) composite is successfully synthesized in some experiments mentioned as in further chapter.

In some cases ineffective side products such as Li_3PO_4 and Fe can reduce the LFP yield towards 80 wt.%. In all cases, Rietveld refinement has been conducted to calculate analytical LFP percentage. Higher calcination temperature above 800 °C tends to destroy the LFP crystal structure and decomposition reactions occur.⁹⁰ The conditions and carbonization methods which give highest yield of LiFePO_4 material have been chosen for further cathode material preparation and electrochemical tests.

3.3.2 Carbon coating and encapsulation strategies

Carbon coating is the crucial step⁹¹ for the synthesis of conductive LiFePO₄/C composite cathode materials. To make LiFePO₄/C composites having good rate capability, high energy density, the carbon content and method for coating carbon onto the LiFePO₄ particles must be given careful attention.

Despite, in general, in-situ carbonization refers to addition of any carbonaceous compounds before calcination step because of actual LiFePO₄ transformation in calcination, carbonization is named according to drying step as a reference for this nomenclatures. Because all carbonaceous materials are added to the solid precursor mix before or during calcination and carbonization which are named as in-situ according to general use. But in the case of this study, to distinguish the difference between the addition sequences, the precursor drying step will be considered as a reference step for the determination of carbon addition method as in-situ and ex-situ, as before and after this step, respectively. Throughout the thesis, the in-situ carbonization refers to the addition of soluble compound on solution (precipitation) phase just before drying.

Carbon ingredient is delivered from different synthesis steps by adding organic materials for growth limitation and conduction. There are three ways to introduce carbonaceous materials into the precursors.

1. Addition into the solution before the formation of precursor. This way can limit growth, direct structure or enhance nucleation.
2. Vaporized additive during calcination deposited on LFP powders
3. Dissolved additive mixed with precipitated solid precursors (evaporated saturation in suspension)

3.3.2.1 Carbon coating with solution based additives

In order to minimize the growth or thickness and control the shape of the crystallites, the encapsulation of precipitates is possible with the same carbonaceous materials used for carbon coating. Possible surface active and water soluble encapsulating compounds have been used right after drying of precipitates and before calcination step for both freeze drying and US assisted methods.

For freeze drying method, three different chelating organic compounds are ascorbic acid (AA), citric acid (CA) and CTAB as carbonaceous compounds. In the precipitation step, they also show reductive properties. So, in this in-situ technique, the carbonization was done by calcination step without any further addition of carbonaceous compound besides these components added during precipitation step.

For US assisted method, ethylene glycol (EG) and citric acid (CA) compounds were used as carbonaceous compounds in precipitation step besides their reductive properties in carbonization.

3.3.2.2 Carbon coating with Chemical Vapour Deposition

In contrast to in situ carbonization, carbon coating can also be implemented externally after LiFePO_4 formation. In chemical vapor deposition (CVD) method, a vaporized organic compound is sent to the furnace, which has the desired material to be coated and carbonized as layer by layer. Tubular type furnaces are preferably used for stable flow of carrier gas and exhaust of gasification products. Decomposition of organic vapor and deposition onto the material surface is maintained along the furnace. For CVD method, toluene vapor has been used. Toluene vapor is sent to be vaporized by bubbling of the carrier gas in the liquid toluene. Carbon coating is continued for 1h deposition at 800°C .

3.3.2.3 Carbon encapsulation with sugar saturation

After precipitation and drying of intermittent products, the whole dried solid material was mixed with appropriate amount of sucrose and subjected to a final drying in a vacuum atmosphere below 60°C . This procedure gives sufficient encapsulation effect and organic compound, which generates carbon layer after carbonization onto the nano crystallite surface.

In freeze drying method, the dried powders are also covered with a conductive carbon layer. In order to limit the growth rate and size during calcination, all carbonaceous materials were added before the calcination step as a common implementation in this thesis. There are two different addition namely as in-situ and ex-situ that refer as added on mixture before and after drying step, respectively.

3.4 Material characterization

The evaluated products' phase and morphological changes are analysed by stepwise X-Ray Diffraction (XRD) and Scanning Electron Microscopy (SEM). Also, Energy Dispersive X-Ray Spectroscopy (EDX) analysis is performed on those products which could be distinguishable from the candidates among the alternative phases determined by XRD patterns. Transmission Electron Microscopy (TEM) analysis is used for further structural analysis of nano-structured and nano-crystalline LFP particles. Selected Area Electron Diffraction (SAED) analysis is used to determine the approximate orientation of LFP crystals. Raman spectrum has shown graphitization degree of the deposited carbon layer onto the synthesized cathode materials.

3.4.1 Scanning Electron Microscopy and Energy Dispersive X-Ray analysis

SEM analysis is used to observe the material morphology and to measure the thickness and sizes of representative nano structured materials. EDX is also used as a supplementary tool to determine the composition and phase identification upon observed specific crystals which can be pictured by SEM.

SEM imaging and EDX analysis of samples after calcination is performed using field emitting scanning electron microscope (FEI-NOVA Nano SEM 450) with an accelerating voltage of 5-10 kV and 18-20 kV, respectively. A thin gold layer is deposited on some of the samples in order to reduce surface charge for better imaging. Some images are taken in a slightly steamized (10mBar) atmosphere with low vacuum detector (LVD). All SEM imaging is carried out at a working distance of 5 mm.

3.4.2 Transmission Electron Microscopy and Selected Area Electron Diffraction analysis

Transmission electron microscopy (JEOL 2010F TEM) is used to examine the nanoscale microstructure of the particles at 200 kV having an ultra-thin beryllium window for EDX, attached with a link analyser. After sonication of samples in ethanol for 30 min, emulsion solution is dropped on the Cu TEM grids and then TEM imaging

and selected area diffraction (SAED) analysis are performed. Other magnetic powder samples including Fe residue particles are dispersed into the EmBed-812 solution then cured at 60 °C overnight. After curing is done, plastic mould including particles are removed and cut with a piezo diamond knife (Leica EM UC6). Then they are placed as 70 nm thick sheets onto a holey carbon coated Cu grids.

3.4.3 X-Ray diffraction analysis

X-Ray diffraction patterns were obtained by Rigaku DMAX 2200 X-Ray Diffractometer instrument with Cu K α radiation and Bragg-Brentano geometry with fixed slit setup and the scan rate of 2 degrees/minute. For preferred orientation investigation, parallel beam and standard beam geometries are satisfied by Bruker D8 diffractometer. On the synthesized LFP nano structures, the Rietveld method is carried out for the quantitative phase analysis. For quantitative phase analysis Rietveld refinement was computed with Materials Analysis Using Diffraction (MAUD v. 2.5) program.⁹²

3.4.4 Raman spectroscopy

Raman spectroscopy (Horiba Jobin Yvon iHR 550) is used to analyse carbon layers in the powder samples. Laser wave-length was 514 nm (green light source) equipped with a grating 600 lines/mm and a 50X microscope. Raman spectra of selected samples are deconvoluted at around 1300 cm⁻¹ (D band) and 1590 cm⁻¹ (G band) using Lorentzian peaks to find out the I_D/I_G intensity and area ratio.

3.4.5 Particle size measurement

Particle size measurement was done on powder samples which are sonicated in ethanol as a dispersant. Particle size distribution measurement is performed with laser diffraction particle size analyzer (Mastersizer 2000).

3.4.6 Differential scanning calorimetry

Differential Scanning Calorimetry (DSC) analysis is performed in freeze drying method to better understand the nucleation, growth, crystallization, and phase transformation towards the LiFePO_4 formation in calcination. Analysis is conducted with SEIKO SII calorimeter. The acceleration rate is chosen as $40\text{ }^\circ\text{C min}^{-1}$ and the limiting temperature range is between 0 to $400\text{ }^\circ\text{C}$. Lower heating rate, which gives higher resolution is not chosen because of decreased sensitivity of scanned patterns despite of the broad peaks. Otherwise, the faster transformation mechanisms such as growth existed in the crystallizing samples might not be distinguishable well enough. However, slower scan rates can be useful also for analysing each transformation step in detail.

3.4.7 Electrode and cell making procedures

The electrochemical performances of cathode materials are measured in a button cell against lithium metal as anode and a glass microfiber mat separator. The working electrode is prepared by dispersing 80% wt. active materials, 15% wt. carbon black (Timcal C65), and 5% wt. polyvinylidene difluoride (PVDF) binder in the N-methyl pyrrolidone (NMP) solvent to form a uniform slurry using a ball shaker. Carbon content measurements are performed by Eltra CS 80 carbon/sulphur analyser in order to make calculation for appropriate carbon and active mass amount. The slurry is coated by a doctor blade on Al foils keeping the total wet thickness to $250\text{ }\mu\text{m}$. The foil was then dried in vacuum at $120\text{ }^\circ\text{C}$ for 12 h. The electrolyte is 1M LiPF_6 in ethylene carbonate, di ethylene carbonate (EC:DEC) (1:1) mixture. Carbon black content was chosen as well as in literature used for high rate cell cathodes.³⁰

3.4.8 Galvanostatic measurements and electrochemical impedance spectroscopy

Button cells are assembled in an argon-filled glove box and tested by galvanostatic charge and discharge cycles between 2.8 and 3.9V on a test system (Solartron Multistat). Electrochemical performance tests are conducted with galvanostatic cyclic regime as indicated in Table 3. The electrochemical impedance spectra (EIS) test (the

frequency range of 0.3 – 300 000 Hz) was performed on a (Princeton VersaSTAT-3) electrochemical workstation. Electrochemical impedance data are fitted according to the electrical circuit shown in Figure 23.

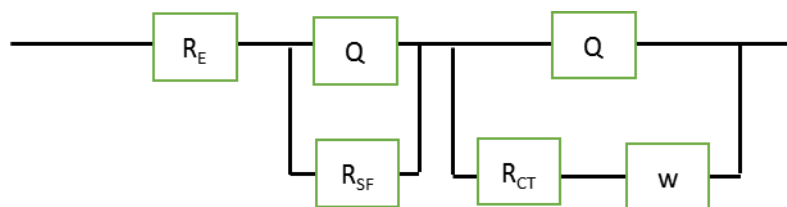


Figure 23. Schematic of equivalent circuit for EIS of cell test.

Table 3. Galvanostatic cell test parameters with currents and respective rates

Cycle	Current (mA)		Rate	
	Charge	Discharge	Charge	Discharge
1	0.125	0.125	C/10	C/10
2	0.125	0.625	C/10	C/2
3	0.125	1.25	C/10	C
4	0.125	6.25	C/10	5C
5	0.125	12.5	C/10	10C
6	1.25	0.125	C	C/10
7	1.25	1.25	C	C
8	1.25	12.5	C	10C
9	0.125	0.125	C/10	C/10

4TH CHAPTER

4. Results and Discussions

The co-precipitation reactions have been investigated with different precursors. Each precursor was selected according to their high solubility, low melting points and easy gasification of side products in calcination step. First, aqueous precipitation in room conditions were studied to get an idea about nucleation rate, suitable intermittent phases and their tunable morphology for the synthesis of LFP. Then freeze drying method was implemented to have control on the morphology and oxidation at low temperatures.

Alternately, some different precipitation techniques were studied within sequential precipitation routes preparing precursor structures. This sequential precipitation processes play delaying effect on the recrystallization of the precursor materials. By this way, it is possible to control the morphology by manipulating the kinetic mechanism of crystal structures with external US irradiation.

4.1 Co-precipitation

4.1.1 Effect of iron sources and pH on precipitation products

In the co-precipitation method, three iron precursors have been used for analyzing preliminary wet solution chemistry and reactions in stable pH region. It is observed that precipitates can be formed in a lower pH (1.5) by using iron (III) nitrate, while higher pH (3.5) values for iron (II) gluconate and iron (II) sulfate sources are achieved. Despite the fact that LiFePO_4 is stable thermodynamically at pH values lower than 11.3, it is not possible to obtain it in strongly acidic pH (< 2.0) conditions. In the case of using FeSO_4 precursor, especially, slow kinetics was observed during precipitation formed around a pH level of 3.15 – 3.75, which is in agreement with literature.⁹³ According to the visual observation, the precipitation is still continuing after several minutes.

For iron nitrate as the iron source, the precipitation pH level is around 1.5 and first precipitated product is LiNO_3 as ion exchanging product as shown in Figure 24 – c. The precipitates were washed up with LiOH solution after products occurred. As we know, lithium nitrate is also a very good oxidizer.⁹⁴ So its thermal decomposition, which gives Li_2O , NO_2 and O_2 products,⁹⁵ can oxidize the iron ions by yielding undesired oxidized products such as $\text{Li}_3\text{Fe}_2(\text{PO}_4)_3$, Fe_2O_3 during calcination reactions. So iron nitrate was no longer used as raw material because of its highly oxidative side products and unsuitable precipitation pH point at acidic range in particularly low temperature solution media.

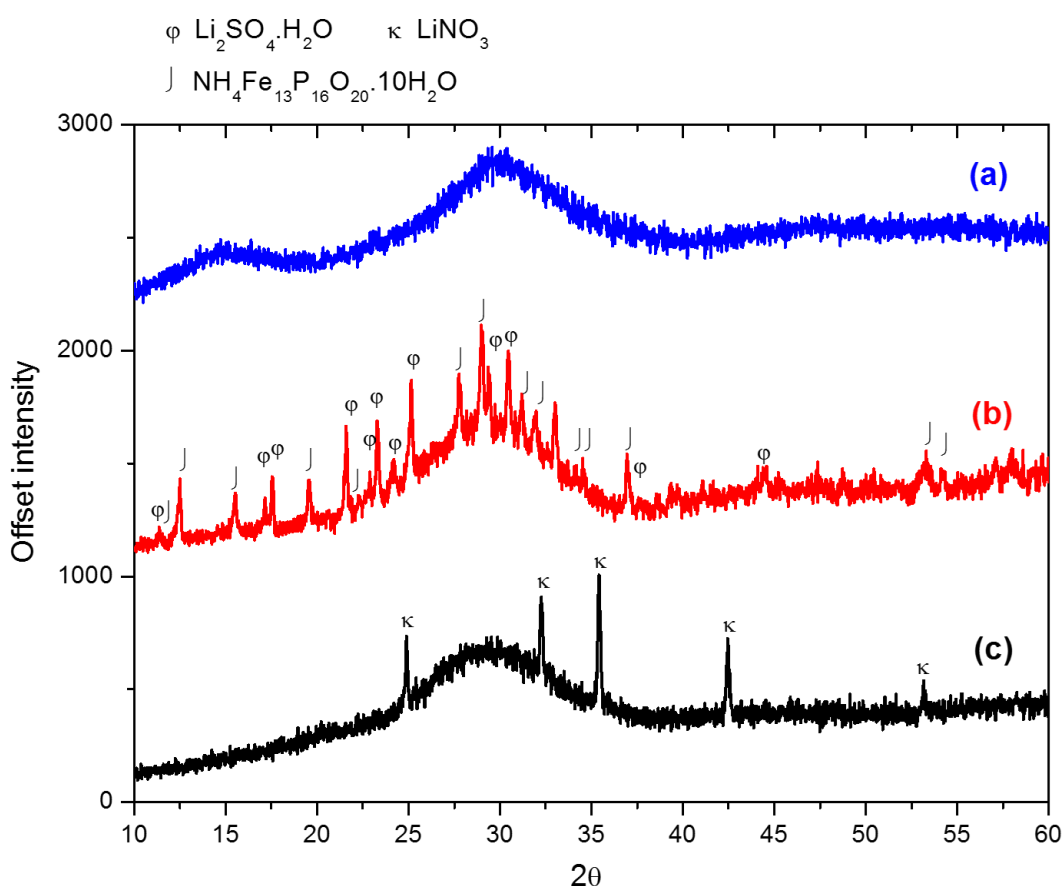


Figure 24. XRD analysis of precipitated products prepared with iron gluconate (a), iron sulfate (b) and iron nitrate (c) after co-precipitation and drying under room condition.

Lithium is ready to react with whatever anion of iron source is because of its higher ionic affinity in solution media. So ion exchange reaction products are observed at first in precipitate powders. So at the beginning of the lithium source addition in iron sulfate experiment, it gives stable $\text{Li}_2\text{SO}_4 \cdot \text{H}_2\text{O}$ salts ($\Delta G_f: -1324.7 \text{ kJ mol}^{-1}$) as given

possibility to form iron phosphate compounds within various hydrated forms (Figure 24 – b).

For iron gluconate as iron source, the precipitation point is similar with the iron sulfate experiments pH around 3.5 – 4.0. However high organic content of iron gluconate keeps away the precipitate powder from higher crystallinity as shown in Figure 24 – a. Thus, the highly amorphous structure of precipitate cannot be analyzed by XRD. However, some precipitated crystal products are observed in higher suspension pH as described in the following section.

4.1.2 Effect of pH and carbon existence on phase morphology and crystallinity

In the experiments using iron gluconate as iron source, the resulted precipitates occurred at the pH level between 3.0 and 4.0 after the addition of LiOH. In this point ammonium dihydrogen phosphate source could arrange the solution pH even after basic LiOH addition because their two more proton, which can enhance the stability of solution pH as a stabilizer. This further ionization orders help to keep pH level at a certain range while adding enough lithium stoichiometry before it precipitates.

Significant morphological differences are observed in co-precipitated powders using various pH values as shown in the SEM images provided in Figure 25. The plate like morphology (Figure 25-a, b) of vivianite crystals, as shown in Figure 26, is produced in between 4.0 to 6.0 pH range with plate like shape. This finding represents that this pH region is crucially important to obtain platelet morphology of crystallites. However, these rough platelets are ready to lose their morphology at higher temperatures in calcination. As explained further in results, the simultaneous crystallization is modified with the help of external forces and conditions. Homogeneous particle distribution are satisfied as well as refinement to nano size by manipulation of crystallization kinetics and transport mechanisms. The aspect ratio of thickness / length could be enhanced from 3 to 30, approximately, with further treatments explained in details in section 4.3.

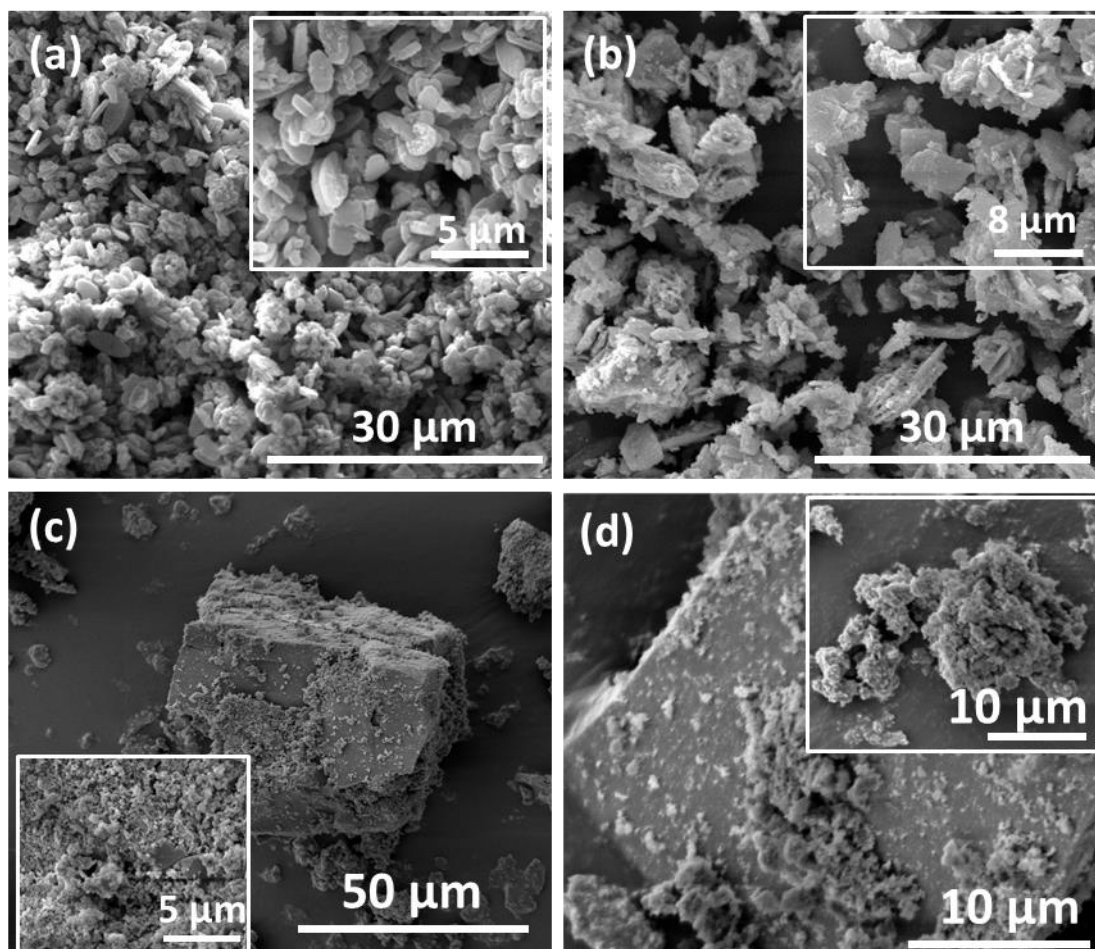


Figure 25. SEM image of co-precipitated structures at pH (a, c) 4.0 and (b, d) 6.0 by using iron sulfate (a, b) and iron gluconate (c, d)

As seen in vivianite crystallites in Figure 25-a, shape of precipitated vivianite crystallites are similar to plate morphology like LFP crystallites reported in literature.^{84,96,97} Moreover this morphology was achieved in this study, without any organic addition into aqueous solution by co-precipitation. Many research activities were focused on one batch production by using various type of organic additives to manipulate the final shape of LFP crystallites as plate like morphology. However, most of them are resulted with bigger crystallites away from nano sizes and required high temperature synthesis.^{98,99} If the shape conservation would be possible at the precursor phase, the morphology manipulation and size determination could be successfully maintained based on a preliminary low temperature production of precursor phases like vivianite. At least this particular high aspect ratio can be conserved along the phase transformation. This idea drives the meta-morphological synthesis strategy as investigated in details of section 4.3.

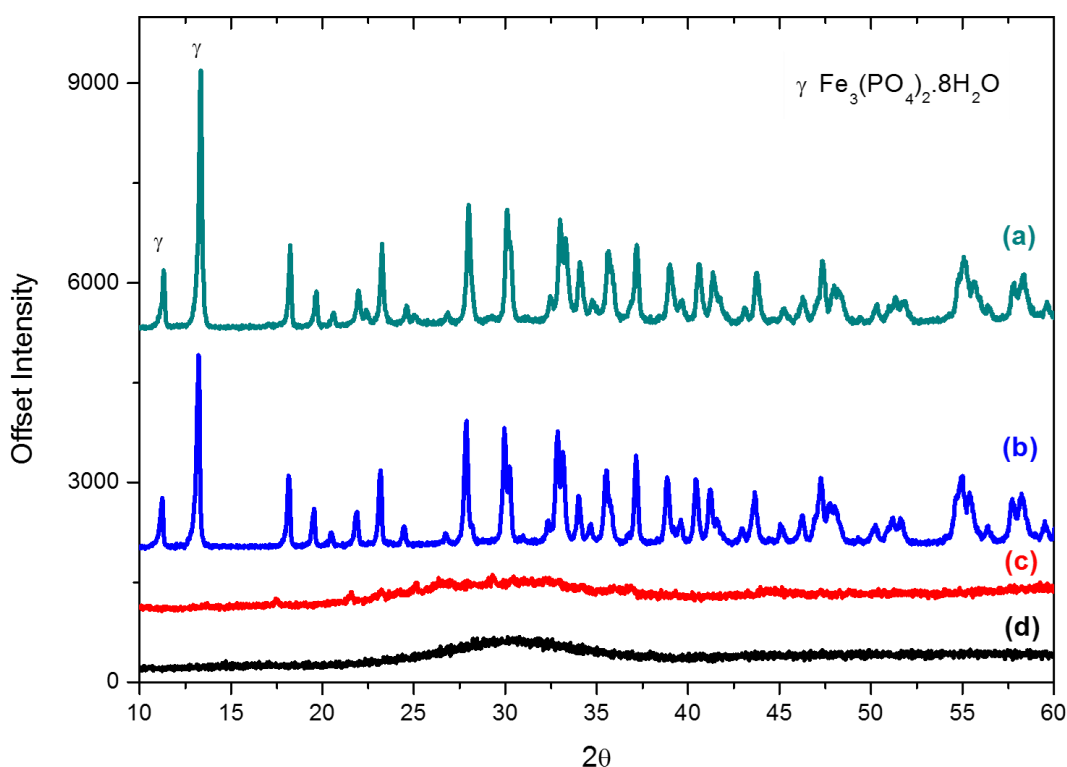


Figure 26. XRD patterns of co-precipitated samples by using different iron (II) precursors as iron sulfate (a, b) and iron gluconate (c, d) at pH 4.0 (b, d) and 6.0 (a, c)

For understanding the effect of iron sources, iron gluconate was used to investigate its strong chelating properties on Fe^{2+} together with the effect of in-situ carbon addition during the co-precipitation step. Besides, carbon addition was also supplied by adding organic acids to the co-precipitation step in the case of FeSO_4 . The presence of carbon in the precursor source acts as an oxidation inhibitor for Fe^{2+} ions in solution phase. Furthermore, the presence of carbon prevents Fe^{2+} from oxidation during the calcination step, too.

The dissolution of FeSO_4 precursor in water is a slow process and a blur solution is observed even before the solubility limit. After an overnight waiting period, orange precipitates are observed at the bottom of the flask. An explanation for the precipitation would be the oxidation of Fe^{2+} ion to Fe^{3+} ion in the aqueous media. The solubility of solution containing Fe^{3+} ions is lower than the solution containing Fe^{2+} ions, which causes precipitation. This phenomenon is well known and managed by co-existence of reducing agent before precipitation.

At low pH ranges, the oxidation of Fe ion is avoided by the presence of excess amount of protons. In addition, it was also observed that the precipitate amount was increased for the solutions in which pH was adjusted.

Iron sulfate and iron gluconate sources have different effects on the precursors' morphology. XRD patterns and SEM images show that samples prepared using iron gluconate precursor did not have crystalline structures as in the case of FeSO₄ both after precipitation and calcination steps. The use of carbon precursor resulted in undefined amorphous structures.

Regarding to these SEM images (Figure 25), it may be speculated that homogenous nucleation is dominant in the case of FeSO₄ usage in order to have well-defined, and uniformly scattered 'plate-like' structures. On the contrary, it may be proclaimed that heterogenous nucleation is more dominant evidenced by bulky and bigger structures observed in SEM images (Figure 25 c and d) through the use of carbon containing iron source. Hence, gaining control on the nucleation is the key point to have well-defined structures in the co-precipitation method. On the other hand, the samples using iron gluconate as precursor, do not show any kind of definite shape rather than its strong carbon encapsulation and size refinement effect on the final LFP particles.

4.2 Freeze drying with co-precipitation

In atmospheric conditions, for co-precipitation methods, there are two ways to start the nucleation, which are increasing concentration or decreasing the solubility by controlling pH and decreasing temperature. In order to control the size of solid particles by enhancing the number of nuclei, rapid nucleation should be conducted, limiting the growth rate of the particles.

After the precipitation, the solid particles has to be separated from water (solvent). Freeze drying can be a suitable treatment for drying by vacuum in freeze dryer. After mixing completed, pH determines the mixture to be a solution or suspension. If pH is high enough to start the nucleation, intermediate phases occur as a result of the reactive precipitation. In order to investigate the nucleation starter effect of temperature or pH, two different final pH were chosen as 2.0 and 5.0, respectively. Then this suspension or solution is frozen suddenly using liquid nitrogen. Freeze drying process is a useful treatment for drying without any agglomeration or crystal growth in solid materials.

4.2.1 Temperature (cryogenic) and pH controlled nucleation in co-precipitation with freeze drying

It is well known that co-precipitation of precursors from solution could be controlled by tuning the pH of the solution. In our solution system, solution pH is adjusted from 3.0 to higher to start co-precipitation of iron phosphate compounds. If the solution media is forced to have acidic property by adding acids, co-precipitation is suppressed at atmospheric conditions with all sources. In the case of suppressed co-precipitation, the solution temperature is rapidly reduced by “*spray freezing*” method into liquid nitrogen (like quenching) where a decrease in the temperature is the driving force for nucleation. Then frozen mixture is dried according to “*freeze drying*” procedure.

Precipitate formation is occurred in a similar pH range to precipitation of solution with iron sulphate or iron gluconate source. In temperature controlled nucleation route, the aim is to have a sudden nucleation during the freezing step by limiting the growth rate. So particle size may be limited with the formation of nano-clusters within early state of nucleation.

For further understanding of the solidification and precipitation during sudden spray freezing of the solution, thermal behavior of precipitated species are investigated by DSC analysis. Measuring the heat dissipation during calcination in inert atmosphere provides useful information on the crystallization and growth of nuclei from amorphous to crystalline phase. Moreover phase transformation temperatures and other reactions can be analyzed in both exothermic and endothermic cases.

Under sublimation (freeze drying) condition high temperatures may cause melting due to the low melting point of starting solution. This melting failure may be seen after drying due to the color change of the sample. Palomares et al. determined this melting point as -16 °C by measuring the increase in conductivity with the similar sources during an increase in temperature.³⁹ It was chosen -20 °C as the highest temperature as fully dried condition according to this information. The sample must be kept away from elevated temperatures before the DSC tests.

Two different lithium sources are used (i.e. LiOH and LiH₂PO₄) to arrange the pH value of 5.0 and 2.0, respectively. Calorimetric profile of heat flux clearly shows that pH driven processes show glass transition (T_g) around 80 – 100 °C (Figure 27).

Otherwise, instead of the T_g , temperature driven precipitated samples have strong exothermic peaks, dominantly, representing the growth and crystallization process of formerly produced nuclei in solidified amorphous phases. After the T_g and nuclei growth temperature, similar series of endothermic peaks follow them in both pH or temperature nucleated cases.

Decreased intensities in XRD patterns in Figure 28 and Figure 29 show phase transformation or melting of phases. So some peaks were hardly distinguishable in the XRD patterns especially in temperature driven procedure as expected. This is because of the amorphous content due to the rapid freezing before crystallization. However, some set of peaks can be identified in early solidified precipitates like $\text{Li}_2\text{SO}_4 \cdot \text{H}_2\text{O}$.

In the temperature driven processes, after freeze drying, $\text{FeSO}_4 \cdot 7\text{H}_2\text{O}$ and $\text{Li}_2\text{SO}_4 \cdot \text{H}_2\text{O}$ phases mainly crystallized up to 120 °C. After this point, LiH_2PO_4 phases forms by ionic exchange with the amorphous phosphate content in the solid material. A delayed transformation of Li_2SO_4 to LiH_2PO_4 means Li_2SO_4 is more stable than lithium phosphate compounds (LiH_2PO_4 and Li_3PO_4) in lower temperature with the existence of $(\text{SO}_4)^{3-}$ ions.

By elevating temperature towards 175 °C, iron sulfate and iron phosphate species appear in dehydrated forms as shown in Figure 28. After 300 °C, other endothermic peaks are seen that represents dehydration of $\text{FeSO}_4 \cdot \text{H}_2\text{O}$ at 250 – 350 °C associated with the gasification of the sulfur content (SO_x , H_xS), which is mainly coming from the conversion reactions of lithium sulfates (Li_2SO_4) to the lithium phosphate (LiH_2PO_4 and Li_3PO_4) species (Figure 28).

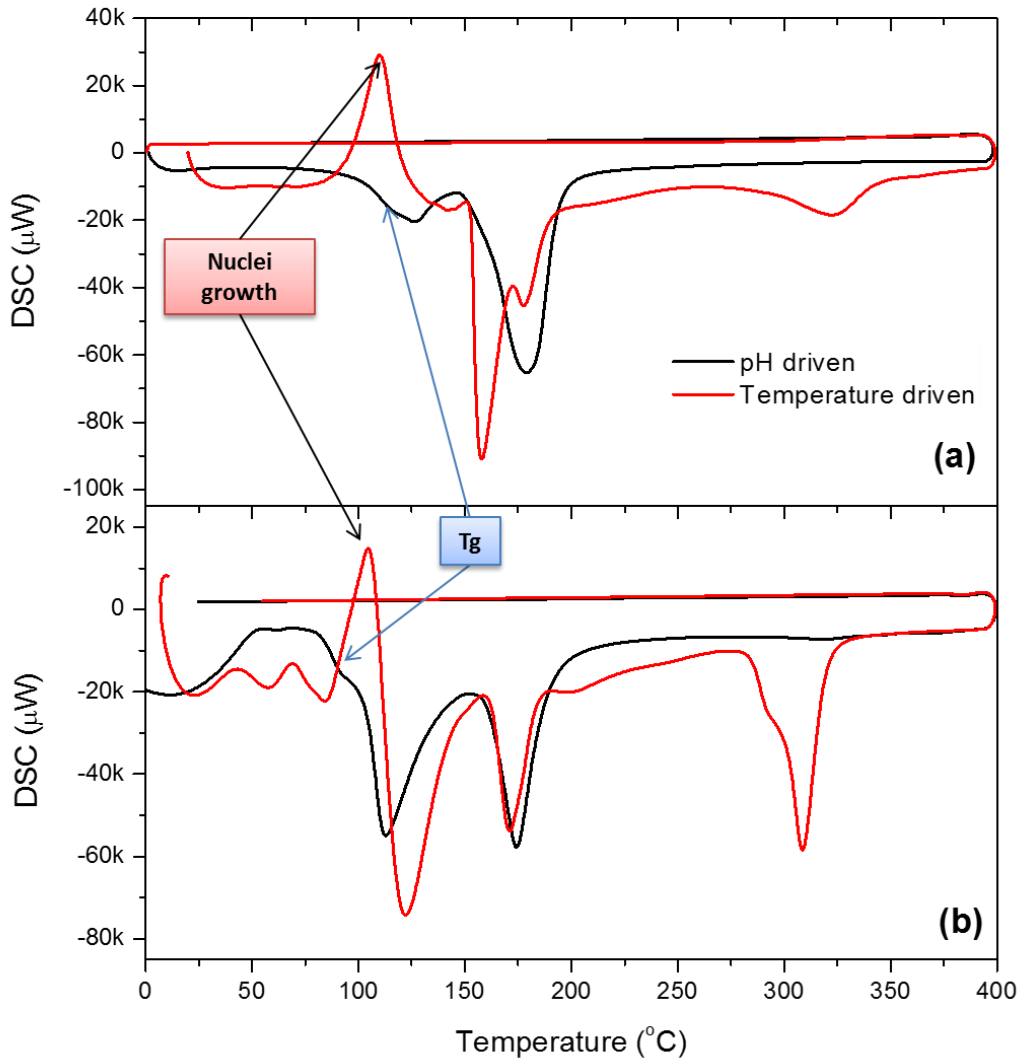


Figure 27. Heat flux profiles (exo-up) in DSC analysis (40 K min^{-1}) of temperature and pH driven precipitated samples with Fe:Li mole ratio of (a) 1:3 and (b) 1:1.2.

In the pH driven processes, dried powder samples include mainly hydrated phases as $\text{Fe}_3(\text{PO}_4)_2 \cdot 8\text{H}_2\text{O}$ and $\text{Li}_2\text{SO}_4 \cdot \text{H}_2\text{O}$ by ion exchange reaction in suspension aqueous media. In heat flux profiles, after the glass transition step, there are two main peaks matching with the dehydration steps of $\text{Fe}_3(\text{PO}_4)_2 \cdot 8\text{H}_2\text{O}$ at $120 - 140 \text{ }^\circ\text{C}$ and $170 - 190 \text{ }^\circ\text{C}$, respectively. They are representing the dehydration steps of formerly produced hydrated crystalline vivianite compounds as shown in Figure 29. Furthermore, according to the DSC and XRD analysis on solid state calcination process, there is no more transition observed until $400 \text{ }^\circ\text{C}$. This means that the LiFePO_4 formation occurs at temperatures higher than $400 \text{ }^\circ\text{C}$. Formerly, LiH_2PO_4 compound is produced as a common intermediate phase at temperatures between $120 - 175 \text{ }^\circ\text{C}$.

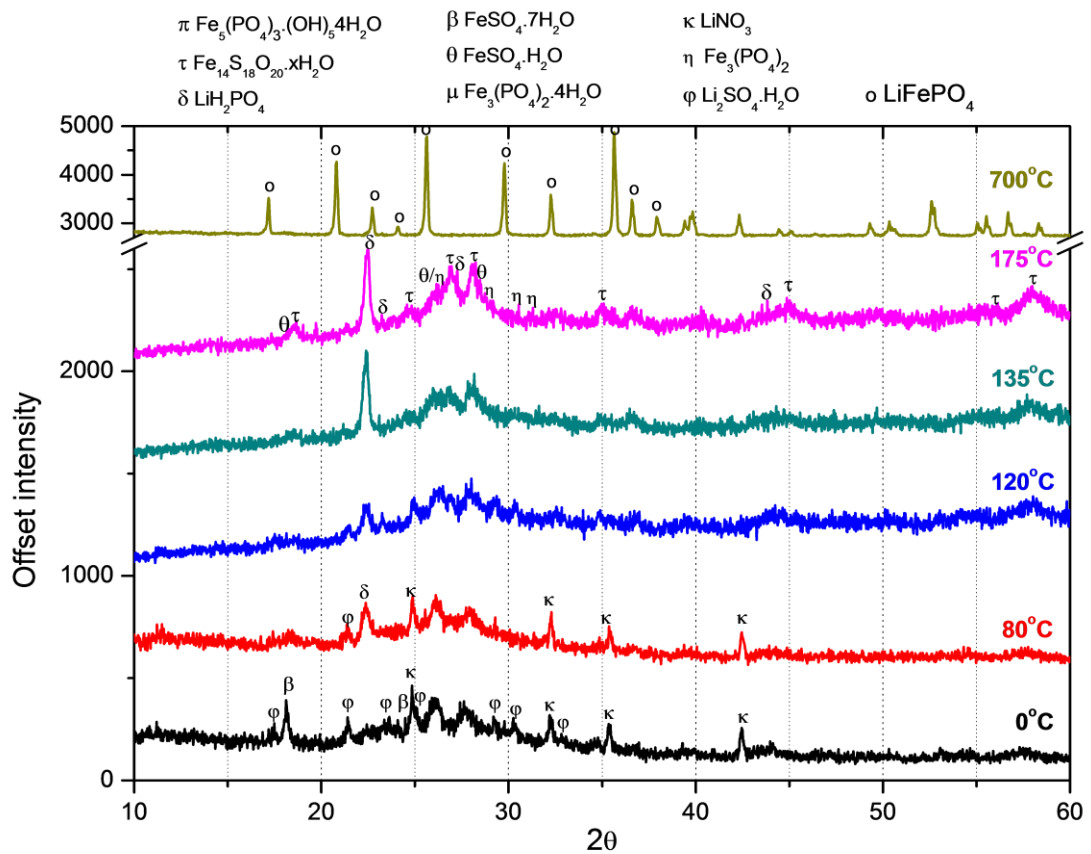


Figure 28. XRD patterns of temperature driven precipitates in heat treatment as increasing temperature from 0 to 175 °C, and calcined at 700 °C.

In both temperature and pH driven precipitations, LiH_2PO_4 seems as an intermediate product synthesized during solid state reactions above 120 °C. It means that solid state reaction mechanism goes through lithium phosphate based compounds first and then iron source intervene the reactions no matter which nucleation route is applied. Before that heating, $\text{Li}_2\text{SO}_4 \cdot \text{H}_2\text{O}$ is the common crystallized product appearing in both nucleation routes within the main dried crystallites before the heat treatment. This points the ion exchange reactions between iron sulfate and lithium salts rapidly formed and lithium sulfate may readily crystallize even in sudden freezing conditions during temperature driven precipitation. So the lately crystallized phases are based on iron compounds, which are crystallized at higher temperatures. This ion exchange reaction favors the iron phosphate formation. But in temperature driven nucleation, the exchange reaction seems to be slow as iron sulfate crystals are still in the dried powder. Moreover, less hydrated compounds are detected in temperature nucleation than in pH nucleated iron phosphate hydrates.

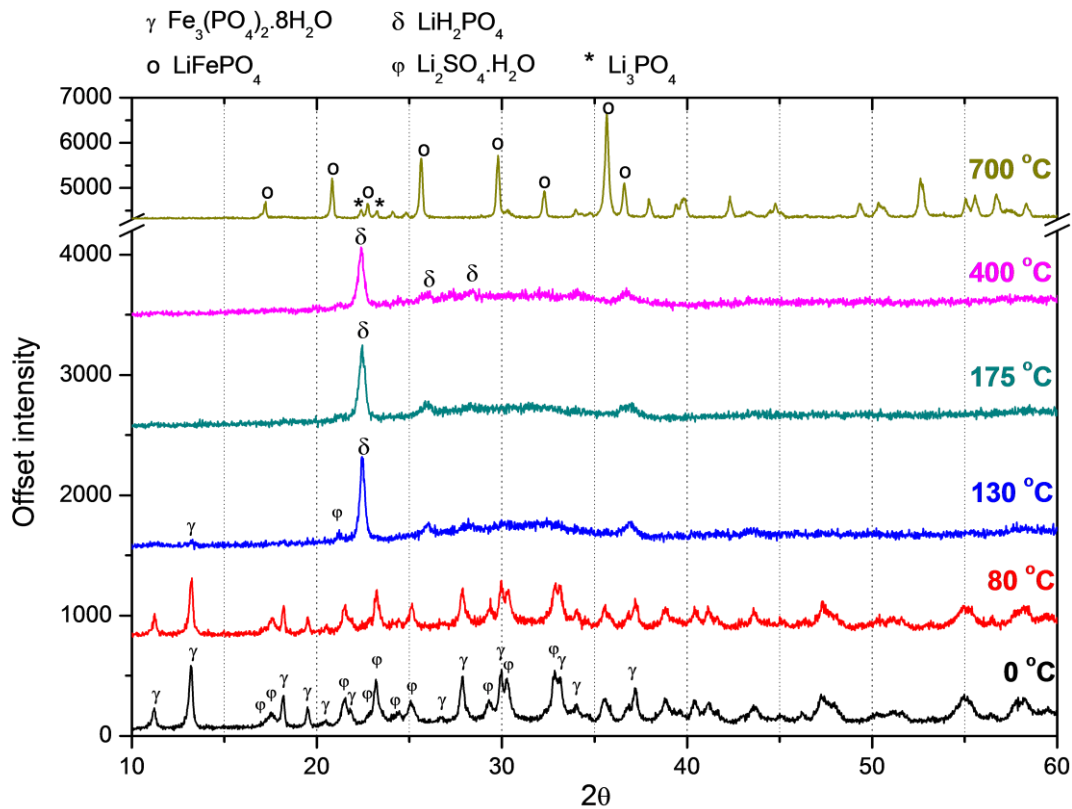


Figure 29. XRD patterns of pH driven precipitates after heat treatment.

Endothermic peaks above 250 °C in Figure 27 are the major difference between DSC profiles of pH and temperature driven precipitates. In temperature driven processes (these peaks mostly correspond to iron sulfate dehydration steps because of the late transformation from iron sulfate to dehydrated iron phosphate species. On the other case, vivianite dehydration steps were seen because of early iron phosphate formation in pH driven nucleated suspension.

Lastly, it was found that LiFePO_4 was successfully synthesized through freeze drying method by both co-precipitation at pH driven (basic) and temperature driven (acidic) nucleation. However, pH driven process has little amount (10-15 wt.%) of Li_3PO_4 impurities after calcination. Therefore, this shows that the key formation step for the synthesis of LiFePO_4 is the calcination step rather than the drying steps. So main phase transformations is summarized in schematic provided in Figure 30.

SEM images show increased agglomeration trend as pH decreases before spray freezing. The crystallization of solid particles start right after the precipitation at around a pH of 4.0. But even these micron sized crystallites' morphology cannot

endure after formation of LiFePO_4 synthesized via both temperature driven and pH driven processes without any carbon additives (Figure 31).

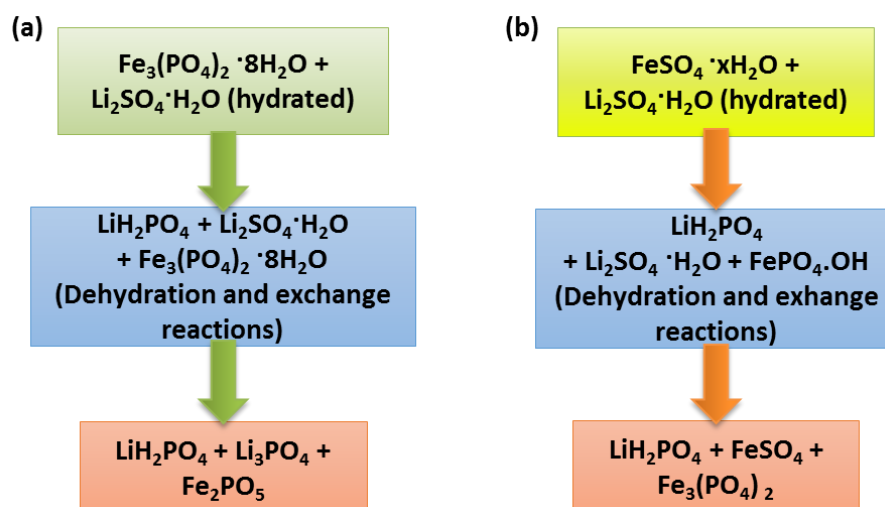


Figure 30. Proposed phase transformation mechanisms during heat treatment following (a) pH driven, and (b) temperature driven precipitation.

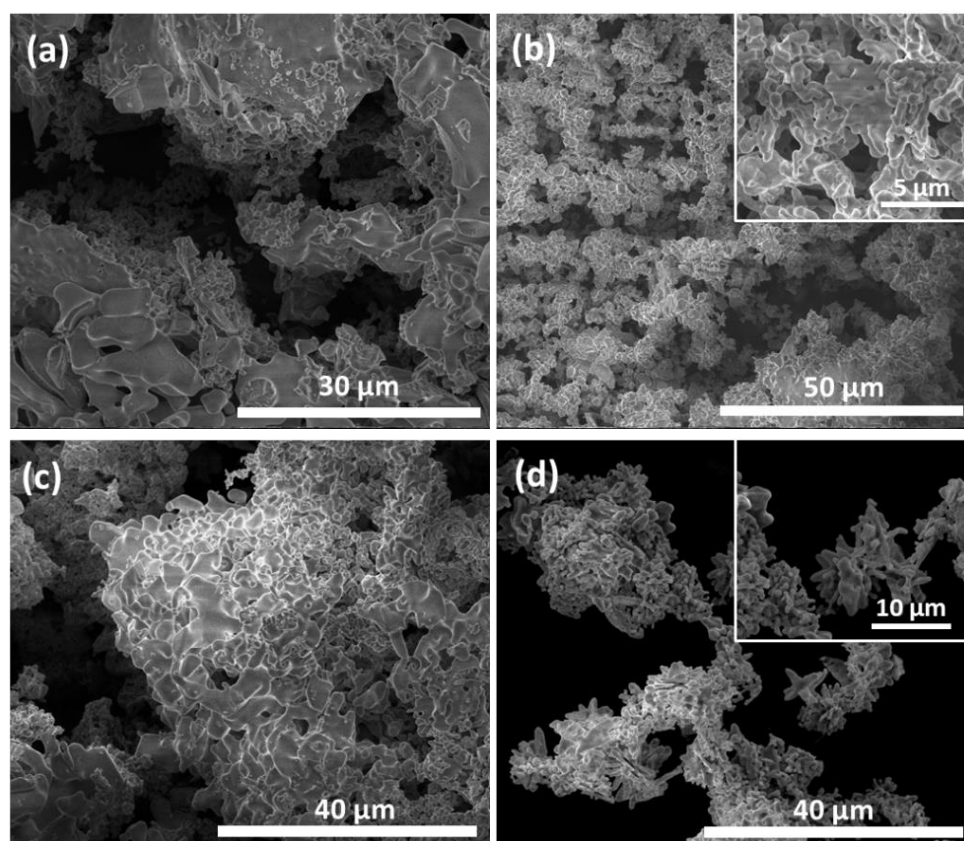


Figure 31. SEM images of synthesized LiFePO_4 via freeze drying of temperature (a, c) and pH driven (b, d) precipitated samples at pH values of 2.0 (a), 3.5 (c), 4.5 (b), and 6.0 (d).

4.2.2 Effect of cation concentration

In general case, during crystallization processes, lower cation concentration gives lower nucleation potential resulting in lower amount of nucleation sites. Thus, the nucleation rate increase with increasing cation concentration during freezing in the presence of inorganic amorphous structures. However, in our case, use of carbonaceous compound such as iron gluconate and other organic acid moieties, yield so much bulky structures buried in carbonaceous precipitates (Figure 32). These organic molecules strongly differ in resulting crystallite size and shape as well as the nucleation mechanism in aqueous solution. On the other hand, carbon coating amount must be strictly arranged because of the quality of final residual carbon content after calcination. So the cation concentration cannot be considered separately from other organic solution additive concentration and Fe:C ratio.

In the case of high concentration usage (0.1M), the precipitation reactions are resulted in micron sized structures. SEM images of the frozen and dried (via sublimation) sample are shown in Figure 32 (a, c). As shown in these images, macro porous structures were synthesized in the high concentration case. The gallery like layered shape morphology might be likely caused by the nucleation and growth of ice crystals. The large temperature difference between the cold droplet surfaces and the inner part yields rapid ice solidification along the direction of temperature profile. Because of rapid solidification in liquid nitrogen, a high rate of ice solidification obtains small crystals which disperse the accumulated organic portion. In the study this gallery like organo-metallic structures appear in a low concentration of 0.05M. This is found as the optimum water / solute content. This mechanism is recently proposed by Sun et al. and used for porous multi layered graphene production named as modified freeze casting process.¹⁰⁰ As atomized frozen droplet nucleates in sudden temperature drop, the 0.05M concentration is high enough to get uniform nucleation and yield closed solid structures to obtain solid state reactions.

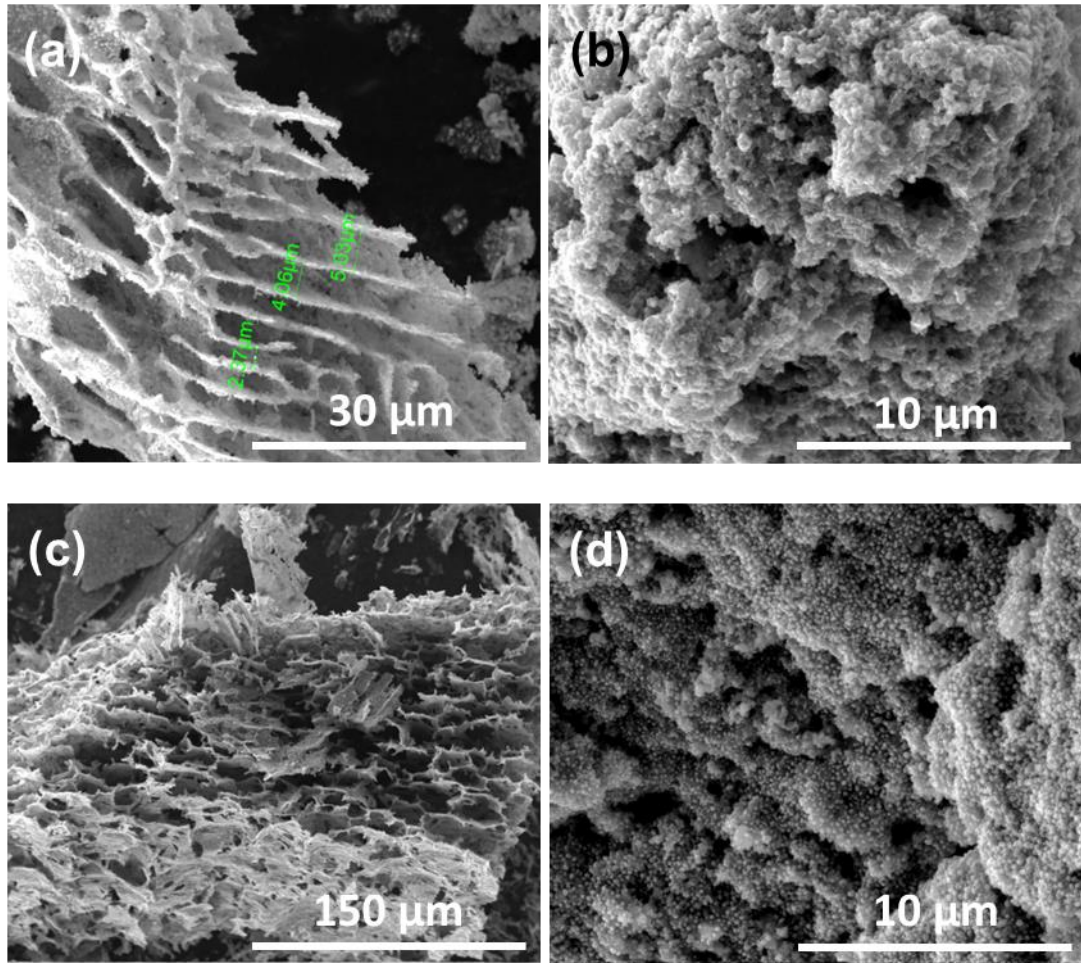


Figure 32. SEM images of the samples after calcination, which are precipitated by using iron (II) gluconate at various concentrations of 0.1M (a, c) and 0.05M (b, d) within pH 4.0 (a, b) and 6.0 (c, d) in suspension

In the low concentration case, amorphous and bulk structures are formed after the sample is frozen and dried (Figure 32). This observation was comparatively different than the porous structure formation in the high concentration case. The reason for this different structure formation depending on the concentration would be related with the pH of the solution. In the high concentration case, solution pH is in the range for the precipitation process and this provided homogeneous environment for the agglomeration.

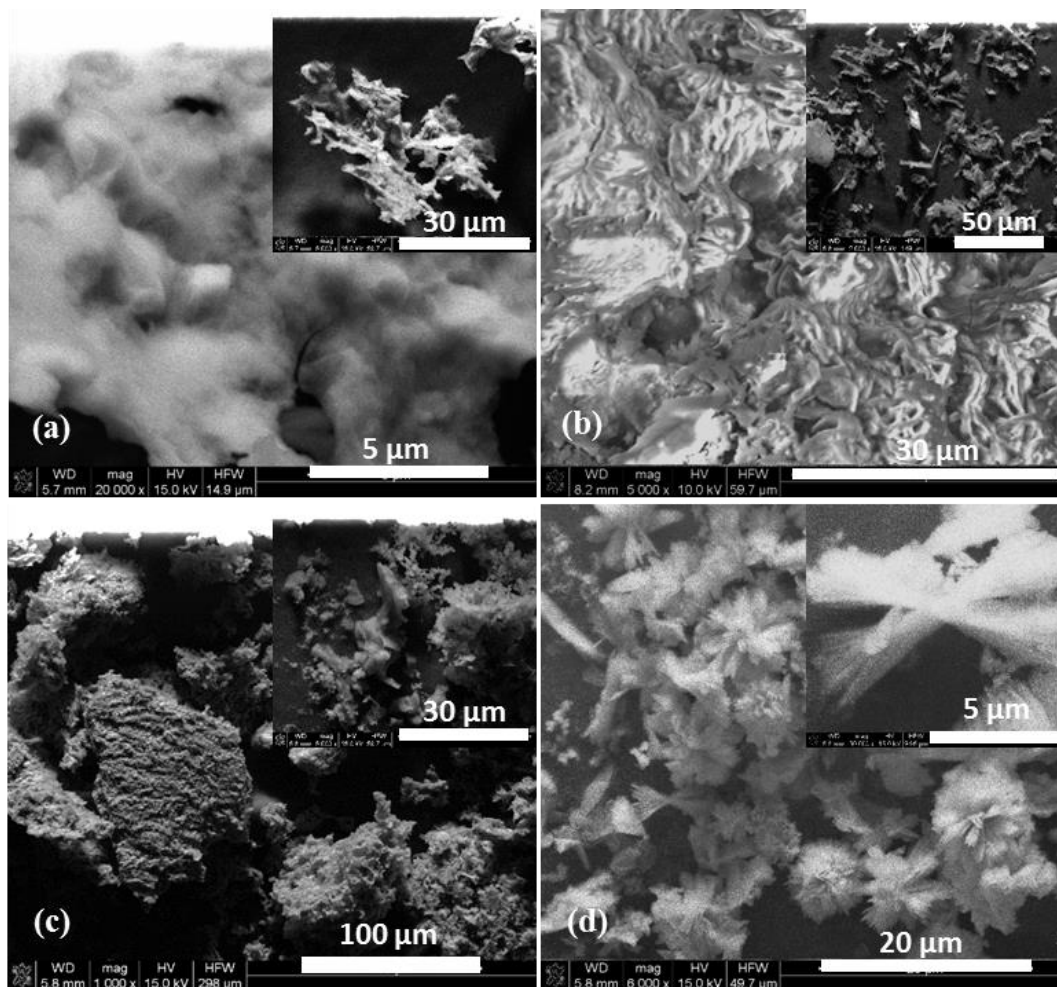


Figure 33 SEM images of the freeze dried samples before calcination which are precipitated by using iron sulfate at concentrations of (a, b) 0.1M and (c, d) 0.05M within pH 4.0 (a, c) and 6.0 (b, d) in suspension

4.2.3 Effect of pH and reactant stoichiometry

Generally in co-precipitation method, the reactant stoichiometry was adjusted to have Li excess to make sure Li intercalation is completed.¹⁰¹ Also to start the-precipitation, the basic media can be supplied by adding LiOH instead of other alkali salts which would bring contaminant. The stoichiometric Li:Fe ratio of precursors were set as 3 and 1.2. The higher impurity phases are present in the final LiFePO_4 rich with the stoichiometric ratio of 3. Beside the side products such as Li_2SO_4 , Li_3PO_4 , the other oxidized phase $\text{Li}_3\text{Fe}_2(\text{PO}_4)_3$ forms especially in a less reducing atmosphere. To increase the yield of LiFePO_4 after calcination, lithium source percentage was decreased to a slightly higher ratio than 1.0. The higher amount of lithium is also unnecessary because actual LFP transformation takes place in the high temperature

calcination step. It is optimized as sufficient to compensate volatile lithium content during high temperature calcination. Even in the lower pH values than 4.0 without excessive LiOH stoichiometry, frozen granulate supplies enough Li⁺ ions to solid state reactions during calcination.

According to phase analysis, the lower pH (3.0) precipitate yields some impurity phases as indicated in the XRD patterns given in Figure 34. Although main portion of calcined powder has LiFePO₄ phase, crystallinity is relatively poor. Identified impurities are reduced phases such as FeS, Fe, and Fe₃(PO₄)₂ because of highly reducing environment with lithium deficiency, coherent with literature.^{99,102,103} In the higher pH (6.0 and 9.0) reduced iron ingredient rises and conversion decreases again. Optimum pH point is around 6.0. Beyond a pH of 6.0, compounds having Fe in oxidized state formed using basic solutions in the emulsion drying method. The precipitation phases having more stable Fe²⁺ cations are favourable for LiFePO₄ in this technique.

Intermediate pH (4.5) results in higher crystallinity and low amount of impurity by comparing the higher pH (6.0) precipitation by using iron sulphate as iron source material as seen in Figure 35. Also there are much more impurities reduce the complete conversion rate to LiFePO₄.

On the other hand, for in-situ carbonization with iron gluconate source yields high amount (90 wt.%) of LiFePO₄ because of its self-reducing organic portion during calcination. However, the more organic portion it has, the more reduced iron is composed by unreacted stable Fe²⁺ cations at higher pH values. Besides, too low pH values yield mainly Li₃PO₄ and other phosphate side products because of increasingly reducing conditions with Li deficiency, as coherent with literature.^{99,102,103}

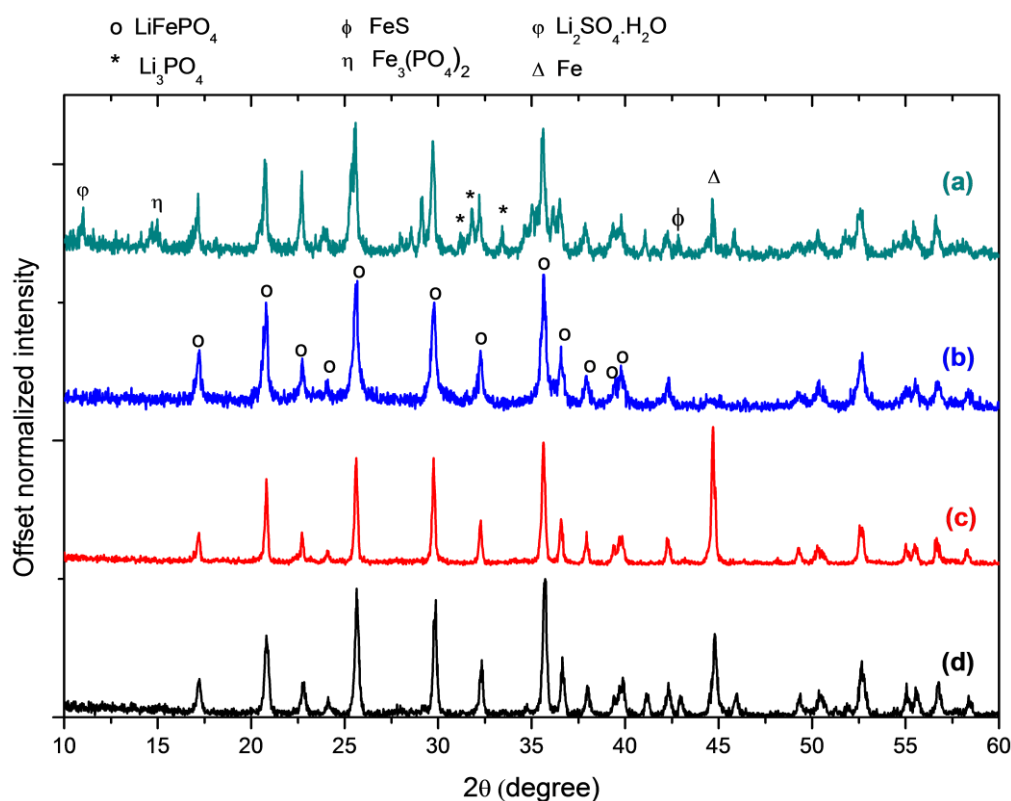


Figure 34. XRD pattern phase analysis of synthesized cathodes within different pH values of (a) 3.0, (b) 4.5, (c) 6.0, (d) 9.0 in co-precipitation media by using iron gluconate.

As a consequence, the formation of phases with individual iron and lithium salts need to have reducing agents besides precipitation with Fe^{+2} . However precipitation pH has to be tuned to have less reduced iron and better conversion of iron source for the synthesis of LiFePO_4 . Even though the well crystalline powder is seen at pH of 6.0 as compared with lower pH (4.5), reduced Fe phase is highly formed in pH 6.0 as reducing the conversion rate. Therefore, for pH driven co-precipitation experiments, optimum pH value is identified as in between 4.5 – 5.0 with respect to phase analysis in Figure 34.

Also for iron sulfate source, carbon addition has to be used externally (ex-situ) after drying. Therefore, some additional carbon sources were investigated according to their effects on morphology, crystallinity and conversion rate before obtaining LiFePO_4/C cathode composites.

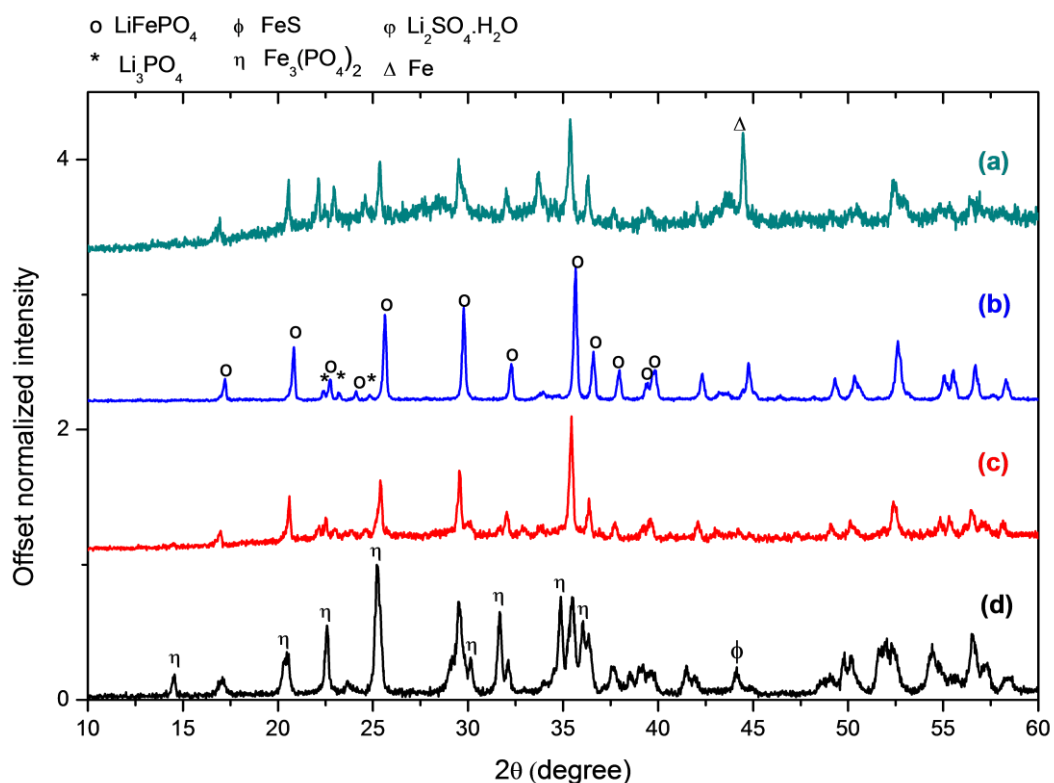


Figure 35. XRD pattern phase analysis of synthesized cathodes within different pH values (a) 3.0, (b) 4.5, (c) 6.0, and (d) 9.0 in co-precipitation media using iron sulfate.

4.2.4 Optimization of calcination temperature on LiFePO₄ powder synthesis

In literature, it is reported that calcination increases the crystallization and dispels the anti-site disordering between Li and Fe atoms within the LiFePO₄ crystal structure around 500 °C and higher temperatures.¹⁰⁴ There are various treatment temperatures between 550 and 900 °C in literature. Also it is known that LiFePO₄ decomposes above 800 °C even in reducing atmosphere.¹⁰⁵ Thus, in this study, to find out the effect of calcination temperatures are used as 600°C and 700 °C to observe the crystallization product of LiFePO₄.

It was suggested that higher calcination temperatures would provide improved structural characteristics. XRD analysis is conducted with both iron gluconate and iron sulfate solution. It is found that higher (700 °C) temperature result in a highly crystalline structure compared to lower temperature counterpart as shown in XRD patterns given in Figure 36.

In freeze drying method, hydrated compounds include nonvolatile moisture at such low temperatures. For that reason, well dried powder calcination in reducing atmosphere is an important step to prevent Fe^{2+} oxidation against to formation of oxidized phases such as Fe_2O_3 , Fe_3O_4 or $\text{Li}_3\text{Fe}_2(\text{PO}_4)_3$. In order to explore the effect of maximum temperature, dried samples were heated under a slightly reducing atmosphere. In addition to formation of LiFePO_4 some secondary phases were observed at 600 °C after XRD results. The calcination product includes reduced iron compounds in coexistence with carbon content from gluconate.

Synthesized LiFePO_4 at 700 °C shows clearly better crystallinity than at 600 °C as seen in Figure 36. Regarding to Rietveld refinement of these patterns, more than a 90 wt.% of calcined powder includes LiFePO_4 , with secondary phases of sulfide and phosphate phases. LiFePO_4 compound was successfully synthesized with more impurity at 700 °C than 600°C.

Below 700 °C, FeS and reduced bcc Fe content were produced in calcination with the existance of carbon ingredient. On the contrary, even with ex-situ carbon addition after drynig, more crystalline and pure LiFePO_4 phase can be synthesized after calcination at 700 °C. EDX mapping of certain elements with same SEM images are presented in Figure 37. FeS crystals appear simultaneously because of glucose addition right before the calcination step. This carbon ingredient is not easily extractable especially in temperature driven processes. So high temperature such as 700 °C should be applied for complete desulfurization. Final calcination temperature is optimized as 700 °C which gives lower impurity, improved crystallinity, and suitable surface carbonization when compared to others.

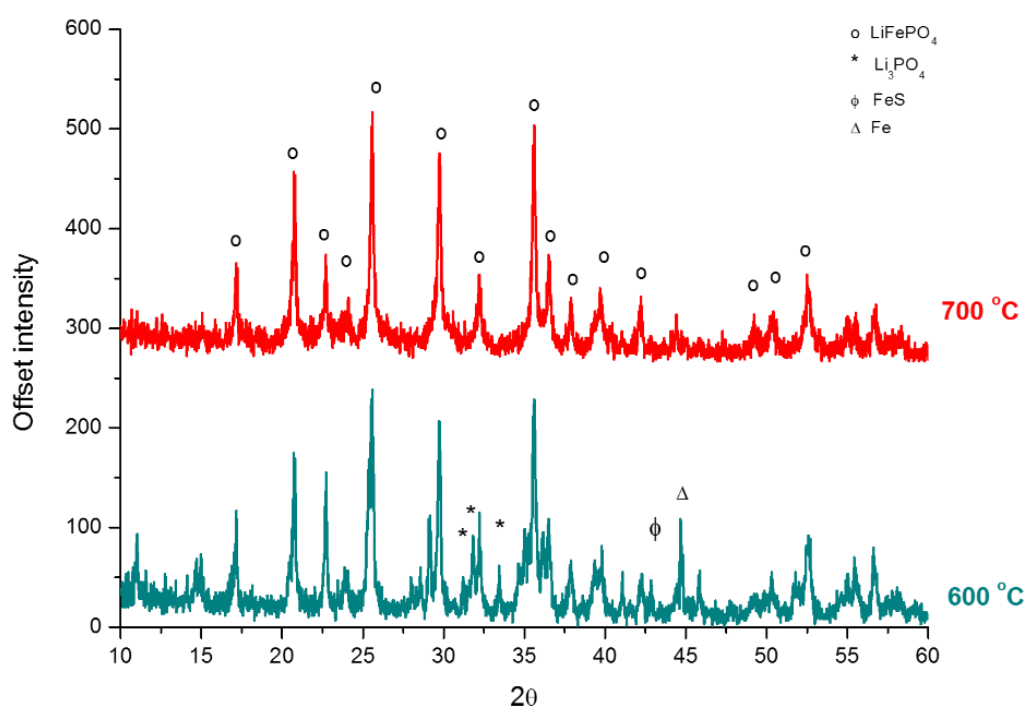


Figure 36. XRD patterns of the cathode material calcined at 600 °C and 700 °C in second annealing step, with iron sulfate source and ex-situ carbonization.

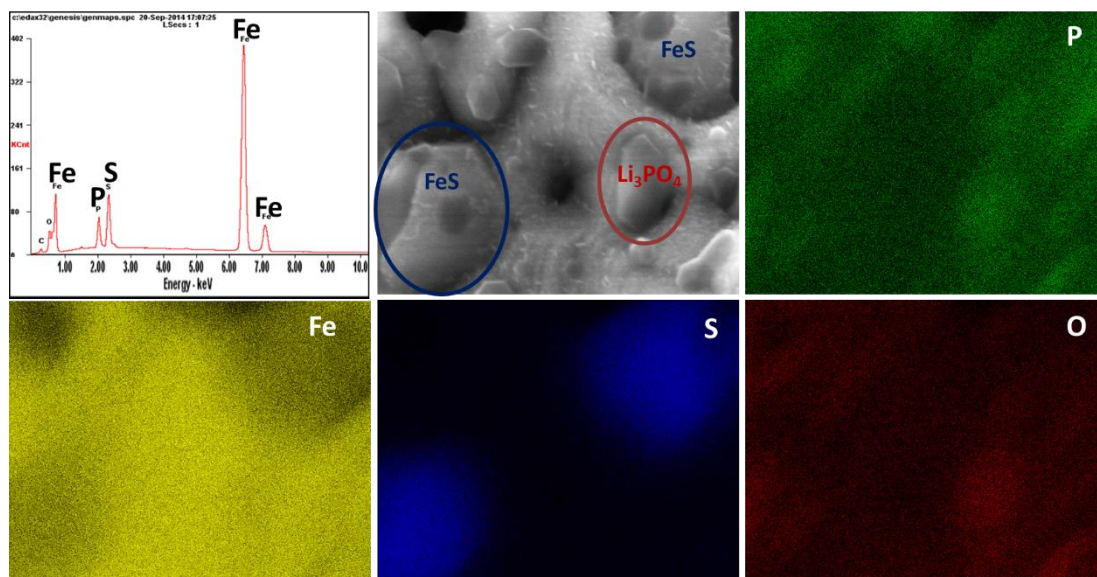


Figure 37. EDX mapping analysis of freeze dried cathode material obtained through temperature driven precipitation using iron sulfate source and ex-situ carbonization.

4.2.5 Effect of carbonization on LiFePO₄/C nano composite formation

Carbonization or carbon coating of the electrochemically active particles play an important role in useable capacity. In order to achieve theoretical values or high utilization rate of active mass, conduction should not be a limiting factor. In other words electronic diffusion between particles should take place. Therefore, all synthesized LFP powder samples should be coated by a conductive layer, carbon in this case. Additionally, the carbon layer can prevent further oxidation, acting as a reducing media by keeping Fe²⁺ ions away from oxidized Fe³⁺ state during calcination. However, the thickness of this conductive layer might be an obstacle for the diffusion of Li⁺ ions through the particle surfaces.

Since, LiFePO₄ has low conductivity (10^{-9} S cm⁻¹), deposition of a thin carbon layer onto its surface is the way to enhance electrical conduction between cathode particles. In the literature there are some proven studies that reports high conduction rates, where the low intrinsic conductivity is improved through the use of carbonaceous materials.^{106,107}

Therefore, the organic solvents are added before the calcination step as well adsorbed by particle surfaces. This carbonaceous ingredients might be supplied by the surface active organic agents from precipitation sequence or externally saturated compound after all precursors was freeze dried. The carbonization method via saturation of sugar based compound after drying of precursors is referred as ex-situ carbonization.

In all in-situ carbonization methods, water soluble organic species are used as carbon sources. There are two different methods for the addition of carbon sources used in solution preparation step. One of these is the use of an organo-metalic salt like iron (II) gluconate as the iron source. Other method is the in-situ addition of aqua soluble organic compounds such as ascorbic acid, citric acid and CTAB in aqua solution. This compounds decrease the surface energy of the precipitates because of their surface active properties that reduce the growth rate.

Beside this conduction layer on the surfaces, the size of the particles could affect the Li⁺ ion diffusivity. Long and disordered structures would be an obstacle for Li⁺ ions

in such 1D channel structures. In solution phase addition of surface active organic compounds could inhibit further agglomeration and growth of the crystals. Hence it would be dried by leaving carbonaceous matrix followed by a further calcination step in a slightly reducing atmosphere. Additionally, as the results given in section 4.2.4, in-situ carbonization experiments yield other impurities such as Li_3PO_4 , Fe, FeS, and other $\text{Fe}_2\text{P}_2\text{O}_7$ in a more acidic environment with the existence of carbonaceous material.

SEM images are provided for the samples synthesized as cathode material using different carbon sources as in-situ and ex-situ carbonization (Figure 38). It is found that morphology of the final product depend on the precursor type. The solution (cation) concentration has been chosen as 0.05M. SEM analysis are performed on samples after calcination and carbonization at 700 °C using iron gluconate and iron sulfate. Ascorbic acid, citric acid and CTAB are used as in-situ (before drying) carbonaceous materials added into the solution phase while glucose saturation is implemented after obtaining freeze dried samples with iron sulfate source for ex-situ carbonization.

Especially in pH driven processes, ascorbic acid is fairly effective on the morphology of the final crystalline LiFePO_4 product. It is found that the particles were formed by 100 – 200 nm thick plates co-originated in “star” like structures. Under the same conditions, porous branch-like connected morphology is observed through citric acid use.

By manipulating the growth rate with sudden temperature drop, morphology changes with respect to nucleation in pH controlled precipitation in solution phase. In the case of ascorbic acid addition, porous structure occurs connected with branches instead of well-shaped originated star-like platelets in pH controlled process. Similar diversity in morphology is seen with citric acid as more accumulated structures including bigger agglomerates. Much more bulky structures connected strongly with carbon matrix is achieved by the use of CTAB. Regarding this morphological changes, it is proposed that the molecular structure and chemical properties of carbon sources have an effect on the morphology as well as the nucleation procedure.

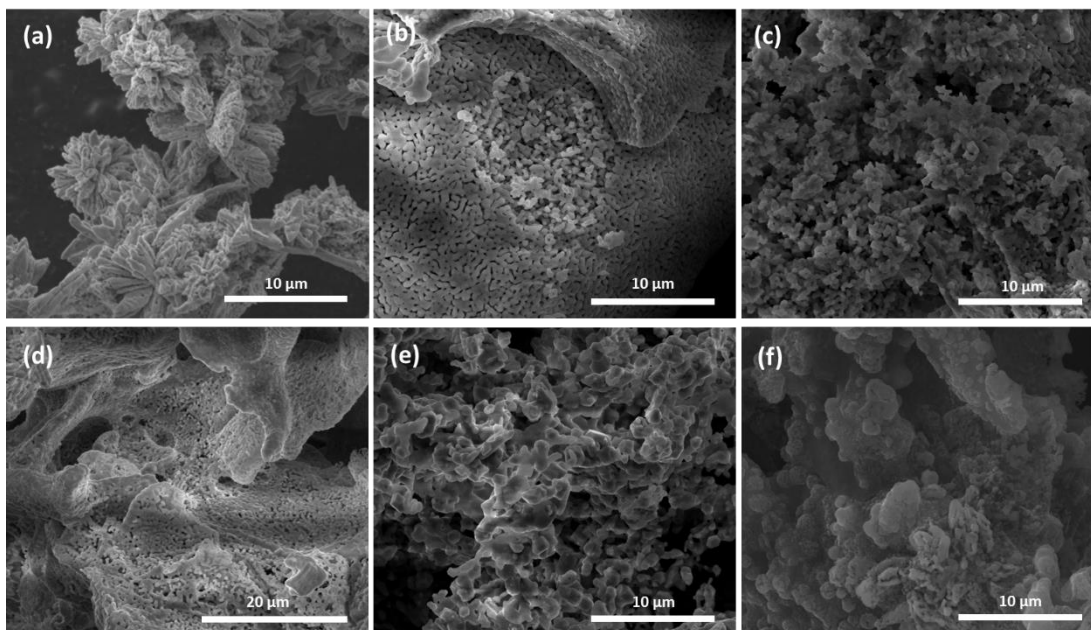


Figure 38. SEM images of as synthesized cathode materials via in-situ (before drying) carbonization of ascorbic acid (0.01M) (a, d); citric acid (0.01M) (b, e), CTAB (0.01M) (f); and ex-situ carbonization (after drying) with sucrose (5wt.%) saturation (c) prepared by pH driven (a, b) and temperature driven (c, d, e, f) nucleation methods.

At this point, carbon coating is essential for improving the conductivity of the cathode materials and lithium ion insertion during conversion to LiFePO_4 . However, attention has to be paid into its thickness. A thick carbon coating on the surface of LiFePO_4 material would give very high electrical conductivity; however, there would be slow Li^+ diffusion process inside the bulk cathode material even there is very high electrical conductivity due to the presence of thick coating. Considering the carbon coating amount, iron gluconate precursor would result in worse electrochemical test due to the thick coating and bulk structured LiFePO_4 compared to the products synthesized by FeSO_4 precursor and carbon containing acids.

Furthermore, the particles can be controlled in size and shape with respect to crystallographic orientation by controlling the further accumulation on nucleated particles with the help of organic compounds. This orienting effect can be clearly seen in other methods taking place at relatively elevated temperatures such as hydro / solvothermal.

Diverse morphological changes lead to detectable orientation differences according to crystalline anisotropy. If there is a preferred orientation along the crystal particles, it is enhanced by the alignment of the anisotropic crystallites during sample preparation procedure for XRD. This distributed or localized orientation creates sensible peak ratio difference than spherical or bulky crystals in XRD patterns provided in Figure 39. Table 4 summarizes peak ratio difference between representative peaks. A noticeable change in (020) peak intensity is observed and concluded as a highly localized orientation distribution towards *b* direction. This localization effect is mostly observed in ascorbic acid use which is coherent with high anisotropic (plate-like) structure formation (Figure 38-a). These effects should be relatively low despite of the shifted orientation by attached morphology of star-like structures of LFP plates. However, this orientation effect on the resulted particles could be seen even in this condition.

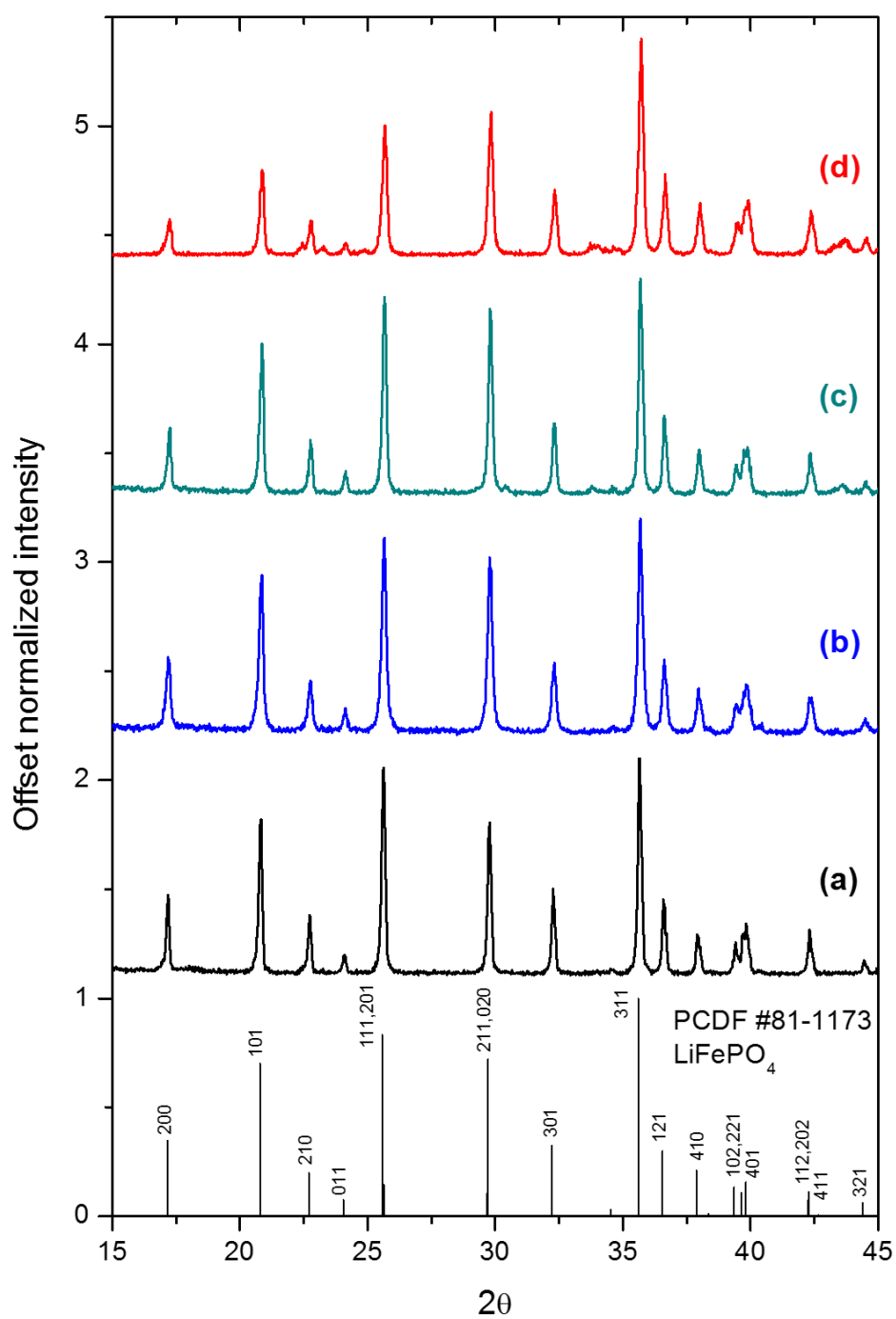


Figure 39. XRD patterns for samples prepared by Temperature driven (spray freezing) freeze drying method through (a) no addition, (b) CTAB, (c) Citric acid, (d) Ascorbic acid addition.

Table 4. (020) peak intensity ratio over other planes.

	$I_{(020)}/I_{(200)}$	$I_{(020)}/I_{(101)}$
d	3.88	1.78
c	2.77	1.23
b	2.28	1.11
a	1.92	0.99

XRD patterns of LFP products that use different carbonaceous agents show systematical change in peak intensity ratio. This is a sign for preferred orientation by crystallographic anisotropy in the microstructures. There is a prominent increase in the height of (020) peak according to the other peak intensities (Figure 39). This crystallographic orientation distribution has been localized around (020) showing highest relative intensity ratio in the ascorbic acid addition.

SEM images (Figure 40) provided from before and after the calcination step show that the morphology of the crystallites are preserved even after 700 °C treatment. Because differently oriented surfaces of newly nucleated particles have different surface energy, adsorbed carbonaceous compound can affect the crystallize morphology by acting like orientation directing features. This adsorbed layer could be carbonized where carbon coating preserves the morphology.

To evaluate the morphology of the products, samples prepared using FeSO₄ precursor are explored after calcination and precipitation steps through SEM analysis. SEM images show that ‘plate-like’ patterned structures composed of aligned plaques are present after the precipitation step. Even the samples after precipitation were subjected to a calcination step, ‘star-like’ morphologies are not decomposed. Hence, according to the SEM images, it is suggested that the morphological evolution occurs during the precipitation, not in the calcination step. Previously stated SEM images (Figure 38) show the effect of carbonaceous compounds on well-defined crystalline structures which are obtained after calcination with different morphologies, star-like, plate-like etc. Beside LiFePO₄ structures, some different morphologies are also observed into them.

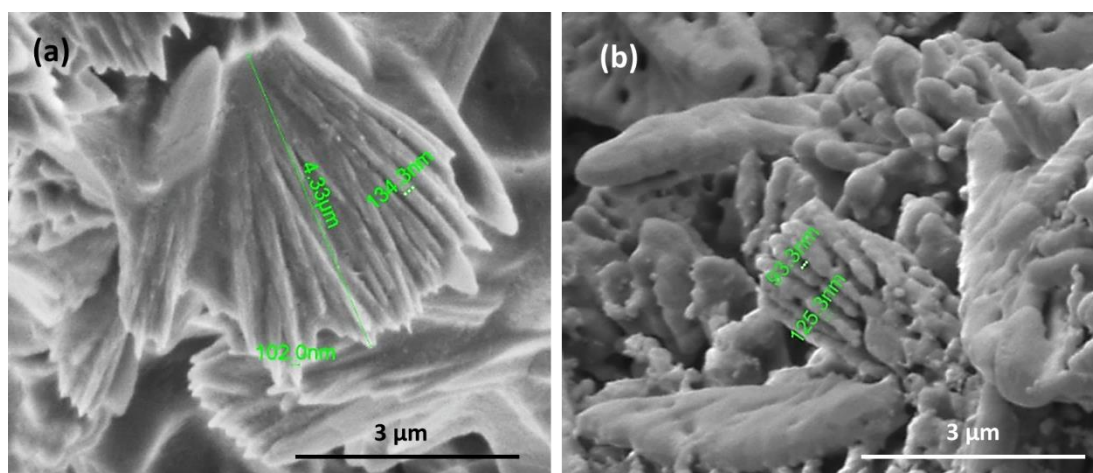


Figure 40. SEM images of synthesized samples by freeze drying with iron sulfate precursor and ascorbic acid addition (a) before and (b) after the calcination.

According to the phase analysis in XRD patterns given in Figure 41, main impurities are Fe and Li_3PO_4 phases. Rietveld refinements show that LiFePO_4 phase portion is in between 80 – 100 wt.%. Some impurity phases of lithium salts was expected because of addition of excess Li ions. High conversion rates above 80 wt.% can be achievable even in off-stoichiometric Li rich conditions. However excess Li^+ can captures PO_4^{3-} source as forming stable crystallites of Li_3PO_4 in spite of high volatility of Li at elevated temperature. Therefore, this may cause some reduced and unreacted iron impurity because of the phosphate deficiency. So excess lithium source reduces conversion of reactant to LiFePO_4 and make the Fe and Li_3PO_4 phases produced beyond their expected amounts. Fortunately, Li_3PO_4 is harmless for battery operations and also used as solid electrolyte in thin film batteries.

For iron gluconate use as in-situ carbonaceous material, high carbon content reduces the crystallinity but refine the crystallite size with respect to CTAB and citric acid. This is evidenced by the broader peaks in the XRD pattern. It also enhances the reducing effect, so additionally produces iron phosphides; Fe_2P , Fe_3P beside FeS . In pH driven nucleation it has more time to capture more Fe^{2+} ions to yield higher impurity than temperature driven process.

Among the all synthesized cathode materials, temperature and pH driven processes have little difference according to the impurity phases. As a main difference, temperature driven process may lead to more refined particle size than the pH driven case. However, the particles have a poor quality of carbon coating in this case. This

may be caused by the limited time for adsorption of large organic molecules properly on the surfaces of early nucleated particles.

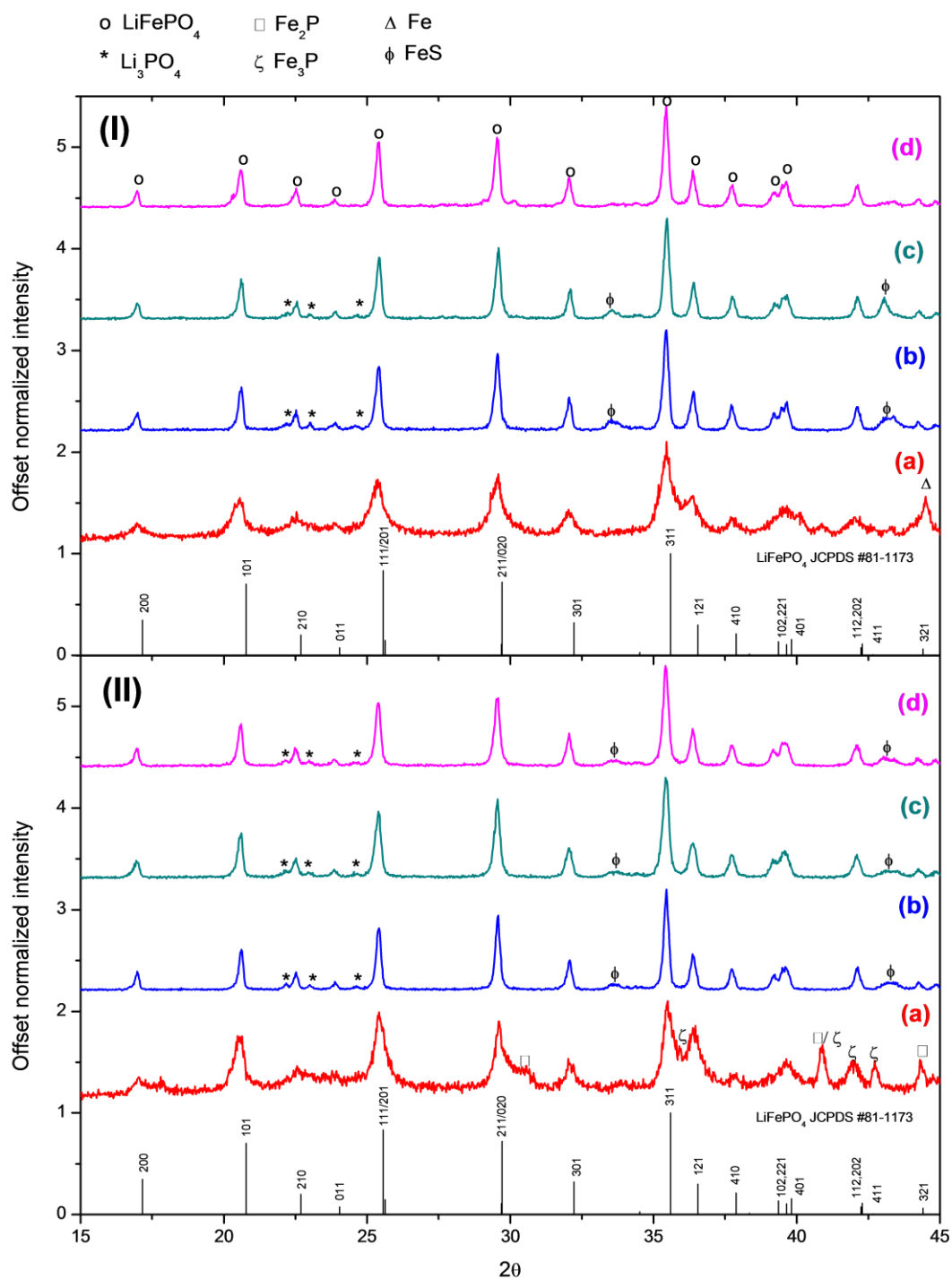


Figure 41. XRD patterns of LiFePO₄/C cathode materials synthesized via temperature (I) and pH (II) driven freeze drying method in-situ carbon addition with iron gluconate (a) ascorbic acid (c) and ex-situ carbon addition on pristine (b) and ascorbic acid added (d) samples.

On the other side pH driven process can give more time to particles to nucleate and grow by the adsorption of soluble organic substances on their surface in order to be saturated during freeze drying. This yields well distributed and better quality coating. Adversely, suddenly solidified organic structures cannot be adsorbed before the nucleation of solid particles in temperature nucleated solution. As a consequence, temperature driven nucleation is better for inorganic particles refinement, while pH driven nucleation has better opportunity to do in-situ carbon coating of particles if it is in case with solution based saturation methods.

XRD results show that LiFePO_4 compounds can be synthesized by CTAB, ascorbic acid and citric acid addition via spray freezing and then freeze drying procedure. Moreover, the crystallinity of the LiFePO_4 product synthesized with these additives is higher than the one synthesized through iron gluconate precursor.

The effect of carbonaceous methods can be examined via Raman analysis through investigating the D/G ratio after coating. All PO_4^{3-} bands at 976, 1022, and 1096 cm^{-1} can be seen together with the carbon bands in the Raman spectra in Figure 43. There is also a shoulder that can be hardly detected at 1200 cm^{-1} through curve fitting according to Gaussian function. This matches with the oxidation product of reduced iron residue during analysis performed at ambient condition. The other features including D (disorder) and G (graphitic) bands at 1376 and 1630 cm^{-1} , respectively, has been deconvoluted according to Lorentzian area function in order to obtain peak area ratio (Table 5).

For graphitization by sugar saturation with ascorbic acid addition, poor graphitization is appeared (Table 5), which has no significant effect on the electrochemical performance. Furthermore, excessive sugar addition for carbonization beside ascorbic acid has detrimental effect on the structure orienting properties of ascorbic acid and yields very poor capacities.

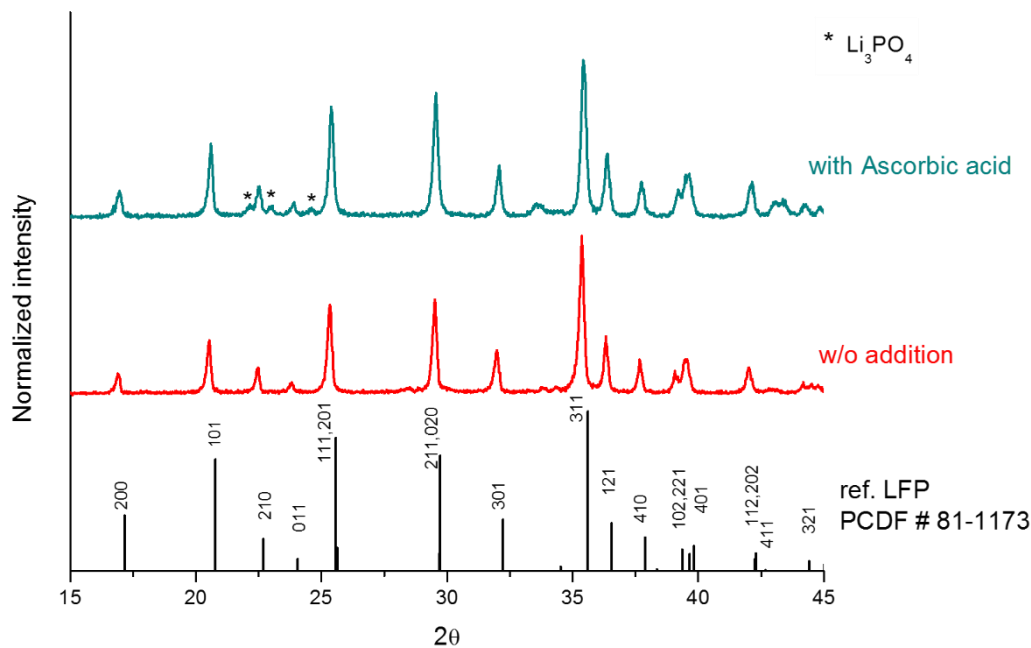


Figure 42. XRD pattern and qualitative analysis of cathode prepared with iron sulfate precursor and ascorbic acid.

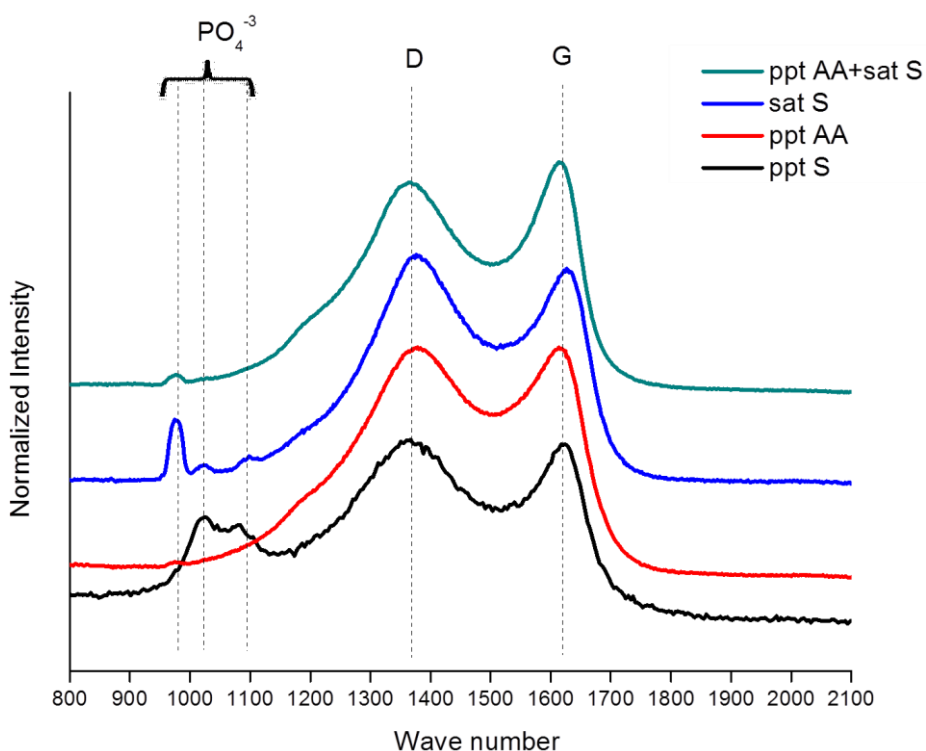


Figure 43. Raman spectrum of cathode materials synthesized by freeze drying with respect to carbon coating methods (during precipitation: ppt, external saturation: sat) and substances (ascorbic acid: AA, sugar: S) respectively.

Table 5. Raman D/G band area ratio of cathode material as synthesized and coated with different carbonaceous agents and methods

Sample	Area(D/G)
sugar precipitation	3.19
Ascorbic acid precipitation	2.66
sugar saturation	2.16
Ascorbic acid precipitation + sugar saturation	1.31

4.2.6 Electrochemical performance of nano structured LiFePO₄/C materials synthesized with freeze drying

In button cell testing experiments, capacity and electrical resistance measurements were conducted besides rate capability for both charge and discharge performance within room temperature. By addition of ascorbic acid in solution, nucleation and growth reaction can be taken under control by giving structure orienting effect on the synthesized rose-like morphological cathode materials. For understanding its effect on the precipitation in various conditions, both temperature and pH driven nucleation has been conducted in ascorbic acid coexistence.

In freeze drying synthesis, the driving force for nucleation strongly affects the electrochemical performance of the synthesized LiFePO₄/C powders. Pristine materials which was prepared with ex-situ sugar carbonization and soluble salts of Li⁺, Fe²⁺, and PO₄³⁻ as source within solution phase, show better discharge capacity as prepared with temperature driven cryogenic nucleation (Figure 44-a-b) than pH driven.

The discharge capacities for pH driven precipitation with ascorbic acid are 119.3, and 84.5 mAh·g⁻¹, at 0.1C and 1C rate, respectively after slow charging (0.1C); while 116.8, and 79.4 mAh·g⁻¹ after fast charging (1C). On the other hand, temperature driven precipitation has 77.1, and 29.7 mAh·g⁻¹ at 0.1 and 1C rate, respectively; after slow charging (0.1C), while 59.5, and 29.5 mAh·g⁻¹ discharge capacity at 0.1 and 1C rate, respectively, after fast charging (1C). Both method has resulted with good

capacity retention of 92.8 and 90.8 % after 25 cycles for pH and temperature driven precipitation, respectively.

According to the galvanostatic charge/discharge results in Figure 44 (c) and (d), structure orienting effect of ascorbic acid enhances fast rechargeability. The star-like oriented structure of LiFePO_4 material shows so closed discharge capacities at both 0.1 and 1C cycling rates. In order to observe this orientation effect ascorbic acid should be adsorbed in solution phase during crystal growth after pH driven nucleation rather than sudden nucleation together with crystals with temperature driven process. This crystal growth mechanism indicates the rather slow adsorption that is needed to be in solution phase during precipitation. This is obviously impossible during rapid solidification by sudden freezing nucleation. Moreover, the carbon coating coverage on the surface should be better in pH driven process because of enough time to adsorption in solution state. So its surface coverage and carbon coating role is diminished with temperature driven process as far as compensated with ex-situ sugar carbonization after drying.

On behalf of previous electrochemical trials, extra coating with ex-situ sugar based carbonization has similar performance data in Figure 44-c which is considered unnecessary. So 0.01M ascorbic acid concentration is enough to get sufficient amount carbon coating (2 wt.%) on the cathode surface by only in-situ carbonization. Because of its highly soluble and reducing feature, ascorbic acid is a powerful carbonaceous material to give enough conductivity as well as manipulating the crystallite shape and size.

Adsorption is also a prior requirement for the quality of ex-situ carbonization. In temperature nucleated samples with ascorbic acid addition have bad discharge capacity under 20 mAh g^{-1} . Eventually the conductivity can barely be improved up to around 70 mAh g^{-1} at 0.1C cycling condition which is still half of the one synthesized by pH nucleation with ascorbic acid existence.

For temperature driven in-situ carbonization with ascorbic acid, it is possible to enhance electrochemical capacities at all rates by doing this additional ex-situ carbonization. Moreover it shows rapid decay in further cycles that leads us to a comment on worse coating quality which is obtained by ex-situ carbonization. It is

also seen from the EIS measurements (Figure 45-I) after galvanostatic test cycles. Temperature driven synthesized cathode using ascorbic acid has almost 3 times greater charge transfer resistance (R_{CT}) than ex-situ carbonized one (Figure 45-I b and c). Ex-situ treatment might lower ohmic resistance; however, increase the R_{CT} which is more important in high power batteries. If R_{CT} is high it is not important how much carbon layer is graphitized (Figure 43 and Table 5). Because graphitized carbon layers may not be good contact with particle surfaces or detached. The thin coating is also first priority for conductive cathode composites. Because of this high resistance results in well graphitized carbon coated cathodes, it is concluded that excessive non-homogeneous carbon layers make the cathode particles to resist the Li ion insertion.

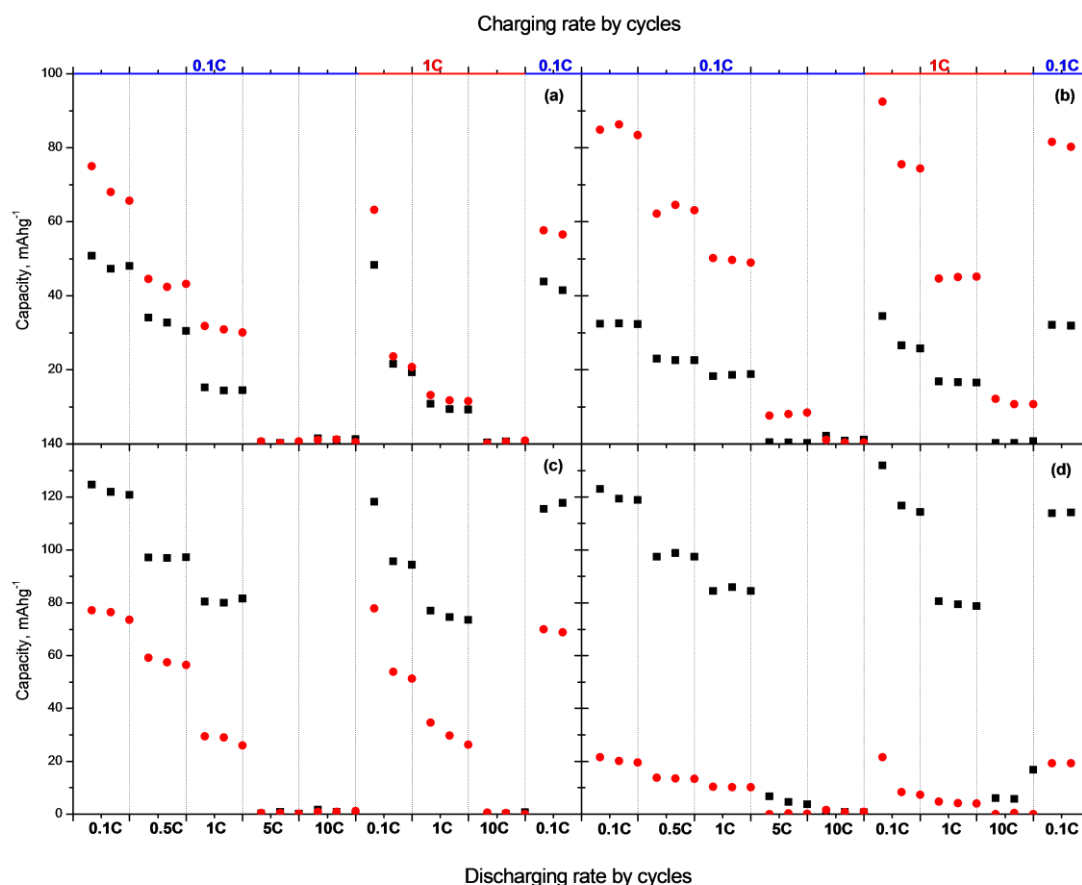


Figure 44. Discharge capacity results on cathode materials as synthesized via freeze drying method as pristine without solution addition and external sugar carbonization (a), with only iron gluconate source (b), with ascorbic acid addition and external sugar carbonization (c), with only ascorbic acid addition in solution (d). pH and temperature driven nucleation represented as ■ and ●, respectively.

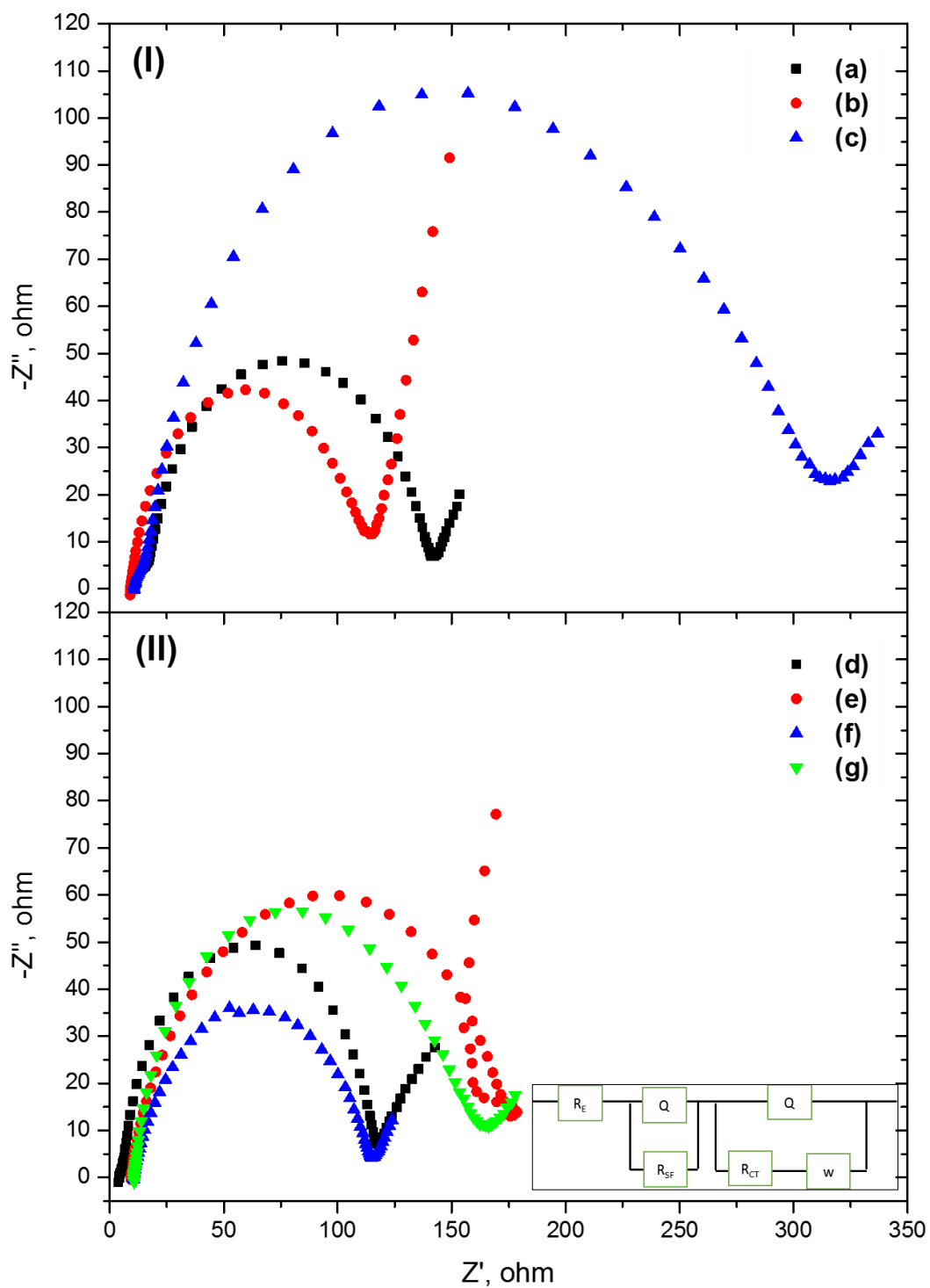


Figure 45. EIS measurements after galvanic cycling done on button cells with cathode materials synthesized in temperature (I) and pH driven processes (II) followed by in-situ carbonization with iron gluconate (a, d), ascorbic acid (b, e), and ex-situ carbonization with sugar saturation (f) and both in-situ ascorbic acid + ex-situ sugar saturation (c, g)

However pH driven synthesized cathode, with ascorbic acid addition, has the best performance at all cycling rates showing better coulombic capacity than with further ex-situ treated sample. Instead of any improvement by additional ex-situ carbonization, the second coating has lowered the fast charging performance in Figure 44. This effect is also seen from the EIS measurements in Figure 45-II, the increasing R_{CT} is %50 greater than without ex-situ treated one. So it may be commented that the real determining factor is the preserved originated plate-like crystallites' structure itself. By considering this, particle size and anisotropy in structure are rather effective than carbon coating.

There are many good (90 – 100 ohm) and bad (350 – 500 ohm) resistance synthesized cathodes by comparing R_{CT} values from the literature. Comparing the best EIS results of cathodes synthesized in this technique, the approximate R_{CT} values are achieved as in between 120 and 175 ohm. However, there is still enough room to improve the conductivity by optimizing the carbonization methods which are discussing in section 4.2.5 in sub-sequential precipitation technique.

As EDX mapping analysis and Rietveld refinements indicate that both nucleation procedures yield above 85 wt.% LiFePO_4 by leaving Fe, Li_3PO_4 and FeS as separately crystallized side products with respect to Li excess (Li:Fe ~ 1.2) reaction stoichiometry in reductive calcination atmosphere. Although it is hard to predict a clear mechanism by step-wise XRD analysis after drying step. It can be claimed that LiH_2PO_4 appears as the common intermediate phase in solid state reactions in early (80 – 170 °C) calcination. High carbon content in solution phase with iron gluconate yields much reduced side products such as Fe_2P or Fe_3P as leaving much more (25 – 30 wt.%) pyrolytic carbon mass than ascorbic acid (~2 wt.%).

By comparing the results from Raman and electrochemical impedance spectroscopy of carbon coated cathodes, increasing carbon content tends to form more ordered (graphitic) carbon layer on the particles; but, its thickening rises surface impedance to get three times higher resistance. Surface adsorbed carbons are easily graphitized leading to a more ordered carbon layers. Unfortunately, temperature driven nucleation forms faster than surface adsorption of carbon which results in non-adsorbed carbonaceous materials giving heterogeneous or less carbon coating after pyrolysis. Hence, ascorbic acid needs solution mediated adsorption in order to show its surface

activity during crystallite formation, which is only possible in pH driven nucleation. If enough time is provided, homogeneous carbon content is achieved with superior conductivity. There is no need for external coating.

4.3 Ultrasound assisted sub-sequential precipitation

In this section ultrasonic wave assisted sub-sequential precipitation method has been proposed as a novel synthesis technique by investigating each steps from precipitation to electrochemical testing. Sub-sequential precipitation is performed using two different routes as presented in Chapter 3 (Figure 16). In each route, sequential precipitation step is conducted with and without the presence of ultrasonic wave irradiation.

High-power ultrasound technique (20 kHz - 1MHz) is a new powerful technology that is not only safe and environmentally friendly but also efficient and cost reductant to supply the energy in microscopic levels. It can be applied to existing processes to reduce or eliminate the need for chemicals or heat treatment in a variety of industrial processes. It is widely used in industrial crystallization process because of its stimulating effect on induction period. Sonochemical treatment was implemented on LiFePO_4 for the first time in 2007 by Jugovic et al.¹⁰⁸ However as a result of this study, brunch like micro porous morphology was obtained.

In this study, there are two different sequences between Li, Fe and PO_4 sources resulting different chemical and morphological phases which are intermediate products on the way to reach the final LFP cathode materials. According to the route of sub-sequential precipitation, $\text{Fe}_3(\text{PO}_4)_2 \cdot 8\text{H}_2\text{O}$ (VVT) and $\text{NH}_4\text{FePO}_4 \cdot \text{H}_2\text{O}$ (AFP) phases were produced at the last precipitation reactions which act as precursors for LFP production after same calcination procedure.

In the first additional path, $\text{NH}_4\text{FePO}_4 \cdot \text{H}_2\text{O}$ is synthesized to be a product of ammonium di hydrogen phosphate and iron sulfate mixing reaction; which is followed by Li diffusion introduced by ion exchange in aqua solution containing lithium source (Figure 46), subsequently. In other path (VVT precursor), sub-sequential precipitate which are Li_3PO_4 and $\text{Fe}_3(\text{PO}_4)_2 \cdot 8\text{H}_2\text{O}$ (VVT) crystals (Figure 47), are precipitated sequentially and the solubility difference provides slow reactive crystallization rate

during VVT precursor formation. The ultrasonic wave assisted procedure was involved into preparation of these precursor materials.

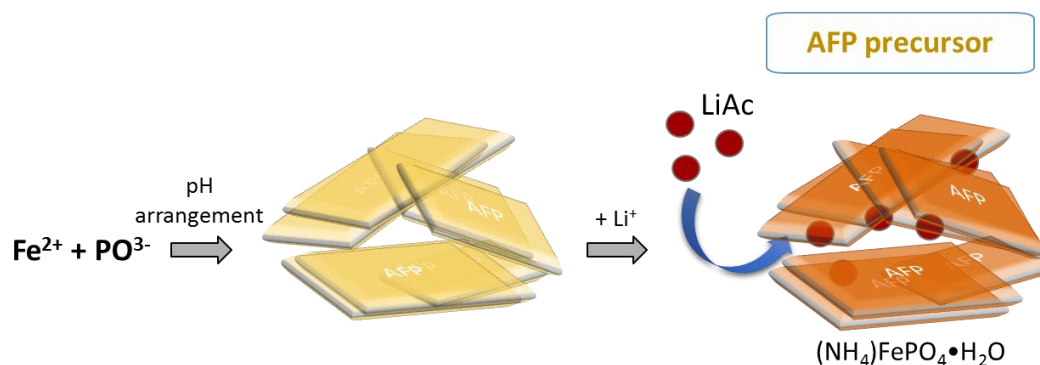


Figure 46. Schematic illustration of AFP crystal formation by sub-sequential precipitation

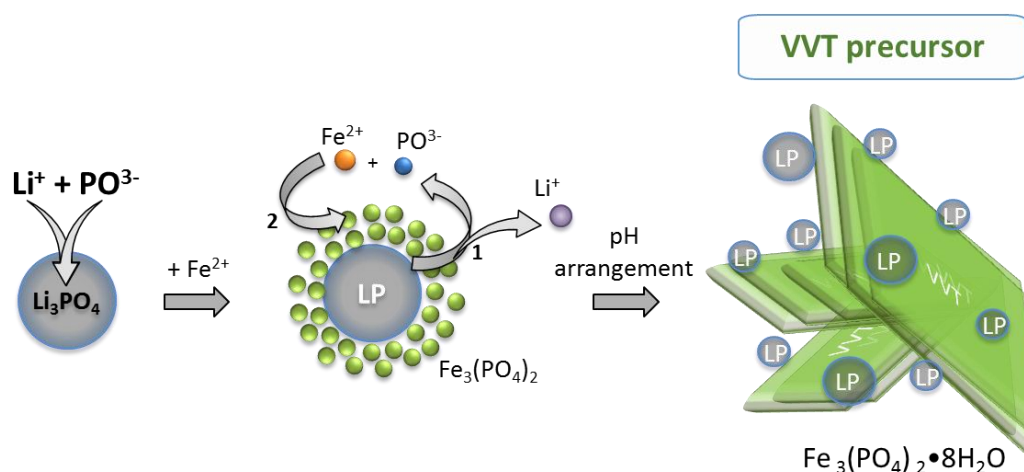


Figure 47. Schematic illustration of VVT crystal formation by sub-sequential precipitation

At the early phase of characterization, the sonochemical effect on reactions, and crystallization process of precipitate have been basically investigated through SEM, and XRD analysis. The real purpose of this sub-sequential procedure is to control the morphology and crystallographic structure of precursors synthesized via ultrasonic irradiation. From the bottom-up approach, having promising 2D nano structured synthesis of LFP is possible by controlling the morphology, orientation and size refinement of its precursor phases at early steps of production.

In order to investigate the sonochemical effect on crystallization process during precipitation, intermediate phases are examined under different pH, time and temperature conditions. Then the optimized conditions as well as sono-crystallization

process are determined to get thin LFP nano-plate synthesis with oriented crystallites (Figure 48). After precursor synthesis, morphology of nano-plate crystallites is preserved by carbonization during LFP transformation.

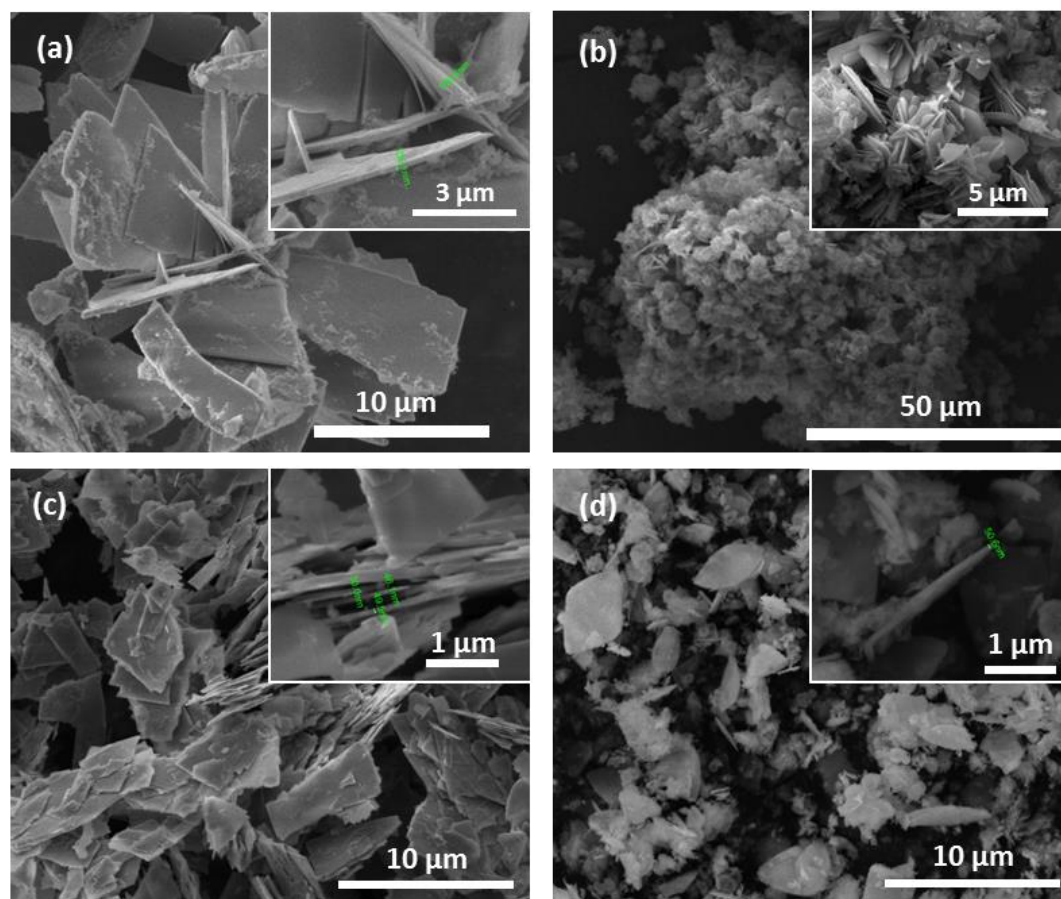


Figure 48 SEM images of AFP (a, c) and VVT (b, d) precursor particles with (a, b) and without (c, d) US treatment.

4.3.1 Ultrasound assisted vivianite nano-plate precursor synthesis

Vivianite and Li_3PO_4 are well known reactants for LFP formation since the first patented high surface conductive cathodes synthesized by Armand et al.¹¹² (Hydro Quebec and University of Montreal). Vivianite synthesis has not been commercialized because of bad reproducibility and high oxidation sensitivity of vivianite with hydrothermal and ball milling process in an inert and pressurized atmosphere conditions.

4.3.1.1 Ultrasound effect on Li_3PO_4 micro seeds synthesis

Solution acidity need to be hold in high pH (9-12) region to synthesize and stabilize the LP micro seed crystals. Thus, for this study, ammonium di hydrogen phosphate is used as phosphate source because of neutral pH region of its solubility products. Phosphate source has been added to LiOH solution (pH: 11.5) while stirring under intense sonication using either flow cell reactor or immersion rod. After mixing sequence is completed, samples are dried and analysed by LD for particle size distribution. The particle size measurements is conducted after 15 minutes sonication of dried powders in ethanol.

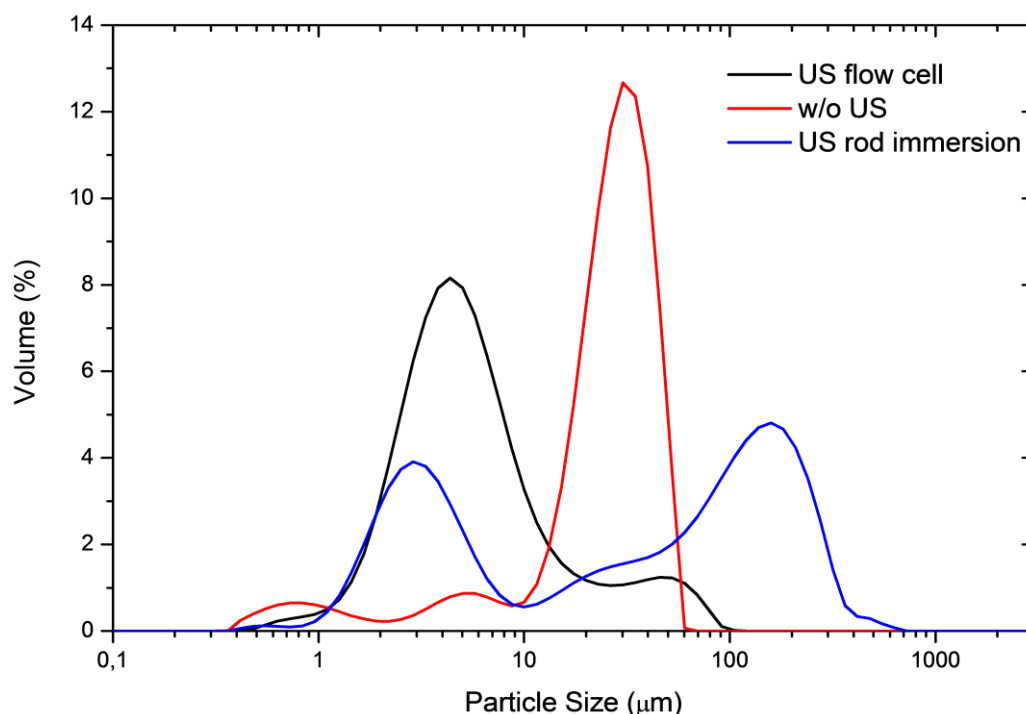


Figure 49. Particle size distribution analysis with LD measurement of Li_3PO_4 seed materials as synthesized with US L equipment or without US irradiation.

According to the particle size analysis results (Figure 49), the particle distribution for normal precipitation without US treatment is around 30 μm in diameter of Li_3PO_4 particles. However in the ultrasonic wave assisted precipitation technique, only few micron sized particles can be synthesized. In the particle size measurement, the left shifts of mean particle size curve represents the size refinement effect of ultrasound. The mean particle size distribution, in both flow cell and immersion rod US treatments, spreads to give higher diameter curves with the presence of left side curvature.

According to these results, SEM and LD analysis are in good agreement at relatively low powder diameters (Figure 49 and Figure 50). However, for the larger particle sizes, LD reveals the size of the agglomerated particles as confirmed by SEM analysis. As they are clearly identified from the SEM images in Figure 50, the lowest diameters are 3 and 4 μm for US assisted flow cell and rod immersion, respectively. These values are considered as actual size of micro seeds while curvatures at bigger diameters belongs to mostly individual particles.

The narrower particle size distribution within for both US treated samples can be observed in Figure 51 compared to the untreated bulky Li_3PO_4 precipitates. After ultrasonic assisted precipitation of LP crystals, hollow LP micro spherical seeds are observed as having the smallest size under 1 μm in diameter, instead of the bulky bigger agglomerates in normal precipitation (Figure 51-c).

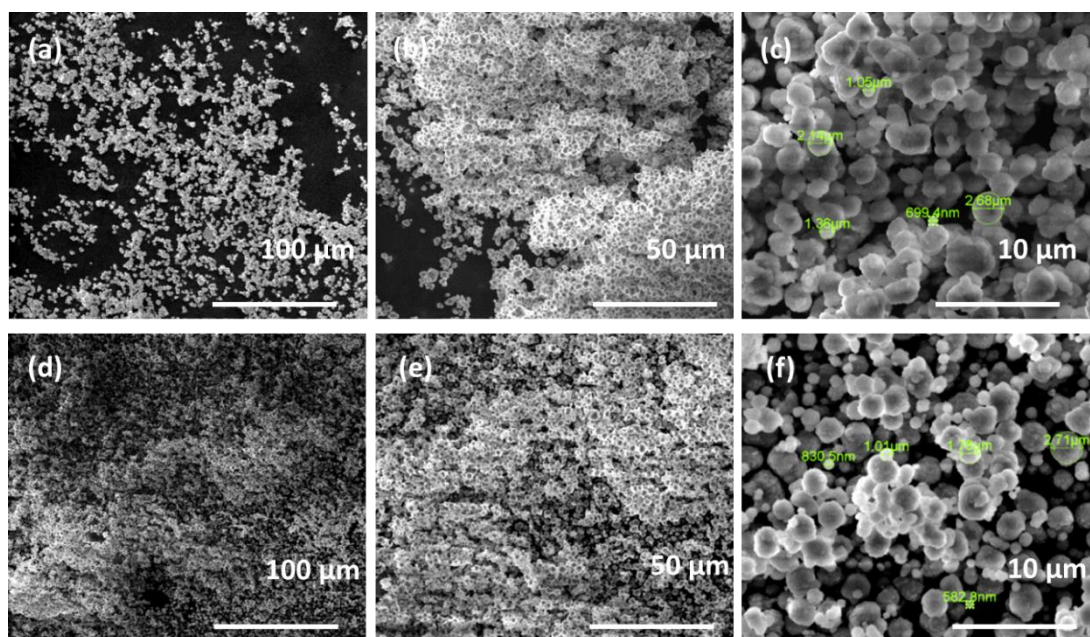


Figure 50. Ultrasonic wave irradiated precipitates of micro spherical seed lithium phosphate crystals achieved by ultrasonic rod immersion (a, b, c), and flow cell reactor (d, e, f).

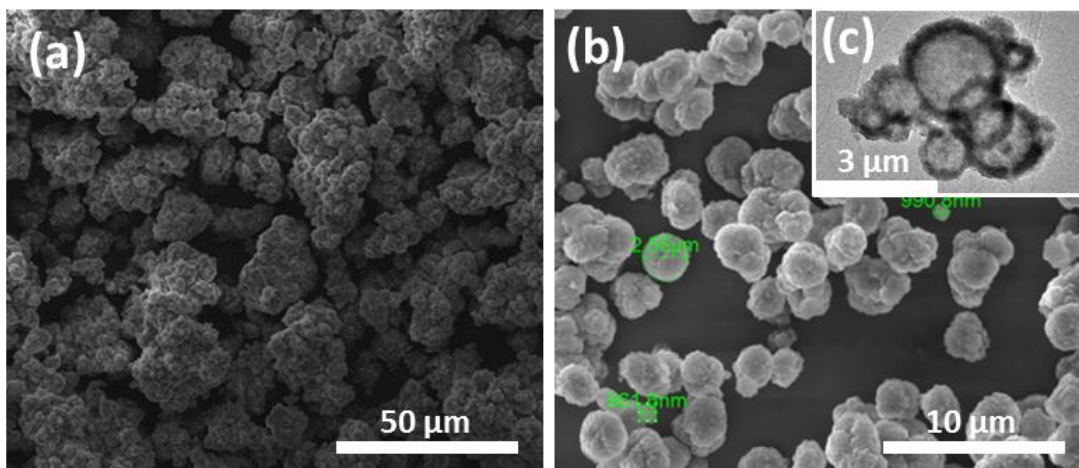


Figure 51. SEM images (a) of lithium phosphate precipitates produced without ultrasonic irradiation; SEM and TEM images (b, c) of ultrasonic wave irradiated precipitates of micro spherical seeds of lithium phosphate crystals.

In the literature, there are many examples of agglomeration effect of ultrasonic wave usage while igniting intense collision between micron size particles.¹⁰⁹ So intense care and optimization should be spent to implement the working parameters of ultrasonication against further agglomeration, especially in progressing time of precipitation. In our case, the further strong physical agglomeration was observed after prolonged US treatment times up to 75 minutes during LP seed precipitation step (Figure 52).

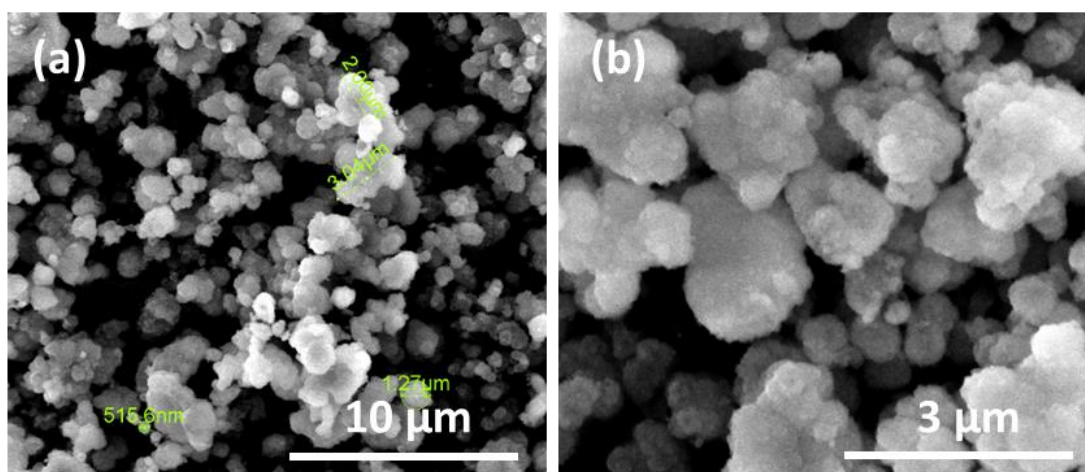


Figure 52. Further agglomeration on the LP micro seeds material upon further ultrasonic treatment after 75 min US irradiation.

After optimization of parameters according to finest size distribution, concentration of lithium and phosphate sources and stoichiometric ratio of P:Li are chosen as 0.1 M and 1:3, respectively. The sonocrystallization has been conducted with frequency of 20 kHz for 45 minutes. The sonication process should be compatible with agglomeration rate in order to obtain individual nano sheet crystal precursors

Although the higher yield of LFP could be achieved by normal precipitation without sonication, controlling the particle morphology and the corresponding size requires US application. Excessive amount of Li_3PO_4 is crucial as a lithium source and pH stabilizer agent for LFP formation. If Li_3PO_4 is desired to be removed, it can be done by washing it with acetic acid.¹¹⁰

4.3.1.2 Sonocrystallization effect on sequential vivianite precipitation synthesis

In early years of its discovery, LiFePO_4 synthesis has been suggested via vivianite formation by Armand et al.¹¹¹ However its role in synthesis has been always underestimated due to its poor reproducible micron size and sensitivity towards oxidation.¹¹² Researchers could not achieve sufficient control on morphology and size neither with hydrothermal nor mechano-chemical production. Then the main production procedures has shifted towards high temperature solvo- or hydro-thermal synthesis after the patent on this synthesis technique was issued by Hydro-Quebec and University of Montreal. Several years after these studies, Nazar group has studied on hydrothermal synthesis to optimize concentration and temperature with surface active agents.⁹⁹ They achieved 0.5 – 1 μm thick, low aspect, diamond like particles after complete LiFePO_4 crystallization.

High power ultrasound wave begins to be used as a new powerful tool which can support the crystallization process by several aspects.^{62,113,114} It is possible control crystal nucleation and growth, so that small sized crystals with clean surfaces are produced. Without ultrasonic wave control, nucleation and subsequent crystallization randomly occur. This yields with inhomogeneous and inefficient crystallization resulting mostly bigger than micron sized particles.

In this thesis, FeSO_4 solution is added to the aqueous suspension of Li_3PO_4 in order to obtain vivianite crystals as a precursor for LiFePO_4 synthesis. This addition stimulate the second reactive crystallization with the phosphate source of Li_3PO_4 . Synthesized

LP seeds were either treated with US and without US to better understand its effect on vivianite formation. Figure 53 represents SEM images for vivianite particles synthesized from US treated and non- treated LP seeds. Micron sized vivianite crystals can be seen after second (sequential) precipitation without existence of US treatment. It also shows a wide distribution of particle size including bulky shaped crystallites due to the enhanced growth rate during crystallization without US control process. Even in non-US treated second precipitation with the initially US treated LP seeds, by the vivianite precursors still have micrometer (50 – 100 μm) sized large crystallites.

Based on SEM images in Figure 53 and Figure 56, the US wave irradiation seems to have a significant role on vivianite crystallization by accelerating the serial reaction of LP dissolution and vivianite formation. Both micro and bulk LP seed materials have been easily react to form vivianite production with respect to XRD patterns (Figure 54-c & d) within accelerated reaction rate in acidic pH. However, the effect of LP micro seeds which are produced with the presence of US irradiation cannot be underestimated since it gives more oriented and fined vivianite crystal structure as compared LP bulk material. It can be also found out from higher intensity ratio and broadening at (020) peak of US-US sample (Figure 54-a and b).

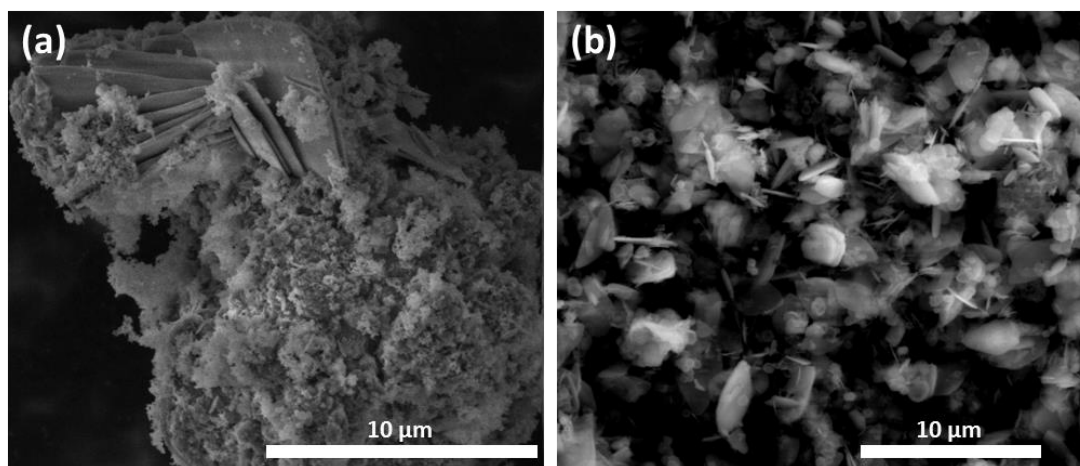


Figure 53. SEM images of micron sized vivianite crystals synthesized (a) non-treated VVT from bulky Li_3PO_4 and (b) US treated VVT from micro spherical Li_3PO_4 seeds

Ultrasound is sufficient enough to gain enhanced control over the nucleation sites with both homogeneous and heterogeneous mechanisms. For homogenous crystallization, in a nearly saturated solution or suspension, induces new nucleation sites. Together with unclarified mechanism on that, it is speculated as related with tremendous

pressure release during cavitation bubbles collapse⁶². On the other side, heterogeneous crystallization is associated with the mechanical effect of shock waves, which breaks up crystals to generate new nuclei for further crystallization which become more simultaneous within whole reaction vessel.

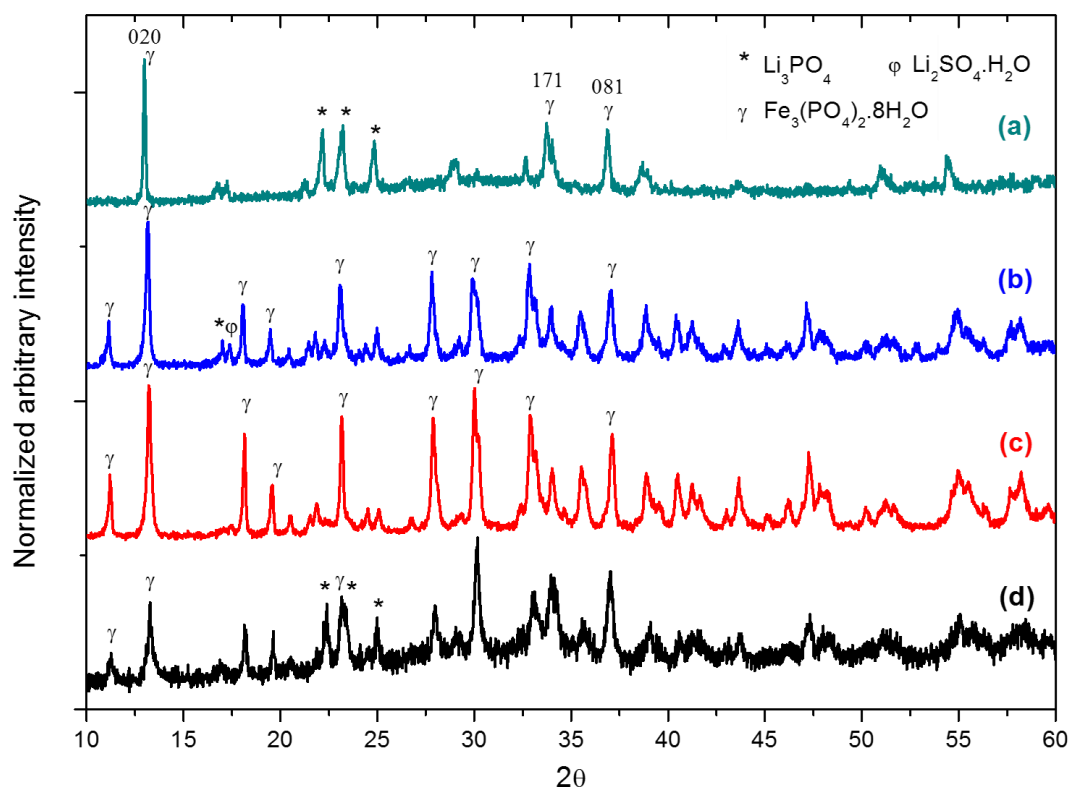


Figure 54. XRD patterns of sequentially precipitated precursor materials synthesized in acidic (pH: 4.5 – 5.0) suspension with (US) or without (None) ultrasonic irradiation during first-and second precipitation step (1st – 2nd), (a) US – US, (b) None – US, (c) US – None, (d) None – None.

US can adjustable to tune the reaction rate. This gives an opportunity to control secondly produced crystal size. The solubility difference, as a driving force for secondary precipitation of vivianite crystals, can be changed in a very small space and time by keeping the rest of the reaction media away from the elevated temperatures.

The rate of the chemical reaction can be managed by US controlled stimulation effect on Li_3PO_4 dissolution and recrystallization of vivianite crystals. The Li^+ and PO_4^{3-} ions can be released by dissolution and the phosphate ions react with iron (II) ions in solution. Therefore, produced iron phosphate compounds can crystallize within the surface region of LP. Ultrasonically assisted crystallization of hydrated iron (II)

phosphate (vivianite) crystallites (Figure 56) can be homogenized in existence with the Li_3PO_4 micro spherical seeds. So these 2D vivianite crystals expose (010) crystallographic plane along the largest surface area (Figure 55).

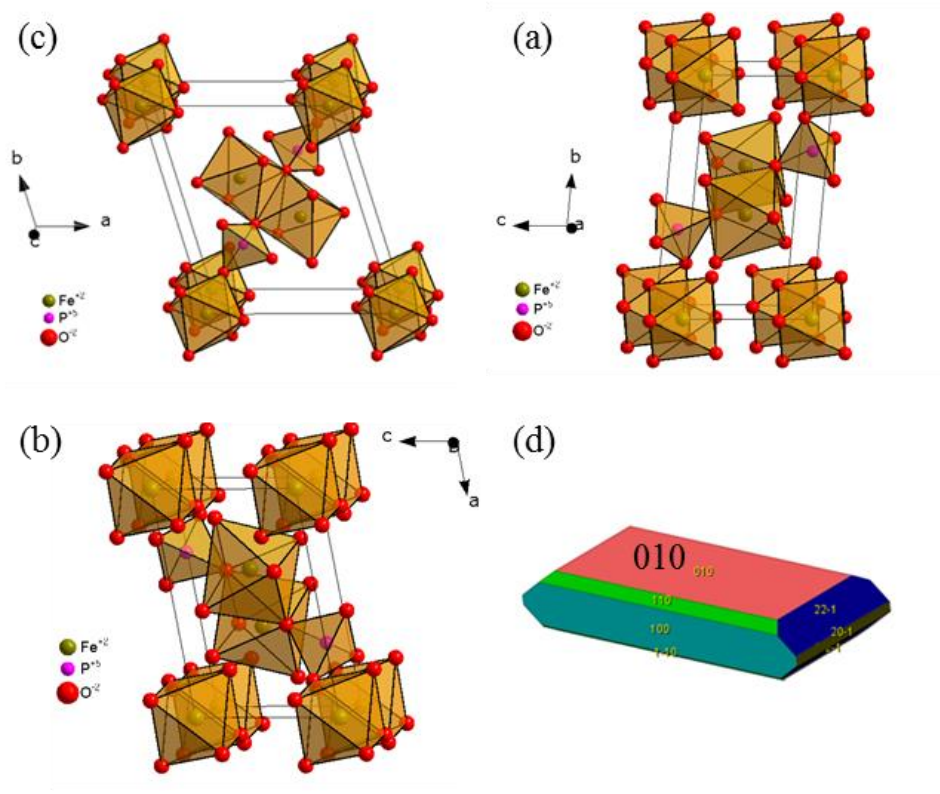


Figure 55. Vivianite crystal structure, viewed along a (a), b (b), and c (c) crystallographic axes and plate orientation (d) (JCPDS # 83-2453 with Diamond 3.2)

Morphological refinement effect of US wave irradiation is also clearly seen from the SEM micrographs of samples before calcination (Figure 57). After US irradiated sub sequential precipitation, thinnest diamond like nano plate structures of vivianite were homogeneously dispersed. Moreover, distinguishable amount of Li_3PO_4 micro spheres can still be detected nearby vivianite nano plate crystals (Figure 57).

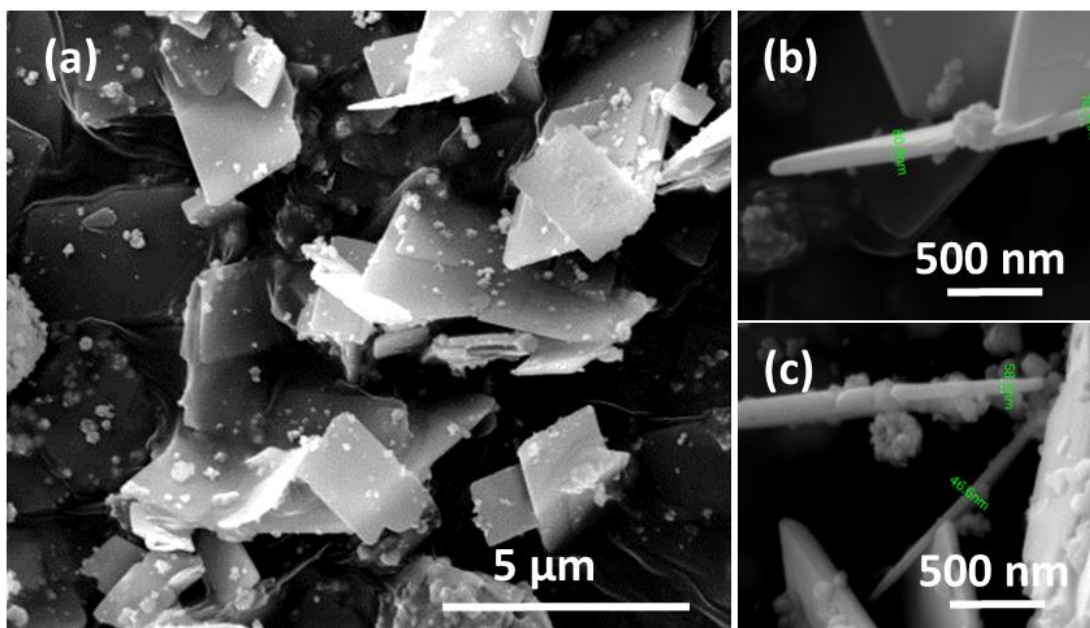


Figure 56. SEM micrograph of well distributed nano sized plate of iron (II) phosphate precursors synthesized by US wave assisted sub-sequential precipitation.

By having micro spherical LP seeds synthesized via US precipitation, Fe source addition without US irradiation has resulted mainly Li_3PO_4 phase formation which still remains same even after calcination (Figure 57-a and b; Figure 58-c and d). This lack of transformation is reasonable due to the deficient formation and crystallization without propagation of insonated reactions. This transformation is stimulated by US waves during second precipitation and synthesis of vivianite crystals as explained in detailed in 4.3.1.5. Attributed primarily to its efficiency of LP reacting with, the formation of vivianite crystal is crucial during the calcination process. After passing to solid state media, it is not possible to complete the whole transformation to LFP even iron source exists.

Homogenization of particle size will be helpful to increase the charge-discharge kinetic. Especially if the one dimensional structure of lithium ion diffusion tunnel could most probably be oriented along to the nano sized thin dimension of the particles. Hence, well and fine distribution of particles can be helpful for increasing the rate of Li ion diffusion into the cathode crystals which allows to a wide exposure (010) oriented channel openings

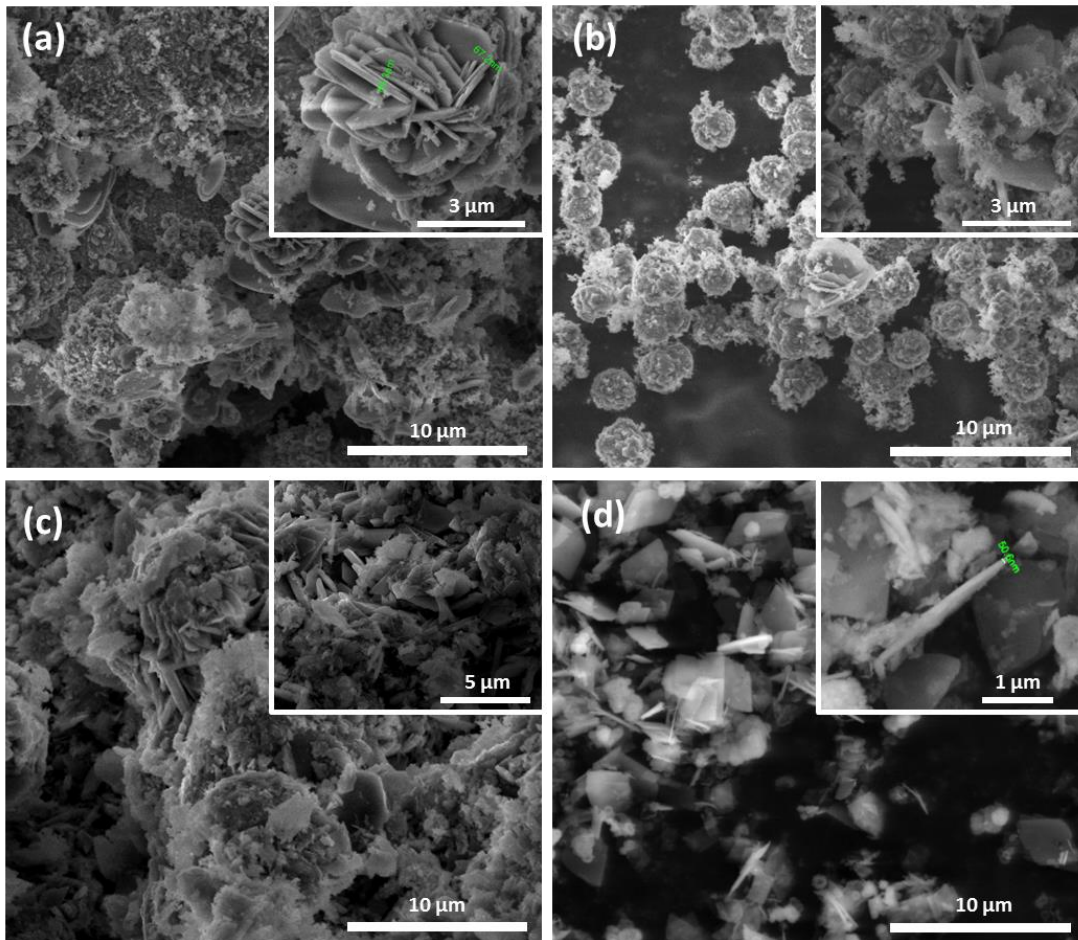


Figure 57. SEM micrographs of precipitated (before calcination) samples synthesized with (a) or without (b) US wave irradiation with bulk LP and with (c) or without (d) US wave irradiation with US treated LP micro seeds.

US distortion effect depends on the surface area which at least several times larger than bubble itself. Therefore, for 20 kHz frequencies, surface distortions coming from micro-jet formation cannot be obtained for solid particles smaller than 200 μm . However, cavitation still takes place in suspensions and bubble collapse creating shock waves through the liquid media. So fine powders are in charge with high velocity collisions stimulated by shock waves passing onto the particles.

In Figure 58, the effect of US wave irradiation on each precipitation reactions can be seen from the XRD patterns of resulted precipitates before calcination step. As the unique contribution of US treatments during precipitation sub-sequential reactions can be accelerated to complete conversion within several minutes instead of several hours in hydro or solvothermal production. After second precipitation with US treatment in both precipitations, broad peaks referring to fine sized structures are observed (Figure 58-a and b). Moreover, increased relative intensity of (010) peak of the obviously

indicates preferred orientation in *b* direction which belongs to thin vivianite nano plates (Figure 56). Enhanced line broadening is also observed, clearly on (010) peak at 13°, for all insonated samples which is an indication of better refinement on size together with preferred orientation on *b* crystallographic axis as well as 2D particles along *ac* directions.

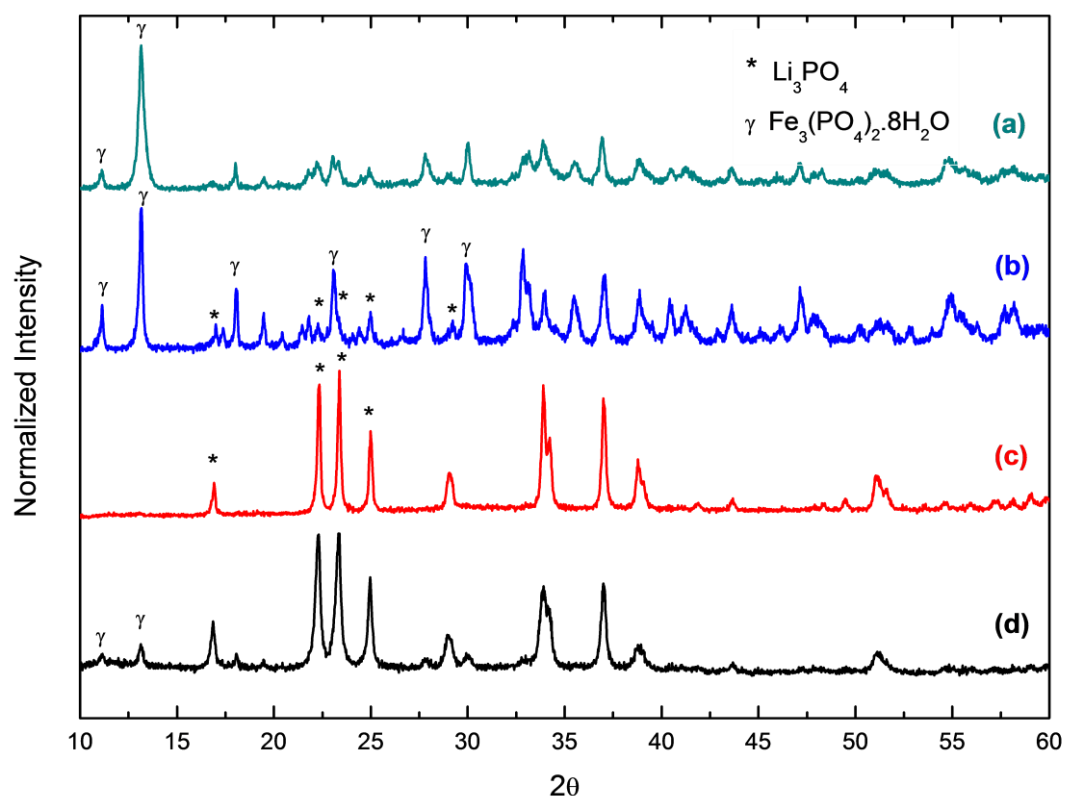


Figure 58. XRD pattern of sequentially precipitated (without calcination) precursor materials synthesized in basic ($\text{pH} > 6.0$) suspension with (US) or without (None) ultrasonic irradiation at each step (1st – 2nd); (a) US – US, (b) None – US, (c) US – None, (d) None – None

The XRD result show the increased preferred orientation on crystallographic plane incorporated with *b* direction. High order in *k* miller indices with respect to other *h* and *l* represents close angle of direction between (020) planes. Together with high (020) peak intensity ratio represents the strong anisotropy as bigger *ac* surface of crystals, this ratio increases with the crystallite size because of their better preferred orientation during sample preparation. So enhanced particle size refinement provides relatively poor preferred orientation in *b* direction which can barely oriented than bigger plate-like particles. Additionally much narrower (020) peak (Figure 54-a and b) represents

highly ordered structure can be obtained under low pH environment in suspension (secondary precipitation).

In lower pH suspension under insonation, the crystallization mechanisms have faster kinetic parameters which favour vivianite formation as clearly seen from XRD patterns of resulted precursors has been previously shown in Figure 54. The improved crystallization rate with US assists vivianite crystallites to generate large 2D structures along the exposing *ac* planes. The highest and sharpest (010) plane intensity can be seen in all insonated vivianite precursors (for LP and VVT) and indicates bigger crystallites as well as proved with Figure 64 in section 4.3.1.3. By eliminating the insonation in precipitation the crystallite orientations are lowered (Figure 54) because, vivianite production is enhanced with improved dissolution kinetics in lower pH of suspension. Therefore reactions are not under control of US intermittent restriction in lower solubility region. So, in acidic environment, insonation enhances the crystallization and growth rate by controlling the production rate of vivianite monomers instead of controlling them.

This results in Figure 58 and Figure 54 show that suspension pH possess a key effect to arrange solution stability while maintaining the suitable solubilisation balance for US improvement on crystallization rate. Thus, the suspension needs to be optimized at pH~ 6.0 while US is subjected within crystallization process to get best particle refinement by supplying high nucleation and low growth rates (Figure 59).

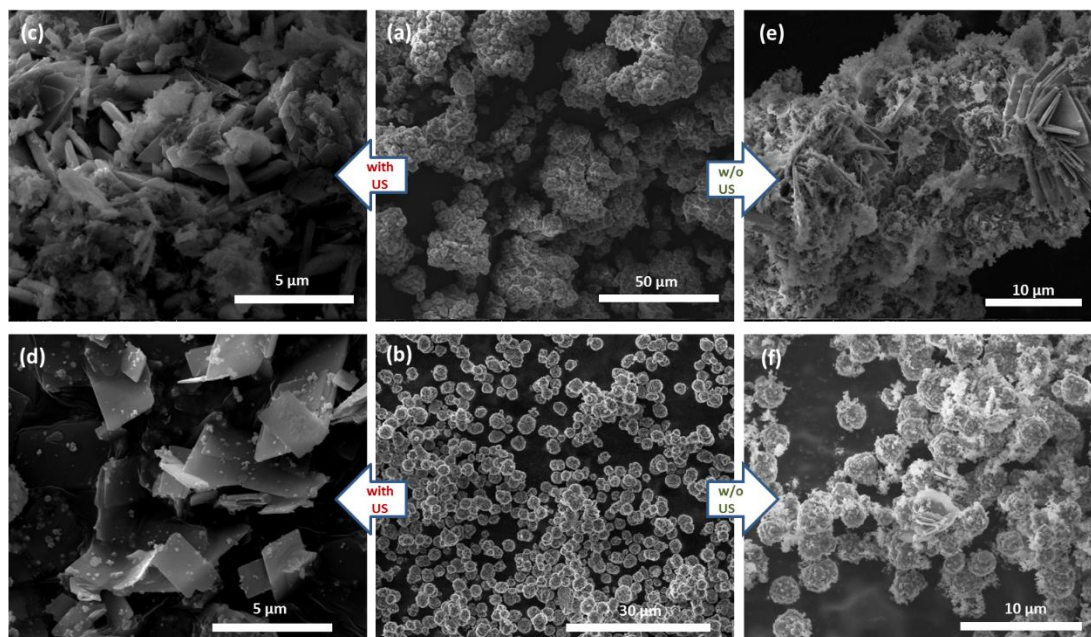


Figure 59. SEM images of US treated (b) or not treated (a) Li_3PO_4 and vivianite precursors synthesized with (US) or without (None) ultra-sonication during first-and second precipitation (pH \sim 6.0) step (1st – 2nd); US – US(d), None – US (c), US – None (f), None – None (e).

4.3.1.3 Effect of suspension pH on morphology and thickness of nano plates

In the synthesis of nano-plate structures, it is important to maintain stable nucleation and growth rate in corporation with US irradiation. In general liquid phase crystallization process, the nano structures appear if clusters are big enough to survive after nucleation occurs in milliseconds. This means that nucleation rate is desired as high as possible to get homogeneous and sufficient amount of nano clusters begin to accumulate simultaneously.

The Lamer diagram in Figure 60-(a) indicates that high initial concentration or super-saturation gives large number of nucleation sites. For a certain concentration of solute, a larger number of nuclei logically indicates smaller sized nuclei. Besides that, lower viscosity and lower critical energy barrier are also favoring the formation of a large number of nuclei. So different surface active and highly ionic additional compounds have effective impact on nucleation and growth processes. Some examples of them are discussed in further chapter 4.3.1.6 related with chelating agents.

The higher growth rate is undesired to get smaller size particles. After enhancing the super-saturation concentration, nucleation rate increases rapidly. Three dominating

region are seen in Figure 60-(b) as stable solution (I), nucleation (II) and crystal growth (III) after nucleation. In order to get evenly distributed nano-sized structures, the concentration and nucleation rate should be enhanced up to a maximum amount of nuclei. Theoretically, the growth rate can be decelerated or limited by decreasing concentration as passing region-III very rapidly to reach the stable region-I. However if vivianite formation reaction is high enough to keep feeding monomers for crystallization, the growth progresses as long as all monomers are consumed which can be seen at higher solubility in lower pH region in this case.

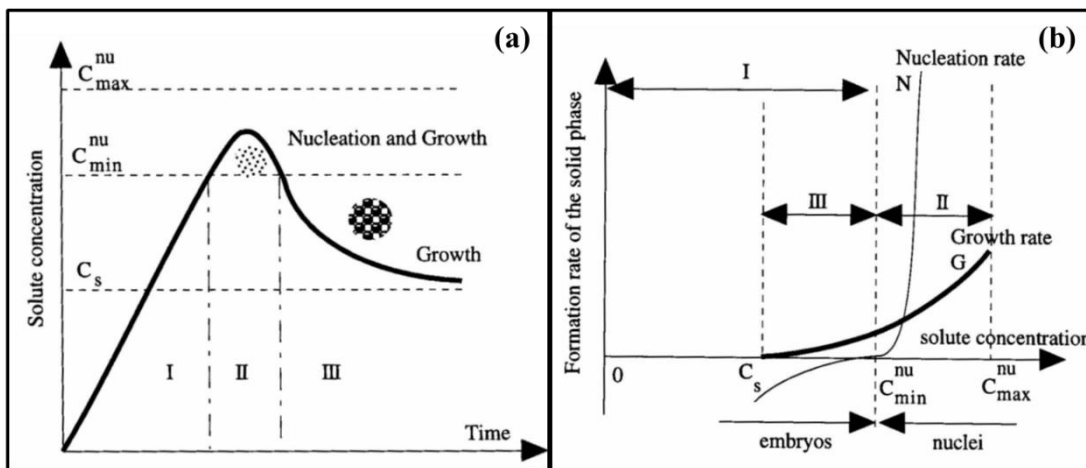


Figure 60. Nucleation and growth process in crystallization depending on time and monomer concentration, Lamer diagram (a), and Formation rate of nucleation and growth (b).¹¹⁵

At this point, the pH value at around 6.0 seems to be optimum to result in smaller particle as slow down the reaction kinetic, for this study. The lower solubility and reaction rate suppressed the vivianite formation. Around pH 6.0 the solubility difference between reactions (equations (6), (7)) allow the ultrasound to keep nucleation rate under control. This intermittent effect with shock waves and cavitation stimulate the reaction in very short time to enhance the concentration and rate in order to get high nucleation rate and density in a very short time and space.

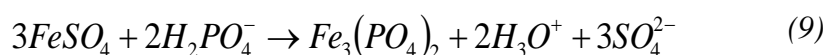
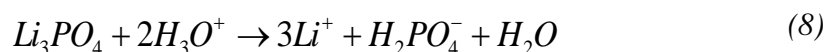
Notwithstanding US waves propagate the dissolution and nucleation mechanisms, crystallization is also effected by the environment of species in solution as crystal growth continues. It is also necessary to pursue the reaction between Li_3PO_4 and $FeSO_4$ in a suitable rate by adjusting the suspension pH. Due to the fact that Li_3PO_4 crystals are easily dissolved under pH 4.0, which is selected as a lower limit for secondary (sequential) precipitation for pH arrangement.

Together with little change in morphology of the vivianite particles, the aspect ratio of thickness over length, slightly increases with crystallite size followed by a decrease in solution pH (Figure 64). By comparing the 2D particle thickness, pH is found to be the key factor on reaction kinetic and phase stability by changing their solubility under atmospheric conditions. So, thickness of US treated nano plates can be minimized by optimization of suspension pH level. As a consequence, different growth rates are favored in different pH conditions by US assisted sub-sequential precipitation method. The reactive crystallization conditions have to be re-optimized by considering the metastable conditions within insonated suspension media.

Throughout the thesis, it is aimed to produce small 2D particles as thin as possible while suppressing their growth. When solution pH increased, the nucleation rate decreases because of lower solubility (concentration) of LP and lower stability of VVT. However, US also increase nucleation rate by increasing solubility and concentration of nucleated monomers. Higher solution pH around 6.0 results in relatively small particles according to lower growth rate because of lower LP solubility beside high nucleation rate in very localized concentration peaks of VVT coming from rapid solubilisation change via US. These balanced mechanism enhances nucleation probability while limiting the further growth conditions in whole aqueous media.

In the solution thermodynamic study of Li-Fe(II)-P-O₂ system⁹³, LiFePO₄ is reported to be stable at all pH values in coexistence with other phases (Li₃PO₄ and Fe(OH)₂) at higher pH than 11.3. Notably, there are no coexistence of Fe₃(PO₄)₂·8H₂O and Li₃PO₄ at stable phase diagram. So these are intermediate metastable forms which can react with each other to form LiFePO₄.

LFP cannot be practically obtained at acidic pH region despite the conflict of computational thermodynamic study.¹⁰¹ This might be explained according to too low reaction probability at acidic region with respect to the dominant existence of H₂PO₄⁻ and H₃PO₄ where solution pH changes from 5.0 to 7.0. The following reactions are assumed to take place.



Based on the metastable solubility diagram (Figure 61-a) and molar ratio of precipitated phases in relevant study,¹¹⁶ there are three dominant regions according to the pH of solution. Vivianite appears to be a stable single phase at pH under 6.6 up to the 3.0 as increasing solubility. At higher pH value, LP precipitates can be seen together with vivianite solid particles up to pH < 10.5. Upon its solubility decreases as pH increases where beyond pH > 10.5, Li_3PO_4 and $\text{Fe}(\text{OH})_2$ again coexist (Figure 61-a). At pH values higher than 6.6, the molar ratio of vivianite rapidly decreases with increasing solid LP stability (Figure 61-b).

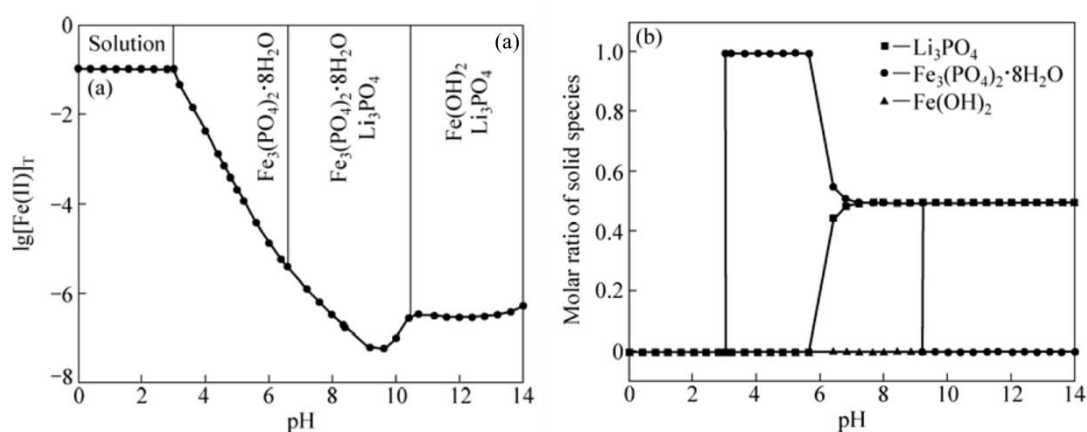


Figure 61. Solubility (a) and molar ratio of species in metastable Li-Fe(II)-P-H₂O system with Li⁺ excess.⁹³

All strategic approach of sub-sequential precipitation technique depends on co-existence of US and solubility difference between LP and VVT. Thus morphology and size can be controlled via US which manipulates the nucleation and growth kinetics of reactive crystallization. Coherent with the particle thickness in SEM images, thickness increases as decreasing pH in accordance with increasing growth rate and higher solubility of sacrificial LP solid phase. So VVT particles grow rapidly rather than spreading nucleation homogeneously. For small particles it is needed to be in fast nucleation regime but keeping away from metastable zone.

Above pH 6.5 region Li_3PO_4 solid phase gains stability in solution and it is possible to exist together with $\text{Fe}_3(\text{PO}_4)_2 \cdot 8\text{H}_2\text{O}$ solid phase. It is proposed to manage sizes and morphologies of these precursor (VVT and AFP) phases by insonation without elevating temperature in aqueous based suspension, whereas LiFePO_4 formation is satisfied with the solid state reaction between these phases.

Although Li-hua et al.¹¹⁷ concluded that equimolar ratio of $\text{Fe}_3(\text{PO}_4)_2 \cdot 8\text{H}_2\text{O}$ and Li_3PO_4 solid precursors is not possible to obtain by co-precipitation. However, equi-molar solid precursor mixing can be achieved by using sequential precipitation (or different additional sequence) and insonation within the aqueous suspension itself as proposed in this thesis. Vivianite crystal structures can be formed easily under the control of US by manipulating the pH effect on reactions and solubilities. Even though equi-molar ratio was reported as only reachable in Li excess and pH 7.0 – 9.2, it is possible to reach by US assistance within lower pH values even together with size refinement of resulted 2D nano structures.

Regarding to the XRD patterns in Figure 62 the vivianite crystal structure can be formed easily in the variation of pH between 4.5 and 6.0. However, in more basic solutions, the prepared structures have much finer crystallites with narrow size distribution (Figure 64). This shows that the dissolution and recrystallization reactions can be more controllable in less acidic pH around 6.0 initiated and developed by insonation.

Moreover, without insonation precursors have mostly bulky and agglomerated structures (Figure 59-e). Otherwise, when pH is low, the solubility balance is broken and fastened dissolution which leads rapid increase on reaction probability to straying from the under control of ultrasound. The resulted vivianite structures, under US effect, are larger at micron size and more agglomerated at micron size as seen as in Figure 64-a. Therefore, pH was optimized as around 6.0 by considering mean particle thickness (Figure 63) having restricted effect of US stimulated crystallization on nucleation rate and solubility.^{60,113,114}

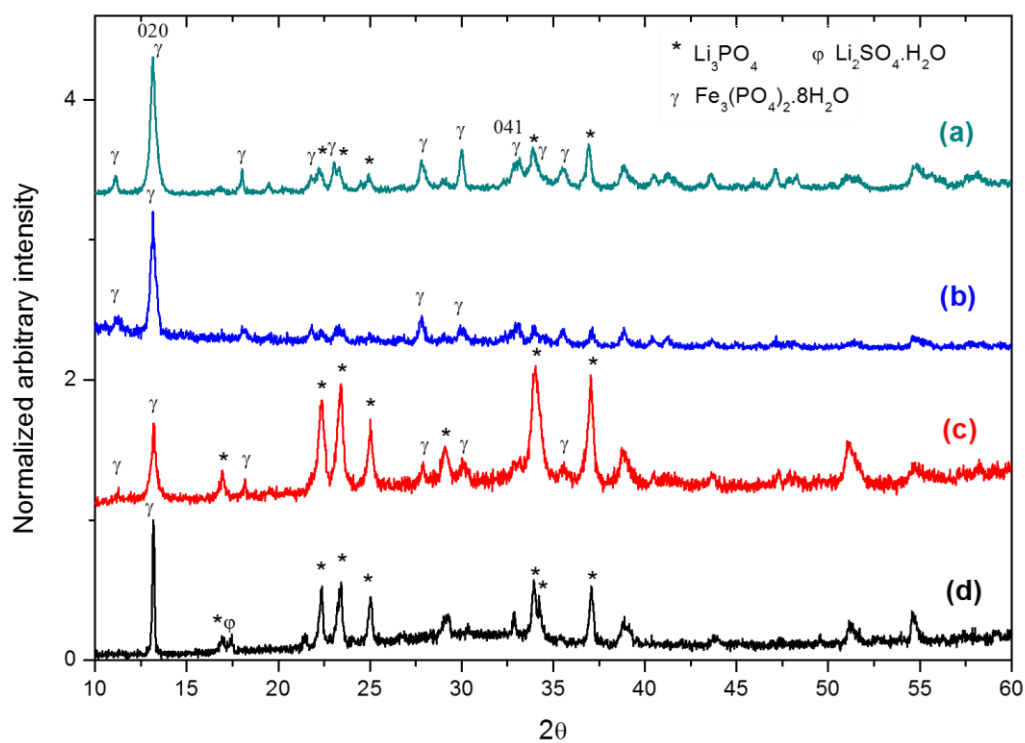


Figure 62. XRD patterns of materials as precipitated (before calcination) by US wave assisted sub-sequential precipitation with different pH at (a) 4.5, (b) 5.0, (c) 5.5, (d) 6.0.

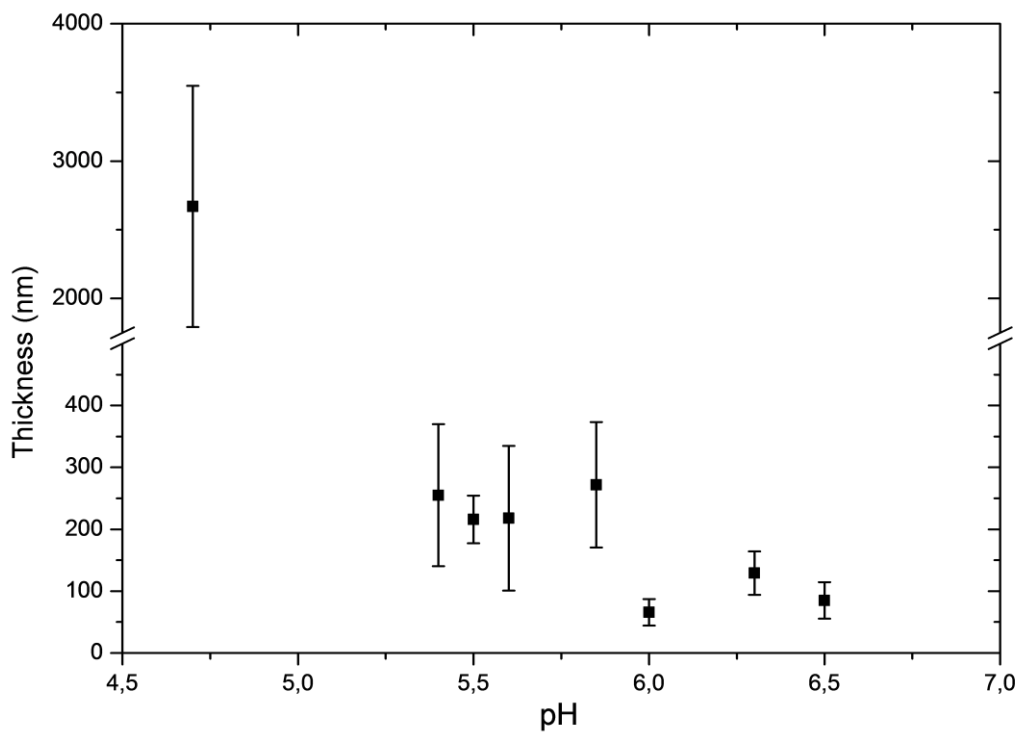


Figure 63. Calculated average thickness of plate like vivianite particles from SEM images

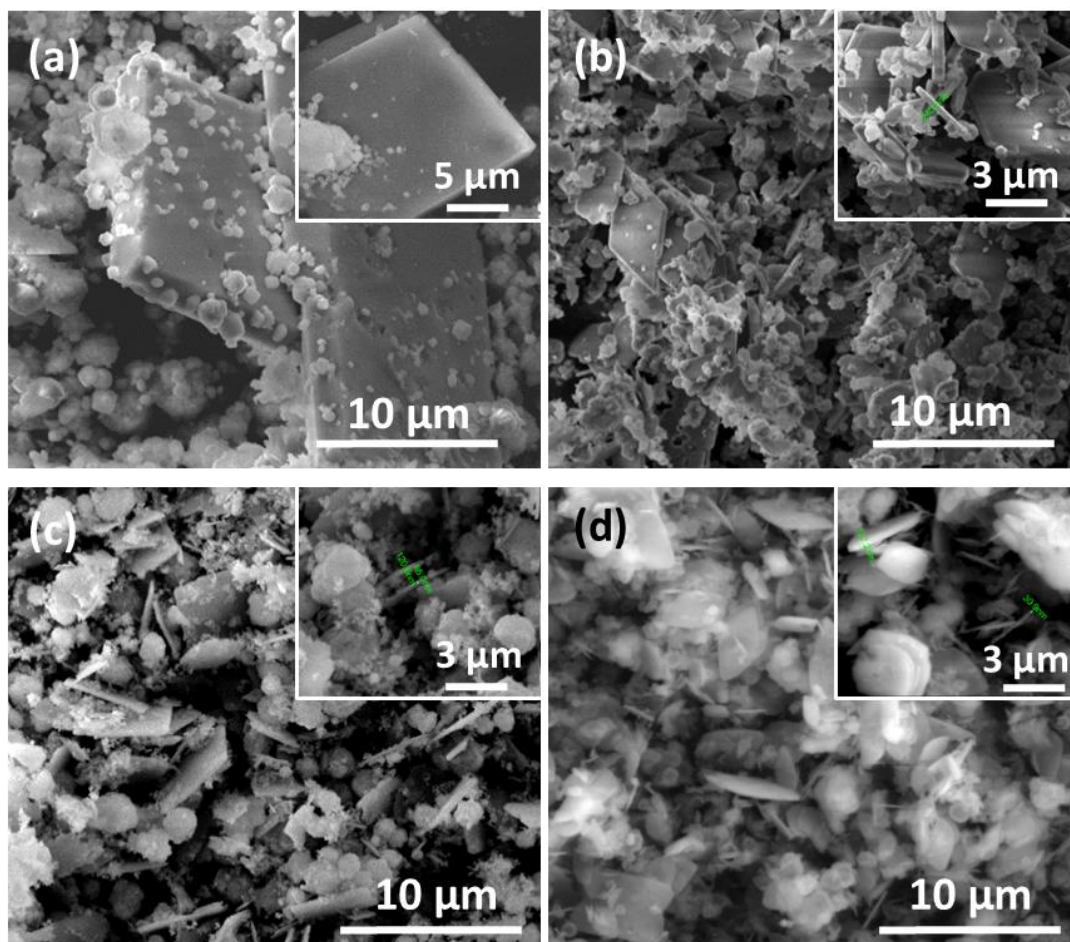


Figure 64. SEM images of all US assisted synthesized particles within given pH (a) 4.5, (b) 5.0, (c) 5.5, (d) 6.0 before calcination.

4.3.1.4 Ultrasound effect on the crystal morphology and structure of LiFePO_4

US waves lead the reduction of both the induction period and metastable zone width (MSZW) in crystallization, so that crystallization process can be more efficiently controlled than without insonation. Agglomeration is also greatly reduced by strong cavitation and shock waves. Furthermore, optimization of the ultrasonic parameters can modulate the crystal size distribution. Although, the mechanism of the sono-process has not been fully understood yet, some explanations were proposed in following section incorporated with the nucleation and growth theories. The whole crystallization and transformation reactions can be controlled with help of US wave propagation of the unique environment in a short time. Because of radicals formation by sonochemical reduction,⁵⁹ it is suitable against further oxidation of Fe^{2+} to Fe^{3+} .

This phenomena helps to maintain reducing environment in suspension with the presence of easily ionizable organic compounds and it is discussed at Section 4.3.1.6.

As mentioned previously, precipitation has been achieved in two ways; with or without US irradiation. When intermediate phases form US assisted or non US precipitation, it is found that the intermediate phase crystallites are distinguishable in size and shape. These intermediate phases are used as precursor to obtain meta-morphologic transformation to final LiFePO_4 cathode material after calcination process. In order to see the effect of ultrasonic wave treatment in each of two steps, calcination products were investigated by SEM and XRD analysis.

The effect of US can be seen through XRD patterns which was taken from every samples synthesized with or without US wave irradiation (Figure 65). After the calcination steps the qualitative analysis shows that the main difference between non US and US irradiated precipitation is the amount of LiFePO_4 synthesized. In Figure 65 it is clearly seen that very limited formation of iron (II) phosphate (vivianite) yields excessive amount of Li_3PO_4 material remaining as unreacted with FeSO_4 without propagation of US waves. This proves that iron (II) phosphate (vivianite) is the key intermediate product to direct the formation reactions of LiFePO_4 . During second (sequential) precipitation, significant difference is poor reactivity resulted in premature phase transformation to vivianite without US irradiation. Oppositely, even in hydrothermal (160 – 200 °C) conditions, not only reaction rate is too long but also crystallization of vivianite compound is unstable because of growth acceleration of elevated temperature. On the other hand in the sub-sequential sequence of precipitation US waves can generate phase transformation within minutes to kinetically active intermediate vivianite species which can be easily lithiated to form LiFePO_4 .

Once the reactants Li_3PO_4 and $\text{Fe}_3(\text{PO}_4)_2 \cdot 8\text{H}_2\text{O}$ are supplied, LFP transformation is capable in the solid state reaction within calcination step according to the *equation (10)*. It seems that US has much more intensive effect on the LFP production by manipulating the crystal structures of vivianite especially. Calcination is destructive on the synthesized LiFePO_4 crystallite morphology at high temperatures (Figure 67-b) but it is also indispensable to satisfy the conductivity.

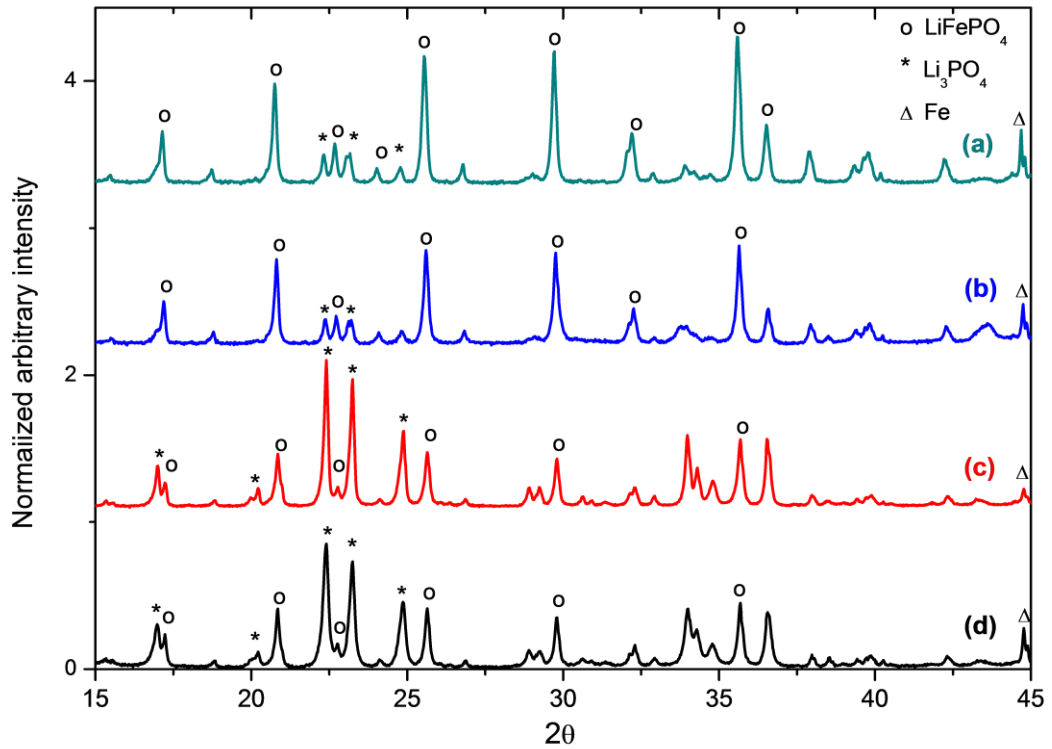
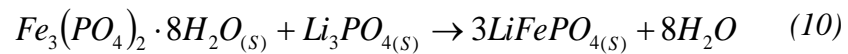


Figure 65. XRD pattern of calcined samples synthesized with (US) or without (None) ultrasonic wave irradiation at each precipitation step (1st – 2nd); US – US (a), None – US (b), US – None (c), None – None (d) (pH ~ 6.0).



The cathode materials need to be also properly carbonized during calcination with extra addition of carbonaceous materials. Carbon coating of cathode materials is crucial for targeting low electrical resistance. On the other side improper coating might be harmful as well as insufficient electrical resistance due to the passivation by thicker layer. Especially, its optimized amount depends on crystallite sizes which determines total surface area. Bigger crystallized materials may lead insufficient lithiation to form LFP because of over carbonization as seen in Figure 67-a. The conduction effect is discussed with optimization of carbonization as an encapsulation strategy of synthesized nano structured cathodes in Section 4.3.3.

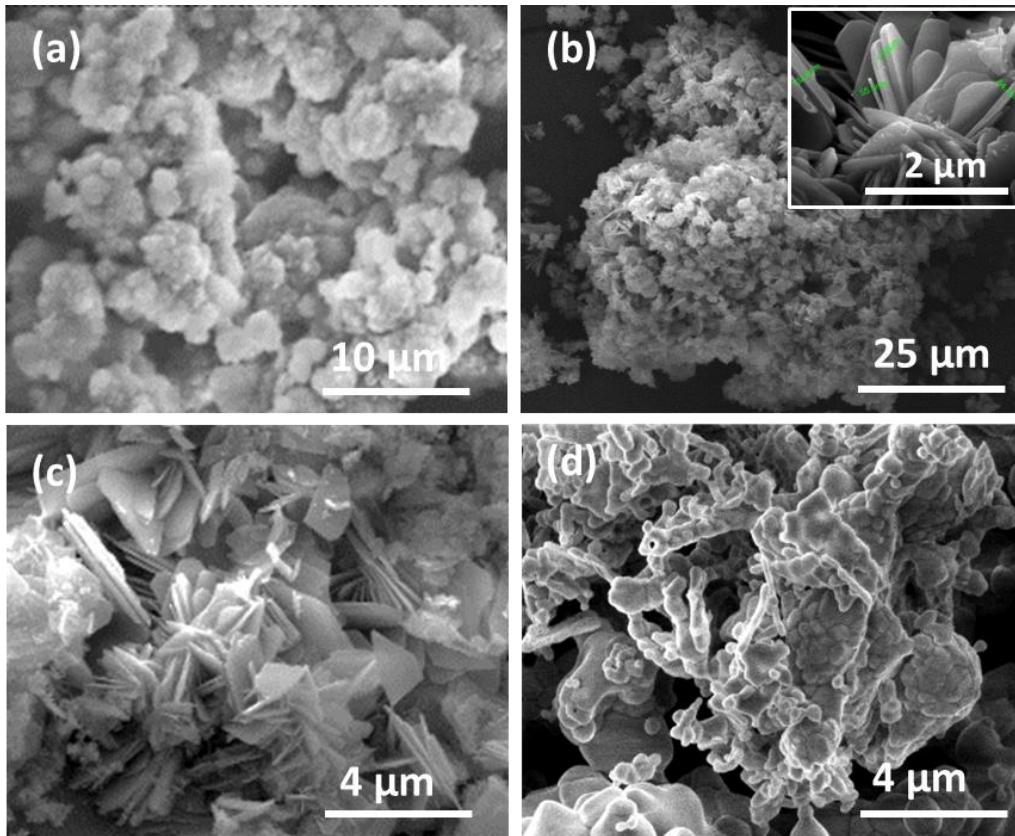


Figure 66. SEM images from (a) Li_3PO_4 and (b, c) vivianite to (d) LFP structure produced via sub-sequential precipitation without US wave irradiation (arrows are indicating on going procedure).

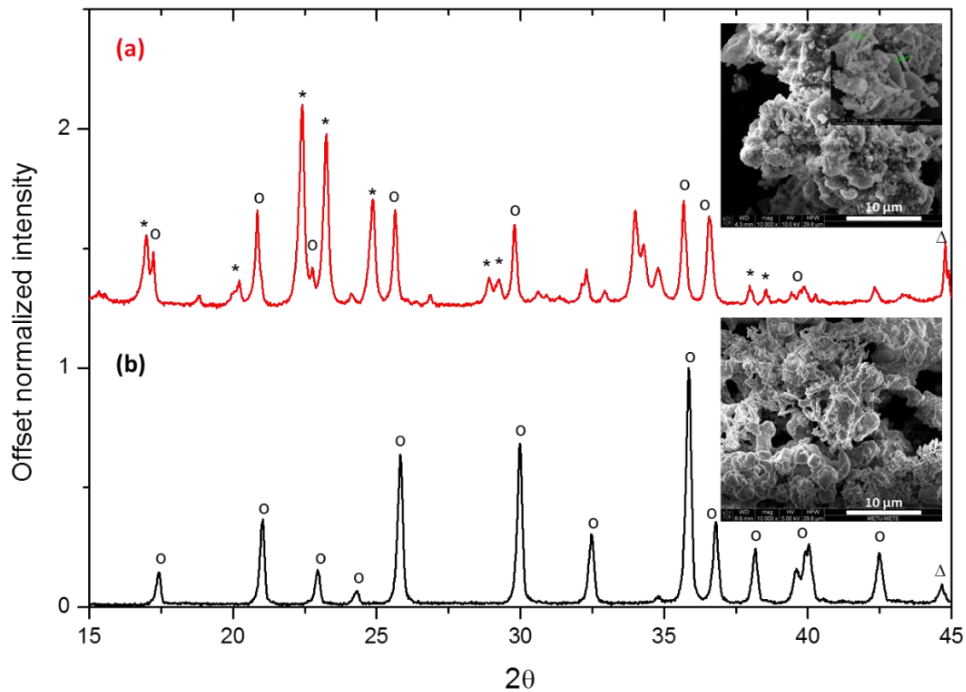


Figure 67. XRD patterns with SEM images of cathode materials calcined with (a) and without (b) carbonization of precursors which synthesized via sub-sequential precipitation without US treatment.

4.3.1.5 Explained mechanism for US assisted sub-sequential precipitation synthesis of LFP/C nano plates

The US wave has a significant role on stimulating the crystallization, refining the size and dispersing particles, homogeneously. US irradiation can accelerate the rate of reactions and provide more on the crystallite size by its energetic nature. The highly energetic nature of US waves may also be conducted with co-existence of other techniques to advancing or manipulating their approximations. In this thesis, US wave irradiation not only accelerates the nucleation in constructive way but also refines the size in a destructive manner via shock waves. It has also reduced the time needed for crystallization reactions from hours to minutes as a very dense emission of energy in space and time.

Nano-crystal formation in solution can be supported by increasing nucleation rate and decreasing growth rate condition. For nucleation to start, key driving force is the concentration passing over the super saturation point as higher than saturation. The size of nuclei depends on the reaction rate as correlated with concentration and temperature. With the help of ultrasound is able to manipulate these parameters in certain time and volume.

Beside the lack of theoretical understanding and prediction of US effect on nucleation and crystallization processes, there are reliable evidences to explain in literature^{60,62,63}. Ultrasonic waves induce primary nucleation at much lower super saturation levels. Moreover, ultrasound reduces induction time between super saturation and nucleation. This phenomena provides advantage to obtain homogeneous crystallization.

Sufficient pH reduction by forming H[•] radicals involves to observe dissolution and recrystallization reactions between intermittent compounds by keeping ionic Fe²⁺ reduced. Sudden and enormous change in temperature and pressure formed by bubble collapse and subsequent release of shock waves had a significant effect to increase super-saturation. An increase in localized pressure decreases the recrystallization temperature.

Ultrasound wave reduces the Meta-Stable Zone Width (MSZW) within saturated media. Metastable zone is described in literature¹¹⁸ as prohibited region for nucleation beyond super saturation which would be reduced by intense US waves. Accelerated super saturation yields more amount of homogenous nucleation within the suspension.

On the contrary, the aim of industrial crystallization procedures is to control the reactions by keeping the conditions in metastable zone width (MSZW) to favors the high growth rate.

According to the Lamer diagram (Figure 60), nucleation mechanism starts localized rapid super saturation by producing iron (II) phosphate compounds after the reaction between dissolved Fe^+ and PO_4^{3-} ions. Then the rapid consumption of newly produced monomers suddenly decreases the concentration below the solubility limit again, without allowing further growth until another super saturation is obtained again with the help of ultrasound stimulation. Sudden concentration decrease stops the nucleation by passing under the growth rate rapidly due to the lack of intermittent cavitation and temperature drop after cavitation effect. In Figure 68, insonation manages the reaction product which is in right enough amount to be nucleated as small crystallites and not to grow.

Phosphate concentration increases dramatically with a rapid increase in solubility of solid Li_3PO_4 in a very limited reaction volume. This stimulation effect triggers the reactions in *equations (8) and (9)* to form vivianite monomers in solution. Highly concentrated monomers are accumulated for nucleation. Rapid cooling spots in solution results in a huge drop on reaction rate to produce vivianite monomers. Then, concentration and temperature conditions move towards the stable zone without experiencing further growth thanks to the shortened metastable zone width and sudden concentration decrease after simultaneous consumption of monomers by nucleation.

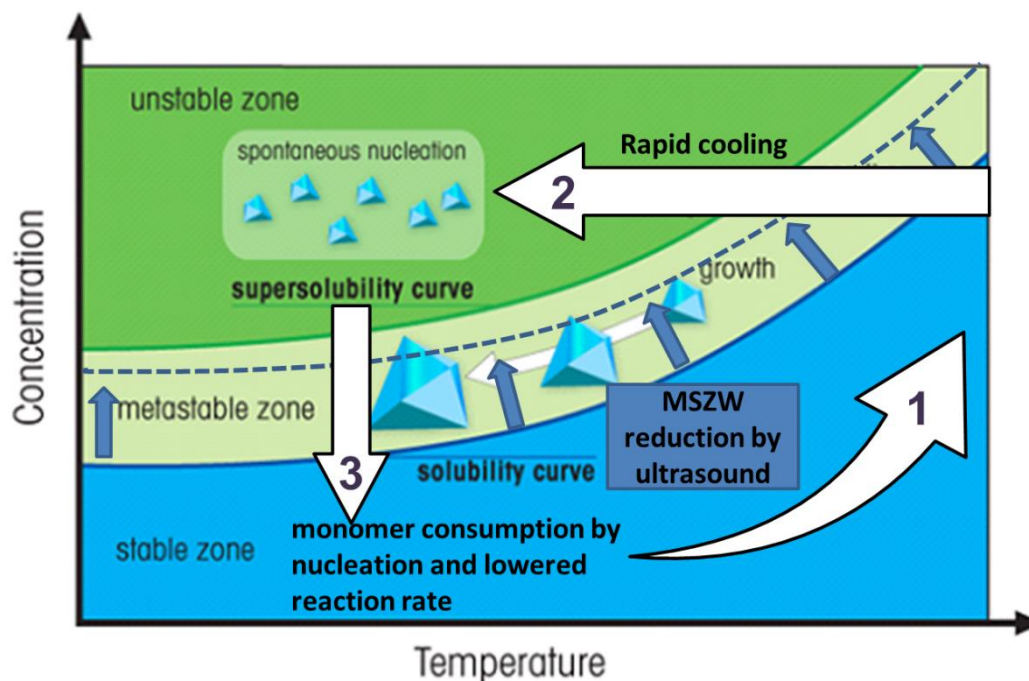


Figure 68. Schematic representation of US assisted dissolution-reaction (1), nucleation-crystallization (2) and consumption-growth step (3) mechanisms on solubility curve with metastable zone width reduction effect of ultrasound.¹¹⁹

The illustration in Figure 69 explains the nano-plate production mechanism for ultrasound assisted sub-sequential precipitation which is used for synthesis of precursors throughout the thesis. Firstly, LP seed material is precipitated with the help of ultrasonic irradiation and this treatment effects the size distribution and shape of the LP seeds. After obtaining the hardened and dried LP seed microspheres, the second precipitation occurs in LP emulsion within reduced pH from 10.0 to 6.0, by simultaneous implementation of ultrasonic wave irradiation. Thanks to the higher solubility coefficient of LP than $\text{Fe}_3(\text{PO}_4)_2 \cdot 8\text{H}_2\text{O}$ the total reaction can be driven to form vivianite crystal on to the near surface of LP micro seeds due to the decreased surface energy for secondary nucleation on their surfaces. The presence of a secondary solid surface can be used to control the nucleation. This is because, the interfacial energy between a crystal nucleus and a solid substrate is lower than that of the crystal in contact with the solution.¹²⁰

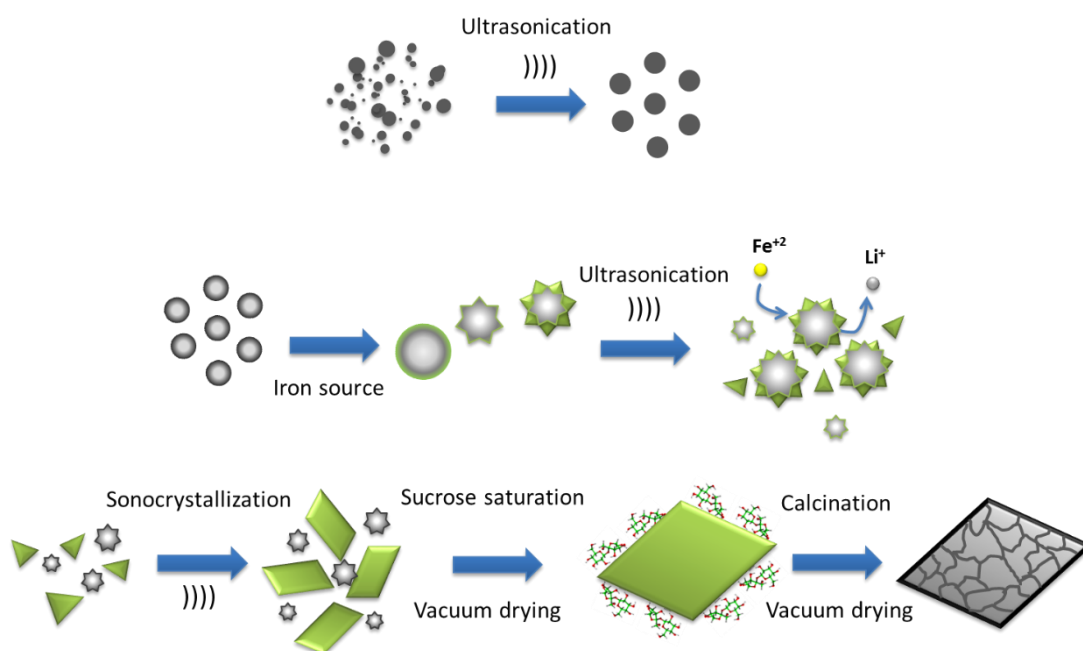


Figure 69. Schematic representation of proposed mechanism of ultrasound assisted sub-sequential precipitation synthesis of LiFePO_4

As crystalline becomes larger in size, agglomeration is being hindered due to low surface to volume ratio compared to newly formed nuclei. US waves also provide excessive amount of turbulence and disturbance resulting in shorten contact between crystals towards the inhibition of agglomeration. In the further crystallization growth, US waves tremendously enhance Ostwald ripening which can grow nano-plate structures building up through homogenously distributed nano crystallites.

Differently from the reported study,¹²¹ which claims that equi-molar ratio of VVT and LP can be obtained in one batch with slightly basic pH (7–9.2), thanks to the sub-sequential precipitation technique with existence of insonation, it is able to result in equi-molar reactant ratio of $\text{Fe}^{2+}:\text{PO}_4^{3-}:\text{Li}^+$ at 1:1:1 at this range. Because the ultrasound induce reactions in micro scale, actually the all conversion rates are possible with the help of sequential pH conditions. Even in slightly acidic pH 5–7 conditions the equi-molar conversion are able to be easily controlled under insonation in spite of unstable thermodynamic condition for whole system.

4.3.1.6 Effect of chelating agent on particle shape and morphology

In case of using the surface active compound that will restrict the growth and further crystallization, the US can control the reaction rate by cleaning the surface and open the new surface area intensely. By the use of various type of carbonaceous materials, morphology of product was altered as well as the yield of product. Furthermore, carbon coating with the use of soluble organic material (citric acid, and ethylene glycol) having chelating and encapsulating behaviours was studied in an aqueous solution before and after the precipitation step.

Nano plate structures can be limited during growth in the precipitation reactions by using organic compounds. Organic additives not only limit the mass transport for growth but also limit the dissolution from the surfaces. So these addition of compounds should be investigated because they can widely affect the reaction and crystallization kinetic as well. After calcination process, these organic compounds are also able to leave sufficient carbon residue to form carbon coating on the surface of LFP particles.

When all sources are mixed up, the solution pH differs from neutral condition because of the acidity of additives. Because pH 6.0 – 8.0 is Fe^{2+} dominant region the pH is adjusted with LiOH or NH_4OH concentrated solutions. During all dissolution and recrystallization reactions with ultra-sonication, pH needs to be adjusted all the time.

When the citric acid addition is used, EDX mapping analysis presents the presence of two separate Fe and P accumulated regions as correlated with two different morphological structure formation (Figure 70). This mapping results indicate the formation of thicker LFP diamond shaped plates and spherical LP seeds after calcination process with the existence of citric acid. Furthermore, XRD patterns show no peak for Fe_2P or Fe_3P formation, these Fe and P rich areas to be associated with LiFePO_4 and Li_3PO_4 phases Figure 70-a.

On the other hand, with existence of ionized citric acid, aqua media became more reductive and yields some reduced side products such as FeS because of its chelating properties on Fe^{2+} cation, especially. FeS does not melt up to 1194 °C and only reacts with high acidic compounds like HCl to outcome with H_2S compound. Due to the unique smell of H_2S during calcination together with negligible S content in the synthesized powder, it can be claimed that sulfur ingredient reacts with H_2 gas then it is released by gasification with exhaust stream.

When citric acid addition uses, much thicker nano plate structure can be observed by SEM images. With the presence of citric acid ultrasonic wave assisted precipitation has an important acceleration on structure growth after second precipitation. These nano plate crystals has shown diamond like shape instead of rhombohedra (Figure 71).

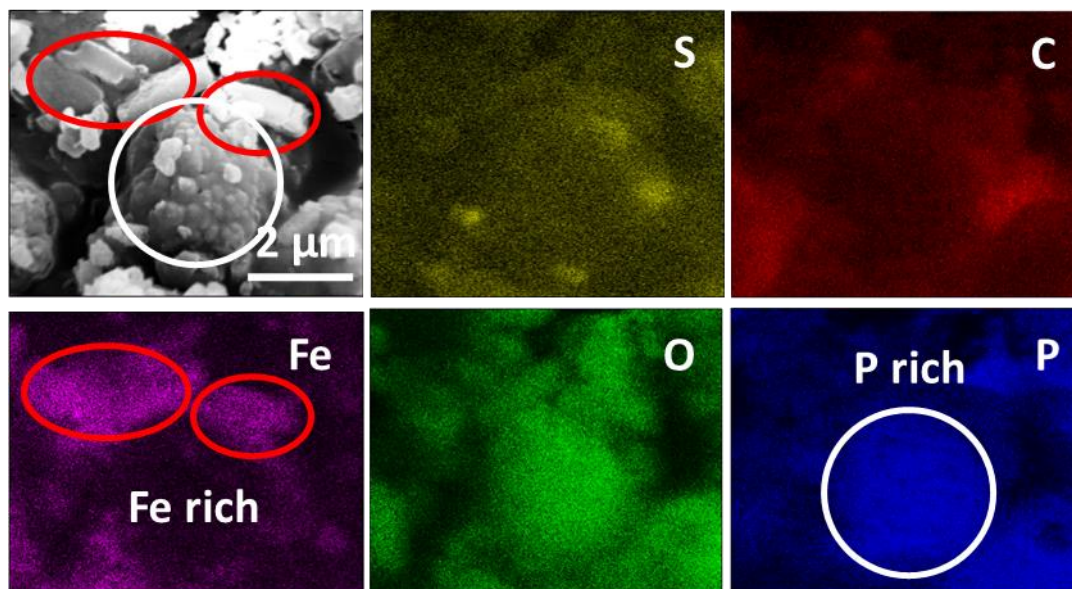


Figure 70. LFP and Li_3PO_4 crystal morphologies detected by Fe and P rich region, respectively, from EDX mapping analysis after calcination step

CA has chelating effects also for Li^+ ions, so after a certain concentration it reduces the mobilization and activation of Li^+ ions. It is remarkably shown that high concentration, 0.1M of CA is responsible for increasing Li_3PO_4 peak in the XRD patterns (Figure 72). CA have a slightly increasing effect on LFP formation at low concentrations as 0.025M. It prevents the oxidation of Fe^{2+} to Fe^{3+} acting as a reducing agent for iron sources. This reducing feature of iron can be observed as in increase in the reduced bcc iron peaks at around 44.5 degree in Figure 73. With increasing amount of CA, the more reduced side product are observed such as FeS in both high and low pH regions.

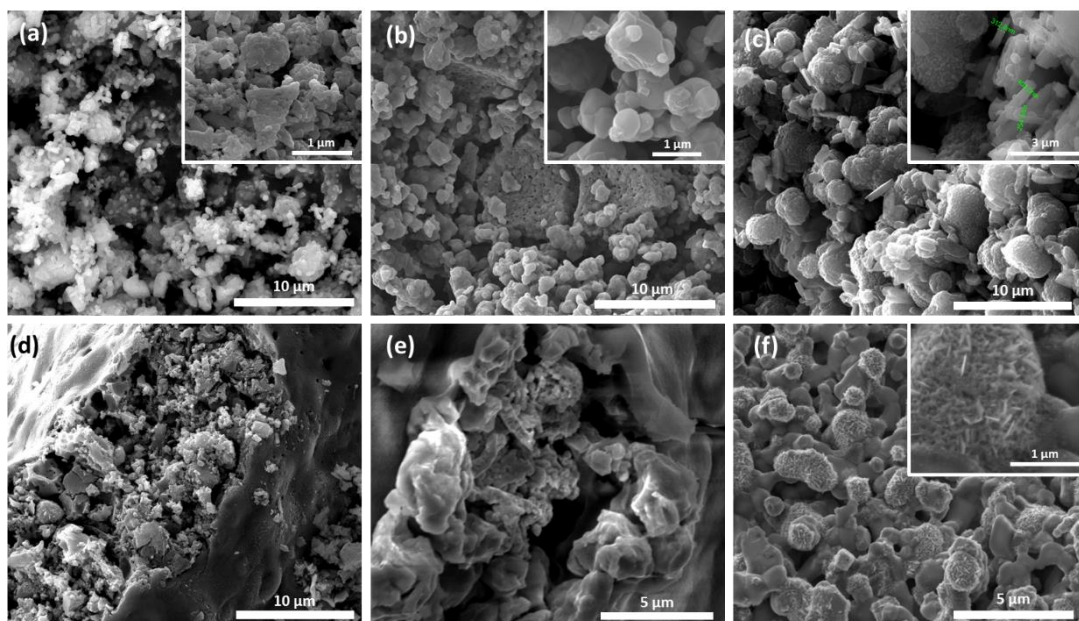


Figure 71. SEM images of synthesized powders after calcination of US assisted precursors with 0.005 M (a), 0.025 M (b), 0.1 M (c, d, e, f) CA addition at pH 3.0 (d), 4.0 (e), 5.0 (f), 6.0 (a, b, c).

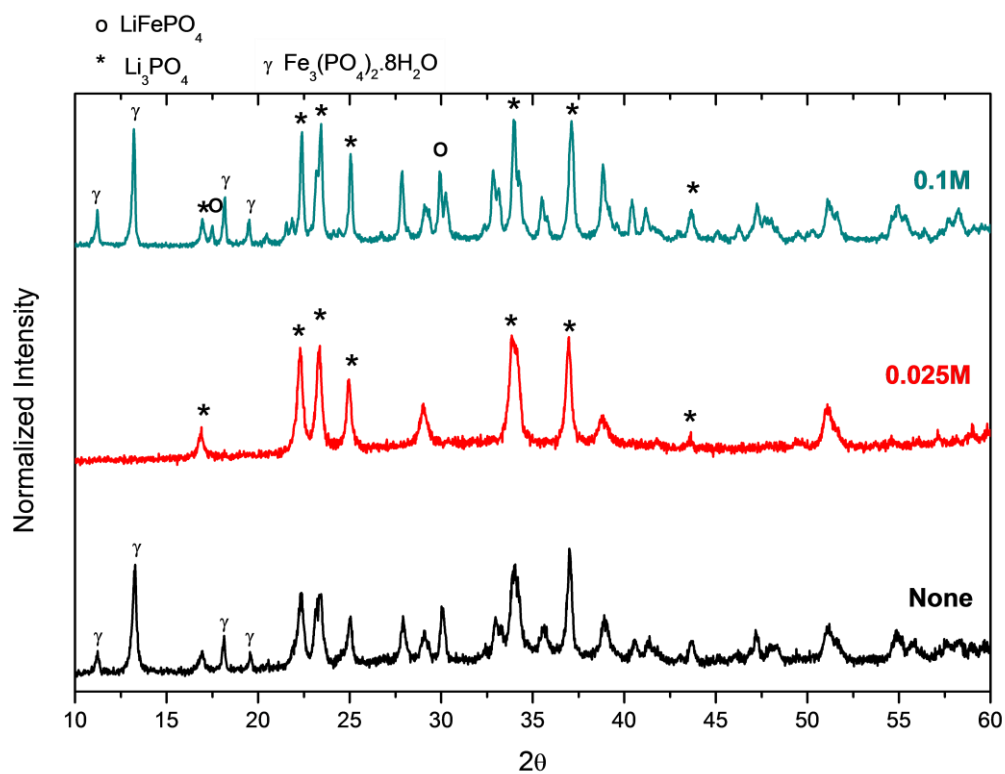


Figure 72. XRD patterns of precipitated (without calcination) samples synthesized via US assisted sub-sequential precipitation with citric acid addition

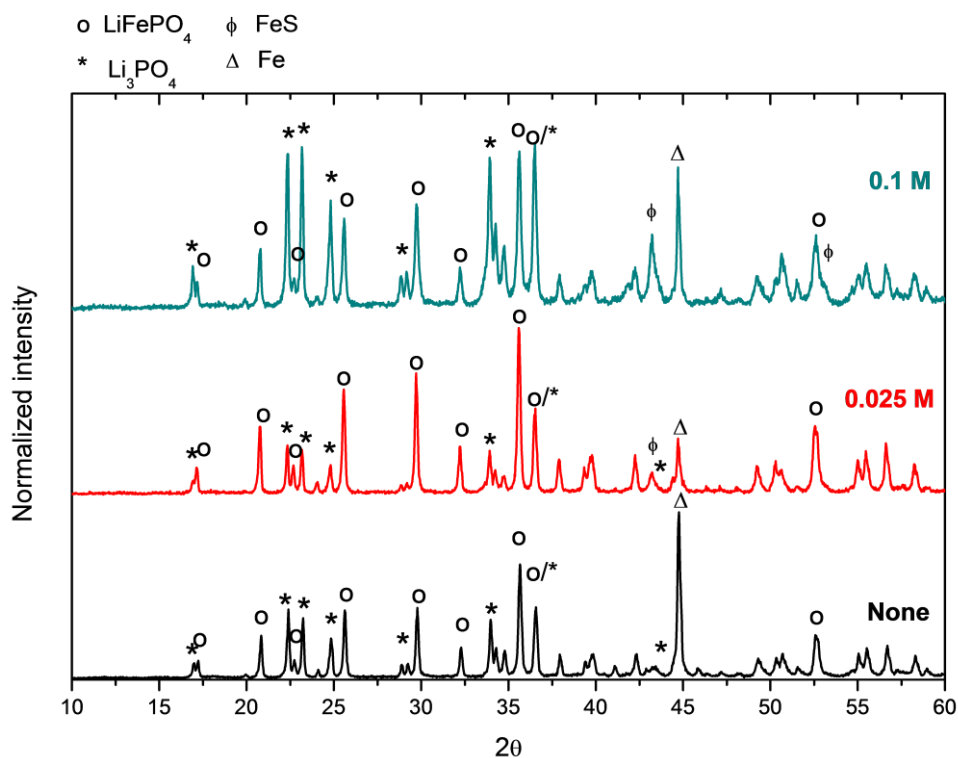


Figure 73. XRD patterns of calcined samples synthesized via US assisted sub-sequential precipitation with citric acid addition

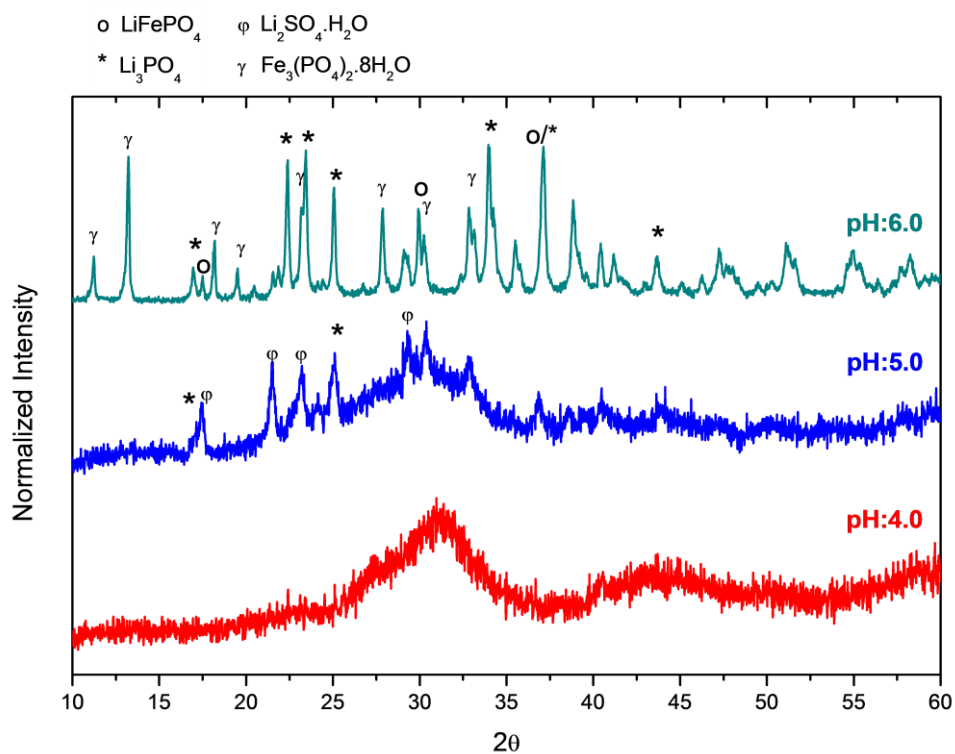


Figure 74. XRD patterns of precipitated (without calcination) samples synthesized via US assisted sub-sequential precipitation at various pH values with 0.1M citric acid

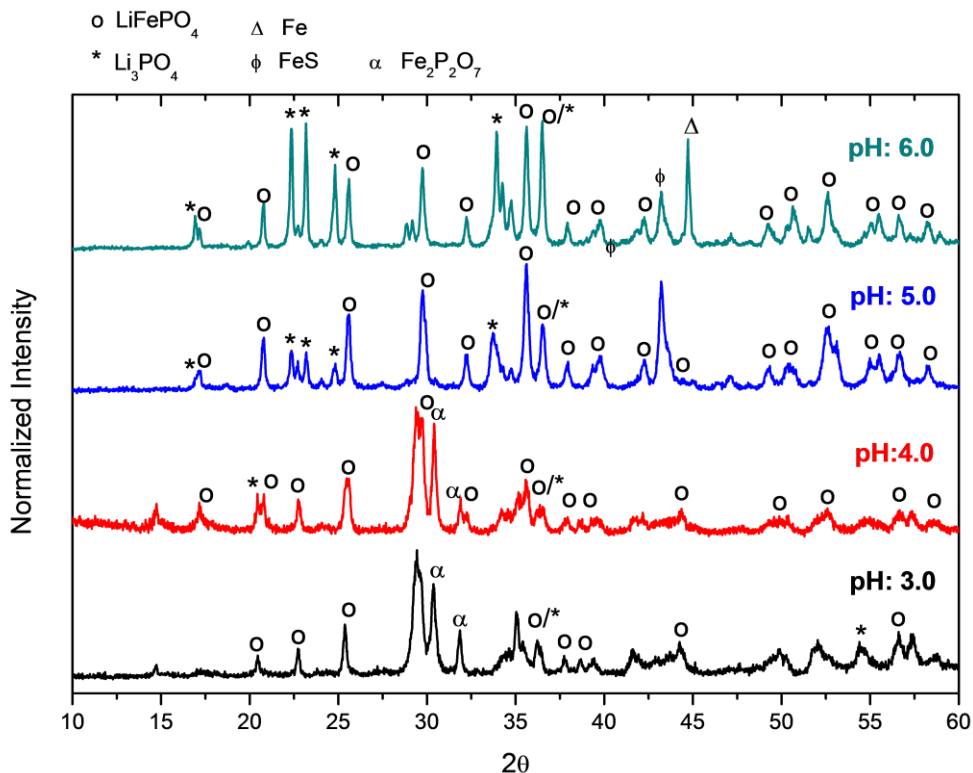


Figure 75. XRD patterns of calcined samples synthesized via US assisted sub-sequential precipitation at various pH values with 0.1M citric acid

Although citric acid can slightly increase the LFP production percentage, unfortunately it can diminish the solubility coefficient balance for LP and vivianite which is critically important to the sub-sequential precipitation strategy. It has strong affinity upon dissolved cations and increase the solubility and reaction rate which will become uncontrollable with US irradiation even in buffered pH around 5.0 - 6.0.

Within the pH region toward 4.0 to 5.0 the reactions occur easily but there is no control on size and morphology at all with citric acid addition. SEM image showing thicker crystals has proven this uncontrolled growth of bigger LFP crystals (Figure 71). The amorphization of dried samples before calcination, was caused by lower pH region and enhancing the solubility of Li_3PO_4 and vivianite species during precipitation. Fast reaction kinetics changes the solubility difference which alters the ordering and kinetic of the reactions between LP and FeSO_4 . Increased solubility has also detrimental effect on restricted mass transportation and increased the Li concentration above the limit that can directly react to form Li_2SO_4 precipitates. Beside its high solubility in water, it has unmatched monoclinic crystal structure and lattice parameters with

orthorhombic LFP instead of orthorhombic Li_3PO_4 . So Li_2SO_4 , with the highest melting point is not a good candidate for Li source especially in solid state reactions.

On the other hand, SEM image and EDX analysis indicate that thicker LFP formation which is probably caused by high mass solubilisation in locally high pH conditions because of chelating citric acid (Figure 70 and 71). Even in higher suspension pH adjustment (5.0 – 6.0) in order to maintain formation of $\text{Fe}_3(\text{PO}_4)_2 \cdot 8\text{H}_2\text{O}$, final calcined product has very large LFP crystals or agglomerated structures. This means that citric acid affects the solubility balance negatively which is essential in the US assisted synthesis.

As reaction time increases in the second precipitation, Fe reduction pursue towards to leave too much unreacted Fe crystals formation after calcination. XRD pattern in Figure 76 shows the increased peak of bcc iron. Under the influence of US irradiation the chelating effect of citric acid is enhanced but this inhibits the desired reaction by keeping iron source away from reactive crystallization of vivianite.

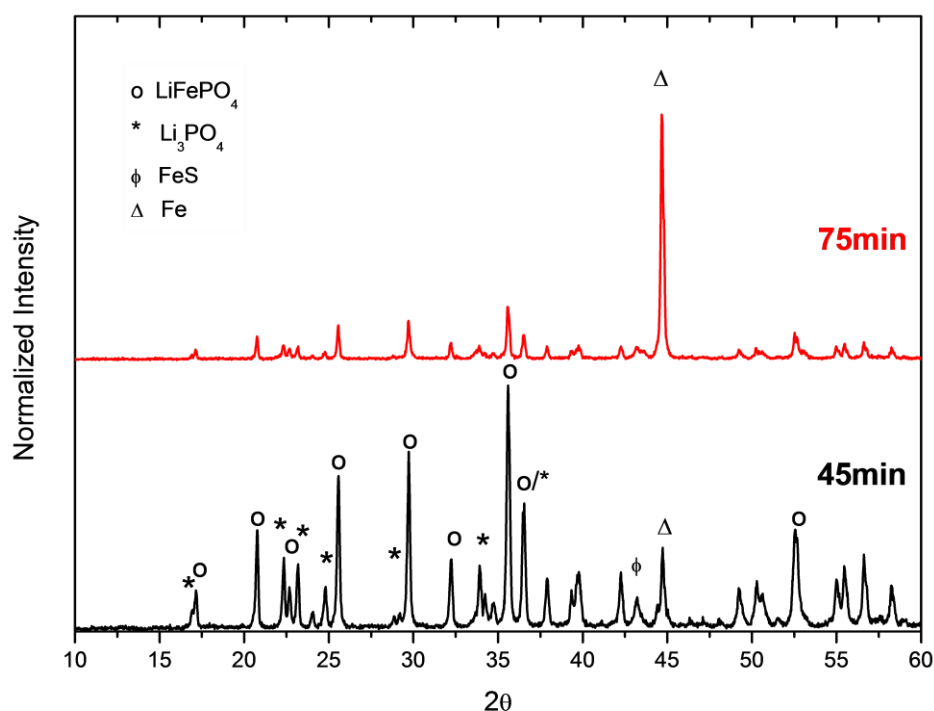


Figure 76. XRD patterns of synthesized LFP with 0.25M citric acid addition via US assisted sub-sequential precipitation within given reaction times.

Even under controlled pH between 5.0 and 6.0, citric acid addition causes tremendously reduced iron content to yield *bcc* ferrite crystallites after calcination step is over. This reaction is probably driven by FeS compound which readily reacts with reductive hydrogen by giving gasification of H₂S. So iron source remains as reduced to elemental crystallites.

Sonochemical synthesis has been used in synthesis of noble metal nanostructures by many researchers.^{122,123} For existence of US waves in aqua media, it is mentioned previously that US waves has a reductive effect on the ionic compound in solutions by sonochemically generated H radicals. In some cases organic additives such as iso propanol or surfactants, are used to form secondary radical species, which enhance the reduction rate. These reductive organic compounds, especially alcohols, transforms into attractive growth limiting surface active agents having high reactive OH· radical groups simulated by US waves.

Ethylene glycol is also used as a solvent to control the morphology of LFP in the literature.⁹⁷ In this synthesis route, ethylene glycol has been reported as chelating agent which has soft template properties. Using ethylene glycol results in bigger aggregate crystals having very low aspect ratio. The crystals which can be obtained as plate-like structures have also micron sized particles being very similar structure to LFP crystal shape reported by Richardson et al⁹⁶. This kind of coarse structures can be resulted by using excessive amount of ethylene glycol (40 wt.%).

In this study, ethylene glycol is used to be another surface active and growth limiting compound by enhancing its effects with US irradiation. Fe²⁺ phosphate content detected XRD analysis (after sub-sequential precipitation) shows that ethylene glycol act as a reducing and growth limiting agents stimulated by US wave irradiation. It is also possible to reach well distributed 50 – 100 nm thick nano plate crystals similar to insonated samples without ethylene glycol (Figure 78). The stoichiometric Li:Fe ratio was chosen as 3:1 and 1:1 for US an non US precipitations. However, it has been continued only with 3:1 for easy separation of precipitates by simple paper filtration to leave excess solid lithium source to be used about chemical lithiation in calcination step.

The addition of ethylene glycol is possible with two different additional and mixing sequences which are together with iron sulphate as solution or LP seeds as suspension. It is found that the mixing sequence has remarkable effect on the phase transformation during precipitation and calcination steps. Based on the chelating property of ethylene glycol, it can dissolve the Fe^{2+} ions when it is mixed with FeSO_4 as solution. In this case, iron ions are intensely surrounded by ethylene glycol molecules. It also acts as a strong chelating compound even after mixed with LP micro seed in the aqua suspension. This addition sequence has yielded excessive amount of Fe which can be described as 6-8 % wt. form its rising peak in XRD patterns around 2θ of 44.5 (Figure 77).

On the other hand the addition of ethylene glycol into the suspension of LP seeds results more homogeneous and thinner nano plate structures of iron (II) phosphates (vivianite) (Figure 78). Also in this route, the iron source is dissolved in water as uncaptured by EG which yields less amount Fe phase become unreacted instead of as dissolved in EG (Figure 77).

Regarding to the XRD patterns, it is found that EG addition with LP suspension yields low impurity (Figure 77-a) and plate like morphology where there is still polycrystalline structures within each platelet after calcination (Figure 81). Even though, vivianite precursor indicates high orientation in [010] together with narrow size distribution, synthesized LFP has weak preferred orientation around [010] direction (Figure 77-a and c).

Figure 79 represents the synthesized powders with EG addition and without US irradiation. Although higher temperature (90 °C) of suspension has been conducted with EG, it is not possible to initiate the phase transformation in precipitation which results in too low LFP formation even in high concentration of EG. In the non US assisted sub-sequential precipitation method, it is impossible to form LFP materials under normal atmospheric conditions. Even after 12 hours of hydrothermal treatment at elevated temperature (120 °C) very low amount of LFP formation is observed. In organic compound addition to control the crystallization, High temperature treatment is required (180 – 200 °C) which necessitates high pressure equipments. So in elevated temperatures, the growth and reaction kinetic become again unstable.

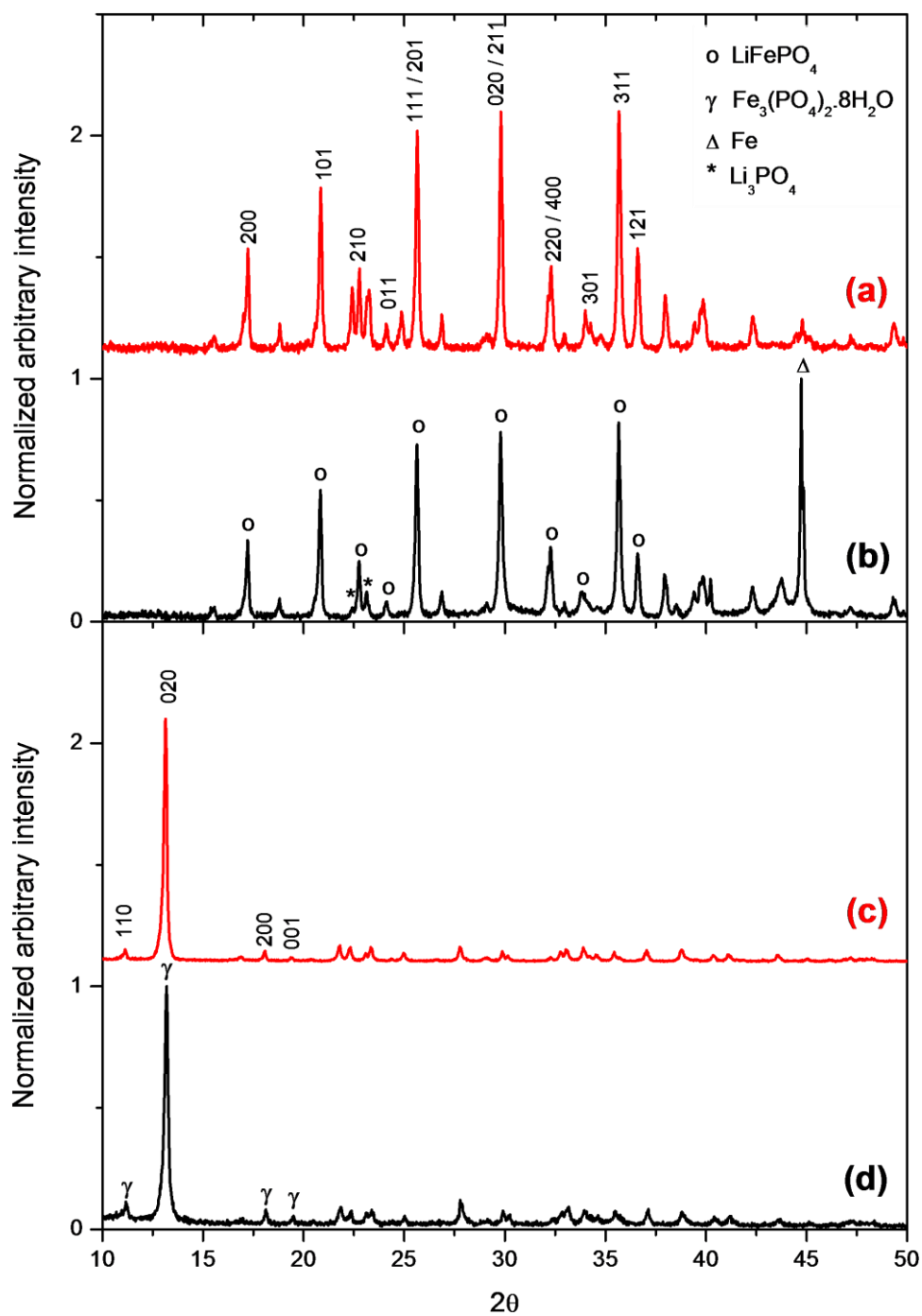


Figure 77. XRD patterns of cathode materials (a, b) as synthesized from precursors (c, d) with addition of EG to LP suspension (a, c) or FeSO_4 solution (b, d)

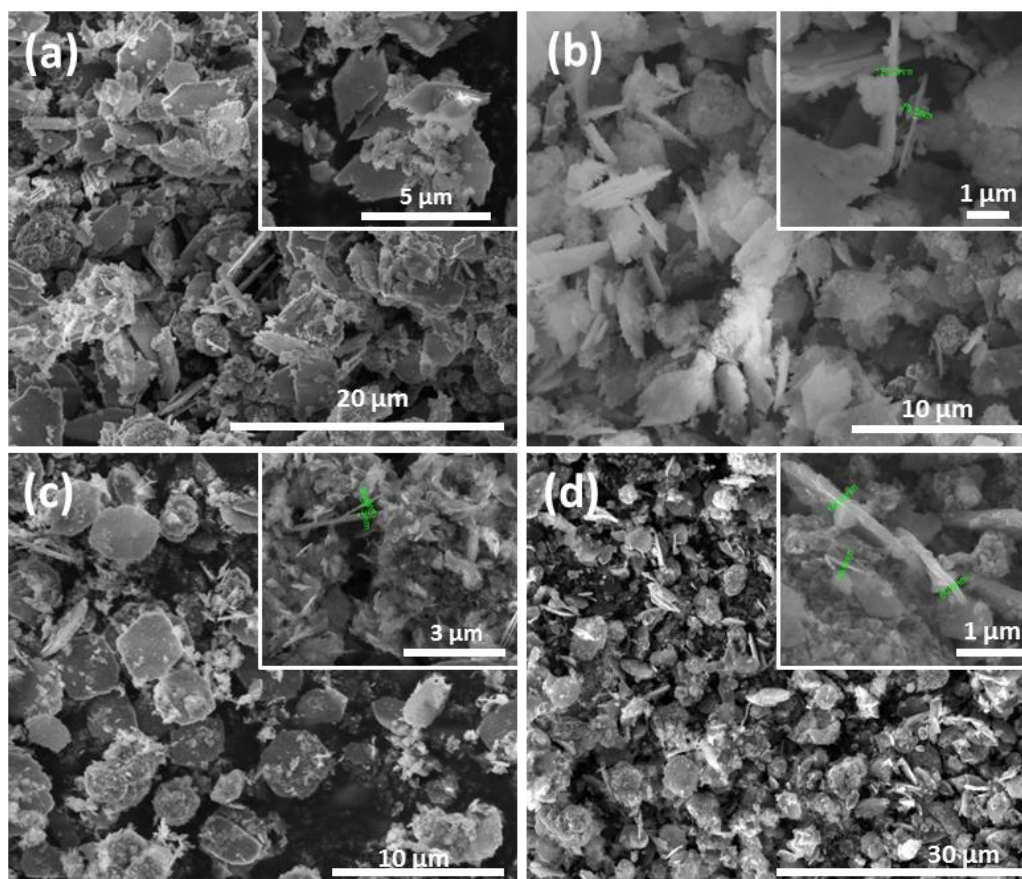


Figure 78. SEM images of US wave assisted precipitated vivianite nano-plates (a, c) and LFP cathode nano-plate (b, d) materials synthesized with addition of ethylene glycol into LP suspension (a, b) and FS solution (c, d).

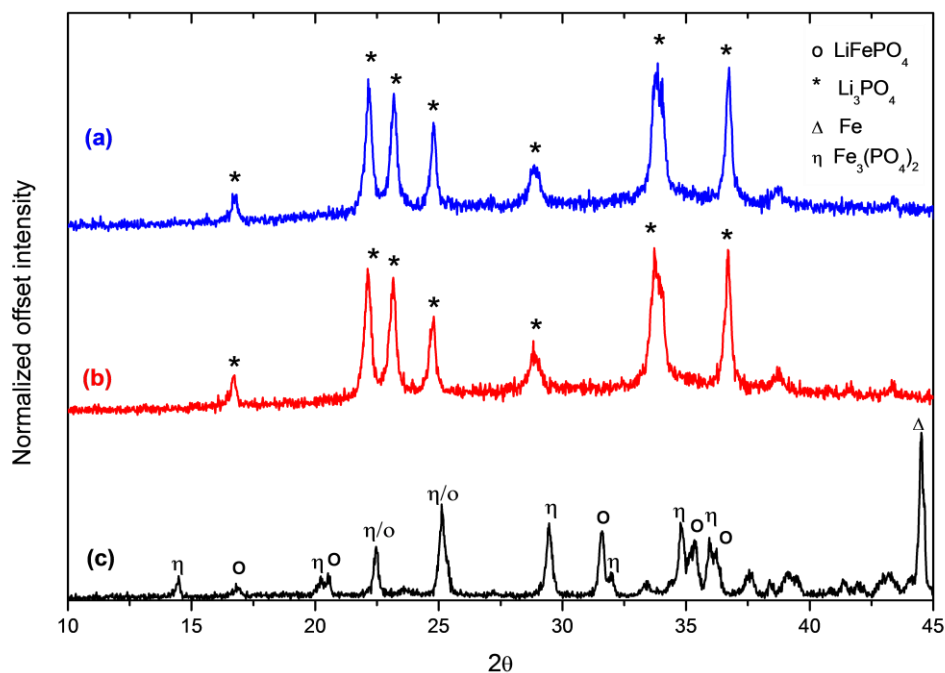


Figure 79. XRD patterns of calcined materials after sub-sequential precipitation with non-US synthesis with 20 wt.% (a), 40 wt.% (c) EG addition on FS and 20 wt.% (b) EG addition on LP sources

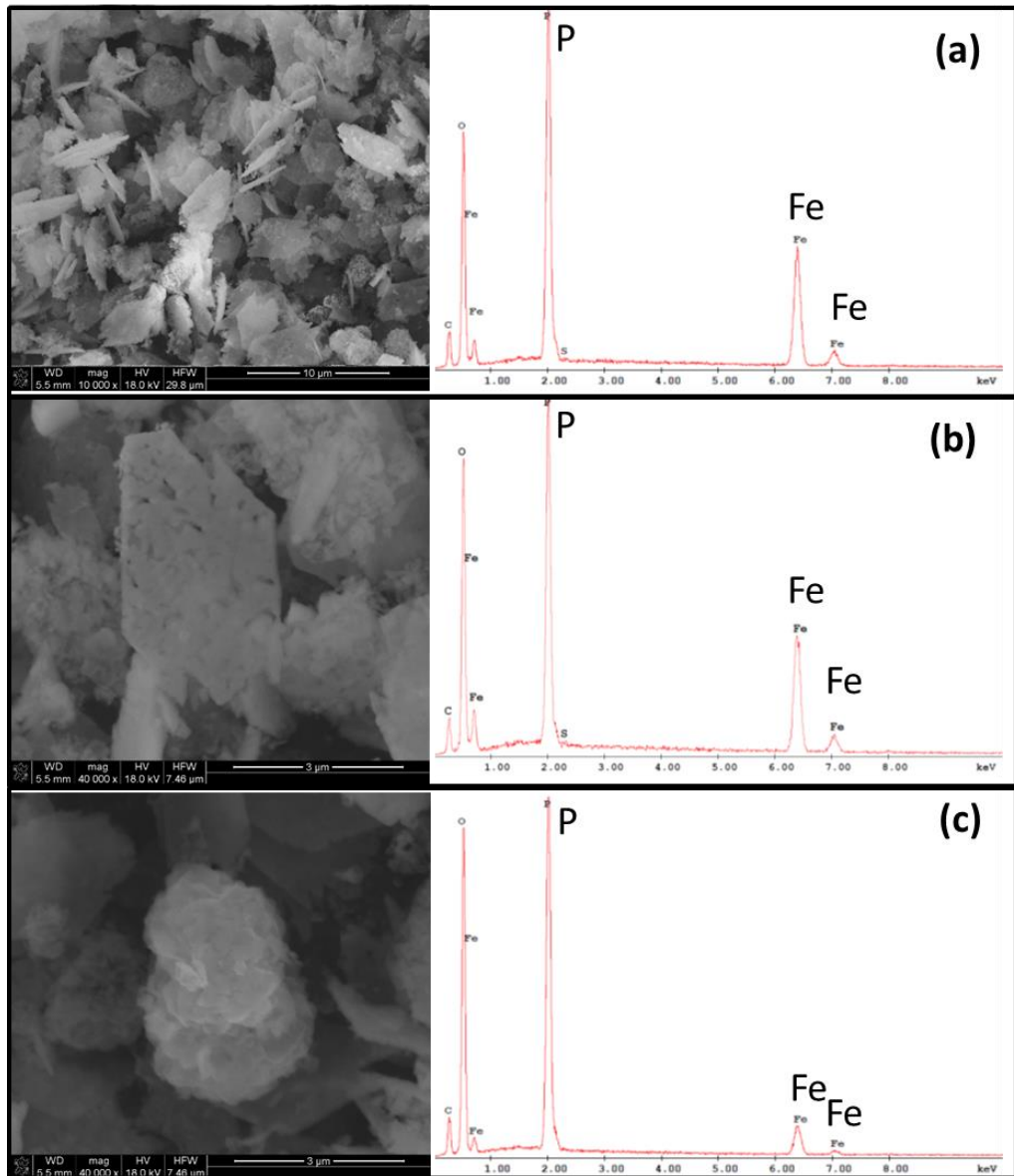


Figure 80. EDX point analysis related with the crystal morphology into the respective SEM images of cathode material with EG addition on LP suspension (LP and LFP crystals indicated with red and blue circles respectively)

Table 6. Elemental analysis results based on EDX for each crystals as referred in Figure 80.

	(a)		(b)		(c)			
Element	Wt%	At%	Element	Wt%	At%	Element	Wt%	At%
S	0.34	0.43	S	0.11	0.14	C	36.01	62.41
P	43.67	58.19	P	42.22	56.82	P	45.90	30.85
Fe	55.99	41.37	Fe	57.67	43.05	Fe	18.09	6.74

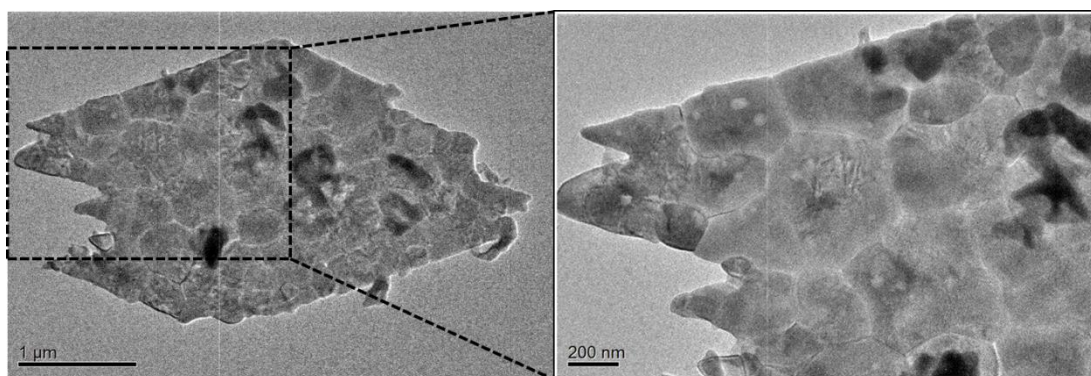


Figure 81. TEM images of polycrystalline LFP nano platelet as synthesized via US assisted sub-sequential precipitation with EG addition on LP suspension

4.3.2 Ultrasound assisted AFP nano-plates synthesis

Being similar with the first trial route of sub-sequential precipitation, there is another route to obtain intermittent crystal structure of $\text{NH}_4\text{FePO}_4 \cdot \text{H}_2\text{O}$ (AFP) by the precipitation reaction. In this new route, FeSO_4 and $\text{NH}_4\text{H}_2\text{PO}_4$ are used as starters for mixing instead of LiOH and $\text{NH}_4\text{H}_2\text{PO}_4$ to synthesize Li_3PO_4 .

AFP has a layered crystal structure including zig-zag layered NH_4 and H_2O molecules which allows lithium intercalation and ion exchange easily. AFP precursor phase has a proximity between Fe-P spatial configuration and lattice parameter in a direction to b direction, which are 5.684 and 6.006 Å, respectively, by transformation from AFP to LFP structure (Figure 82). In both unit cells FeO_6 octahedrons are similarly positioned according to PO_4 tetrahedrons. This transformation, in AFP route, is obviously understandable that one lattice axis may likely be transformed to the closest one in length. Phase transformation occurs especially via an ion exchange stoichiometry (Li^+ insertion with extraction with NH_4^+) between $(\text{NH}_4)\text{FePO}_4 \cdot \text{H}_2\text{O}$ to LiFePO_4 .

Besides, this orientation shows structural proximity between AFP and LFP especially in a (5.684 Å) and b (6.006 Å) lattice of them,¹²⁴ respectively which can be reduced after deformation effect of high temperature calcination on crystal morphology above 500 °C. Lithium acetate yields much [100] orientated LFP crystals as it seems to preserve the morphology with carbonaceous acetate ions adsorbed on surface just before lithium insertion.

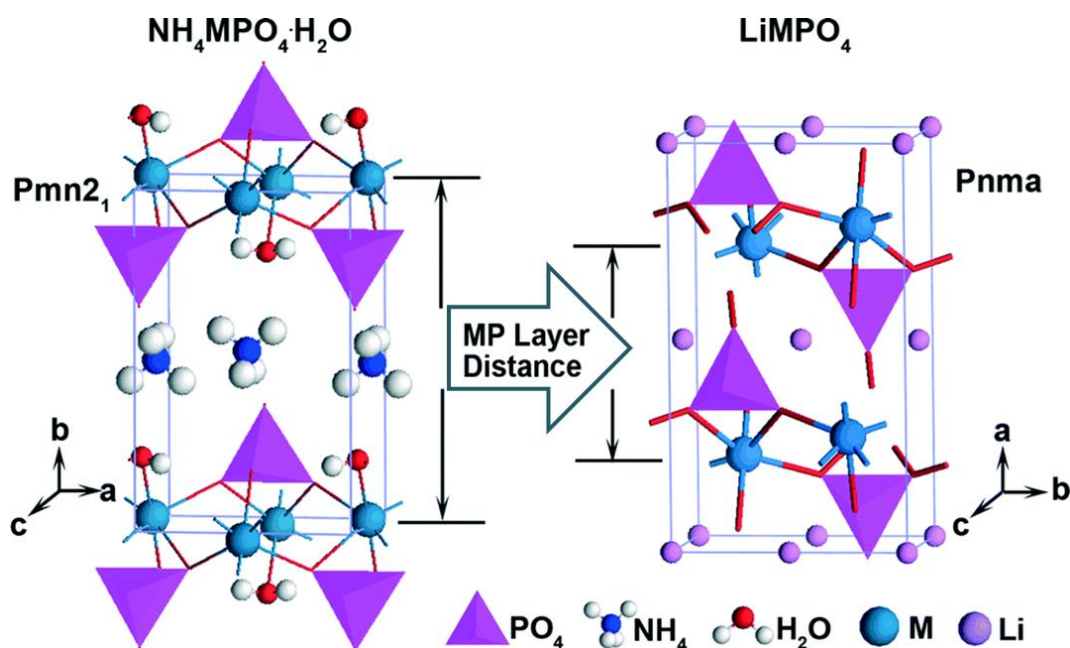


Figure 82. Crystal structure of AFP and LFP as given transformation on crystallographic axes.¹²⁴

Neutral to basic pH region (7 – 9) was tried to optimize the stable pH region which is necessary to form nano plate like structures. Precipitation steps are performed either with US irradiation or not. Although it is also possible to synthesize layered AFP structure with non US route, US has again an accelerating effect on formation and ion exchange reaction of precursor structure. So Li source addition and ion exchange reactions can be enhanced with the existence of US. In the first step $\text{NH}_4\text{FePO}_4\cdot\text{H}_2\text{O}$ precipitate shows very strong anisotropy having the thinnest dimension through the $[010]$ (b axis) direction, detected by strong preferred orientation through increased (010) peak intensity in the XRD analysis of the precipitated sample (Figure 84).

Although there is little crystallization effect of AFP as a layered and oriented structure, US wave can refine the dimension in b direction as 2 to 3 times lower in thickness. SEM images in Figure 83, and Figure 84 show the plate-like structures having thicknesses lower than 50 nm synthesized with US irradiation during precipitation.

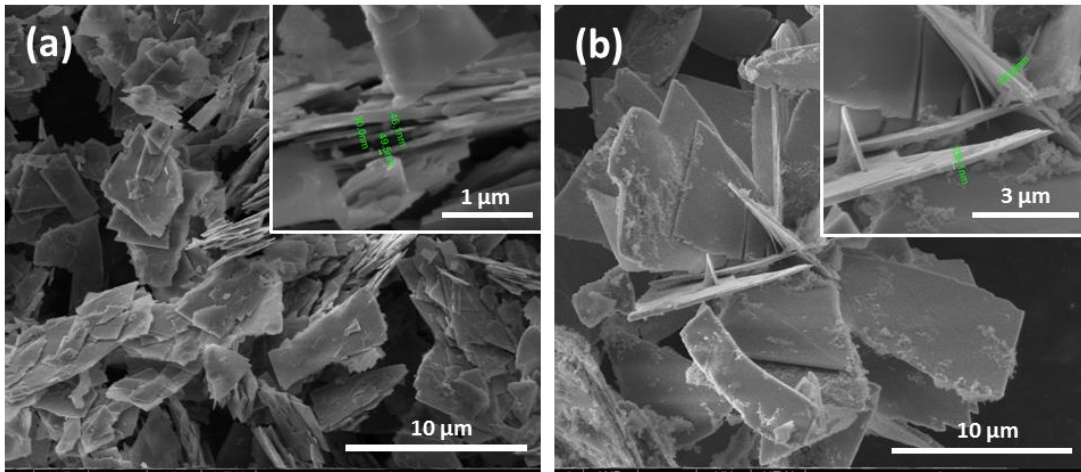


Figure 83. SEM images of $\text{NH}_4\text{FePO}_4 \cdot \text{H}_2\text{O}$ nano-plate structures synthesized with (a) and without (b) US wave irradiation

There is distinguishable preferred orientation on [100] direction which is decreasing with pulverization. Lithiation compounds strongly cause this anisotropic change during high temperature lithium insertion (Figure 85). Primarily Li^+ diffusion is incorporated with lithium compound adsorption into the particle. The rest anionic parts of this compounds have crucial role on Li^+ exchange or insertion following the adsorption and dissociation reaction onto the surface of nano plate.

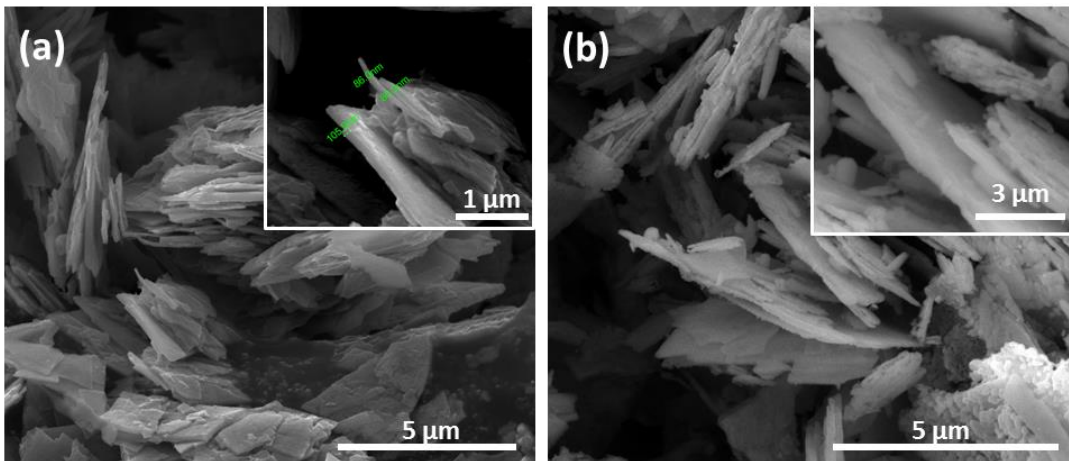


Figure 84. SEM images of LFP nano-plate structures synthesized with various lithiation compound as lithium acetate (a) and lithium hydroxide (b) via US assisted sub-sequential AFP route.

In spite of preferred orientation in [100] crystallographic direction of final cathode structure, the higher capacities (Figure 104 in section 4.4) are achievable for AFP route nano-plate structures in slow currents. Lithium acetate has played an important role for preserving anisotropy of crystallographic orientation of LFP crystals as exposing

bc plane on the surface. By transforming to LiFePO_4 , nano sheets have remained in similar size and shapes. So it can be said that nano-sheets transform by ion exchange rather than intercalation of lithium ions. AFP have same stoichiometric formulation comparing with LiFePO_4 compound and this makes the ion exchange mechanism essential. Although the exact mechanism of orientation ordering effect of lithium acetate to lithium hydroxide is still not clear, lower acidity of lithium acetate might provide less destruction effect on $\text{NH}_4\text{FePO}_4\cdot\text{H}_2\text{O}$ nano-sheets during lithium insertion. Further investigations need to be done to clarify the exact transformation kinetic of LiFePO_4 synthesized with the help of $\text{NH}_4\text{FePO}_4\cdot\text{H}_2\text{O}$.

Lithiation was done by using various water soluble compounds via impregnation and the saturation method. In the calcination after surface adsorption on AFP, lithium ions form and insert through the inner parts of the crystal structure to transform into LFP platelets. So lithiation compounds determine the final crystalline morphology. In-situ XRD studies was conducted to better understand the orientation changes. The in-situ XRD patterns reveal that [100] orientation remains same up to 500 °C in lithium hydroxide (LH) and lithium nitrate (LN) usage (Figure 86). Lithium acetate yields more crystalline product based on XRD patterns showing the indication of early [100] orientation even in 300 °C. After temperature passed 500 °C during calcination, a significant drop on [100] preferred orientation is observed for all lithiation compound use (Figure 85). This effect is related with increased morphology destruction appears especially after 500 °C.

More preserved LFP plate morphology is observed in lithium acetate (LAc) used sample (Figure 86). Due to its low melting point (286 °C) adsorbed acetate anion forms into a well distributed surface film on the particle to be preserved at elevated temperature by forming carbonaceous remnant of acetate part. As crystal deformation degree increases, the anisotropy disappears in an order of LiAc, LH, and LN compounds usage. Regardless of the lower melting point of LN (255 °C), it is very oxidative within thermal decomposition products such as Li_2O and O_2 after 500 °C. Even though calcination takes place in reductive atmosphere, this decomposition can have some detrimental effect not only on ammonium iron (II) phosphate crystals but also on lithium insertion itself. Thus, it appropriately explains how the [100] orientation drops distinctively after 500 °C.

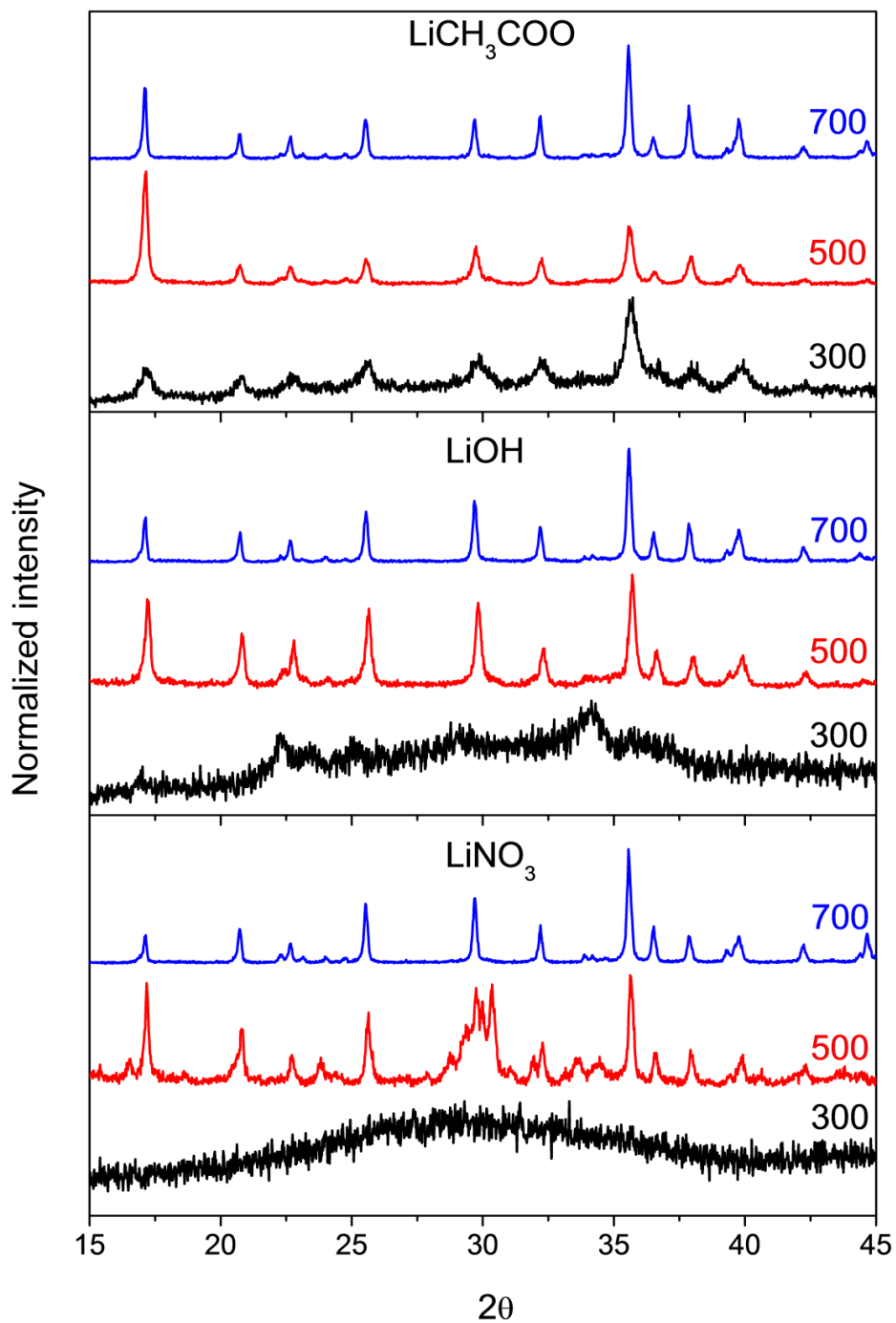


Figure 85. In-situ XRD patterns from samples calcined at various temperatures using different lithiation sources via US treatment of $\text{NH}_4\text{FePO}_4 \cdot \text{H}_2\text{O}$

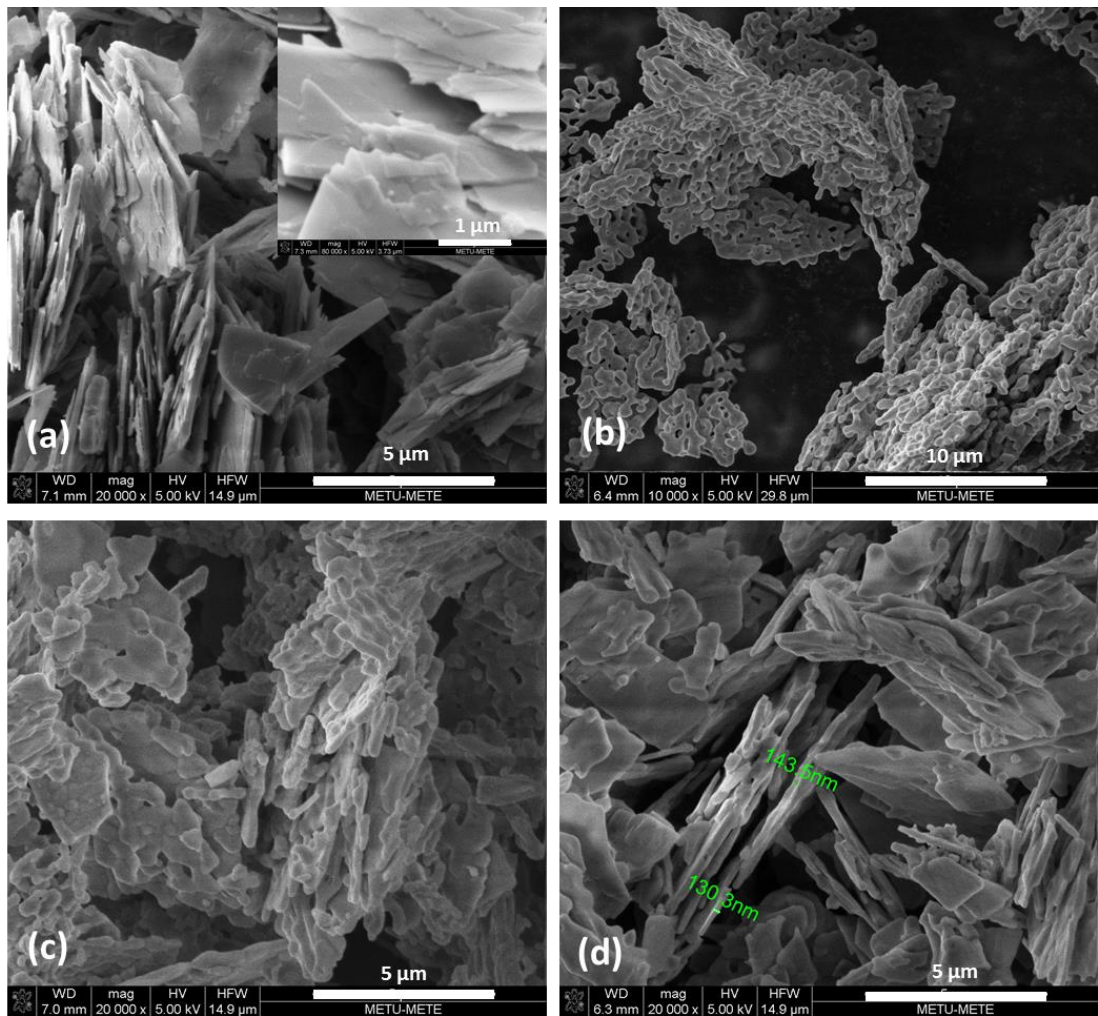


Figure 86. SEM images of AFP (a) and LFP (b, c, d) nano plates synthesized with calcination at 700°C after lithium nitrate (b), lithium hydroxide (c) and lithium acetate (d) solution impregnation.

4.3.3 Optimization of encapsulation strategy and carbon coating during calcination

Carbon coating has a critical role on the performance of LiFePO_4 cathode materials because of its poor electric conductivity. In order to overcome the lack of electronic motion, conductive coating is widely used such as carbonization of organic salts. Sugar based organic compounds are widely used for conductive cathode composite synthesis as subjected in solid state pyrolytic carbonization.^{125–127} Sucrose is melting around 150 °C and higher temperatures in accordance with lack of addition of mineral salts to recrystallization process during its production.¹²⁸ It can be carbonized in an inert atmosphere in elevated temperature (250 – 300 °C) by leaving pyrolytic carbon layer behind. The key point in carbon coating is the thickness. It must be as thin as possible and permeable to allow lithium ion from the solution penetrating to reach the LiFePO_4 particle surface without any resistance.

In order to achieve thin nano-plate structures even after the transformation of vivianite crystals to LFP crystallites, the temperature effect has been investigated on phase transformation, crystallization and structural deformation of particles. It is observed that crystals can stand firm even after calcination at 500 °C without any encapsulation with carbon. However at low temperatures, undesired site occupancy increases between Fe and Li atoms in the crystal structure of LFP. Higher defect and disordering density is going to be an obstacle for Li ions kept away from free to move into channels during insertion and extraction.

Samples were subjected to the calcination at temperatures of 500 °C and 700 °C under slightly reductive atmosphere to explore the effect of annealing temperature on both crystallinity and morphology. XRD patterns indicate that there is sufficient LiFePO_4 formation with low crystallinity at the temperature of 500 °C and the shape of the crystals can be mostly preserved without sucrose addition, indeed (Figure 87). However severe sub-grain formations can be observed after calcination at both 500 °C and 700 °C. (Figure 88) and orientation is distributed.

Despite preserving the crystal shape after calcination at 500 °C, the complete crystallization could not be obtained and there is still high disordering in the synthesized material. For that purpose, sucrose saturation seems to be a sufficient way

for the encapsulation process that could survive at temperature as high as 700 °C. Moreover, XRD patterns of calcined samples at 700 °C clearly indicate the presence of LiFePO₄ compound. Regarding to these patterns, more than 90% of the product was composed of LiFePO₄. The rest of the product impurities are mostly iron sulfide and phosphate phases.

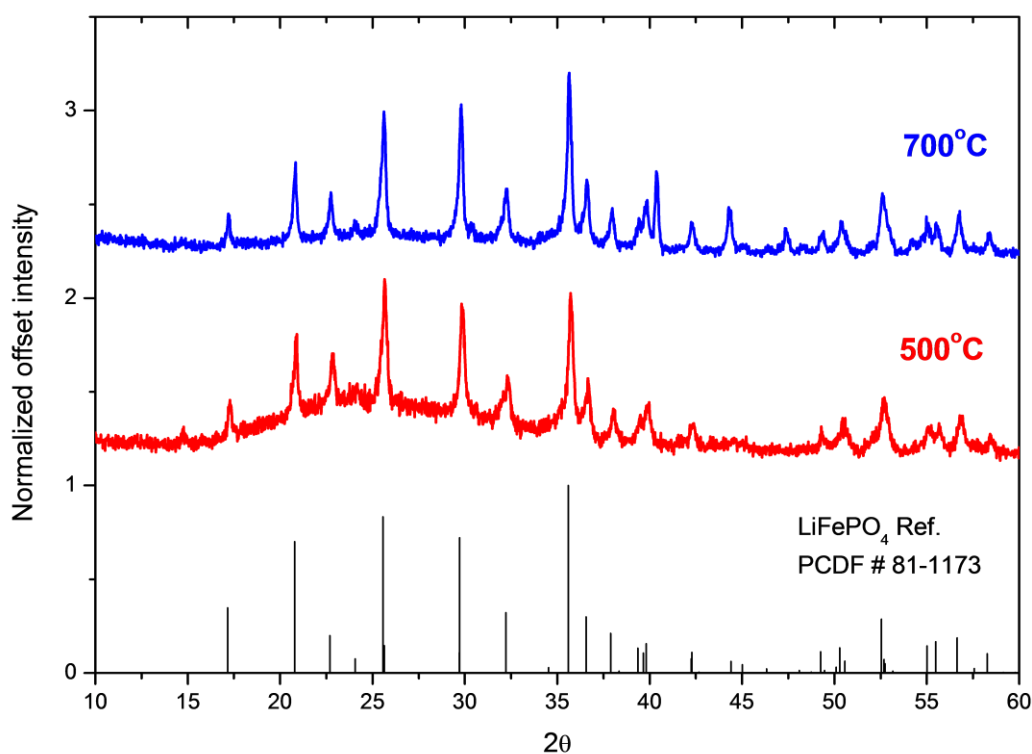


Figure 87. XRD patterns of nano-plate LFP cathodes calcined at different temperatures with sucrose carbonization.

Carbonization of simple sugars such as glucose and sucrose is widely used to create carbon layers on inorganic structures^{51,129} which is possibly processed at 400 °C under an inert gas flow. Besides being crucial for electrical conductivity, in this thesis, carbon coating is also used for the preservation of the crystals in the shape which can be formed in the second precipitation step. As calcined LiFePO₄ nano plate structures are presented in Figure 88 shows the effect of sucrose adsorption. It is also playing an important role on supplying reductive atmosphere during calcination by depositing sufficient carbon layer.

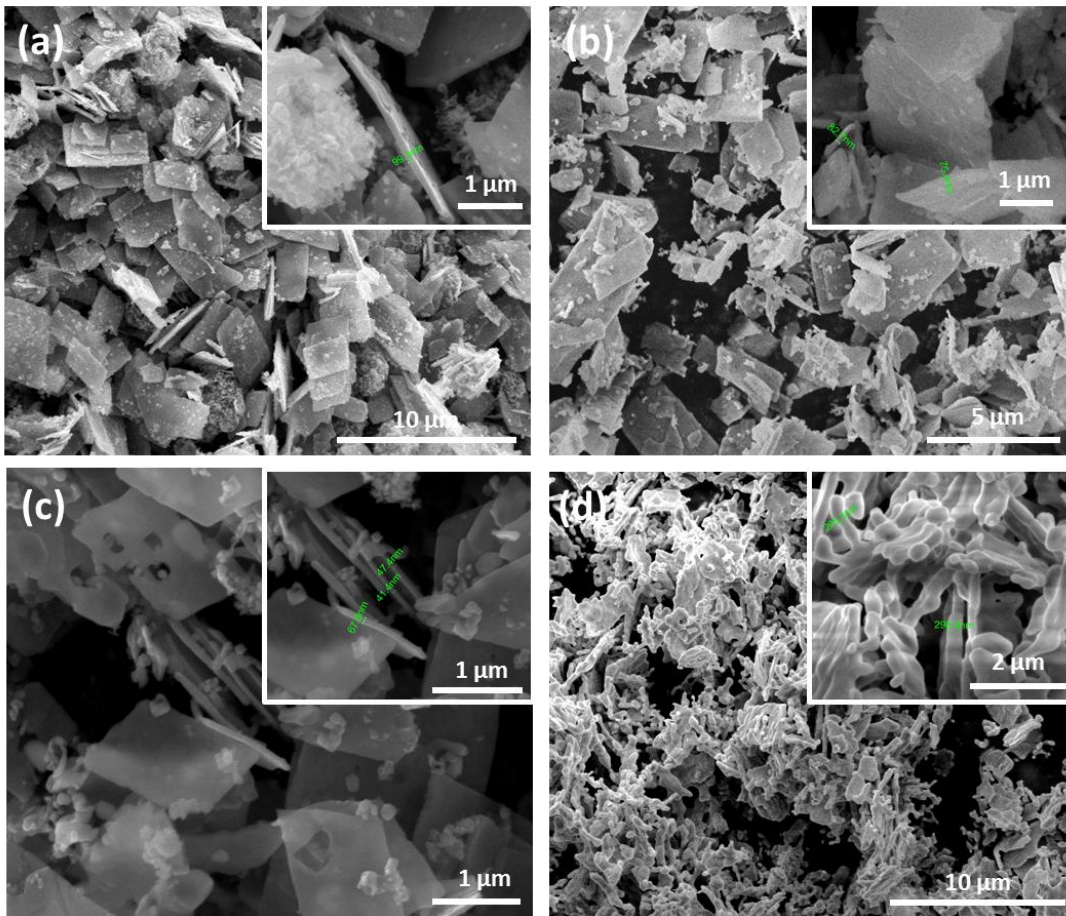


Figure 88. SEM images of synthesized LFP materials at 500 °C (a, b) and 700 °C (c, d) with (a, c) and without (b, d) sucrose carbonization

XRD analysis was performed and compared with samples calcined without sucrose presence to better understand the crystal structure of calcined samples with sucrose saturation. It is found that XRD peaks of calcined samples with sucrose are more broadened after calcination at 700 °C than without sucrose. This broadening points out that the phase transformation is accomplished while keeping the nano-plates as refined in thickness by sucrose saturation method (Figure 89).

Sucrose encapsulation strategy was successfully performed on the samples not only for carbon coating but also for prevention from oxidation with carbon coverage. Shape and morphology control during metamorphological transformation can be realized by the impregnation and drying into sucrose solutions. However, having carbon coating on surface is not enough to get high performance from cathode material. Thickness of

carbon coating should be optimized resulting high electrical and ionic (Li^+) conductivity after synthesis of LiFePO_4/C cathode material.

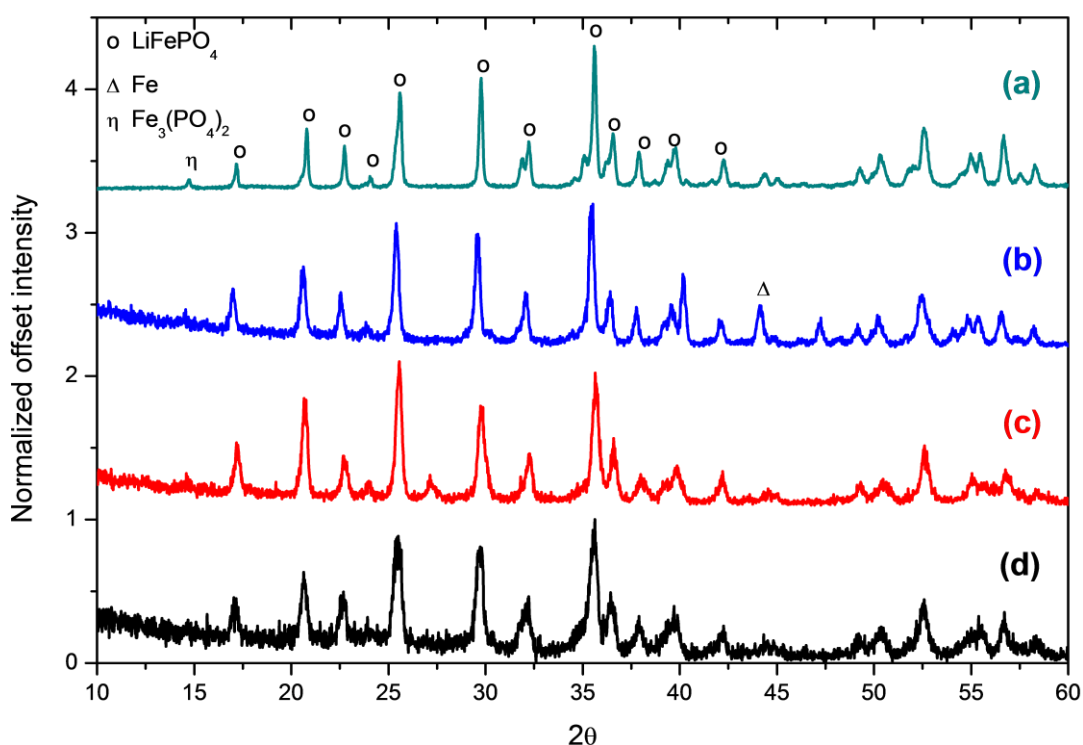


Figure 89. XRD patterns of samples calcined at 500 °C (a, b) and 700 °C (c, d); with (b, d) and without (a, c) sucrose (S) saturation

Excessive carbon presence on the surface of particle can be an obstacle for the ionic conductivity and it should be finely tuned for appropriate percentage to have thin as permeable layer. The thickness of carbon coating strongly depends on the surface area of precursor structure. So, in this thesis, this coating procedure has been optimized by observing electrochemical capacity measurement of encapsulated nano plate cathode structures in button cell with different amount of carbon content.

At first optimization of carbon coating procedure has been refined in case of the reliable electrochemical performance. Then the required amount of carbon has been studied by measuring the electrochemical performance of first prototype batteries having 12, 5 and 2 wt.% of cathode materials. When samples with these carbon content percentage are compared, it is found that 2% wt carbon content of active mass would be conductive enough without further passivation loss of capacity (Figure 90).

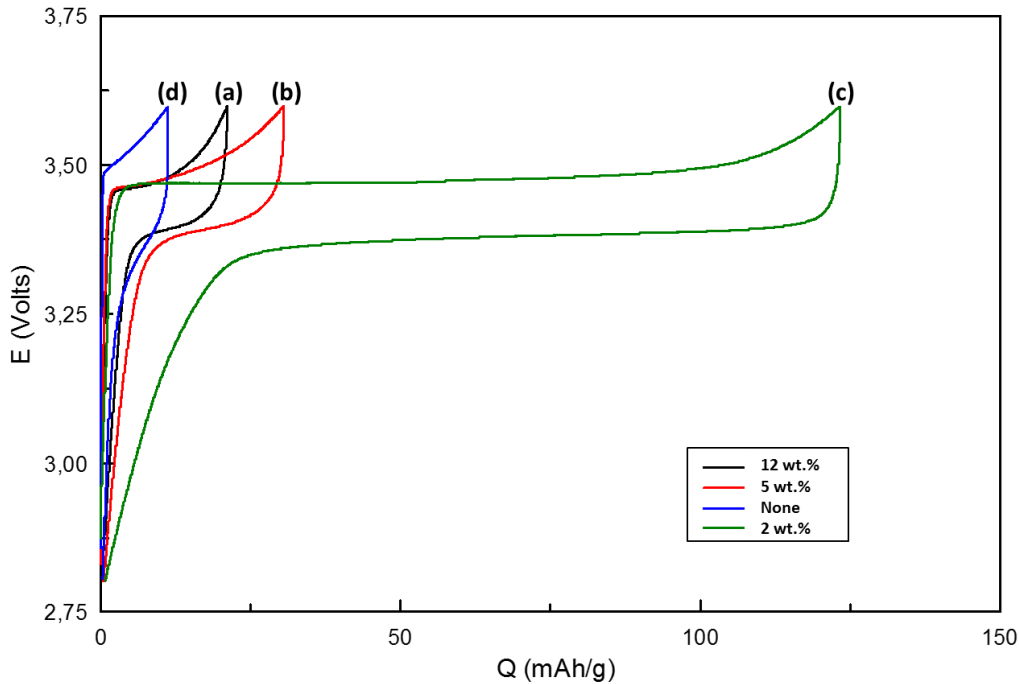


Figure 90. Electrochemical charge/discharge curves of 12 wt.% (a), 5 wt.% (b), 2 wt.%, and 0 wt.% carbon coated LiFePO₄ cathodes at 0.1C rate

The carbon coating is detected in the first trial of encapsulation strategy with the excessive amount of sucrose saturation giving up to 30 nm thick carbon layer with 12wt.% carbon content in cathode material. After proven examples of morphology controlled synthesis of LiFePO₄ nano plate with reduced (1-2 wt. %) carbon content, carbon coating thickness is found at optimum range around 5 – 10 nm thickness. Furthermore, enough electrical conductivity without further resistance for Li⁺ ions was also achieved with 1-2 wt. % carbon (Figure 91-b and c). Besides, this amount is still able to give preservation of crystal shape and structure by suppressing the further growth and shape destruction.

Two more different carbonization methods have been tried to enhance electronic flow between particles which are Carbon vapor deposition (CVD) and EG addition. CVD is known as pyrolytic deposition onto substrate surface. In this method, it is also possible to add the organic material before the calcination step. The water soluble material can easily be implemented by dissolving within an aqua suspension of material and vacuum drying right before the calcination step.

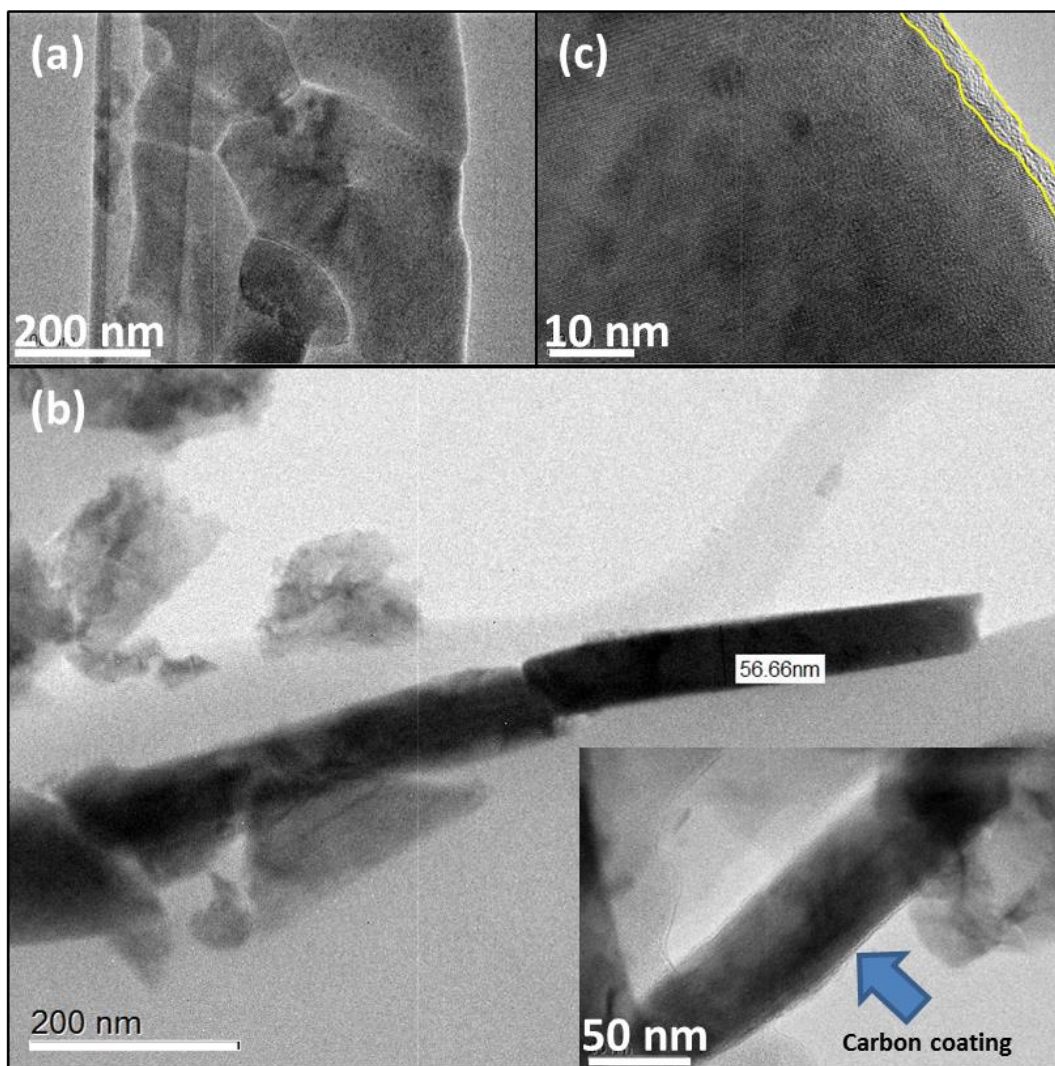


Figure 91. TEM images of encapsulated LiFePO_4 cathode particles with grain structures (a) and a cross section view from thinnest edge (b) encapsulated with sucrose saturated carbon coating (b, c) after calcination process

In the third method, EG was used as a solution based addition as explained previously in section 4.3.1.6. EG addition yields an organic residue after drying and these residue was carbonized in calcination step. These three different carbon coating method has been investigated by Raman spectroscopy to better understand the carbon coating type. Moreover, these samples are also subjected to electrochemical cycle test to obtain more information about their conductivities and discharged capacities of coated cathodes.

In Raman spectroscopy, there are two characteristic peaks of carbon which are called as D and G band modes around 1350 and 1630 cm^{-1} wavelength, respectively. The intensity ratio of these two bands provides information about the graphitic structure of

carbon. According to the Raman spectrum in Figure 92, graphitic carbon bands, which have less charge transfer resistance against electronic motion (Figure 93), are the highest for the cathode material carbonized with CVD method. This is followed by sucrose saturation method. PO_4^{3-} bands appear in all samples which shows that carbon coating thickness of all samples are less than 30 nm as their detectable limit of depth in Raman spectroscopy. To have better information about the graphitization degree of carbon coating, D and G bands are deconvoluted according to the Lorentzian curve. Although the calculated D/G intensity ratios are similar for all methods, the highest D/G ratio is given in CVD method (Table 7). By comparing the D and G bands of all samples coated with different methods, it is concluded that the higher graphitic structure and higher electronic conductivity is achieved via CVD method (Table 7).

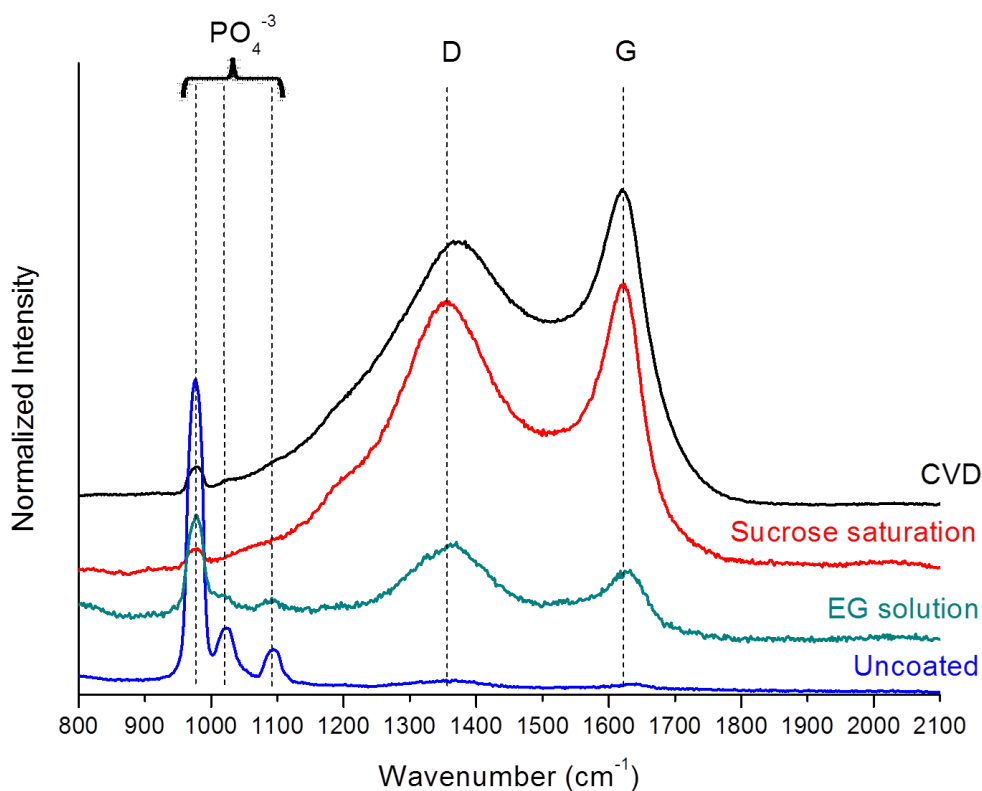


Figure 92. Raman spectrum from multiple cathode materials non-coated and coated by using CVD, sucrose saturation and EG solution method.

Table 7. D/G band area ratio of cathodes coated with different methods.

Sample	A(D/G)	I(PO ₄ /(D/G))
Uncoated	N/A	27.67
EG	2.82	0.73
Sucrose saturation	2.57	0.08
CVD	2.17	0.07

The effect of carbon coating method on conductivity of samples coated with different methods is analyzed via EIS (Figure 93). Even in CVD of toluene vapor could have lower charge transfer resistance than sucrose saturation, sucrose saturation method could stand and give sustainable performance after 40 cycles (Figure 94).

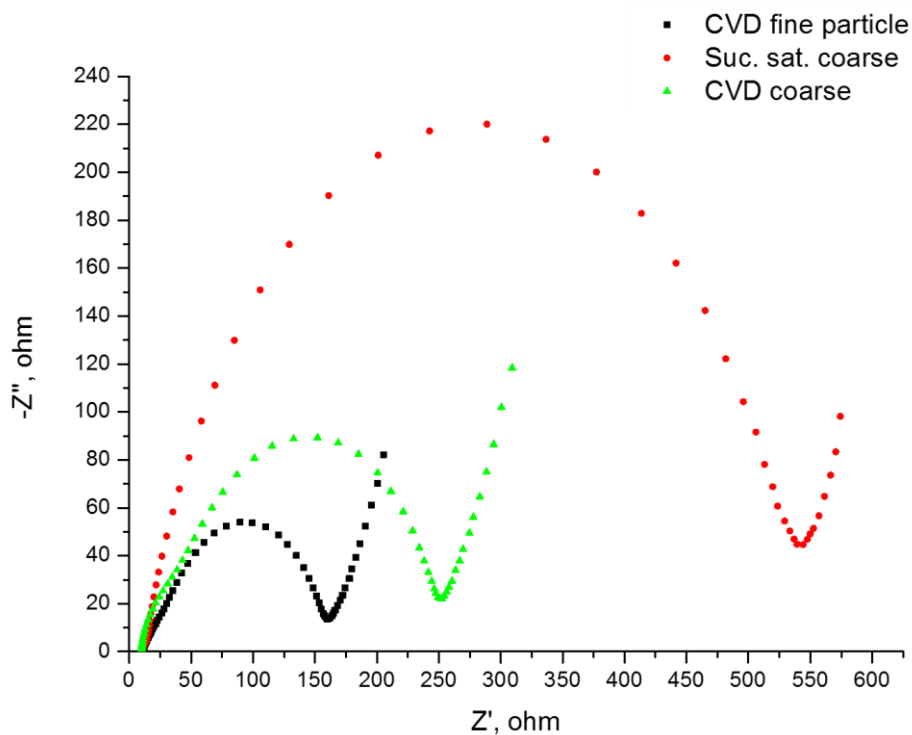


Figure 93. EIS analysis of cathodes synthesized with US assisted VVT route as coated fine and coarse particles with CVD and sucrose saturation (suc. sat.) methods

Resulted carbon coating has to be enduring enough against detaching from the surface of the particles by high currents in the case of high power applications. Charge and discharge tests providing some prediction about coating durability were performed in the button cell against lithium anode material (Figure 94).

The discharging rate has been slightly increased within each 5 cycles. Although the highest initial capacity was achieved in CVD coating that could be explained by high portion of graphitic layers, the sucrose saturation is the last long after several charge and discharge cycles. In addition to poor reliability in cycling, insufficient encapsulation was detected from SEM images of coated cathode materials synthesized with CVD method (Figure 95).

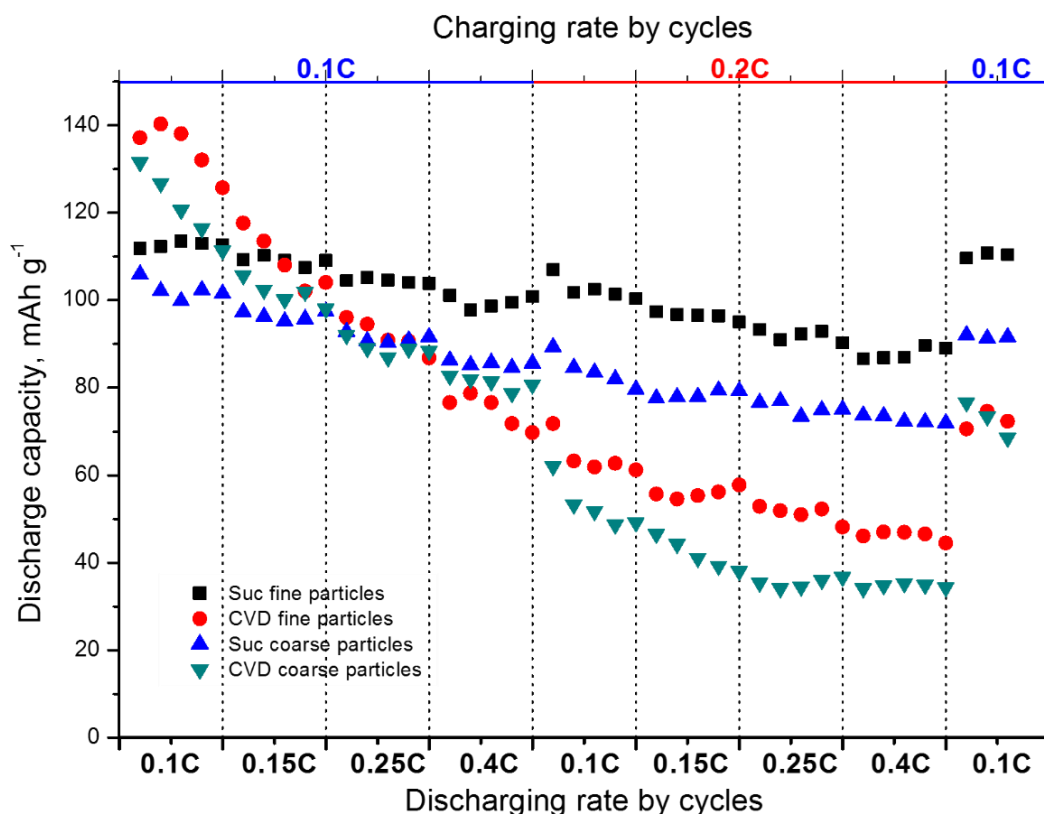


Figure 94. Electrochemical performance test of carbon coated cathode materials via CVD or sucrose saturation (Suc) method

In spite of good initial performance (140.3 mAh g^{-1} at 0.1C cycling rate) in CVD procedure, as coherent with its best graphitization rate. There is almost 50% capacity loss in few cycles. This poor performance can be explained by carbon layer detachment.

Consequently, with the help of sucrose saturation, very reliable capacity is obtained like around 97.5 and 86.9 %, for fine and coarse particles, respectively. Moreover, since its enduring coating layer, particle size effect on capacity retention seems to become more perceptible in last cycles. This points out that the particle size becomes more limiting factor if coating quality is enhanced. On the contrary, because of its poor

capacity retention around 54.4 and 55.8 % for fine and coarse particles, respectively, CVD process has not been chosen to go further investigation in this thesis (Figure 94). Despite this thin carbon coating seems to have more graphitic content, it seems easily detachable from the cathode surface along the harsh electrochemical cycling. Whereas, the reliable coating is more important than peak capacities to maintain resistivity as same as it is along the test cycles, the sucrose saturation has adapted as standard method for all US treated or not treated cathode materials. But the highest initial capacities makes it clear to lead to reach more utilization capacities likewise.

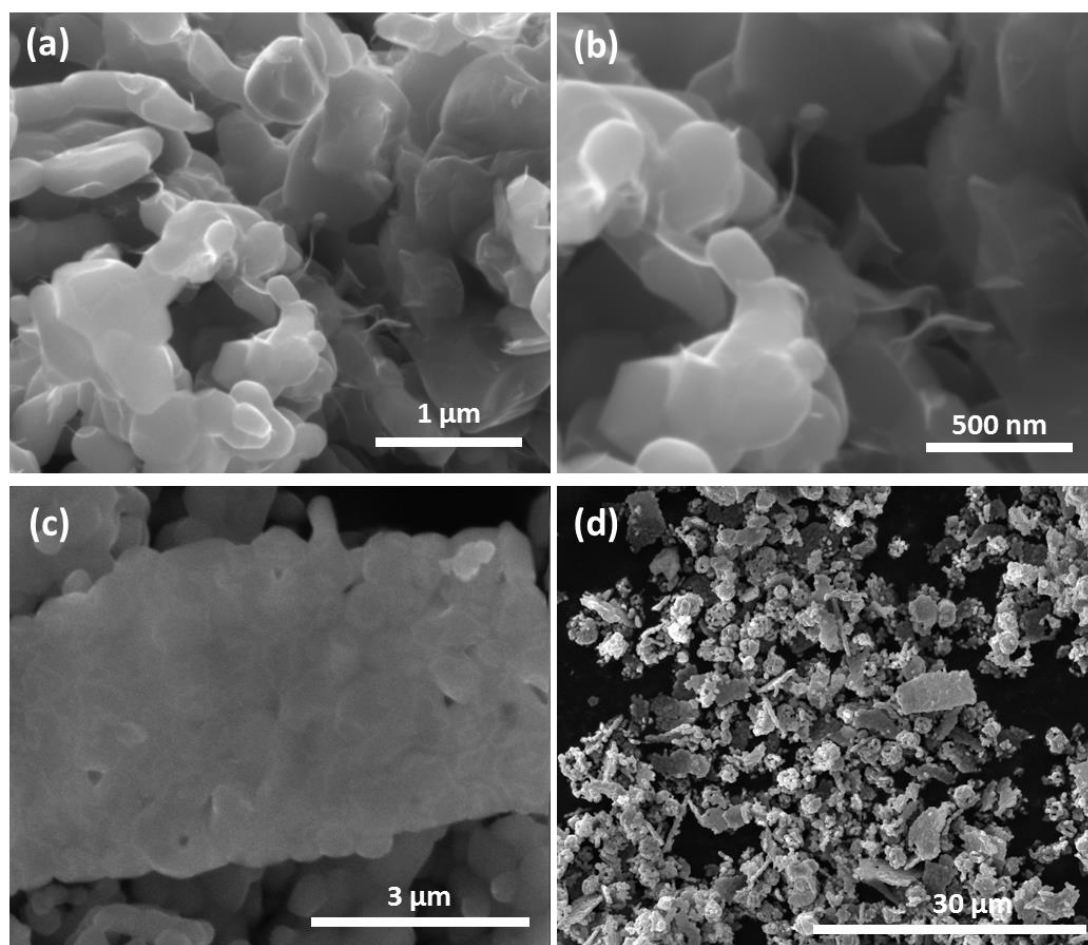


Figure 95. SEM images of carbon coated fine (a, b) and coarse (c, d) LFP cathode particles by CVD

LiFePO_4/C composite materials could achieve high final crystallinity, however solution based additives do not give sufficient carbon coating alone (Figure 92) in order to gain enough conductivity. Therefore, the saturation of sugar based carbon coating method was applied, additionally. Further investigation on electrochemical characterization of cathode materials are going to be needed to see performance in

battery application. Growth limiting effect of ethylene glycol is examined regarding to both addition onto Li_3PO_4 suspension and Fe source solution in section 4.4.

In our case of metamorphological production of nano structured LFP cathodes, to stabilize the structure of nano-plates as synthesized in precipitation right before the calcination step, LFP nano plates must be covered with sufficient carbon layer onto these intermittent crystals. The meta-stable effect of carbonaceous materials can be seen having strong preservative for shape morphology and the well conductor layer itself after carbonization process in calcination step.

EDX analysis was performed to define the impurities on nano plate structures synthesized via US-US sub-sequential precipitation. EDX analysis shows the presence of high contrast tiny crystallites located around the LFP plates. EDX mapping analysis confirms that smaller crystallites are made up with iron. The morphological properties of these crystals are seen in point EDX data on that particle (Figure 96-I and II). Furthermore, Fe residue was detected as 5-10% by Rietveld analysis from XRD patterns.

Unique diamond shape nano-plate LFP crystals can be detected from mutual signals of Fe, P elements coming from platelets. Reduced *bcc* Fe crystals can be seen in Figure 96-I. These Fe residue crystals have well-shaped mineral morphology which are frequently seen on the surface nano-plate LFP particles. The excessive regional Fe^{2+} might be extracted from vivianite crystals transforming to LFP crystals. The α -iron residue can also be detected as its *bcc* form by XRD analysis.

Some reduction impurities like iron phosphides has been also reported by other researchers especially for calcination in reductive environments.⁹⁹ Iron phosphide formation is explained as forming in the case of lithium deficiency. But in our case reduced *bcc* iron crystals are widely detected as seen on SEM images which may be explained with another formation mechanism since there is sufficient amount lithium delivery.

In the calcination step, plate like structures have lithium ion incorporated phase transformation from vivianite to lithium iron phosphate crystals by solid state reactions. Together with the exact mechanism lying beneath the ferrite (α -iron) formation is still not clear, but it may be explained by the extraction from transforming

vivianite crystals to LiFePO_4 form. Because of the limited mass transport for encapsulated plate like particles, only lithium ion can move freely and intercalate into the vivianite crystals in order to form LiFePO_4 compounds. Also melted sucrose may help to dissolve and transport Li^+ ions passing through itself to particle surface.

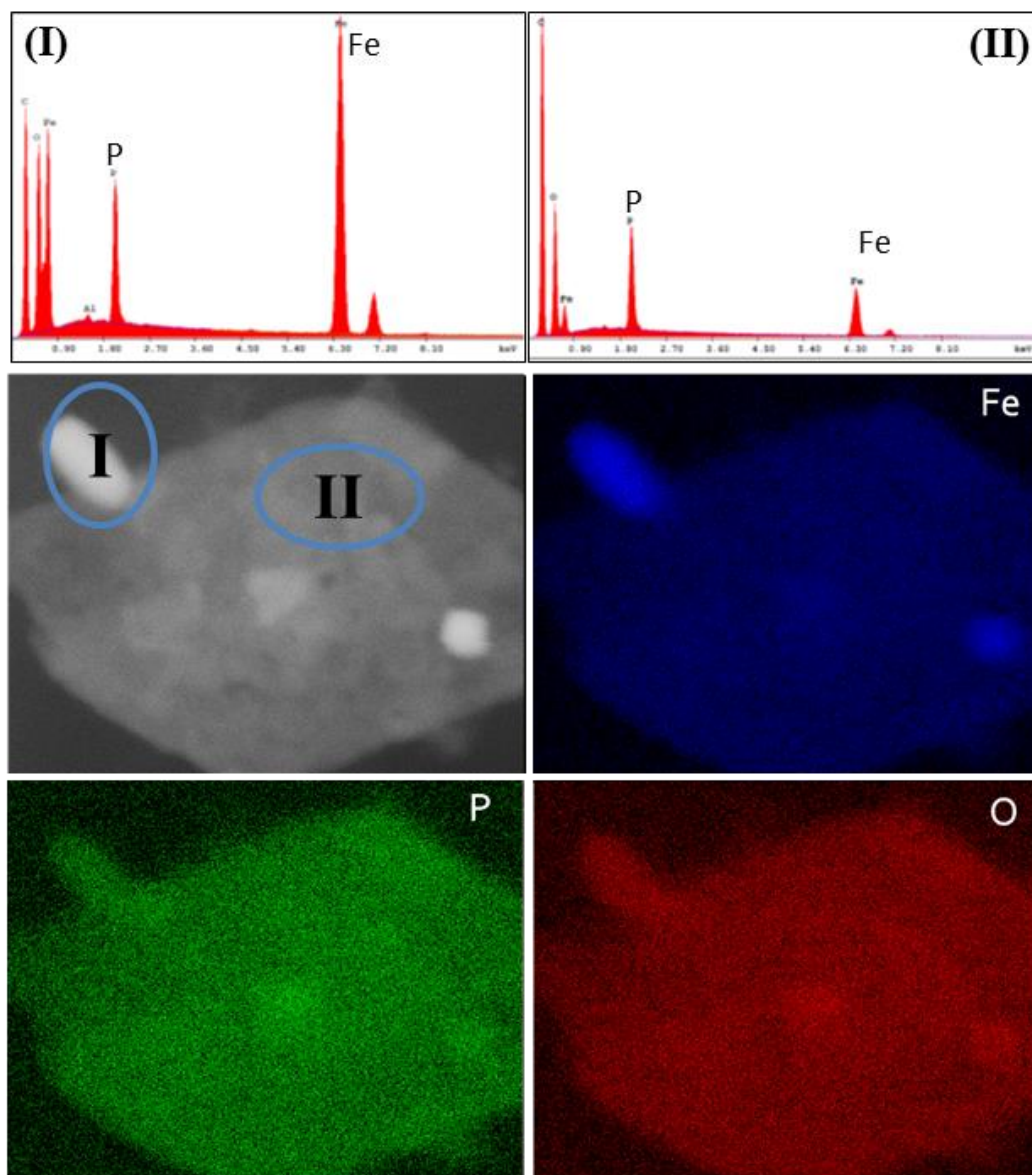


Figure 96. EDX mapping analysis of nano plate structure synthesized by US-US sub sequential precipitation

Since there is different stoichiometric ratio of Fe:P for $\text{Fe}_3(\text{PO}_4)_2 \cdot 8\text{H}_2\text{O}$ (3:2) and LiFePO_4 (1:1), an excessive iron in vivianite needs to react with outsourced PO_4^{3-} ions which might be insufficient while in a carbon encapsulation. The excessive iron atom might be extracted from newly transformed LiFePO_4 structure due to this excessive stoichiometry. It is well known that very little carbon solubility can be possible only

with interstitial space in ferrite mineral. Therefore undissolved and unreacted iron might be accumulated as form as ferrite crystallites on very near surface of LFP crystal plates. Also, nonvolatile Li_3PO_4 formation because of Li rich environment captures some phosphate portion and may lead some reduced iron impurity which becomes unreacted because of phosphate deficiency.

Because of carbon encapsulated solid structure, in both AFP and VVT routes, Fe and Li_3PO_4 phases appear as main impurities which yield more than 85 wt.% of cathode powder as LFP. EDX mapping analysis with SEM indicates iron (bcc) crystallites presence at nearby LFP nano plate surface with point contact (Figure 96). In the VVT route with an impurity less than 5wt.%, iron content increase with respect to the reducing strength of increasing carbon addition. Iron (bcc) crystal location makes its formation mechanism is considerable to be resulted from structural encapsulation by carbonaceous material. During the chemical insertion, Fe excess stoichiometry of vivianite remains unbalanced with slower diffusion rate of PO_4^{3-} ions than Li^+ ions in the carbon layer. Unreacted Li_3PO_4 hollow sphere morphology remains same as observed in TEM images (Figure 51). Both electrical conductive iron and lithium ion conductive Li_3PO_4 impurities are harmless for battery operations.

4.3.4 Localized orientation distribution in the nano plate LFP/C structure

In carbon encapsulation strategy, the LiFePO_4/C synthesis is performed in the solid state reactions by delivering Li and Fe sources. Solid state Li^+ diffusion and phase transformation occurs via chemical lithiation into physically restricted single crystalline particles by a carbonaceous barrier. Even so, precursor structures have single crystalline structure, SAED analysis shows the orientations of nano plate LFP phase at the final step after complete transformation. As shown in Figure 97 there is sub-grain formation in each individual nano plate particle. During the lithium ion incorporated phase transformation, sub-grains are formed within each individual plate like crystals. Grain formation shows different orientation between grains in nano-plate crystal as seen in Figure 97.

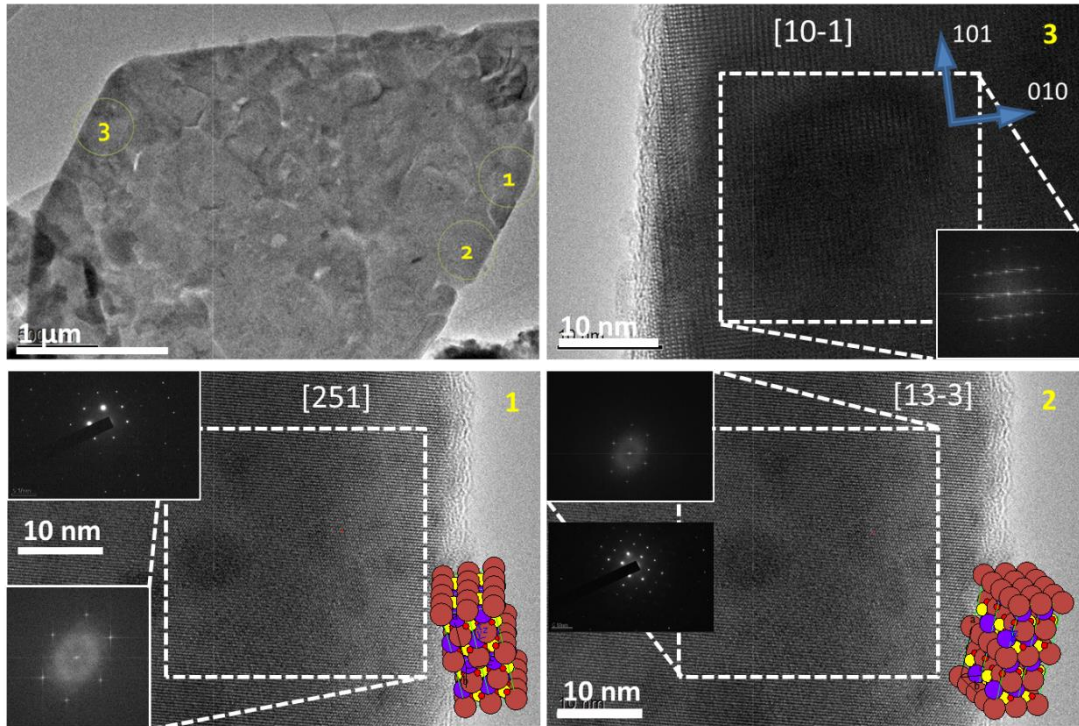


Figure 97. TEM image of nano-plate LFP cathode materials with electron diffraction analysis on selected sub-grains (1, 2, 3) represented with circular SAED aperture (yellow) and calculated zone axis directions in $[uvw]$ form which makes different angles as 35° , 44° , 90° with $[010]$ direction, respectively.

Although, it is difficult to collect SAED analysis from each sub-grains, a representative analysis was done on one selected nano plate particle to better describe the orientation of the structure. The calculated zone axis and plane directions with angles between b axis directions are given in Figure 97.

Even there are some examples having $[010]$ zone axis orientation along the thinnest dimension (Figure 98), the main plate structure is formed by sub-grains after LiFePO_4 phase transformation is completed. Presence of grains can be easily detected by patchwork vision into the main plate morphology in dark field TEM images in Figure 99.

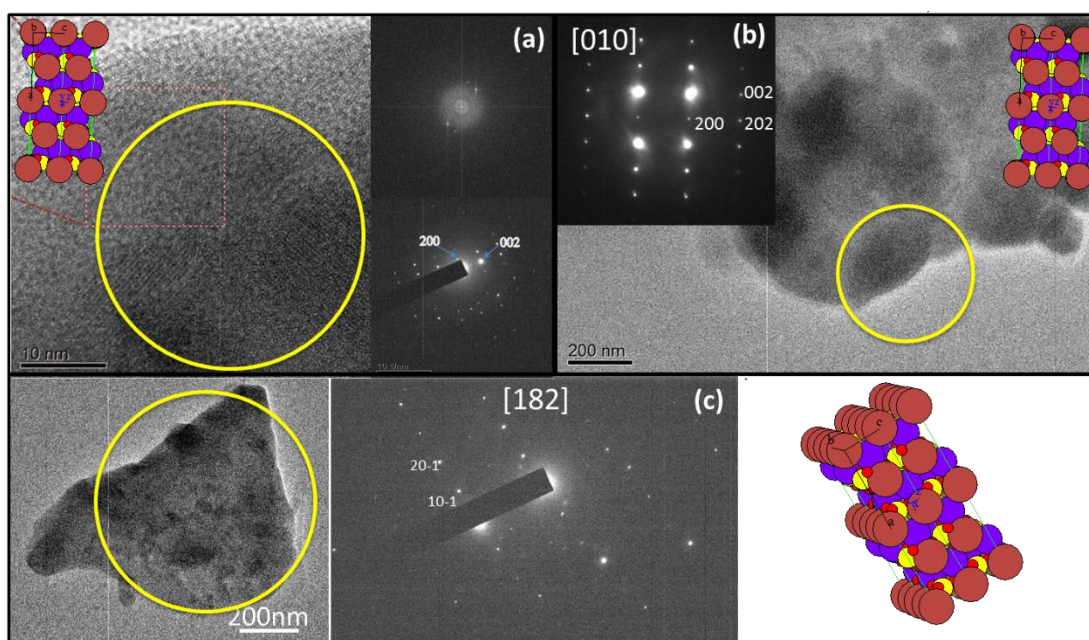


Figure 98. TEM image of US assisted synthesized LiFePO_4/C cathode particles with (c) and without (a, b) ethylene glycol addition represented with SAED (yellow) and orientation analysis results (simulated with Carine 3.1)

The sub-grain formation with different orientations shows that larger ones have been accumulated on central region of the plate cross-section. Larger, approximately double sized, sub-grains seems to be located at inner sites behind the smaller edge sub-grains. Although solid-state Li diffusion in phase transformation, and interface reactions remain poorly understood even in chemical lithiation process, these dark field images (Figure 99) pointed out that sub-grain formation may support Li incorporated multi nucleation mechanism followed by boundary migration in nano plates. Because nucleation rate is faster than the solid state diffusion in the particle.²⁷ Van der Ven et al.¹³⁰ have tried to explain Li diffusion mechanism as depending on much fluctuated concentration even in electrochemical cycle conditions which is obviously valid for the solid state chemical lithiation or transformation.

Moreover, by considering non-stoichiometric nature of the reaction between Li_3PO_4 and $\text{Fe}_3(\text{PO}_4)_2 \cdot 8\text{H}_2\text{O}$ an inequivalent diffusion conditions for Li^+ and PO_4^{3-} may possibly affect the phase transformation rates and crystallographic orientation of newly formed LFP phase differently. Different Li diffusion rates occur in different nucleation sites and different concentration conditions. This reaction mechanism may be homogenized with respect to precursor orientation by controlled reaction conditions such different than solid state which might be subjected by another research studies.

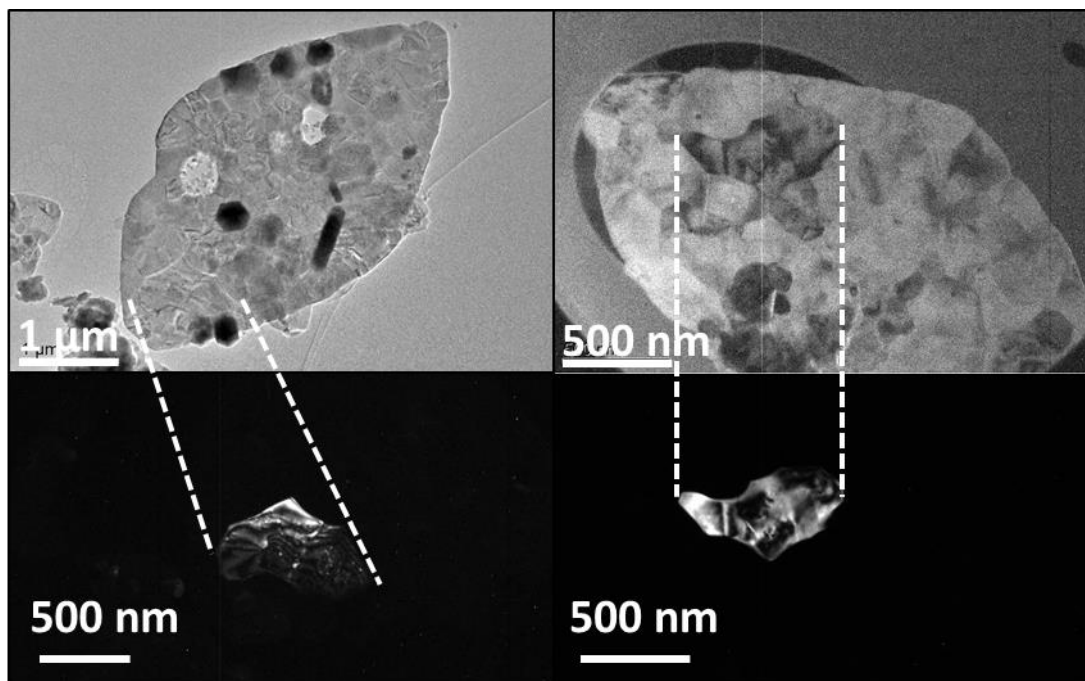


Figure 99. Dark (down) and bright field (up) TEM images of nano-plate structures as synthesized with US irradiation in both sub-sequential precipitation from vivianite metastable structure

If there is a localized or dominant direction in orientation distribution among the grainy structures in synthesized LFP nano-plates, there must be difference between the peak intensity with respect to the standard powder pattern of LFP. The difference between standard and parallel beam geometry can be seen in the relative intensity of the peaks (Figure 100). The intensity of the (020) peak in parallel beam XRD is slightly increased in standard beam XRD, indicating (020) oriented grains. This comparative XRD study represents weak orientation is localized around (020) peak.

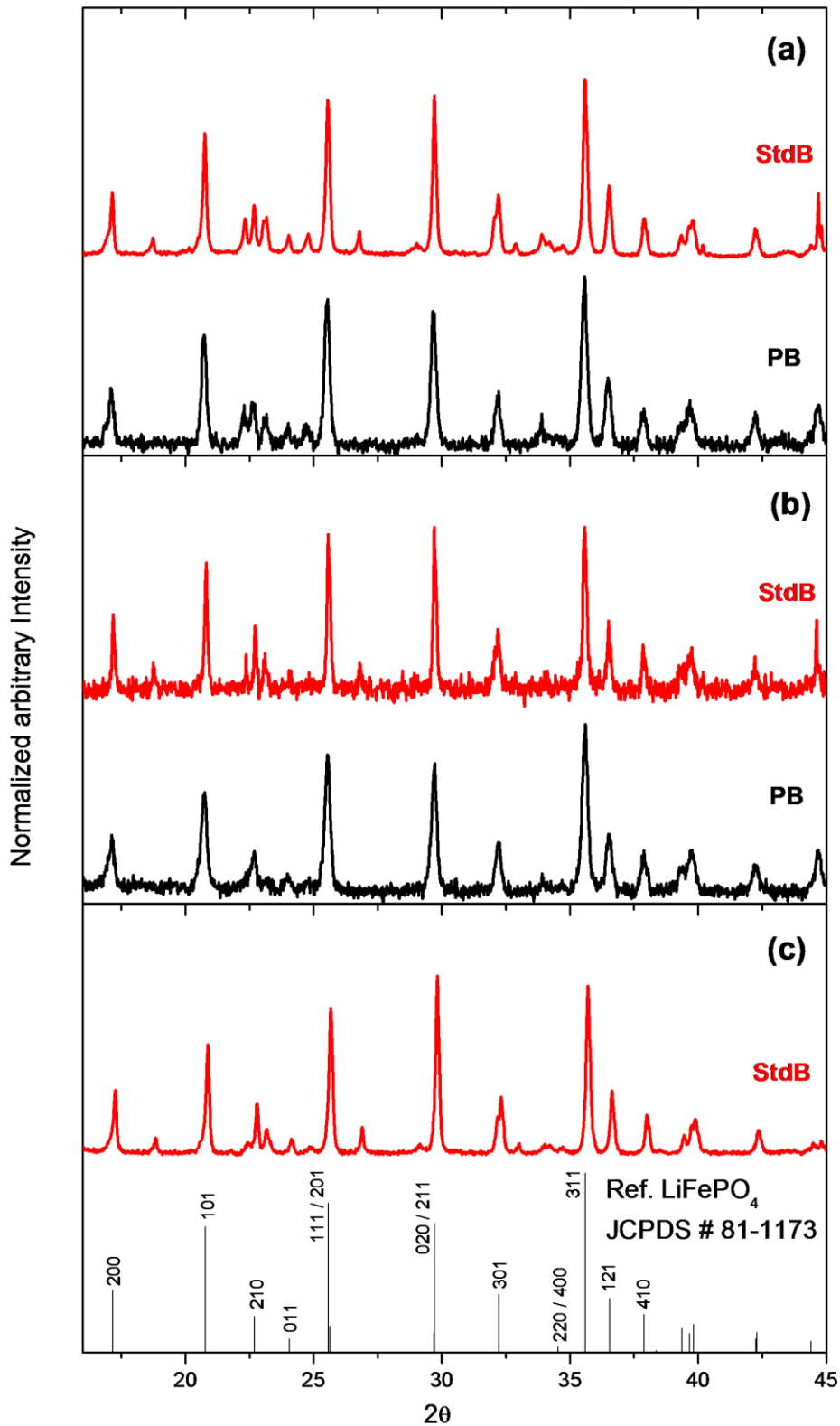


Figure 100. Comparison of parallel beam (PB) and standard beam (StdB) XRD analysis for localized orientation distribution around (020) plane in LFP (a) 80 – 100 nm, (b) 120 – 150 nm, (c) 220 – 250 nm thick nano-plates as synthesized via US assisted sub-sequential precursor precipitation without addition.

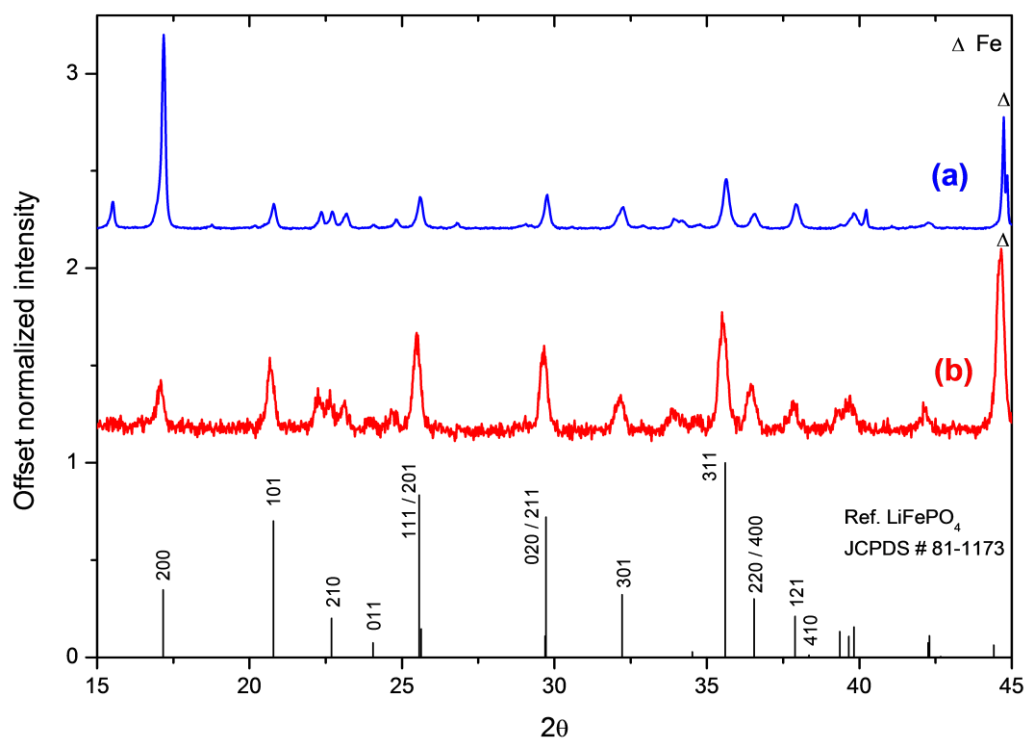


Figure 101. Standard (a) and parallel (b) beam XRD patterns of cathode materials synthesized via US assisted sub-sequential precipitation with AFP route

The sub-grain formation might be explained by nucleation induced mechanism which is based on nucleation through different side of solid vivianite particle in solid state calcination. The physically sucrose should be firstly melt down¹²⁸ and incorporate Li diffusion into the crystals. This coated layer of liquid sugar is believed that facilitate Li^+ diffusion in solid state reactions at lower temperatures. Li incorporated nucleation of new LiFePO_4 phase have slightly different orientation because of simultaneous nucleation on multi-sites on the vivianite surfaces as different crystallographic planes exposed to surface. It will result different lithium insertion stoichiometry and path ways at the surfaces for boundary diffusion. This poly-crystallization of nano plate structures within physical encapsulation conditions, makes some proposed mechanisms such as oriented attachment¹³¹ to be very questionable. After all consequences, this grain refinement may also enhance lithium diffusion by existence of grains where lithium diffusion is fast enough between very thin (40 – 80 nm) grain boundaries.

4.4 Electrochemical performance of nano structured LiFePO₄/C cathode materials

Nano plate cathodes have been synthesized having different thickness with respect to precipitation conditions as explained in section 4.3.1.3. Electrochemical performance test is applied by increasing discharge currents for both slow and fast charging rates defined as 0.1 and 1C, respectively.

In the case of nano-plate structures synthesized by vivianite route, LFP can provide high discharge capacity during both slow (0.1C) and fast (1C) charging regions. Comparing the fast rechargeability, it is able to achieve 125 mAh g⁻¹ with good capacity retention up to 92% after 25 cycles (Figure 102) with US assistance.

As a comparison of the electrochemical performance results, it is found that US irradiation on sub-sequential precipitation has significant improvement on discharge capacity, especially at fast charge. Despite its surface active properties for inhibiting growth of crystals, EG has no essential effect on the performance within co-existence of US irradiation even in use with suspension of LP micro seeds. It has strong adsorbing effects on iron cations to retain them from the suspension reactions within both solution with Li and Fe source. Thus, because of high cation solubility in EG, it is hard to activate cations for further crystallization reactions especially in addition with Fe source and at low temperatures under 100 °C. However it has only a minor improving effect on the discharge capacity when compared with the poorest capacity of normal sequential precipitated cathodes without insonation. This means that EG use have only positive effect on hydrothermal production conditions at elevated temperatures above 200°C to get rid of its passivation effect.

Within the all insonated cathodes, third best discharge capacity is achieved by only using insonated micro spherical LP seeds followed by normal precipitation without insonation. However according to the Rietveld analysis only 28 % (v/v).of LFP is synthesized. This poor production rate is originated from a very limited formation of VVT crystals (Figure 57-b) without US treatment in 2nd precipitation. It is not possible to pursue solubilisation and recrystallization reactions without insonation effect during VVT precipitation even in fast mixing (900 rpm) conditions at 90 °C temperature. The effect of US treatment on homogeneous particle morphology and improved

crystallization can obviously be seen also from the galvanic performance test results in Figure 102.

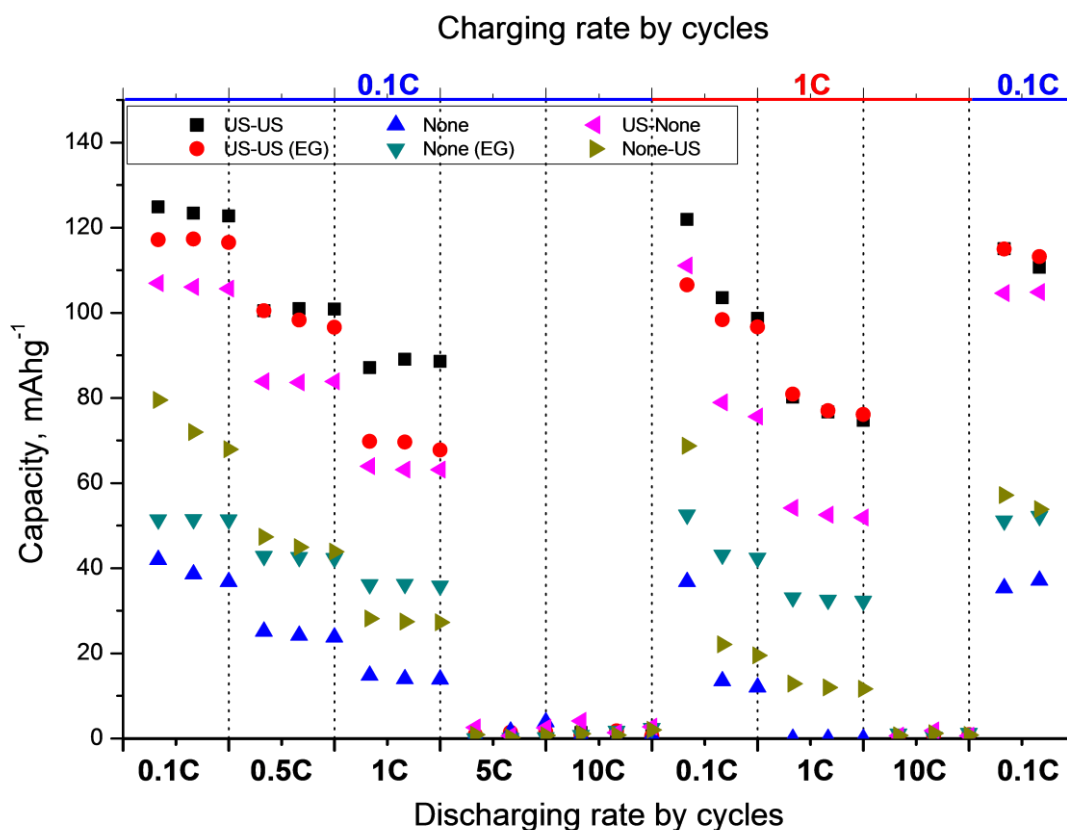


Figure 102. Capacity test results of carbon coated cathode materials as synthesized with (US) and without (None) US assistance for related precipitation sequences (1st – 2nd) with (EG) or without ethylene glycol addition.

In consideration of sub-sequential route of ultrasound assisted precipitation, nano plate structures synthesized via both AFP and VVT routes were tested in galvanic cycles within fast and slow charging. In AFP route, two different lithiation compounds were used to better understand effect of lithiation compound on nano plate performance. in order to test the thickness effect of cathodes synthesized via VVT route especially on fast charging performance, nano plate cathode materials having different average thicknesses (Figure 107) have been prepared by pH arrangement as explained in section 4.3.1.3. Regardless of the crystallographic orientation, the cathode materials have diverse electrochemical performance with derivations in thickness.

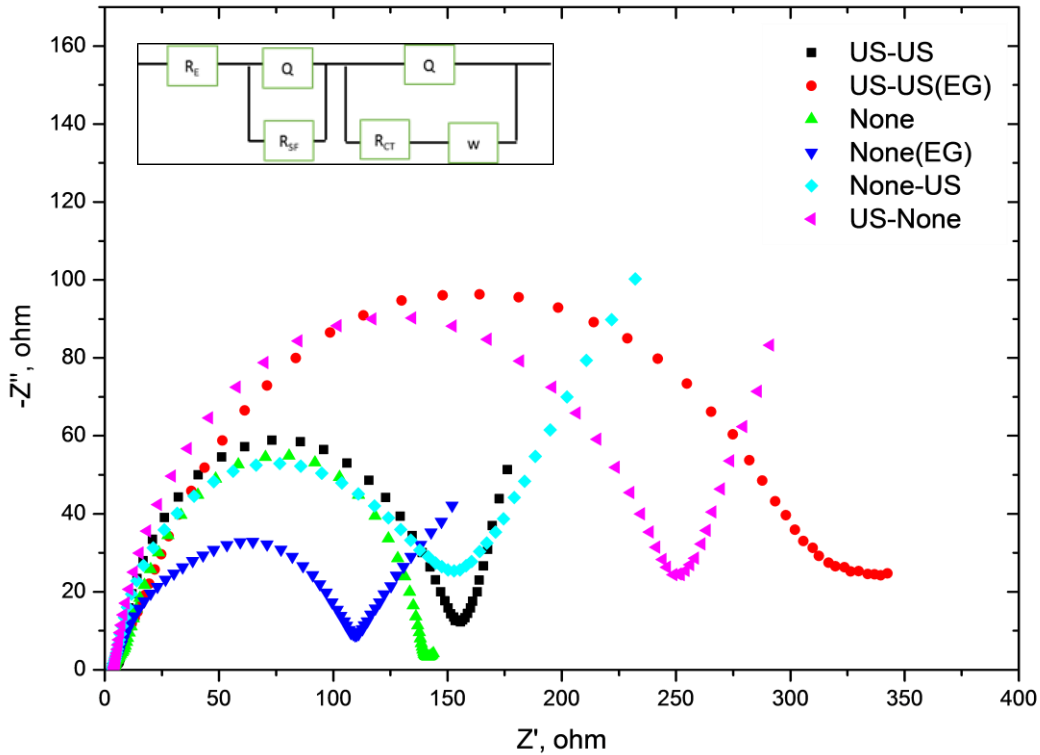


Figure 103. EIS analysis results of cathodes materials as synthesized with (US) and without (None) US assistance for related precipitation sequences (1st – 2nd) and with (EG) or without ethylene glycol addition.

In the case of LFP nano-plate synthesized with AFP route, very reliable high discharge capacity can be achieved up to 117 and 79 mAh g⁻¹ as lithiated (US assisted) with lithium acetate and lithium hydroxide, respectively, in slow rate (0.1C) charging region. However after passing fast charging current (1C), the capacity fades out, drastically. This rapid decay is resulted from unreachable capacity at fast (1C) charging because of its low Li ion conductivity due to the crystallographic orientation according to 2D plate morphology which has mostly higher energetic migration barrier along the thinnest axis against lithium ion diffusion. The more channel openings are located on the surface. So the fast lithium extraction can be possible during charging. The *bc* plane orientated 2D structures expose much less channel openings to lithium ions to be extracted easily from the most probable lithium migration paths, along [010] direction. This means that the lithium ions, to be extracted from *bc* surface, has to overcome much thicker solid portion of crystal or try more energetic way along other directions, which have high activation barriers at low temperature. The dramatic rate decreasing effect can be seen clearly as charging current increased in Figure 104. At

1C charging the cathode materials synthesized by AFP route lost their dischargeable capacity after each fast charging cycle, even in slow (0.1C) discharging rate.

As an intrinsic property, defect concentration effect on rate capability, blocking 1D channels in [010] direction, can be examined by the high capacity retention after two cycle they charged slowly at 0.1C. As comparable with the initial capacity, it can give 119.5 mAh/g capacity after 25 cycle. Despite the superior capacity retention (102.5%), these nano-plate LFP structures have suffered from bad power capability especially in fast (1C) charging region by showing rapid decay to $\sim 20 \text{ mAh g}^{-1}$ even in 0.1C discharging rate. It could not be possible to restore its capacity because of stuck lithium ions into the channels along [010] direction.

Although the same calcination and carbonization procedure has been applied on AFP route, there is a significant difference between lithiation compounds in electrochemical performance. Various preferred orientation distribution of LFP platelets seems to be related with different structural deformation that resulted in diverse cathode morphologies. Lithium acetate critically enhances (200) peak intensity at final LFP XRD analysis which means that the *bc* axis orientation is well parallel aligned to the largest surface of 2D crystallites. This preferred orientation is reduced by adding lithium hydroxide as a lithiation compound instead of lithium acetate. The cathode material as lithiated with lithium hydroxide (LH) has endured almost 3 times better than as lithiated with lithium acetate (LAc) as giving 69.7 and 28.7 mAh g⁻¹, respectively. Lithium acetate shows very poor capacity at fast charging rate (1C) due to its more preserving behavior on *bc* oriented crystal structure of AFP after lithiation. Because the thickness along the [010] crystallographic direction was found a very effective parameter on electrochemical kinetics.

Other significant difference which supports the capacity results is also observed at surface resistance measurement which are 450 Ω and 150 Ω in accordance with lithium acetate and lithium hydroxide use, respectively (Figure 105). Therefore, the calculated impedance values by fitting to equivalent circuit model can be taken as intrinsic properties of cathode material representing crystallographic orientation in 2D morphology. This orientation degree seems to have a significant role not only on capacity but also on surface resistance.

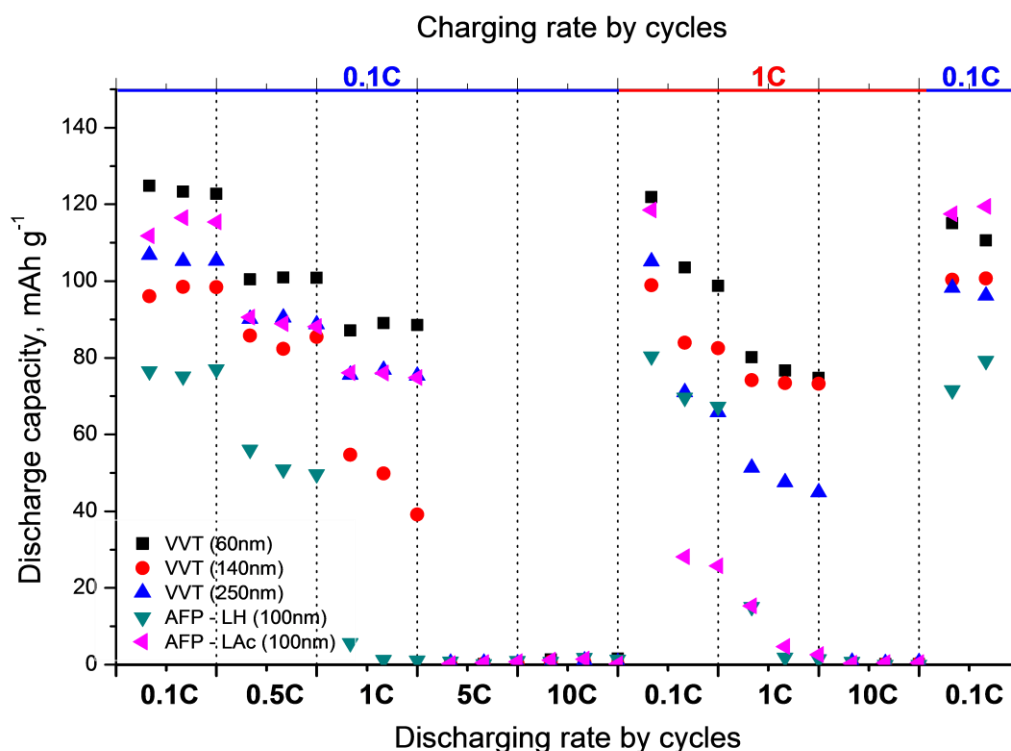


Figure 104. Galvanic discharge capacities at high (1C) and low (0.1C) charging rates for 2D LFP nano-plate cathode materials synthesized via US assisted sub-sequential precipitation with respect to their thickness

Olivine structure also has some defects and anti-site disordering that can block the inner part of channel structure. In lithium acetate use, this strong orientation gives less surface openings that can leave the higher blocked portion of material within same defect concentration. However, lithiated cathode with lithium acetate, shows better discharge capacities than lithium hydroxide lithiated as 116.5 and 77 mAh g⁻¹ at slow charging, respectively. Consequently, crystallographic orientation notably appears as a limitation factor only in fast charging operations, In other words, it should essentially be considered for fast charging applications beyond 1C rate. As another outcome from electrochemical results, anionic species of lithium salts has a lateral effect on morphology and crystallographic orientation distribution, consequently, which has a key role for fast rechargeability at nano-scale.

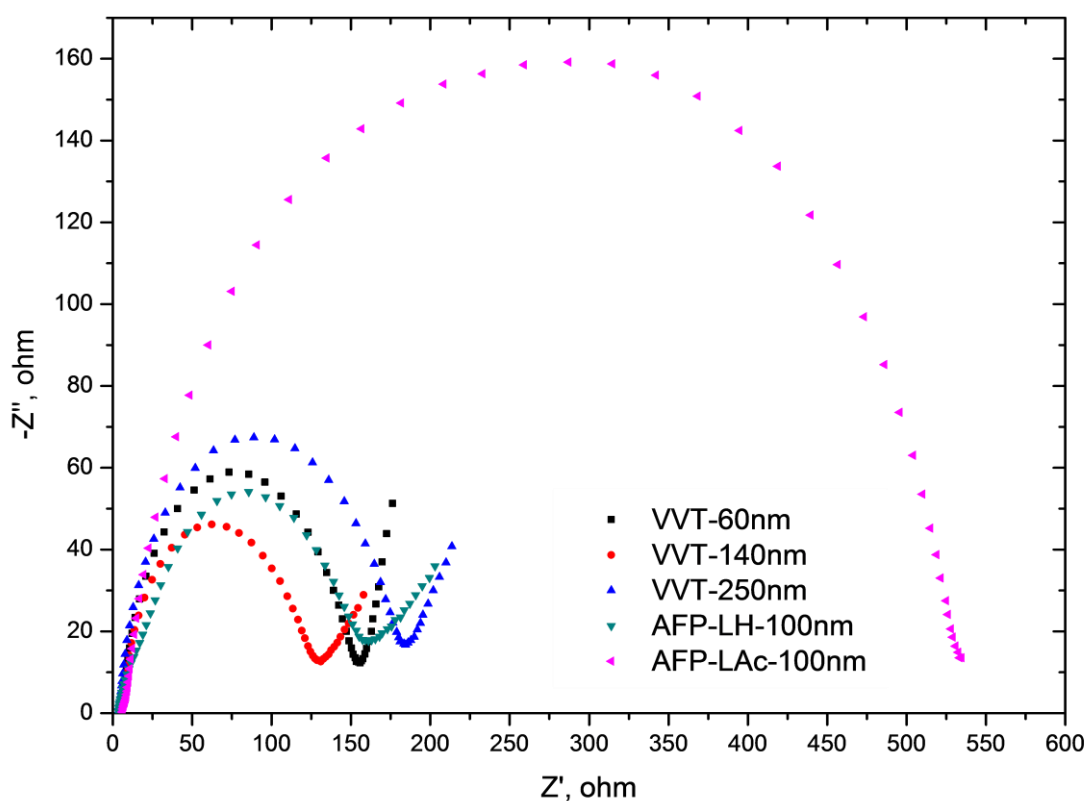


Figure 105. EIS analysis of nano plate cathode materials synthesized by precursor routes; $\text{Fe}_3(\text{PO}_4)_2 \cdot 8\text{H}_2\text{O}$ (VVT) having different thicknesses and $\text{NH}_4\text{FePO}_4 \cdot \text{H}_2\text{O}$ (AFP) calcined with different lithiation compounds (LH, LAc) as all synthesized via US assisted sub-sequential precipitation

Without any significant capacity loss in slow charge region (116.5 and 76 mAh g^{-1} at 1C and 0.1C discharge rate, respectively) by comparing with VVT routed cathodes, strongly $[100]$ oriented LiFePO_4 cathode via AFP route represents very low capacity (28 mAh g^{-1}) at fast (1C) discharge current. Considering rapid 1C discharge capacity decrease of AFP-LAc from 76 mAh g^{-1} after 0.1C to 4.6 mAh g^{-1} after 1C rate charging, it can be concluded that the lithium diffusion mechanism as rate determining step is the most limiting factor for fast charging conditions. This harsh drop depends on its stronger orientation in $[100]$ direction than deformed AFP-LH morphology. This difference may be resulted from the recharging mechanism having outer region of the solid particle as resistance against lithium de-intercalation process as coherent with shrinking core model proposed by Newmann et al.^{132,133} Thus the Li ions have to diffuse through different conditions which are Li rich and Li deficient region during discharge and charge, respectively.

Furthermore, the preferred orientation at [010] direction (Figure 101) contributes the poorest rechargeability at high rate (1C) by penalizing the nano scale behavior. But the important finding is that expanded hysteresis is correlated with crystallographic orientation. So lithium diffusion in solid state is not only affected by anisotropy in LiFePO_4 crystal structure but also asymmetric behavior in charge and discharge operations.

The inhomogeneous distribution of Li^+ ions between the reacting cathode nano particles at high current charging, are confirmed by many observational techniques to react particle by particle.¹⁴⁴⁻¹⁴⁷ According to the recent studies,¹⁴⁰ high current rate induces more particles to contribute phase transformations at similar times during charge. By observing high rate capability in Figure 104 with VVT routed cathodes with polycrystalline morphology, sub-grain formation in an individual nano plate gives 4 times more rated capacity with respect to high ionic conductivity in plenty of grain boundaries as well as ten order of magnitude higher than in crystal²⁴. Polycrystalline material with sufficient size refinement in one dimension enhances power and fast charging capability.

On the other hand, for all nano-plate cathode materials based on VVT route, the thinnest (60 nm as average) nano-plate particles gives 125 and 80 mAh g^{-1} discharge capacities as best electrochemical performances in both slow and fast charging regimes. It can be remarkably charged up to 65% of its initial capacity within an hour. In slow charging region, discharge capacity performance is ordered as 125, 98.5 and 109 mAh g^{-1} at 0.1C; 89, 54.7 and 78.6 mAh g^{-1} at 1C discharging rate, with respect to thickness of nano-plate structures having 60, 140, and 250 nm in average thickness (Figure 104). Similarly, charge transfer resistance are 138, 103 and 170 Ω as thickness of nano plate structure increases (Figure 105).

Their slightly oriented polycrystalline morphology makes the spherical particle size approximations and theories applicable. According to the decrease in size from micrometer scale, electronic wiring is important and it is not possible to close the gap between tiny particles by external carbon powder addition because of bended curvature. As explained in literature review, the blocked capacity is reduced dramatically with respect to size reduction at nano scale. A reported computational study¹³⁴ by Ceder et al. has claimed that under the same defect concentration unblocked capacity is expended sharply under 140 nm particle size limit.

Furthermore, electronic conductivity is not a limiting factor anymore because electronic conductivity ($6.4 \times 10^{-11} \text{ Scm}^{-1}$) becomes much higher than ionic conductivity ($3 \times 10^{-9} \text{ Scm}^{-1}$)²⁵ as particle size goes lower than 140 nm limit. After a certain size in refinement, electronic conductivity is satisfied with the active double layer on the particle surface as observed in many studies.^{135,136} At the nano scales, particle smaller than a certain size ($\sim 140 \text{ nm}$), and ionic conductivity is less than electronic conductivity and becomes a limiting factor so that even only point contact can give sufficient electronic conductivity themselves. In nano scale, the total surface area of particle is tremendously increased with decreasing in size. For much bigger particles, the thickest plates in this study, have good carbon coverage needed less amount of surface carbonaceous material than thinner platelets with the same amount of carbon content while thinner plates may lack of full coverage of conductive layer. So medium sized platelets may suffer from the limited carbon coating with poor electronic conductivity because of dramatically increased total surface area per unit weight. At the same time, these medium sized particles are not smaller enough to overcome electronic resistance with lack of coating. So by further decrease in size as 60 - 80 nm in thickness, particle becomes more electrochemically active because of high electronic conductivity even in point contact instead of full coverage. This phenomena is similarly observed as proving with high performance at slow (0.1C) charging of 2D nano plates which are thinner than 100nm.

At high rate charging kinetic, particle size effect becomes more important on power capacity. At nano scales, especially in charging kinetic, charge transfer resistance becomes a rate determining step rather than Li diffusion within solid state material because of shorter diffusion paths in small particles. Even so thicker nano plates have good carbon coating quality, charge transfer resistance for the thickest plates is measured 50% higher than the smaller particles within EIS experiments (Figure 105). In the case of thinner nano plates under 150 nm, charge transfer resistance drops from 169.4 to 137.7 Ω , by the thickness refinement from 140 to 60 nm, respectively. Moreover, at high charging currents, the rising over-potential makes easier to reach larger area for active double layer improving charge transfer kinetics to exceedingly compensate lower electronic conductivity.¹³⁷ Therefore superior power density has been observed at 1C fast charging regime in as correlated with decreasing nano plate thickness. These findings, in this study, correlates with the theoretical conclusion of

modelling studies by Gaberscek et al.^{25,138} which emphasizes the importance of particle size minimization to achieve a high rate capability of LiFePO₄ electrodes. Due to the fact that polycrystalline nature of synthesized nano plates, as compatible with uniaxial particles, it can be mentioned that the grain boundary migration gives also relatively high enough diffusion rate to Li ions in order to enhance ionic diffusion within the nano plates.

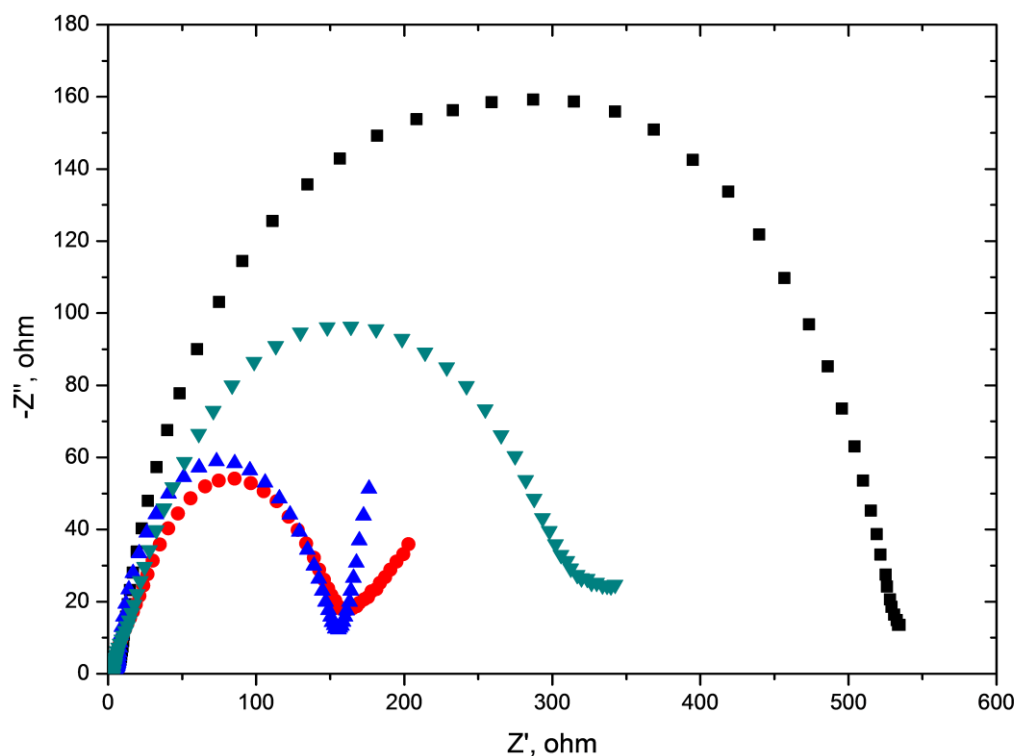


Figure 106. EIS analysis of cathodes as synthesized via US assisted sub-sequential precipitation methods

In the next decade, fast charging of electrochemical devices will draw the most attention for energy storage research field. Grey's group has proposed that solid solution mechanism can be formed during fast charging rates (5 – 20 C) as very recently confirmed by both computational and experimental studies^{139,140} In the pioneer study of Ceder group,¹⁴¹ the alterable orientation of diffusion phase boundary has been attainable by size and morphology difference. By taking all these recent studies and our electrochemical performance results into account, it encourages surface improvement studies, together with the size refinement in [010] orientation. In this study, US assisted sub-sequential aqua precipitation synthesis is proposed to

modulate cathode structure by manipulating facile reaction and crystallization procedures which can localize the orientation detectably around [010] within metamorphologic phase transformation. And this method is also applicable for another olivine structures or together with dopant materials because of its easy application to aqua soluble reactants like Mn. Apparently, Li-Mn-P-O₂ system can be also subjected to this technique because of the common thermodynamic stability in metastable system.¹⁴²

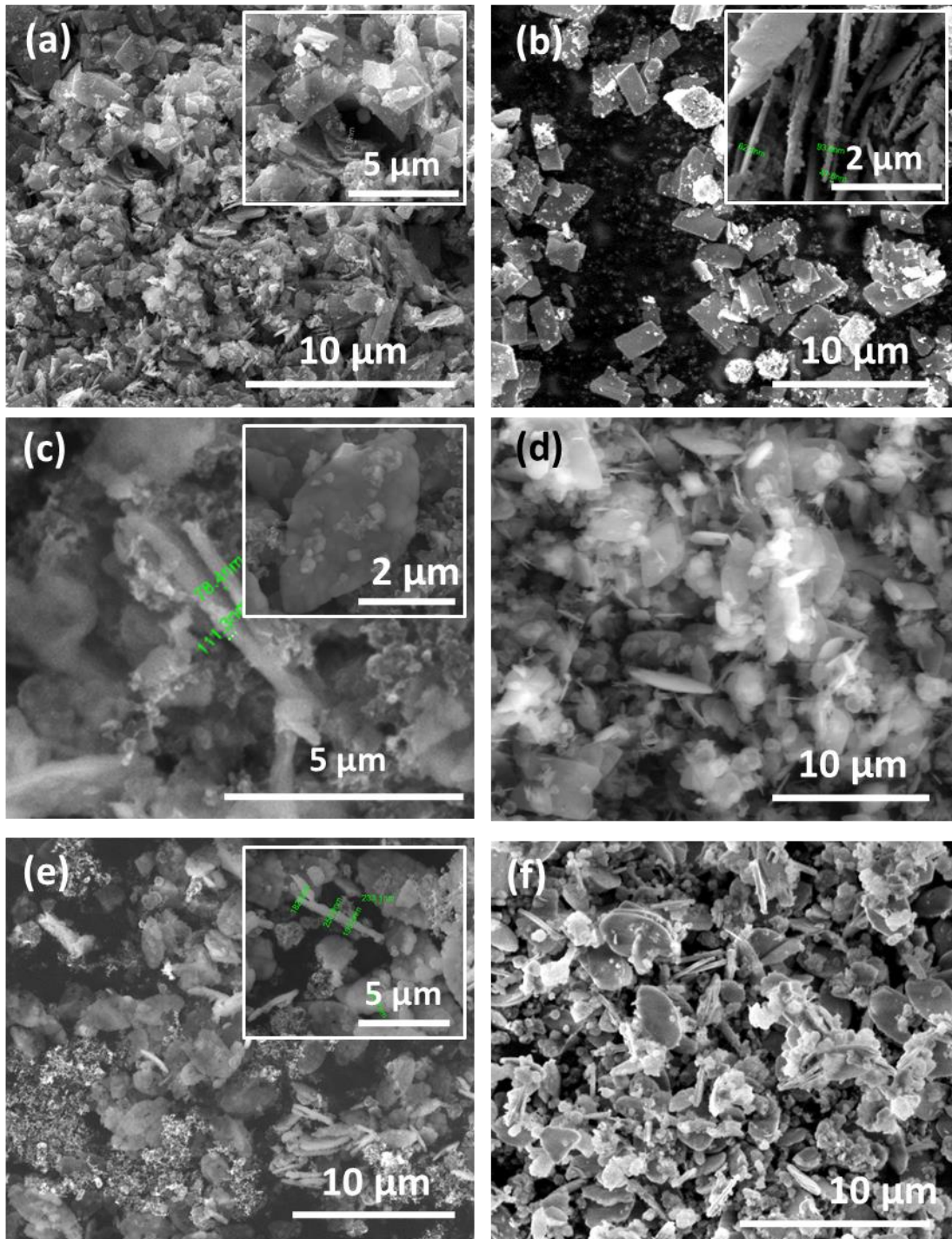


Figure 107. SEM images of carbon coated nano-plate LFP cathode materials as synthesized by US assisted sub-sequential precipitation having different average thickness as 60nm (a, b), 140nm (c, d), and 250nm (e, f).

5TH CHAPTER

5. Conclusion and future remarks

The objective of this study was to investigate power capability of LiFePO₄ cathode materials in lithium ion batteries. Lithium transport is improved by reducing particle size and conductive layer thickness without blocking lithium extraction and insertion as well as electron movement. Low cost, low temperature, aqua based, reliable and facile precipitation techniques were used to synthesize fast rechargeable nano structured LiFePO₄ cathode materials. Freeze (cryogenic) drying synthesis with co-precipitation and US assisted sub-sequential precipitation with normal drying were implemented.

In freeze drying technique with co-precipitation, two possible precipitation mechanisms (temperature and pH nucleated) resulted in different morphological structures which are micro porous and co-axial star-like platelet structures, respectively. Temperature driven precipitation with ascorbic acid addition led the solid particles form tiny nuclei which crystallized (~80 °C detected by DSC) and turned into micro porous (500 - 700 nm) structures with 85 wt.% LiFePO₄ conversion. Due to its surface active properties during precipitation, ascorbic acid reduced the surface energy during nucleation and growth within pH driven conditions to get star-like structures formed with 300 nm co-originated thin platelets. Structural lattice parameters matched with bulk LiFePO₄ structure (a : 10.324 Å, b : 6.004 Å, c : 4.692 Å), because of very close to micrometer sizes in both articulated micro porous and star-like structures.

Graphitization becomes less important if carbon layer resistance is high and heterogeneous. Therefore, carbon layer thickness is aimed to be as thin as possible. Small charge transfer reaction resistance becomes more important as refining the size. Therefore in freeze drying synthesis, ascorbic acid with pH driven nucleation resulted in co-originated thin platelet crystallites. Improved discharge capacities of 120 and 70 mAh g⁻¹ at 0.1C and 1C cycling rates were obtained, respectively.

Sub-sequential precipitation provides control on precipitation reactions and precursor morphologies making possible to dry in normal atmospheric conditions by keeping

nano structures away from further growth and agglomerations. There are two possible precipitation sequences to produce different 2D nano structured precursors such as AFP and VVT modified by thickness via ultrasound treatment during precipitation before the actual LFP phase formation in solid state calcination. For metamorphological LiFePO_4 nano plate structures based on precursor synthesis, ultrasound appears to be a powerful manipulating tool on reactive crystallization kinetic. Ultrasound technique induces controlled reactions and crystallization in order to get homogeneous and nano size distribution within a very small space and time period. Moreover, it creates reducing media within the aqua based solutions in atmospheric conditions.

AFP precursor only forms above $\text{pH} > 8.0$ giving much thicker, 150 – 200 nm, nano plates without ultrasound than 30 – 50 nm thick US assisted nano plates. Size refinement effect gets stronger in VVT nano plates formation to refine the thickness from micro meter scale to 40 – 100 nm by ultrasound stimulation and control on dissolution and crystallization kinetics. Ultrasound increases the homogeneous nucleation rate and possibility by keeping away crystals from growth region because of reduced MSZW and rapid temperature rise and drop within irradiation cycles. Reactive crystallization mechanisms without any surface active organic compounds during the sub-sequential precipitation are controlled by insonation.

Preferred orientation [010] is detected in AFP routed LFP nano plates in an increasing order of lithiation compounds such as lithium nitrate, lithium hydroxide and lithium acetate, respectively. TEM observation and SAED analysis show that single crystalline structures are preserved after LFP transformation is completed. Therefore, structural deformation in calcination is responsible for reduction of preferred orientation. Structural preservation during metamorphological synthesis is correlated with surface adsorbing and reducing properties of lithiation compounds.

In contrary to many computational and experimental studies reporting equi-molar existence of Li_3PO_4 and $\text{Fe}_3(\text{PO}_4)_2 \cdot 8\text{H}_2\text{O}$ phases, LiFePO_4 is not formed in one batch metastable conditions. Ultrasound assisted stimulation shows facile control on tunable conversion rate within reactive crystallization in aqua media in order to obtain less impurities from unreacted precursors. Considering the studies on thermodynamically stable and metastable region, the only way to achieve high conversion by equi-molar

precursor existence is to separate the reaction conditions and rule the kinetic parameters at microscopic level with an external tool such as ultrasound.

In VVT synthesis route, final LFP lattice parameters are well matched with database (JCPDS # 81-1173). These well matched lattice parameters (a : 10.323 Å, b : 6.003 Å, c : 4.690 Å) for both routes are apparently related with other two dimensions of nano plate structures in micron scale. Thanks to their 2D morphology, high tap density is obtained for adequate processability for high power dense battery production.

2D material synthesis via proper thinning up to nano scales is improved to overcome kinetic barriers of ionic and electrical motion. The synthesized cathode materials are still compatible with separation and handling processes in industrial scale as well. Moreover, thickness of precursor nano-plates as well as final LiFePO₄ is readily controllable by solubilisation rate with respect to suspension pH and insonation.

Conductive coating is also crucial for electron transport as well as permeable for lithium transportation. After synthesis of 2D vivianite nano plates as single crystalline structure, applied encapsulation strategy are used to preserve the nano plate morphology. Among the carbon encapsulation methods, sugar saturation in suspension was optimized giving 1-2 wt.% carbon content and 100 – 170 Ω surface resistance with 5 – 10 nm carbon layers. Despite a high initial capacity (>140 mAh g⁻¹) at 0.1C and good impedance (106 Ω) obtained from CVD, the comparative electrochemical tests were done by sucrose saturation because of unreliable conductive layer by CVD along the evaluated cycles. By comparing saturation, CVD yields more homogeneous surface coating to reach high graphitization and low surface resistance. However, CVD coated carbon layers are easily detachable. Therefore, at least 25% of its capacity was still remained inactive with sucrose saturation procedures.

SAED analysis show that final LiFePO₄ nano-plate structure resulted in polycrystalline structure via VVT route. On the other side, AFP route yields well oriented single crystalline nano plate structures. Comparative study of parallel and standard beam geometry in XRD proves some evidence upon preferred orientation distribution around [010] direction. However, the orientation of each sub-grain is detected by SAED as different from each other

Polycrystalline LiFePO₄ nano plates via VVT route give superior discharge (0.1C) capacities as 125.1 and 103.4 mAh g⁻¹ even in both slow (0.1C) and fast (1C) charge regions, respectively. Furthermore, the more [100] oriented LFP structure from AFP route suffers from limited lithium ion diffusion as charging current increases because of the micro meter sized dimension of 2D nano plates lying along preferable diffusion orientation [010]. The capacity decay of LH lithiated cathode at slow charge is caused by bad coating in high roughness together with coarsening (250 – 300 nm) on overall particle dimensions due to the branch-like formation. There is a hysteresis in capacity decay in terms of different orientation strength between LAc and LH lithiated cathode structures. This indicates that the particle size in [010] orientation is much more definitive parameter how the particle behaves in nano or bulk region. That means AFP routed LFP nano plates exhibits more likely bulk material properties rather than nano scale, since ionic diffusion as rate determining step is enhanced at [100] orientation resultantly. As a unique strategy to AFP routed LFP materials, fragmentation may be a successful way to expose other plane orientations rather than [100].

Sub-grain boundaries of VVT based LiFePO₄ nano plates have many sub-grain boundaries as serve as a fast diffusion paths having 40 – 100 nm in thickness. Increased total surface area compensates the low electronic conductivity by forming large active double layer spreading on particle surface. Superior performance is delivered with this micro structure combining the improved ionic diffusion within shorter path and plenty grain boundaries.

Crystallographic orientation becomes an obstacle for fast rechargeability if only [010] channel length becomes higher than other directions within anisotropic particles. As indicated by electrochemical results, the nano size effect appears at fast charging operations as well as [010] orientation. Apart from crystallographic orientation, In keeping [010] orientation in concern for especially 2D morphology, size refinement favors the high rate application because of the low importance on electronic conductivity at nano size, ionic conductivity becomes rate determining step as correlated with the charge transfer reactions at surface. Increasing current stimulates more particles to charge simultaneously – instead of particle by particle mechanism – and to use very near surface portion of the particles. This means that high rate charge increases the average size limit to have nano scale properties. Therefore, critical nano

size limit cannot be considered apart from the kinetic processes that electrochemically driven by the current applied on cathode.

Widely investigated solution based, hydro/solvothermally synthesized LiFePO_4 , typically suffers from anti site defects, which especially exchanges between Li and Fe sites, circumstantially cannot allow to reach expected capacity. Therefore, it is essential to be ordered by calcination above $500\text{ }^\circ\text{C}$ to maintain relaxation accomplished⁶⁹. For LiFePO_4 synthesis, high temperature or at least high energetic procedures seem to be indispensable for high power cathode material unless nano sized crystallites are produced. Improvement up to 40% of comparable discharge capacity is obtained by US assisted sub-sequential precipitation according to other high temperature solvothermal synthesis.⁸⁵

6TH CHAPTER

6. References

1. Winter, M. & Brodd, R. J. What are batteries, fuel cells, and supercapacitors? *Chem. Rev.* **104**, 4245–4270 (2004).
2. Myung, S. & Chung, H. Preparation and characterization of LiMn₂O₄ powders by the emulsion drying method. *J. Power Sources* **84**, 32–38 (1999).
3. Shin, H. C., Park, S. Bin, Jang, H., Chung, K. Y., Cho, W. Il, Kim, C. S. & Cho, B. W. Rate performance and structural change of Cr-doped LiFePO₄/C during cycling. *Electrochim. Acta* **53**, 7946–7951 (2008).
4. Whittingham, M. S. Electrical energy storage and intercalation chemistry. *Science* **192**, 1126–1127 (1976).
5. Besenhard, J. O. & Fritz, H. P. Cathodic reduction of graphite in organic solutions of alkali and NR₄⁺ salts. *Electroanal. Chem. Interfacial Electrochem.* **53**, 329–333 (1974).
6. Yazami, R. & Tazain, P. A reversible graphite-lithium negative electrode for electrochemical generators. *J. Power Sources* **9**, 365–371 (1983).
7. Whittingham, M. S. Materials Challenges Facing Electrical Energy Storage. *MRS Bull.* **33**, 411–421 (2008).
8. Palacín, M. R. Recent advances in rechargeable battery materials: a chemist's perspective. *Chem. Soc. Rev.* **38**, 2565–2575 (2009).
9. Oh, S.-M., Oh, S. W., Myung, S.-T., Lee, S.-M. & Sun, Y.-K. The effects of calcination temperature on the electrochemical performance of LiMnPO₄ prepared by ultrasonic spray pyrolysis. *J. Alloys Compd.* **506**, 372–376 (2010).
10. Liang, C., Gao, M., Pan, H., Liu, Y. & Yan, M. Lithium alloys and metal oxides as high-capacity anode materials for lithium-ion batteries. *J. Alloys Compd.* **575**, 246–256 (2013).
11. Li, Z., Huang, J., Yann Liaw, B., Metzler, V. & Zhang, J. A review of lithium deposition in lithium-ion and lithium metal secondary batteries. *J. Power Sources* **254**, 168–182 (2014).
12. Zaghbi, K., Mauger, A., Groult, H., Goodenough, J. & Julien, C. Advanced electrodes for high power Li-ion batteries. *Materials (Basel)*. **6**, 1028–1049 (2013).

13. Ferrari, S., Lavall, R. L., Capsoni, D., Quartarone, E., Magistris, A., Mustarelli, P. & Canton, P. Influence of particle size and crystal orientation on the electrochemical behavior of carbon-coated LiFePO₄. *J. Phys. Chem. C* **114**, 12598–12603 (2010).
14. Wagemaker, M. & Mulder, F. M. Properties and promises of nanosized insertion materials for Li-ion batteries. *Acc. Chem. Res.* **46**, 1206–1215 (2013).
15. Wang, G., Liu, H., Liu, J., Qiao, S., Lu, G. M., Munroe, P. & Ahn, H. Mesoporous LiFePO₄/C nanocomposite cathode materials for high power lithium ion batteries with superior performance. *Adv. Mater.* **22**, 4944–4948 (2010).
16. Yi, T.-F., Hao, C.-L., Yue, C.-B., Zhu, R.-S. & Shu, J. A literature review and test: Structure and physicochemical properties of spinel LiMn₂O₄ synthesized by different temperatures for lithium ion battery. *Synth. Met.* **159**, 1255–1260 (2009).
17. Mizushima, K., Jones, P. C., Wiseman, P. J. & Goodenough, J. B. Li_xCoO₂ (0 < x < 1); A new cathode material for batteries of high energy density. *Mater. Res. Bull.* **15**, 783 – 789 (1980).
18. Greger R. D. & Kalle E. S. *Lithium Batteries: Research, Technology and Applications*. 24 (Nova science, 2010).
19. Yamada, A., Hosoya, M., Chung, S.-C., Kudo, Y., Hinokuma, K., Liu, K.-Y. & Nishi, Y. Olivine-type cathodes. *J. Power Sources* **119-121**, 232–238 (2003).
20. Huang, H., Yin, S.-C. & Nazar, L. F. Approaching theoretical capacity of LiFePO₄ at room temperature at high rates. *Electrochem. Solid-State Lett.* **4**, A170–A172 (2001).
21. Tarascon, J. M. & Armand, M. Issues and challenges facing rechargeable lithium batteries. *Nature* **414**, 359–367 (2001).
22. Malik, R., Abdellahi, A. & Ceder, G. A Critical review of the Li insertion mechanisms in LiFePO₄ electrodes. *J. Electrochem. Soc.* **160**, A3179–A3197 (2013).
23. Wang, L., Zhou, F., Meng, Y. S. & Ceder, G. First-principles study of surface properties of LiFePO₄: Surface energy, structure, Wulff shape, and surface redox potential. *Phys. Rev. B* **76**, 1–11 (2007).
24. Park, M., Zhang, X., Chung, M., Less, G. B. & Sastry, A. M. A review of conduction phenomena in Li-ion batteries. *J. Power Sources* **195**, 7904–7929 (2010).

25. Gaberscek, M., Dominko, R. & Jamnik, J. Is small particle size more important than carbon coating? An example study on LiFePO₄ cathodes. *Electrochem. commun.* **9**, 2778–2783 (2007).
26. Chen, J., Hsu, C., Lin, Y., Hsiao, M. & Fey, G. T. High-power LiFePO₄ cathode materials with a continuous nano carbon network for lithium-ion batteries. *J. Power Sources* **184**, 498–502 (2008).
27. Padhi, A. K., Nanjundaswamy, K. S. & Goodenough, J. B. Phospho-olivines as positive-electrode materials for rechargeable lithium batteries. *J. Electrochem. Soc.* **144**, 1184–1194 (1997).
28. Wang, Y., Sun, B., Park, J., Kim, W.-S., Kim, H.-S. & Wang, G. Morphology control and electrochemical properties of nanosize LiFePO₄ cathode material synthesized by co-precipitation combined with in situ polymerization. *J. Alloys Compd.* **509**, 1040–1044 (2011).
29. Sun, X., Sun, K., Chen, C., Sun, H. & Cui, B. Controlled preparation and surface structure characterization of carbon-coated lithium iron phosphate and electrochemical studies as cathode materials for lithium ion battery. *Int. J. Mater. Chem.* **2**, 218–224 (2012).
30. Delacourt, C., Poizot, P., Levasseur, S. & Masquelier, C. Size effects on carbon-free LiFePO₄ powders. *Electrochem. Solid-State Lett.* **9**, A352–A355 (2006).
31. Yang, M.-R., Ke, W.-H. & Wu, S.-H. Preparation of LiFePO₄ powders by co-precipitation. *J. Power Sources* **146**, 539–543 (2005).
32. Park, K. S., Son, J. T., Chung, H. T., Kim, S. J., Lee, C. H. & Kim, H. G. Synthesis of LiFePO₄ by co-precipitation and microwave heating. *Electrochem. commun.* **5**, 839–842 (2003).
33. Liu, Y. & Cao, C. Enhanced electrochemical performance of nano-sized LiFePO₄/C synthesized by an ultrasonic-assisted co-precipitation method. *Electrochim. Acta* **55**, 4694–4699 (2010).
34. Saravanan, K., Balaya, P., Reddy, M. V, Chowdari, B. V. R. & Vittal, J. J. Morphology controlled synthesis of LiFePO₄/Cnanoplates for Li-ion batteries. *Energy Environ. Sci.* **3**, 457–464 (2010).
35. Ou, X., Gu, H., Wu, Y., Lu, J. & Zheng, Y. Chemical and morphological transformation through hydrothermal process for LiFePO₄ preparation in organic-free system. *Electrochim. Acta* **96**, 230–236 (2013).
36. Jugović, D., Mitrić, M., Kuzmanović, M., Cvjetičanin, N., Marković, S., Škapin, S. & Uskoković, D. Rapid crystallization of LiFePO₄ particles by facile emulsion-mediated solvothermal synthesis. *Powder Technol.* **219**, 128–134 (2012).

37. Qin, X., Wang, J., Xie, J., Li, F. & Wang, X. Hydrothermally synthesized LiFePO₄ crystals with enhanced electrochemical properties: simultaneous suppression of crystal growth along [010] and antisite defect formation. *Phys. Chem. Chem. Phys.* **2677**, 2669–2677 (2012).
38. Wu, L., Wang, Z., Li, X., Li, L., Guo, H., Zheng, J. & Wang, X. Electrochemical performance of Ti⁴⁺-doped LiFePO₄ synthesized by co-precipitation and post-sintering method. *Trans. Nonferrous Met. Soc. China* **20**, 814–818 (2010).
39. Palomares, V., Goñi, A., Muro, I. G. De, de Meatza, I., Bengoechea, M., Miguel, O. & Rojo, T. New freeze-drying method for LiFePO₄ synthesis. *J. Power Sources* **171**, 879–885 (2007).
40. Zhecheva, E., Mladenov, M., Zlatilova, P., Koleva, V. & Stoyanova, R. Particle size distribution and electrochemical properties of LiFePO₄ prepared by a freeze-drying method. *J. Phys. Chem. Solids* **71**, 848–853 (2010).
41. Yu, W., Zhao, Y. & Rao, Q. Rapid and Continuous Production of LiFePO₄/C Nanoparticles in Super Heated Water. *Chinese J. Chem. Eng.* **17**, 171–174 (2009).
42. Xu, C., Lee, J. & Teja, A. S. Continuous hydrothermal synthesis of lithium iron phosphate particles in subcritical and supercritical water. *J. Supercrit. Fluids* **44**, 92–97 (2008).
43. Orlenius, J., Lyckfeldt, O., Kasvayee, K. a. & Johander, P. Water based processing of LiFePO₄/C cathode material for Li-ion batteries utilizing freeze granulation. *J. Power Sources* **213**, 119–127 (2012).
44. Palomares, V., Goñi, A., Gil de Muro, I., de Meatza, I., Bengoechea, M., Cantero, I. & Rojo, T. Influence of carbon content on LiFePO₄/C samples synthesized by freeze-drying process. *J. Electrochem. Soc.* **156**, A817–A821 (2009).
45. Myung, S., Komaba, S., Hirosaki, N., Yashiro, H. & Kumagai, N. Emulsion drying synthesis of olivine LiFePO₄/C composite and its electrochemical properties as lithium intercalation material. *Electrochim. Acta* **49**, 4213–4222 (2004).
46. Panero, S., Scrosati, B., Wachtler, M. & Croce, F. Nanotechnology for the progress of lithium batteries R&D. *J. Power Sources* **129**, 90–95 (2004).
47. Koleva, V., Zhecheva, E. & Stoyanova, R. A new phosphate-formate precursor method for the preparation of carbon coated nano-crystalline LiFePO₄. *J. Alloys Compd.* **476**, 950–957 (2009).
48. Koleva, V., Stoyanova, R. & Zhecheva, E. Nano-crystalline LiMnPO₄ prepared by a new phosphate–formate precursor method. *Mater. Chem. Phys.* **121**, 370–377 (2010).

49. Kang, F., Ma, J. & Li, B. Effects of carbonaceous materials on the physical and electrochemical performance of a LiFePO₄ cathode for lithium-ion batteries. *New Carbon Mater.* **26**, 161–170 (2011).
50. Xi, X., Chen, G., Nie, Z., He, S., Pi, X., Zhu, X., Zhu, J. & Zuo, T. Preparation and performance of LiFePO₄ and LiFePO₄/C cathodes by freeze-drying. *J. Alloys Compd.* **497**, 377–379 (2010).
51. Yang, S., Hu, M., Xi, L., Ma, R., Dong, Y. & Chung, C. Y. Solvothermal synthesis of monodisperse LiFePO₄ micro hollow spheres as high performance cathode material for lithium ion batteries. *Appl. Mater. Interfaces* **5**, 8961–8967 (2013).
52. Bang, J. H. & Suslick, K. S. Applications of ultrasound to the synthesis of nanostructured materials. *Adv. Mater.* **22**, 1039–1059 (2010).
53. Kim, K. & Kim, K. Ultrasonics sonochemistry ultrasound assisted synthesis of nano-sized lithium cobalt oxide. *Ultrason. Sonochem.* **15**, 1019–1025 (2008).
54. Zhu, S., Guo, J., Dong, J., Cui, Z., Lu, T., Zhu, C. & Zhang, D. Ultrasonics Sonochemistry Sonochemical fabrication of Fe₃O₄ nanoparticles on reduced graphene oxide for biosensors. *Ultrason. - Sonochemistry* **20**, 872–880 (2013).
55. Ruan, Q., Zhu, Y., Zeng, Y., Qian, H., Xiao, J., Xu, F., Zhang, L. & Zhao, D. Ultrasonic-irradiation-assisted oriented assembly of ordered monetite nanosheets stacking. *J. Phys. Chem. B* **113**, 1100–1106 (2009).
56. Tang, B., Yuan, L., Shi, T., Yu, L. & Zhu, Y. Preparation of nano-sized magnetic particles from spent pickling liquors by ultrasonic-assisted chemical co-precipitation. *J. Hazard. Mater.* **163**, 1173–1178 (2009).
57. Suslick, K. S. Sonochemistry. *Science* **247**, 1439–1445 (1990).
58. Edward, F. B. & Suslick, K. S. The temperature of cavitation. *Science* **253**, 1397–1399 (1991).
59. Suslick, K. S. & Price, G. J. Applications of ultrasound to materials chemistry. *Annu. Rev. Mater. Sci.* **29**, 295–326 (1999).
60. Castro, M. D. L. De. Ultrasound-assisted crystallization (sonocrystallization). *Ultrason. Sonochem.* **14**, 717–724 (2007).
61. Zheng, L. & Sun, D. Innovative applications of power ultrasound during food freezing processes — a review. *Trends Food Sci. Technol.* **17**, 16–23 (2006).
62. Roy, S. D., Chimankar, O. P., Lanje, N. Y. & Rangari, A. D. High power ultrasonic for crystalization. *Int. J. Sci. Res. Proceeding*, 320–321 (2015).
63. Zeiger, B. W. & Suslick, K. S. Sonofragmentation of molecular crystals. *J. Am. Chem. Soc.* **133**, 14530–14533 (2011).

64. Liu, Y. & Cao, C. Enhanced electrochemical performance of nano-sized LiFePO₄/C synthesized by an ultrasonic-assisted co-precipitation method. *Electrochim. Acta* **55**, 4694–4699 (2010).
65. Kim, H., Kim, J., Kim, W., Koo, H., Bae, D. & Kim, H. Synthesis of LiFePO₄/C cathode materials through an ultrasonic-assisted rheological phase method. *J. Alloys Compd.* **509**, 5662–5666 (2011).
66. Shen, P., Huang, Y., Liu, L., Jia, D. & Guo, Z. Synthesis and electrochemical performance of LiCr_xMn_{2-x}O₄ (x=0,0.02,0.05,0.08,0.10) powders by ultrasonic coprecipitation. *J. Solid State Electrochem.* **10**, 929–933 (2005).
67. Yi, T., Hu, X. & Gao, K. Synthesis and physicochemical properties of LiAl_{0.05}Mn_{1.95}O₄ cathode material by the ultrasonic-assisted sol–gel method. *J. Power Sources* **162**, 636–643 (2006).
68. Jugovic, D., Mitric, M., Cvjeticanin, N., Jancar, B., Mentus, S. & Uskokovic, D. Synthesis and characterization of LiFePO₄/C composite obtained by sonochemical method. *Solid State Ionics* **179**, 415–419 (2008).
69. Chen, J. & Graetz, J. Study of antisite defects in hydrothermally prepared LiFePO₄ by in situ x-ray diffraction. *Appl. Mater. Interfaces* **3**, 1380–1384 (2011).
70. Gim, J., Song, J., Nguyen, D., Hilmy Alfaruqi, M., Kim, S., Kang, J., Rai, A. K., Mathew, V. & Kim, J. A two-step solid state synthesis of LiFePO₄/C cathode with varying carbon contents for Li-ion batteries. *Ceram. Int.* **40**, 1561–1567 (2014).
71. Chen, Z., Ren, Y., Qin, Y., Wu, H., Ma, S., Ren, J., He, X., Sun, Y.-K. & Amine, K. Solid state synthesis of LiFePO₄ studied by in situ high energy x-ray diffraction. *J. Mater. Chem.* **21**, 5604–5609 (2011).
72. Kosova, N. On mechanochemical preparation of materials with enhanced characteristics for lithium batteries. *Solid State Ionics* **172**, 181–184 (2004).
73. Maccario, M., Croguennec, L., Wattiaux, a, Suard, E., Lecras, F. & Delmas, C. C-containing LiFePO₄ materials — Part I: Mechano-chemical synthesis and structural characterization. *Solid State Ionics* **179**, 2020–2026 (2008).
74. Yamada, A., Chung, S. C. & Hinokuma, K. Optimized LiFePO₄ for lithium battery cathodes. *J. Electrochem. Soc.* **148**, A224–A229 (2001).
75. Fey, G. T.-K., Huang, K.-P., Kao, H.-M. & Li, W.-H. A polyethylene glycol-assisted carbothermal reduction method to synthesize LiFePO₄ using industrial raw materials. *J. Power Sources* **196**, 2810–2818 (2011).
76. Wang, L., Huang, Y., Jiang, R. & Jia, D. Preparation and characterization of nano-sized LiFePO₄ by low heating solid-state coordination method and microwave heating. *Electrochim. Acta* **52**, 6778–6783 (2007).

77. Bilecka, I., Hintennach, A., Djerdj, I., Novák, P. & Niederberger, M. Efficient microwave-assisted synthesis of LiFePO₄ mesocrystals with high cycling stability. *J. Mater. Chem.* **19**, 5125 (2009).
78. Guo, X.-F., Zhan, H. & Zhou, Y.-H. Rapid synthesis of LiFePO₄/C composite by microwave method. *Solid State Ionics* **180**, 386–391 (2009).
79. Yang, S., Zavalij, P. Y. & Stanley Whittingham, M. Hydrothermal synthesis of lithium iron phosphate cathodes. *Electrochem. commun.* **3**, 505–508 (2001).
80. Chen, J., Vacchio, M. J., Wang, S., Chernova, N., Zavalij, P. Y. & Whittingham, M. S. The hydrothermal synthesis and characterization of olivines and related compounds for electrochemical applications. *Solid State Ionics* **178**, 1676–1693 (2008).
81. Zhao, R., Hung, I.-M., Li, Y.-T., Chen, H. & Lin, C.-P. Synthesis and properties of Co-doped LiFePO₄ as cathode material via a hydrothermal route for lithium-ion batteries. *J. Alloys Compd.* **513**, 282–288 (2012).
82. Kuwahara, A., Suzuki, S. & Miyayama, M. Hydrothermal synthesis of LiFePO₄ with small particle size and its electrochemical properties. *J Electroceram* **24**, 69–75 (2010).
83. Yang, H., Wu, X., Cao, M. & Guo, Y. Solvothermal synthesis of LiFePO₄ hierarchically dumbbell-like microstructures by nanoplate self-assembly and their application as a cathode material in lithium-ion. *J. Phys. Chem. C* **113**, 3345–3351 (2009).
84. Nan, C., Lu, J., Chen, C., Peng, Q. & Li, Y. Solvothermal synthesis of lithium iron phosphate nanoplates. *J. Mater. Chem.* **21**, 9994–9996 (2011).
85. Zhu, J., Fiore, J., Li, D., Kinsinger, N. M., Wang, Q., DiMasi, E., Guo, J. & Kisailus, D. Solvothermal synthesis, development, and performance of LiFePO₄ nanostructures. *Cryst. Growth Des.* **13**, 4659–4666 (2013).
86. Yang, S., Zhou, X., Zhang, J. & Liu, Z. Morphology-controlled solvothermal synthesis of LiFePO₄ as a cathode material for lithium-ion batteries. *J. Mater. Chem.* **20**, 8086–8091 (2010).
87. Sanchez, M., Brito, G., Fantini, M., Goya, G. & Matos, J. Synthesis and characterization of LiFePO₄ prepared by sol–gel technique. *Solid State Ionics* **177**, 497–500 (2006).
88. Peng, W., Jiao, L., Gao, H., Qi, Z., Wang, Q., Du, H., Si, Y., Wang, Y. & Yuan, H. A novel sol–gel method based on FePO₄·2H₂O to synthesize submicrometer structured LiFePO₄/C cathode material. *J. Power Sources* **196**, 2841–2847 (2011).
89. Li, X., Wang, W., Shi, C., Wang, H. & Xing, Y. Structural and electrochemical characterization of LiFePO₄/C prepared by a sol–gel route

- with long- and short-chain carbon sources. *J. Solid State Electrochem.* **13**, 921–926 (2008).
90. Trudeau, M. L., Laul, D., Veillette, R., Serventi, a. M., Mauger, a., Julien, C. M. & Zaghbi, K. In situ high-resolution transmission electron microscopy synthesis observation of nanostructured carbon coated LiFePO₄. *J. Power Sources* **196**, 7383–7394 (2011).
 91. Chen, Z. & Dahn, J. R. Reducing carbon in LiFePO₄/C composite electrodes to maximize specific energy, volumetric energy, and tap density. *J. Electrochem. Soc.* **149**, A1184–A1189 (2002).
 92. Lutterotti, L., Matthies, S. & Wenk, H. MAUD: a friendly Java program for material analysis using diffraction. *News. - Int. Union Crystallography* **21**, 14–15 (1999).
 93. He, L., Zhao, Z., Liu, X., Chen, A. & Si, X. Thermodynamics analysis of LiFePO₄ precipitation from Li–Fe(II)–P–H₂O system at 298 K. *Trans. Nonferrous Met. Soc. China* **22**, 1766–1770 (2012).
 94. Stern, K. H. High temperature properties and decomposition of inorganic salts Part 3. Nitrates and Nitrites.pdf. *J. Phys. Chem. Ref. Data* **1**, 747–772 (1972).
 95. Ruiz, M. L., Lick, I. D., Ponzi, M. I., Castellón, E. R., Jiménez-López, A. & Ponzi, E. N. Thermal decomposition of supported lithium nitrate catalysts. *Thermochim. Acta* **499**, 21–26 (2010).
 96. Chen, G., Song, X. & Richardson, T. J. Electron microscopy study of the LiFePO₄ to FePO₄ phase transition. *Electrochem. Solid-State Lett.* **9**, A295–A298 (2006).
 97. Miao, W. U., Zhaohui, W., Lixia, Y., Wuxing, Z. & Xianluo, H. U. Morphology-controllable solvothermal synthesis of nanoscale LiFePO₄ in a binary solvent. *Chinese Sci. Bull.* **57**, 4170–4175 (2012).
 98. Alyoshin, V. A., Pleshakov, E. A., Ehrenberg, H. & Mikhailova, D. Platelike LiMPO₄ (M=Fe, Mn, Co, Ni) for possible application in rechargeable Li ion batteries: Beyond nanosize. *J. Phys. Chem. C* **118**, 17426–17435 (2014).
 99. Ellis, B., Kan, W. H., Makahnouk, W. R. M. & Nazar, L. F. Synthesis of nanocrystals and morphology control of hydrothermally prepared LiFePO₄. *J. Mater. Chem.* **17**, 3248–3254 (2007).
 100. Xie, X., Zhou, Y., Bi, H., Yin, K., Wan, S. & Sun, L. Large-range control of the microstructures and properties of three-dimensional porous graphene. *Sci. Rep.* **3**, 1–6 (2013).
 101. Ping Ong, S., Wang, L., Kang, B. & Ceder, G. Li–Fe–P–O₂ phase diagram from first principles calculations. *Chem. Mater.* **20**, 1798–1807 (2008).

102. Kim, D.-K., Park, H.-M., Jung, S.-J., Jeong, Y. U., Lee, J.-H. & Kim, J.-J. Effect of synthesis conditions on the properties of LiFePO₄ for secondary lithium batteries. *J. Power Sources* **159**, 237–240 (2006).
103. Herle, P. S., Ellis, B., Coombs, N. & Nazar, L. F. Nano-network electronic conduction in iron and nickel olivine phosphates. *Nat. Mater.* **3**, 147–1452 (2004).
104. Chen, J., Bai, J., Chen, H. & Graetz, J. In situ hydrothermal synthesis of LiFePO₄ studied by synchrotron x-ray diffraction. *J. Phys. Chem. Lett.* **2**, 1874–1878 (2011).
105. Gao, P., Yan, B., Wang, L., Liu, W., Gong, W. & Liu, X. Influence of calcined temperatures on the microstructure and electrochemical properties of LiFePO₄/C nano-particles with a core-shell structure and It's thermal stability study. *J. Ceram. Process. Res.* **16**, 137–145 (2015).
106. Kuwahara, A., Suzuki, S. & Miyayama, M. High-rate properties of LiFePO₄/carbon composites as cathode materials for lithium-ion batteries. *Ceram. Int.* **34**, 863–866 (2008).
107. Li, J., Qu, Q., Zhang, L., Zhang, L. & Zheng, H. A monodispersed nano-hexahedral LiFePO₄ with improved power capability by carbon-coatings. *J. Alloys Compd.* **579**, 377–383 (2013).
108. Jugović, D., Cvjetičanin, N., Mitrić, M. & Mentus, S. Comparison between different LiFePO₄ synthesis routes. *Mater. Sci. Forum* **555**, 225–230 (2007).
109. Doicrycz, S. J. & Suslick, K. S. Interparticle collisions driven by ultrasound. *Science* **247**, 1067–1069 (1990).
110. Cras, L. & Bourbon, C. Comparison between different LiFePO₄ synthesis routes and their influence on its physico-chemical properties. *J. Power Sources* **119-121**, 252–257 (2003).
111. Ravet, N., Besner, S., Simoneau, M., Vallee, A., Armand, M. & Magnan, J. Electrode materials with high surface conductivity. **2**, (2013).
112. Ravet, N., Magnan, J.-F., Gauthier, J. M. & Armand, M. Lithium iron phosphate: towards an universal electrode material. in *ICMAT 2001, International Conference on Materials for Advanced Technologies* (2001).
113. Li, H., Li, H., Guo, Z. & Liu, Y. The application of power ultrasound to reaction crystallization. *Ultrason. Sonochem.* **13**, 359–363 (2006).
114. Technology, C., Ox, O. & Kingdom, U. Sonocrystallization: The Use of Ultrasound for Improved Industrial Crystallization. *Org. Process Res. Dev.* **9**, 923–932 (2005).

115. Haruta, M. & Delmon, B. Preparation of homodisperse solids. *J. Chim. Phys.* **83**, 859–868 (1986).
116. Aimable, A., Aymes, D., Bernard, F. & Cras, F. Le. Characteristics of LiFePO₄ obtained through a one step continuous hydrothermal synthesis process working in supercritical water. *Solid State Ionics* **180**, 861–866 (2009).
117. Li-hua, H. E., Zhong-wei, Z., Xu-heng, L. I. U., Ai-liang, C. & Xiu-fen, S. I. Thermodynamics analysis of LiFePO₄ precipitation from Li–Fe(II)–P–H₂O system at 298 K. *Trans. Nonferrous Met. Soc. China* **22**, 1766–1770 (2012).
118. Lyczko, N., Espitalier, F., Louisnard, O. & Schwartzentruber, J. Effect of ultrasound on the induction time and the metastable zone widths of potassium sulphate. *Chem. Eng. J.* **86**, 233–241 (2002).
119. <http://www.iycr2014.org/participate/crystal-growing-competition/info-for-newcomers/how-to-grow>.
120. Mullin, J. W. *Crystallization*. 193–194 (Elsevier, 2001).
121. Lee, J. & Teja, A. S. Characteristics of lithium iron phosphate (LiFePO₄) particles synthesized in subcritical and supercritical water. *J. Supercrit. Fluids* **35**, 83–90 (2005).
122. Nemamcha A, Rehspringer JL, K. D. Synthesis of palladium nanoparticles by sonochemical reduction of palladium(II) nitrate in aqueous solution. *J Phys Chem B* **110**, 383–387 (2006).
123. Zhang, J., Liu, H., Wang, Z. & Ming, N. Synthesis of high purity Au nanobelts via the one-dimensional self-assembly of triangular Au nanoplates. *Appl. Phys. Lett.* **91**, 1–2 (2007).
124. Wu, C., Xie, J., Cao, G. & Zhang, S. Ordered LiMPO₄ (M=Fe, Mn) nanorods synthesized from NH₄MPO₄·H₂O microplates by stress involved ion exchange for Li-ion batteries. *CrystEngComm* **16**, 2239–2245 (2014).
125. Oh, S. W., Myung, S.-T., Oh, S.-M., Oh, K. H., Amine, K., Scrosati, B. & Sun, Y.-K. Double carbon coating of LiFePO₄ as high rate electrode for rechargeable lithium batteries. *Adv. Mater.* **22**, 4842–4845 (2010).
126. Ni, H., Liu, J. & Fan, L.-Z. Carbon-coated LiFePO₄-porous carbon composites as cathode materials for lithium ion batteries. *Nanoscale* **5**, 2164–2168 (2013).
127. Kim, J.-K., Cheruvally, G. & Ahn, J.-H. Electrochemical properties of LiFePO₄/C synthesized by mechanical activation using sucrose as carbon source. *J. Solid State Electrochem.* **12**, 799–805 (2007).
128. Beckett, S. T., Francesconi, M. G., Geary, P. M., Mackenzie, G. & Maulny, A. P. E. DSC study of sucrose melting. *Carbohydr. Res.* **341**, 2591–2599 (2006).

129. Spong, A. D., Vitins, G. & Owen, J. R. A solution-precursor synthesis of carbon-coated LiFePO₄ for Li-ion cells. *J. Electrochem. Soc.* **152**, A2376–A2382 (2005).
130. Van der Ven, A., Bhattacharya, J. & Belak, A. Understanding Li diffusion in Li-intercalation compounds. *Acc. Chem. Res.* **46**, 1216–1225 (2013).
131. Zhang, S. M., Zhang, J. X., Xu, S. J., Yuan, X. J. & He, B. C. Li ion diffusivity and electrochemical properties of FePO₄ nanoparticles acted directly as cathode materials in lithium ion rechargeable batteries. *Electrochim. Acta* **88**, 287–293 (2013).
132. Srinivasan, V. & Newman, J. Discharge model for the lithium iron-phosphate electrode. *J. Electrochem. Soc.* **151**, A1517–A1529 (2004).
133. Srinivasan, V. & Newman, J. Existence of path-dependence in the LiFePO₄ electrode. *Electrochem. Solid-State Lett.* **9**, A110–A114 (2006).
134. Malik, R., Burch, D., Bazant, M. & Ceder, G. Particle size dependence of the ionic diffusivity. *Nano Lett.* **10**, 4123–4127 (2010).
135. Delacourt, C., Poizot, P., Levasseur, S. & Masquelier, C. Size effects on carbon-free LiFePO₄ powders. *Electrochem. Solid-State Lett.* **9**, A352–A355 (2006).
136. Kim, D.-H. & Kim, J. Synthesis of LiFePO₄ nanoparticles in polyol medium properties. *Electrochem. Solid-State Lett.* **9**, A439–A442 (2006).
137. Heubner, C., Schneider, M. & Michaelis, A. Investigation of charge transfer kinetics of Li-intercalation in LiFePO₄. *J. Power Sources* **288**, 115–120 (2015).
138. Dominko, R., Bele, M., Gaberscek, M., Remskar, M., Hanzel, D., Pejovnik, S. & Jamnik, J. Impact of the carbon coating thickness on the electrochemical performance of LiFePO₄/C composites. *J. Electrochem. Soc.* **152**, A607–A610 (2005).
139. Recham, N., Casas-Cabanas, M., Cabana, J., Grey, C. P., Jumas, J.-C., Dupont, L., Armand, M. & Tarascon, J.-M. Formation of a complete solid solution between the triphylite and fayalite olivine structures. *Chem. Mater.* **20**, 6798–6809 (2008).
140. Liu, H., Strobridge, F. C., Borkiewicz, O. J., Wiaderek, K. M., Chapman, K. W., Chupas, P. J. & Grey, C. P. Capturing metastable structures during high-rate cycling of LiFePO₄ nanoparticle electrodes. *Science* **344**, 1480–1487 (2014).
141. Abdellahi, A., Akyildiz, O., Malik, R., Thornton, K. & Ceder, G. Particle-size and morphology dependence of the preferred interface orientation in LiFePO₄ nano-particles. *J. Mater. Chem. A* **2**, 15437–15447 (2014).

142. Delacourt, C., Poizot, P., Morcrette, M., Tarascon, J. & Masquelier, C. One-step low-temperature route for the preparation of electrochemically active LiMnPO_4 powders. *Chem. Mater.* **16**, 93–99 (2004).
143. Barker, J., Saidi, M. Y. & Swoyer, J. L. Lithium iron(II) phospho-olivines prepared by a novel carbothermal reduction method. *Electrochem. Solid-State Lett.* **6**, A53–A55 (2003).
144. Delmas, C., Maccario, M., Croguennec, L., Le Cras, F. & Weill, F. Lithium deintercalation in LiFePO_4 nanoparticles via a domino-cascade model. *Nat. Mater.* **7**, 665–671 (2008).
145. Brunetti, G., Robert, D., Rouvi, J. L., Rauch, E. F., Martin, J. F. & Colin, J. F. Confirmation of the domino-cascade model by $\text{LiFePO}_4/\text{FePO}_4$ precession electron diffraction. *Chem. Mater.* **23**, 4515–4524 (2011).
146. Chueh, W. C., Gabaly, F. El, Sugar, J. D., Bartelt, N. C., Mcdaniel, A. H., Fenton, K. R., Zavadil, K. R., Tyliczszak, T., Lai, W. & Mccarty, K. F. Intercalation pathway in many-particle LiFePO_4 electrode revealed by nanoscale state-of-charge mapping. *Nano Lett.* **13**, 856–872 (2013).
147. Sugar, J. D., El Gabaly, F., Chueh, W. C., Fenton, K. R., Tyliczszak, T., Kotula, P. G. & Bartelt, N. C. High-resolution chemical analysis on cycled LiFePO_4 battery electrodes using energy-filtered transmission electron microscopy. *J. Power Sources* **246**, 512–521 (2014).

VITA

ŞAFAK DOĞU

Academic Affiliation: Department of Micro and Nanotechnology and Metallurgical and Department of Materials Engineering, Middle East Technical University

Date/Place of Birth: 10.02.1981 / Ankara

Posta Address: ODTÜ, Metalurji ve Malzeme Bölümü, D-214, 06800, Ankara-Turkey

Phone: +90-312-210-5831

E-mail: safak.dogu@gmail.com, e169691@metu.edu.tr

EDUCATION

University	Subject of Study	Degree	Country	Graduation
Middle East Technical University	Micro and Nanotechnology	Ph.D.	Turkey	2015
Gazi University	Chemical Engineering	M.Sc.	Turkey	2008
Gazi University	Chemical Engineering	B.Sc.	Turkey	2005

ACADEMIC EXPERIENCE

University	Department	Country	Title	Dates
Middle East Technical University	Metallurgical and Materials Engineering	Turkey	Research Asisstant	04/2009-10/2013
Gazi University	Chemical Engineering	Turkey	Research Asisstant	03/2008-03/2009

WORK EXPERIENCE

Institution	Department	Country	Title	Dates
Yigit Battery	R&D and Engineering	Turkey	Chief of R&D	04/2009-10/2013
GIGATEK	Engineering	Turkey	Project Engineer	12/2006-07/2007

AREAS OF EXPERTISE

Nanoscience, Battery manufacturing, Lithium-ion batteries, Lead-Acid batteries, Material processing and characterization, Electric vehicle technology, Crystallization, Sonocrystallization, Fuel cells, Solar cells, Energy storage technologies, Hydrogen production, Coal industry processing, Biodiesel production.

RESEARCH EXPERIENCE

Materials characterization and structural analysis:

Galvanostatic and potentiostatic tests, Electrochemical Impedance Spectroscopy (EIS), Conductivity measurements, CV by making button cell configuration, Scanning electron microscopy (SEM), Transmission Electron Microscopy (TEM), Selected Area Electron Diffraction (SAED) analysis, Polishing, Grinding equipment, Mounting press, Cross-sectional TEM-sample preparation techniques, Electron Back-Scattered Diffraction (EBSD), X-Ray powder Diffraction (XRD), Rietveld refinement, X-Ray Fluorescence (XRF), Raman spectroscopy; Fourier transform infrared spectroscopy (FTIR), BET and mercury porosimetry, Differential Scanning Calorimetry (DSC); Thermal Gravimetric Analysis (TGA); Energy Dispersive X-ray spectroscopy (EDX), Cyclic Voltammetry (CV), Gas Chromatography (GC), Electrochemical test bench and setups (Solartrone, Versastat, CHI), Optical microscopy, ultraviolet-visible spectroscopy (UV-Vis)

Synthesis techniques:

Co-precipitation, Hydrothermal synthesis, Sonocrystallization, Lyophilization, Spray pyrolysis, Chemical Vapor Deposition (CVD), Electro-catalytic oxidation, Membrane operations, esterification, Leaching, separation processes.

Experience in software:

GSAS, MAUD, OriginPro, ImageJ, Carine, Digital Micrograph, CorrWare, ChemCAD, AutoCAD(3D), Peak Fit, MATLAB, Simulink, Polymath, Fortran, MS Project, Microsoft Office, Linux (suse).

AWARDS

Ph.D. scholarship from Ministry of Science, Industry and Technology (project no. 00714.STZ.2010-2 SANTEZ) (2010-2013)

PERSONAL DEVELOPMENT

SPC, MSA, and FMEA (Bureau VERITAS, Feb 2012), AMDEC, ANPQP, PPAP, and Process Auditor (Renault Automotive Factory-Bursa, March 2009)

PUBLICATIONS

S. Dogu, M. K. Aydinol, Investigation on cold cranking performance of SLI batteries produced with nucleation additive in their positive and negative electrodes, EnCAMP Proceedings, May 2011, Cappadocia, Turkey

S. Dogu, M. K. Aydinol, A study on the cold cranking capability of SLI batteries having a tetra-basic lead sulfate nucleation additive in their positive and negative electrodes 12th European Lead-Acid Battery Conference Proceedings, September 2010, Istanbul, Turkey

S. Dogu, U. Gunduz Zafer, O.M. Dogan, T. Aydemir, B.Z. Uysal, Hydrogen production via electrolysis; Energy efficiency and cell designs” UKMK-8 Proceedings, Aug 2008, Inonu Univ.,Malatya, Turkey

CERTIFIED INDUSTRIAL DESIGNS

Battery electronic voltage display (Akıllı Akü-Smart Battery), 2011, Turkish Patent Institution (TPE)

Battery electronic failure mode inspection and wireless data analysis system (Akıllı Akü-Smart Battery), 2011, TPE

Electrolyte circulation apparatus for formation charging of lead-acid batteries, 2012, TPE

New design of high current collector for lead-acid batteries (Tetra), 2012, TPE

Battery grid compression apparatus, 2013, TPE

INDUSTRIAL EXPERIENCE

Management of a Pilot Plant (10MWh/yr) installation with process equipment for production of large pouch type Li-ion batteries

First production of Li-ion battery cells (20-30Ah) in Turkey for automotive use, and Ramp-up activities on process (mixing, coating, stacking, cell assembly making, formation charging and quality analysis)

Product designs, process specifications and optimization for cost reduction Lead-Acid battery production

Preparation of process and material instructions, technical specifications, installation and ramp-up procedure for all type of Lead-Acid battery production equipment (SLI, Gel, stationary, marine, military etc.)

Leading to funded R&D projects and Foundation of Yigit Battery Corp. R&D Center authorized by Ministry of Science and Technology in Turkey

Design and development of enhanced flooded type stop & start batteries, co-designing project with Renault S.A.

Research on high performance Lead-acid battery electrode materials

Project assistant in the project of “Reclamation of Turkish Lignite; Humic Acid and CMA Production”, experimental research, design, installation of a pilot plant and start-up (supported by Turkish Coal Enterprises – TKİ Humas)

Research assistant in the project of “Plant design on canola oil extraction and esterification for bio-diesel production” Clean Energy Research and Application

Project Engineer in GIGATEK responsible for air duct design and cost estimation for industrial and medical applications